MECHANICS, DYNAMICS, AND STABILITY OF ORTHOGONAL TURN-MILLING OPERATION

by

KAVEH RAHIMZADEH BERENJI

Submitted to the Graduate School of Engineering and Natural Sciences

in partial fulfilment of the requirements for the degree of

Doctor of Philosophy

Sabancı University

June 2022

MECHANICS, DYNAMICS, AND STABILITY OF ORTHOGONAL TURN-MILLING OPERATION

Approval Date: 29.06.2022

ABSTRACT

MECHANICS, DYNAMICS, AND STABILITY OF ORTHOGONAL TURN-MILLING OPERATION

KAVEH RAHIMZADEH BERENJI

Manufacturing Engineering, Ph.D. Dissertation, June 2022

Thesis supervisor: Prof. Dr. Erhan Budak

Keywords: Turn-milling, Chatter Stability, Special Tools, Structural Dynamics

As the demand for higher quality and productivity increases in industry, multi-tasking machine tools attract increasing attention due to their ability to produce complex parts in a single set-up. The mill-turn machining center is a multi-tasking machine tool capable of performing a variety of machining operations simultaneously, including turning, drilling, boring, and multi-axis milling. As a multi-axis machining operation, turn-milling is a combination of milling and turning processes, in which the material is removed as a result of simultaneous rotations of the cutter and workpiece and translational feed of the tool. While turn-milling offers several advantages in manufacturing large-scale parts with hard-to-cut materials, it presents specific challenges in terms of surface form errors, process mechanics, and dynamics. Improper selection of process parameters, tool geometry, and eccentricity may result in undesired form errors and excessive cutting forces leading to workpiece, tool, and machine component failures. Moreover, self-excited chatter vibration may occur, leading to poor surface finish and tool failure.

In this study, process kinematics and cutter-workpiece engagement are modeled for orthogonal turn-milling. A novel mathematical uncut chip geometry model for the side and minor edges of the tool is presented. Based on the chip geometry and cutting kinematics, a guideline is developed to avoid surface form errors, namely cusps, while increasing productivity. The cutting forces resulting from minor and side cutting edges are calculated analytically and verified through experiments. The effect of eccentricity on cutter-workpiece engagement and cutting forces is presented.

A fully analytical model is developed to predict the stability of orthogonal turn-milling in the discrete-time and frequency domains for the first time in the literature. In this regard, the regenerative dynamic chip thickness in feed, cross-feed, and axial are modeled, and the corresponding directional coefficients are formulated mathematically. A novel approach is proposed to calculate the varying time delay caused by the simultaneous rotation of the tool and workpiece. The stability diagrams are computed by solving the coupled time-varying delayed differential equations using semi-discretization and zero-order approximation methods. The effect of eccentricity on process stability is discussed for both end mills and inserted tools. The process parameter selection approach is proposed to achieve the highest stable depth of cut and cusp-free surface.

The verified models for the mechanics and dynamics of orthogonal turn-milling are generalized to implement serrated and crest-cut tools. The cutting forces are calculated analytically using the updated cutter-workpiece engagement model and verified experimentally. The stability of orthogonal turn-milling using crest-cut tools is predicted in both the discrete-time and frequency domains for the first time in the literature. Another novel study is performed to study the effectiveness and performance of standard, variable-pitch, and crest-cut tools on chatter suppression in milling thin-walled parts. The novel stability maps are generated based on varying stability limits caused by in-process workpiece dynamics. Using the obtained stability maps, the performance of different cutting strategies is compared, considering productivity and surface finish quality.

As the main contributors to the stability of a process, the dynamics of spindle and workpiece assemblies are modeled analytically and verified through experiments. The spindle shaft dynamics are modeled based on receptance coupling theory. Then a predictive bearing dynamics model is coupled with the shaft's model using the structural modification technique. The model can predict spindle dynamics at different speeds. A similar approach is used to model in-process cylindrical workpiece dynamics considering contact mechanics.

This thesis proposes comprehensive physics-based digital models of orthogonal turn-milling that predict the most productive cutting conditions with improved part quality for different types of tools. The presented models encompass the process parameters as well as the machine tool structural dynamics. The presented models can be used in industry either at the process planning stage to avoid costly physical trials or during the process for monitoring and fault-detection purposes.

ÖZET

DİK FREZEYLE TORNALAMA İŞLEMİNİN MEKANİĞİ, DİNAMİĞİ, VE KARARLILIĞI

KAVEH RAHIMZADEH BERENJI

Üretim Mühendisliği, Doktora Tezi, Haziran 2022

Tez Danışmanı: Prof. Dr. Erhan Budak

Anahtar Kelimeler: Frezeyle tornalama, Tırlama kararlılığı, Özel takımlar, Yapısal Dinamik

Endüstride daha yüksek kalite ve üretkenlik talebi arttıkça, çok amaçlı takım tezgahları, tek bir kurulumda karmaşık parçalar üretebilme yetenekleri nedeniyle artan bir ilgi görmektedir. Freze-tornalama (mill-turn) işleme merkezleri, tornalama, delme, delik işleme ve çok eksenli frezeleme dahil olmak üzere çeşitli talaşlı imalat operasyonlarını aynı anda gerçekleştirebilen çok amaçlı bir takım tezgahıdır. Çok eksenli bir talaş kaldırma işlemi olarak tanınan frezeyle tornalama (turn-milling), kesici ve iş parçasının aynı anda döndürülmesi ve takımın ilerlemesinin bir sonucu olarak malzemenin kaldırıldığı frezeleme ve tornalama işlemlerinin bir kombinasyonudur. Frezeyle tornalama, kesilmesi zor malzemelerle büyük ölçekli parçaların üretiminde çeşitli avantajlar sunarken, yüzey biçimi hataları, proses mekaniği ve dinamikler açısından belirli zorluklar içerir. Proses parametrelerinin, takım geometrisinin ve eksantrikliğin yanlış seçilmesi, istenmeyen kalite hatalarına ve iş parçası, takım ve makine arızalarına yol açabilecek aşırı kesme kuvvetlerine neden olabilir. Ayrıca, zayıf yüzey kalitesine ve takım kırılmasına yol açan, tırlama titreşimi meydana gelebilir.

Bu çalışmada, dik torna frezeleme için proses kinematiği ve kesici-iş parçası kesişimi (cutter-workpiece engagement) modellenmiştir. Takımın yan ve alt kenarları için yeni bir matematiksel kesilmemiş talaş geometrisi modeli sunulmuştur. Talaş geometrisi ve kesme kinematiğine dayalı olarak, üretkenliği arttırırken yüzey form hatalarından, yani çıkıntılardan kaçınmak için matematiksel bir metot geliştirilmiştir. Alt ve yan kesme

kenarlarından kaynaklanan kesme kuvvetleri analitik olarak hesaplanıp ve deneylerle doğrulanmıştır. Eksantrikliğin kesici-iş parçası kesişimi ve kesme kuvvetleri üzerindeki etkisi sunulmuştur.

Dik frezeyle tornalamanın kararlılık modeli literatürde ilk kez ayrık zaman ve frekans alanlarında tam analitik bir model geliştirilmiştir. Bu bağlamda, 3 boyuttaki rejeneratif dinamik talaş kalınlığı modellenme ve karşılık gelen yön katsayıları matematiksel olarak formüle edilmiştir. Takım ve iş parçasının aynı anda dönmesinden kaynaklanan değişen zaman gecikmesini hesaplaması için yeni bir yaklaşım önerilmiştir. Kararlılık diyagramları, kısmi-ayrıştırma ve sıfır dereceli yaklaşım yöntemleri kullanılarak birleştirilmiş zamanla değişen gecikmeli diferansiyel denklemlerin çözülmesiyle hesaplanmıştır. Eksantrikliğin proses stabilitesi üzerindeki etkisi hem parmak frezeler hem de uçlu takımlar için tartışılmıştır. İşlem parametresi seçim yaklaşımı, en yüksek kararlı kesme derinliğini ve hatasız yüzey elde etmek için önerilmiştir. Dik frezeyle tornalama mekaniği ve dinamiği için doğrulanmış modelleri, tırtıklı ve dalgalı yüzeyli (Crest-Cut) takımlara uygulama amacıyla genelleştirilmiştir. Kesme kuvvetleri, güncellenmiş kesici-iş parçası kesişim modeli kullanılarak analitik olarak hesaplanıp deneysel olarak doğrulanmıştır. Crest-cut takımları kullanarak dik frezeyle tornalama kararlılığı, literatürde ilk kez hem ayrık zaman hem de frekans alanlarında tahmin edilmektedir. İnce cidarlı parçaların frezelenmesinde tırlama bastırmada standart, değişken aralıklı ve crest-cut takımların etkinliğini ve performansını incelemek için başka bir yeni çalışma gerçekleştirilmiştir. Yeni stabilite haritaları, proses içi iş parçası dinamiklerinin neden olduğu değişken stabilite limitlerine dayalı olarak oluşturulmuştur. Elde edilen stabilite haritaları kullanılarak, verimlilik ve yüzey kalitesi dikkate alınarak farklı kesme stratejilerinin performansı karşılaştırılmıştır. Bir sürecin kararlılığına ana katkıda bulunanlar olarak, iş mili ve iş parçası düzeneklerinin dinamikleri analitik olarak modellenir ve deneylerle doğrulanır. İş mili dinamiği, Receptances Coupling teorisine dayalı olarak modellenmiştir. Daha sonra, yapısal modifikasyon tekniği kullanılarak şaft modeli ile tahmini bir yatak dinamiği modeli birleştirilmiştir. Model, farklı hızlarda iş mili dinamiklerini tahmin edebilir. Temas mekaniği dikkate alınarak proses esnasındaki silindirik iş parçası dinamiğini modellemek için benzer bir yaklaşım kullanıldı.

Bu tez, farklı tipteki takımlar için geliştirilmiş parça kalitesi ile en verimli kesme koşullarını öngören kapsamlı fizik tabanlı dijital dik torna frezeleme modelleri önermektedir. Sunulan modeller, proses parametrelerinin yanı sıra takım tezgahı yapısal dinamiklerini de kapsamaktadır. Bu modeller, endüstride maliyetli fiziksel denemelerden kaçınmak, süreç planlama aşamasında ya da süreç boyunca izleme ve hata tespiti amacıyla kullanılabilir.

ACKNOWLEDGMENTS

First and foremost, I want to express my deepest and warmest gratitude to my supervisor Prof. Erhan Budak. I appreciate his patience, guidance, and invaluable mentorship during my Ph.D. years. I am indebted to Prof. Budak because of his unconditional support, continuous encouragement, and trust in me in different research and industrial projects throughout my M.Sc. and Ph.D. years. His academic excellence, inspiration, precious vision, and ideas in research and industry have shaped my research career; meanwhile, his kind personality and compassionate leadership have influenced my personal development. It has been a great pleasure and privilege working, traveling, having discussions, and learning from him at every moment. He is and will be more than a supervisor to me.

It has been a great privilege to work in a collaborative environment in Manufacturing Research Laboratory (MRL). I feel lucky to have the chance to participate in several projects and collaborate with invaluable scholars. In this regard, I want to give my sincere thanks to Dr. Emre Özlü for his support and guidance during my Ph.D. years. His valuable comments and ideas in both the analytical and experimental aspects of my research helped me greatly. I owe him my utmost respect. I am deeply grateful to Dr. Umut Karagüzel for his support and fundamental comments at the starting point of my research. It has been a great pleasure to work with him during my M.Sc. and Ph.D. years. I am also thankful to Dr. L. Taner Tunç for his technical and academic support during my doctoral research and collaboration in the TUBITAK project. I have always learned so much from him during our discussion on different aspects of multi-axis machining. Moreover, I would also express appreciation to Dr. Orkun Özşahin for his unconditional help, guidance, and consultation in the H-SPIN project as a part of my dissertation.

I am also thankful to my Ph.D. supervisory committee members, Prof. Mustafa Bakkal and Dr. Bekir Bediz, for their constructive comments and inputs.

I am happy that I had the chance to make great memories and work with many passionate and valuable colleagues and students in MRL. Among them, I would like to thank Dr. Faraz Tehranizadeh and Dr. Zahra Barzegar for their sincere friendship and support during all these years. It was a precious experience to work and collaborate on projects in the laboratory and be a close friend outside. I am also thankful to Arash Ebrahimi, Esra

Yüksel, Saltuk Yıldız, and Milad Azvar for their valuable friendship and collaborations in several projects during all these years.

I am deeply grateful to the engineers and technicians in MRL who helped me technically and experimentally. Special thanks to Mr. Ertuğrul Sadıkoğlu and Mr. Süleyman Tutkun for their technical assistance during all the experiments in MRL. Also, I am thankful to the Maxima Company group, including Mr. Muharrem Erberdi, Mr. Veli Nakşiler, Emir Drama, Ahmet, and Tayfun, for their practical and technical help.

I appreciate the support from DMG Mori for providing a Mori Seiki NTX 2000 mill-turn center to MRL. The machine is extensively used in verification experiments of this thesis. Moreover, I would like to thank Akım Metal and İğrek Makina companies for providing machine tools and materials for performing experiments.

The cutting tools used for the experiments in this thesis are provided by several companies. I sincerely thank Karcan Cutting Tools Company for their help and support in designing special end mills. I am also grateful to Mr. Burak Aksu, Mr. Alper Kalkan, and Mr. Sepehr Firouzi for their support and consultation in providing cutting tools conveniently.

This research is partly supported by the Faculty of Engineering and Natural Sciences of Sabanci University. I am thankful to all staff and the administration of the faculty. I would also like to acknowledge the support from the Scientific and Technological Research Council of Turkey (TÜBİTAK) for this work within the research project framework under the grants 217M210 and 120N896. I am grateful for the cooperation from Sabanci University – Project Management Office.

I have gained many precious friendships during all these years at Sabanci University. I am thankful to Leila Haghighi Poudeh, Adnan Taşdemir, and Isa Emami as my flat mates, and I am grateful for their support and memorable times in the flat. I will never forget the memories with Farzad Rokhsar Talabazar, Pouya Yousefi, Tamay Jalalypour, Araz Sheibani Aghdam, and Vahid Tavakkol. Thank you for your friendship and emotional support.

Last but not least, I cannot express how thankful I am to my family for their unconditional support, inspiration, and love throughout my life. My dear mother and father, Mahin and Rahim, and my lovely and kind sister, Nastaran, I love you and am happy to have you.

To my dear family,

Dünyada her şey için, maddiyat için, ma'neviyât için, hayât için, muvaffakiyet için en hakikî mürşid ilimdir, fendir. îlim ve fennin hâricinde mürşid aramak gaflettir, cehâlettir, dalâlettir. Yalnız; ilmin ve fennin yaşadığımız her dakikadaki safhalarının tekâmülünü idrâk etmek ve terakkiyâtını zamânında tâkib eylemek şarttır.

Mustafa Kemal Atatürk
Samsun, 1924

Saygıyla,

TABLE OF CONTENTS

LIST OF FIGURES

LIST OF TABLES

LIST OF SYMBOLS

A_1	Summation of dynamic forces of all axial elements on side edges of all contributed teeth
A_2	Summation of dynamic forces of all axial elements on minor edges of all contributed teeth
A_j	Edge wave amplitude in special tools
a_i	Instantaneous depth of cut
a_e	Radial depth of cut
a_{lim}	Critical stable depth of cut
a_p	Axial depth of cut
a_w	Feed per workpiece revolution (stepover)
a_{wmax}	Allowable stepover
B	Width of bearing
$B(t)$	Directional coefficient matrix at present time
$\mathcal{C}$	Cross-feed direction in $\mathcal{FCN}$ coordinate system of tool
c_y, c_θ	Translational and rotational damping coefficient values
D	Outer ring diameter of bearing
D_a	Diameter of a ball in bearing
DC	Directional Coefficient matrix
DC^0	Zeroth-order term of Fourier expansion of DC.
D_t	Tool Diameter
$\mathcal{D}$	Modification matrix in structural modification tecnique
d	Inner ring diameter of bearing
D_w	Workpiece Diameter

$dF^{s}_{r,t,a,j}$	Differential static cutting force of side edge at *rta* frame
$dF^{m}_{r,t,a,j}$	Differential static cutting force of minor edge at *rta* frame
$dF^{s}_{x,y,z}$	Differential static cutting forces of side edge at TCS frame
$dF^{m}_{x,y,z}$	Differential static cutting forces of minor edge at TCS frame
$\left\{dF^{s}_{xyz,j}\right\}_{d}$	Differential dynamic milling forces exerted on side edge at TCS frame
$\left\{dF^{m}_{xyz,j}\right\}_{d}$	Differential dynamic milling forces exerted on minor edge at TCS frame
dl	Length of discrete element on minor edge
d_m	Bearing pitch diameter
ds	Spindle speed interval
dz	Differential axial element height
$\mathbb{E}$	Characteristic equation
e_{circ}	Circularity error
e	Eccentricity
e_g	Critical eccentricity
e_{max}	Maximum eccentricity
F	Feed
F_0	Force magnitude
F_C	Centrifugal force
$[FC(t)]$	Force coefficient matrix in present time
$F^{s}_{x,y,z}$	Total cutting forces on side edge contributed by all teeth at *x, y, z* directions at TCS frame.
$F^{m}_{x,y,z}$	Total cutting forces on minor edge contributed by all teeth at *x, y, z* directions at TCS frame.
$\bar{F}_{x,y,z}$	Total cutting forces produced by both side and minor cutting edges
$\bar{F}^{m}_{t}$	Total tangential force imposed on the tool by minor edge

$\bar{F}_t^s$	Total tangential force imposed on the tool by side edge
$\mathcal{F}$	Feed direction in $\mathcal{FCN}$ coodinsta system of tool
f_a	Axial feed
f_k	Harmonic force applied on point k
f_r	Radial feed
f_t	Feed per tooth
$\breve{f}_t$	Transferred feed per tooth in FCN coordinate system
G_i	Transfer function linking two augmented state vectors at current and next states.
g_j	Unit step function
$\bar{H}$	Receptance function between transverse displacements and harmonic forces
h	Uncut chip thickness on side edge
h_m	Uncut chip thickness of minor edge
h^d	Dynamic chip thickness
h_m^d	Dynamic chip thickness corresponds to minor edge
h^s	Static chip thickness
i	Time instant
j	Tooth number
K	Stiffness matrix of bearing
K_i, K_e	Load-displacement proportional coefficients corresponding to inner and outer rings
K_{tc}, K_{rc}, K_{ac}	Cutting force coefficients at tangential, radial, and axial direction of the tool
K_{te}, K_{re}, K_{ae}	Edge force coefficients at tangential, radial, and axial direction of the tool
$\overline{K_{tc}}, \overline{K_{rc}}, \overline{K_{ac}}$	Average cutting force coefficients at tangential, radial, and axial direction

	of the tool
K_y, K_θ	Translational and rotational complex stiffness expressions
$K_{y\theta}, K_{\theta y}$	Off-diagonal complex stiffness expressions
$\bar{L}$	Receptance function between transverse displacement and harmonic moment
$L(t)$	transient part of the state-space equation at present time
l_1, l_2	Engagement boundaries of minor edge
l_k	Distance of element k on minor edge from the beginning of the engagement
l_m	Length of instantaneous minor edge engagement
l_t	Minor cutting edge length
M	Total number of modes of tool and workpiece
M_0	Moment magnitude
m	Principle period resolution
m_b	balls' mass in a bearing
m_k	Harmonic moment
m_g	Gyroscopic moment
m_t	Number of modal modes of tool
m_w	Number of modal modes of workpiece
N	Number of teeth
$\mathcal{N}$	Normal direction in $\mathcal{FCN}$ coordinate system of tool
$\bar{N}$	Receptance function between the bending rotation and harmonic forces
N_D	number of unique delays
n	Number of the axial element at elevation z
O_T	Tool center point
P	Perimeter

$\bar{P}$	Receptance function between rotational displacement and harmonic moment
$P_{i,j}^{*}$	Indicator of points
P_t	Tool spindle power
P_w	Workpiece spindle power
$p_t(j)$	Angular position of the tooth j with respect to the first edge
p_u	pitch angle of the tooth u
$\{Q(t)\}$	Relative displacements between tool and workpiece at present time (t)
$\{Q(t-\tau_{i,j})\}$	Relative displacements between tool and workpiece at one delay period before
Q_i, Q_e	Contact force between the ball and the inner and outer ring
$Q_{xyz}(s)$	Relative displacement between tool and workpiece in Laplace domain at *x, y, z* directions
$\{q(t)\}$	Modal states of the coupled tool-workpiece system at time t
$\{q(t-\tau_{i,j})\}$	Modal states of the coupled tool-workpiece system at one delay period before
q_j	Unit step function
R_{im}	Local radius of an axial element on serrated tool
R_t	Tool radius
R_w	Workpiece Radius
r	Unique delay matrix
$r_{i,j}$	Delay resolution
r_s	Ratio of rotational speeds of tool over workpiece
r_r	Ratio of radii workpiece over tool
r_{max}	Maximum number of unique delays of the system
rta	Coordinate frame defined at radial, tangential and axial directions of the

	tool
s	Laplace domain operator
T	Spindle period
T_M	Transformation matrix for forces on minor edge if minor edge has an approach angle
T_S	Transformation matrix of differential cutting forces acting on the side cutting
T_t	Tool spindle torque
TL	Tail length of spindle shaft
T_w	Workpiece spindle torque
T_ψ	Transformation matrix between the coordinates center of the inner ring curvature radius and the global coordinates
t	Indicator of time
U_t	Mass normalized mode shape of the tool
U_w	Mass normalized mode shape of the workpiece
$u_{x,y,z}$	Mass normalized mode shape
V_c^t	Tool's cutting speed
V_c^w	Workpiece's cutting speed
V_c	Overall cutting speed
v	Number of contact points along the engagement length of the flexible structure.
W	Workpiece surface area generated by the previous tooth in serrated tools.
w	Transverse displacement
$X_TY_TZ_T$	Cartesian coordinates defined on tool tip with respect to tool coordinate system
$X_MY_MZ_M$	Cartesian coordinate system defined with respect to machine tool coordinate system

$X_W Y_W Z_W$	Stationary cartesian coordinate system defined with respect to workpeice coordinate system
$x_p(t), x_p(t-\tau)$	Displacement in x direction at time t and one delay period before p: c(cutter), w(workpiece)
$y_p(t), y_p(t-\tau)$	Displacement in y direction at time t and one delay period before p: c(cutter), w(workpiece)
y	Linear displacement
Z	Number of balls
$z_p(t), z_p(t-\tau)$	Displacement in z direction at time t and one delay period before p: c(cutter), w(workpiece)
z	Axial elevation of n^{th} discrete axial element
z_i, z_{i+1}	Augmented state vectors at current and next states.
z_{n+1}, z_n	Upper and lower limit of discrete element *n*
α	Initial contact angle in bearings
α_i	Phase difference in varying time delay model
α_m	Minor edge approach angle
α_n	Normal rake angle
α_r	Rake angle
α_{pp}	Directional force coefficients relating dynamic cutting forces and dynamic displacements ($p = x, y, z$)
α_{pp}^0	Zeroth-order component of directional force coefficients relating dynamic Cutting forces and dynamic displacements ($p = x, y, z$)
β	Angular displacement of the workpiece per tooth passing period of the tool
β_b	Angle between the ball's rotation axis and the bearing axis
β_l	Instantaneous angle β
β_n	Friction angle on normal plane

β_s	Friction angle
$\beta_{i,a}(t), \beta_{i,b}(t)$	Discrete state weights for the approximation of the time delay
Γ_t	Modal displacement vector of tool in modal space
Γ_w	Modal displacement vector of workpiece in modal space
$\{\bar{\Gamma}(t)\}$	Coupled modal states vector of tool and workpiece
Γ_C	Rearranged receptance matrix
Γ'_C	Receptance matrix of modified system in structural modification technique
$\gamma_{x,y}$	Rotational displacement around x and y axes
γ_j	Helix angle of tooth j
$\bar{\gamma}$	Loss factor
$\Delta x, \Delta y, \Delta z$	Relative displacements of the workpiece and cutter to each other in x, y, and z directions
$\Delta\mathrm{t}$	Time interval (tooth passing period)
$\Delta\bar{\varphi}_j(z)$	Local pitch angle at n^{th} disc element between the j^{th} and $(j+1)^{th}$ teeth
ΔP	Pitch variation
$\delta_{x,y,z}$	Translational displacement in x, y, z directions
δ_i, δ_e	Amount of deformation between the inner ring and the ball, and the outer ring and the ball
ζ	Damping ratio
$\bar{\zeta}$	Diagonal damping ratio matrix
η_c	Chip flow angle
θ	Angular displacement
θ_x	Helix angle of helical trajectory of tool around workpiece in orthogonal turn-milling
θ_r	Angle between workpiece and tool cutting velocities.
Λ	Eigenvalue of characteristic equation

λ_i, λ_e	Support ratios of the inner and outer rings to the gyroscopic moment
λ_j	Edge wave length in crest-cut tools
μ	Characteristic multipliers (eigenvalues)
τ	Time delay
τ_0	Tooth passing period
τ_s	Shear stress
Φ	Transfer function, Frequency response function
φ_j	Angular position of minor cutting edge of tooth j
φ_c	Angle where the definition of engagement length changes
φ_r	Mass-normalized eigenfunctions of bending rotation
$\bar{\varphi}_{n,j}$	Angular position of point n on tooth j in polar coordinate
$\varphi_{st}, \varphi_{ex}$	Entry and exit angles of engagement of minor cutting edge
ϕ_j	Angular position of side cutting edge of tooth j
ϕ_p	Pitch angle of tool
ϕ_n	Shear angle on normal plane
ϕ_r	Mass-normalized eigenfunctions of transverse displacement
ϕ_s	Shear angle
ϕ_{st}, ϕ_{ex}	Entry and exit angles of engagement of side cutting edge
$[\mathbf{\Psi}]$	Monodromy (transition) matrix
ψ	Bending rotation
Ω_t	Rotational speed of tool (rpm)
Ω_{t}^*	Rotational speed of tool (rps)
Ω_w	Rotational speed of workpiece
ω_b	Rotational speed of bearing
ω_c	Chatter frequency

ω_n	Natural frequency
$\bar{\omega}_n$	Diagonal natural frequency matrix
ω_r	Ball's speed in bearing
ω_t	Tooth passing frequency

LIST OF ABBREVIATIONS

ACCB	Angular Contact Ball Bearing
CAD	Computer-Aided Engineering
CAM	Computer-Aided Manufacturing
CC	Crest-Cut
CFAP	Chatter-Free Area Percentage
CL	Cutter Location
CNC	Computer Numerical Control
CWE	Cutter-Workpiece Engagement
CPU	Central Processing Unit
DAQ	Data Acquisition
DDE	Delayed Differential Equation
FCN	Feed, Cross-feed, Normal coordinate system
FE	Finite Element
FFT	Fast-Fourier Transform
FRF	Frequency Response Function
IPW	In-Process Workpiece
MCS	Machine Coordinate System
MRR	Material Removal Rate
NP	Number of Passes
ODE	Ordinary Differential Equation
RCSA	Receptance Coupling Substructure Assembly
RSI	Relative Stability Index
SDM	Semi-Discretization Method

SD	Semi-Discretization
SFQ	Surface Finish Quality
ST	Standard
STG	Strategy
TCS	Tool Coordinate System
VP	Variable-Pitch
WCS	Workpiece Coordinate System
ZOA	Zero-Order Approximation

1. INTRODUCTION

Machining is a subtractive manufacturing process that removes the material from the bulk material to achieve net-shape parts in different industries. Machining operations are widely used in manufacturing precise parts in automotive, die & mold, marine, aerospace, and medical industries. Machining operations can be applied on different materials such as various alloy steels, non-ferrous metals, composites, ceramics, plastics, and wood. The material removal process is performed by a cutting tool penetrating the workpiece material and removing the chips from the bulk material due to relative motion between the tool and the workpiece. Depending on the relative motion between the tool and workpiece, machining operations can be categorized as drilling, milling, turning, and boring. A rotating tool removes the material with multiple cutting edges in milling and drilling operations. However, a stationary single-point or multi-point cutter removes the material from a rotating cylindrical workpiece in turning and boring operations. During milling operation, each cutting edge of the milling tool periodically enters and exits the workpiece leading to intermittent cutting and short (discontinuous) chips, as seen in Figure 1.1b. On the other hand, turning and boring operations produce continuous and long chips due to the continuous contact of the cutting edge and workpiece (see Figure 1.1a). From the industrial and feasibility point of view, short and discontinuous chips are preferred in the industry due to their convenience in evacuation, transportation, and storage.

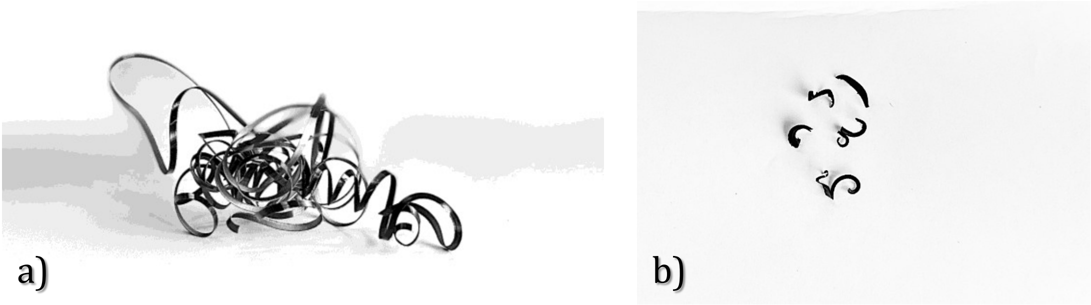

Figure 1.1: a) Continuous chip produced during turning, b) Discontinuous chip produced during milling operation.

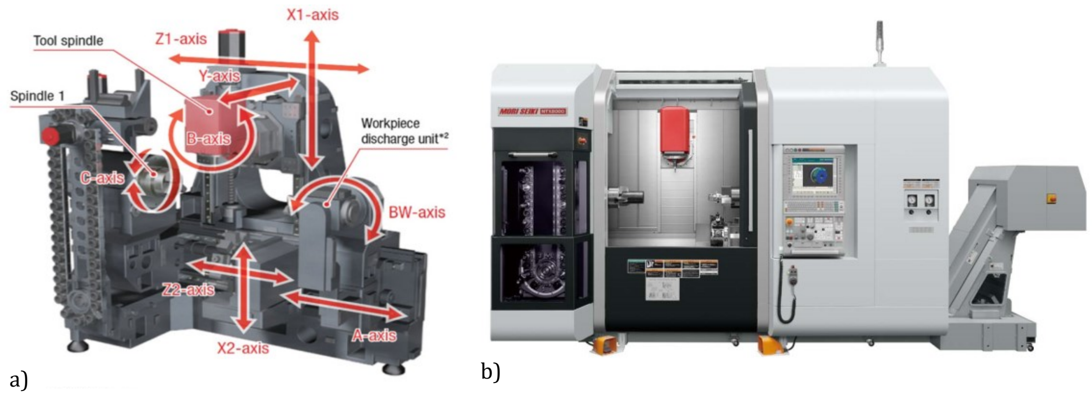

Figure 1.2: a) Axis Structure of Mori Seiki Mill-turn center [1], b) Mori Seiki NTX 2000 mill-turn center.

Usually, for turning and boring cylindrical parts, CNC lathes are used. 3-axes milling centers are used for machining prismatic parts, while 5-axis milling centers are used for more complex surfaces. However, due to the limitations in the number of independent axes, each machining center has a specific application and limited performance.

Multi-tasking machining centers introduce significant practical advantages over conventional machining centers in terms of productivity and finished part precision due to their capability to perform multiple machining operations in a single set-up without changing the workpiece. As a multi-tasking machining center, a mill-turn machining center can perform several machining operations such as turning, milling, multi-axis milling, and parallel machining operations.

Turn-milling, as a multi-axis machining operation, is an emerging machining technology in which both turning and milling spindles are actively employed to shape the desired final geometry. Turn-milling can be carried out in multi-tasking machining centers as a combination of milling and turning operations simultaneously. While the workpiece is clamped to a rotating chuck during turn-milling process, a milling tool mounted on a high-speed milling spindle carries out the material removal operation by adding multi-axes feed motions. In addition, the tool can be positioned in different Cartesian coordinates to define the axial depth of cut and cutter-offset value, which will be discussed extensively in the following sections. As a result, the final workpiece produced by turn-milling has a cylindrically symmetric cross-section similar to the one manufactured by turning operation.

Depending on the machine tool configuration and axes limitations, there exist various turn-milling set-ups where the relative position of rotational axes of the milling tool and workpiece are different. The most common turn-milling process is called orthogonal turn-milling, where the rotation axis of the milling tool is perpendicular to the rotation axis of the workpiece (Figure 1.3a), and the chip is removed by the side and bottom edges of the milling tool. In this configuration, a certain eccentricity between tool and workpiece axes can be defined, which alters process forces and stability, thus increasing tool life.

The second configuration is tangential turn-milling, where the milling tool is placed at the tangent to the workpiece periphery (Figure 1.3b). As a result, the chip is formed only by the side edge of the milling tool as opposed to orthogonal turn-milling. Another possible configuration in which the rotational axes of the milling tool and workpiece are parallel to each other is called co-axial turn-milling (Figure 1.3c), and the side edge of the tool removes the chip. Apart from these three most common turn-milling configurations, depending on the machine tool configuration and control, the relative position between the milling tool and workpiece can be continuously changed (i.e., the addition of tilt angle) along the toolpath, and complex chip geometry is generated as a result of the Cutter-Workpiece Engagement (CWE) geometry.

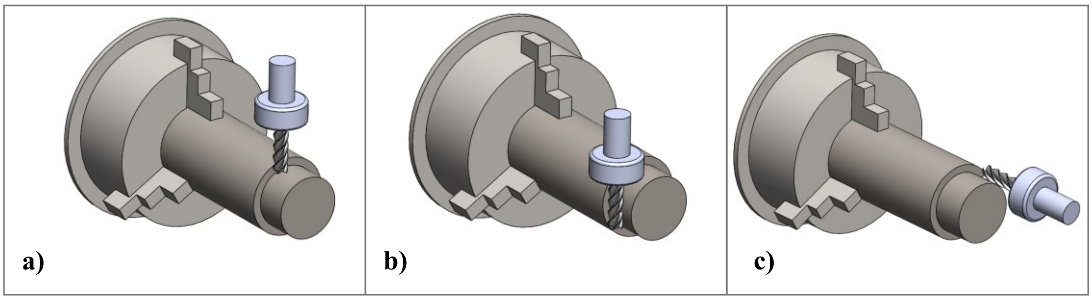

Figure 1.3: Three possible turn-milling configurations; a) Orthogonal, b) Tangential, c) Co-axial turn-milling processes.

The intermittent nature of cutting in turn-milling reduces the contact between the cutting edge of the milling tool and workpiece significantly, which lets the milling tool cool down until the next rotation period. A tool wear comparison of two turn-milling configurations with conventional turning operation is performed by Berenji et al. [2], and shown in Figure 1.4. Based on the results given in [2], it is deduced that despite the high number of inserts required for milling tool, turn-milling operations present an average of 35% lower cost in roughing and finishing both hard-to-cut materials.

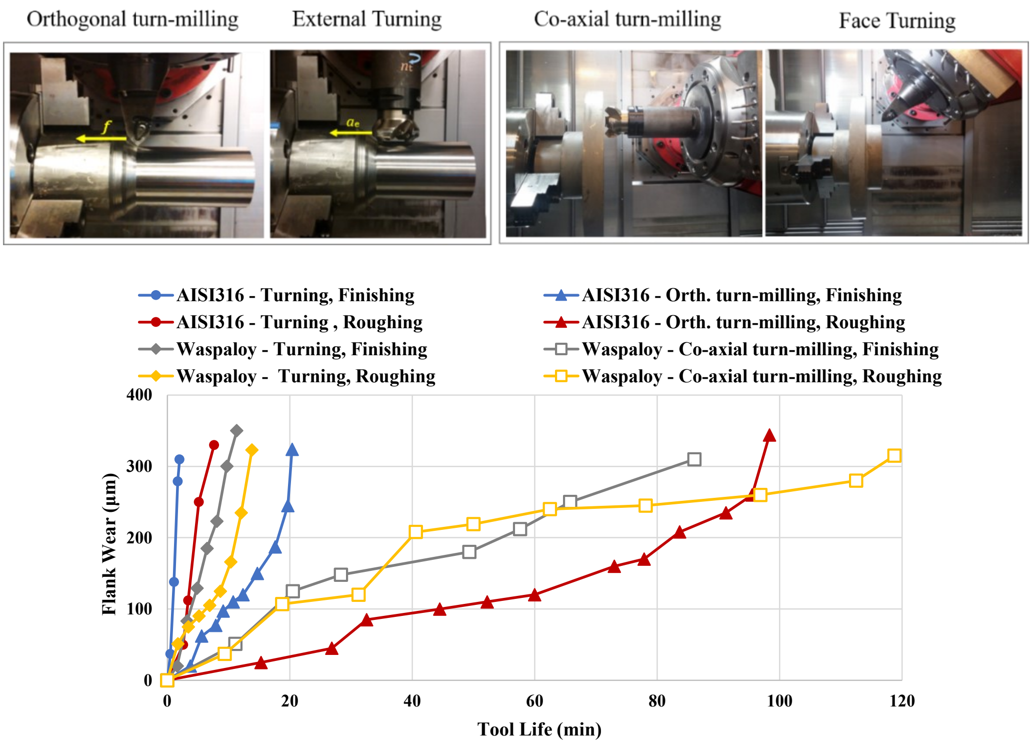

Figure 1.4: Tool life comparisons at different configurations and cutting strategies [2].

In addition to higher tool life, turn-milling offers easier chip evacuation because of producing discontinuous chips, lower workpiece temperature, and reduced surface roughness compared to single-point turning operation when the process parameters are defined accurately. Furthermore, during manufacturing large-scale parts with hard-to-cut material where the cutting speed is decreased to achieve high process rigidity, the turn-milling operation can achieve the required cutting speed and productivity.

In this study, the most commonly used configuration, orthogonal turn-milling, where the tool axis is perpendicular to the workpiece axis, is considered. While the workpiece is clamped on a chuck rotating at a particular speed, the milling tool cuts the workpiece with its specific rotational speeds while having translational feed along the workpiece axis (see Figure 1.5). Furthermore, the offset between the tool and workpiece, called eccentricity, provides several versatility and limitations to the operation.

Based on the advantages mentioned above, turn-milling provides several superiorities compared to conventional turning. However, in some cases, the material removal rates (MRR) are competitive. Nevertheless, orthogonal turn-milling introduces more part precision and productivity in manufacturing large-scale, thin-walled, or flexible parts.

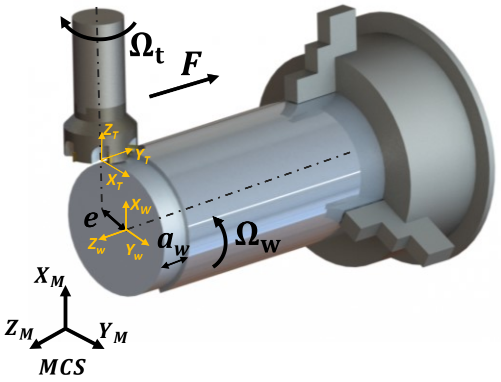

Figure 1.5: General kinematics of orthogonal turn-milling operation.

For instance, orthogonal turn-milling has been reported as an effective operation in manufacturing combustion and compression casings used in the aerospace industry (see Figure 1.6a). In addition, orthogonal turn-milling is used in the production of large-scale and long crankshafts (see Figure 1.6b) with high productivity and lower dimensional errors. Furthermore, orthogonal turn-milling is widely used in manufacturing spirals and screw shafts used in various industries, as shown in Figure 1.6c. Since there is no possibility of support in the middle of the shaft, higher workpiece speeds are not achievable. The orthogonal turn-milling provides reasonable productivity and precision in machining screw shafts. However, like other machining operations, the selection of improper machining parameters leads to undesired surface quality, lower tool life, and higher cutting forces and torque.

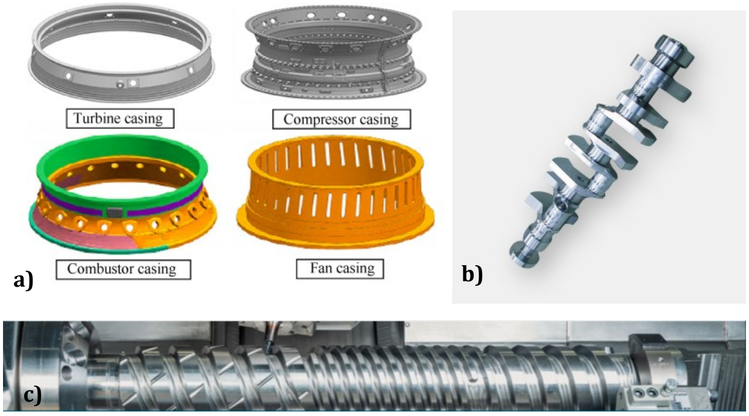

Figure 1.6: a) Different type of casings produced by turn-milling [3], b) A large-scale crankshaft produced by turn-milling (https://www.wfl.at/), c) Large-scale screw shaft produced by turn-milling (https://www.wfl.at/).

Moreover, erroneous parameter selection can result in self-exited chatter vibrations leading to tool failure, low surface quality, and machine tool component damage.

In order to overcome the potential drawbacks and prevent surface and dimensional errors in turn-milling, it is essential to profoundly understand the system's kinematics, mechanics, and dynamics. Although there have been several works on the mechanics and dynamics of turn-milling, a fully analytical approach including all the particular parameters of turn-milling has not been studied. This thesis provides a general approach to model the mechanics and dynamics of orthogonal turn-milling in any conditions.

Firstly, a general kinematics model is proposed for the orthogonal turn-milling process based on the cutting geometry and CNC programming parameters. Then an analytical cutter-workpiece engagement (CWE) model is presented to predict the uncut chip geometry resulting from the tool's side and minor cutting edges. The effect of cutting parameters such as eccentricity and stepover on CWE is investigated through simulations. Based on the proposed CWE model, a guideline is proposed to achieve a cusp-free surface while increasing the MRR in orthogonal turn-milling. This guideline is based on the cutting geometry and relates eccentricity and stepover through conditional formulations. Beyond the given guideline for the selection of eccentricity and stepover, unfavorable surface and chip geometries can be seen during the process.

Next, CWE is used to calculate the cutting forces, torque, and cutting power for various cases. Cutting forces affect the part accuracy and energy consumption during the operation. Excessive axial forces in turn-milling can lead to poor part accuracy due to the deflections and form errors resulting from axial forces. In addition, tool breakage and overloading of the machine tools can be seen if the cutting forces are high. Therefore, an analysis is presented to select the cutting parameters properly to avoid excessive cutting forces and cusp formation simultaneously.

Being one of the significant and challenging problems in machining, self-excited chatter vibrations must be avoided to prevent excessive cutting forces, tool failure, and poor part quality. Stability diagrams calculated based on the structural dynamics of the system and process parameters are the best way to predict chatter-free conditions. Due to the complex CWE and additional and specific process parameters in orthogonal turn-milling, stability calculation becomes more complicated compared to that of conventional 2D milling. One of the significant differences compared to conventional milling is the variation of instantaneous depth of cut within the CWE in orthogonal turn-milling. This variation trend depends on the tool and workpiece geometries and the eccentricity, which alters the uncut chip volume and resultant forces. Moreover, the minor edge of the tool is engaged in the cutting process leading to higher chip load and different force distribution in all directions. Another significant difference is the existence of additional time delay contributed to the system's dynamics by the simultaneous rotation of the tool and the workpiece, resulting in time-varying delay.

Having all said, the stability of orthogonal turn-milling becomes more sophisticated than conventional milling. In this regard, dynamic chip thickness and dynamic cutting forces that emerged in orthogonal turn-milling are evaluated in a three-dimensional frame. The varying time delay at each angular position of the tool and its distribution along the tool axis is modeled by proposing a novel approach. The dynamics of the system, including the tooling and workpiece systems and their substructures, are modeled in modal space and included in regenerative dynamic chip thickness definitions. The periodic dynamic cutting forces generated at the tool-workpiece engagement zone are combined with the structural dynamics of the machine tool, and the process dynamics are modeled as periodic, time-varying, delayed-differential equations (DDE). The differential equations are coupled and solved in both discrete-time and frequency domains. A time-marching and iterative approach is employed to calculate the stability lobes in the discrete-time domain solution by taking the varying time delay characteristic of the system. In addition, the frequency domain solution is performed using Fourier series expansions to evaluate the critical stable depth of cut for the first time in the literature. The proposed models are validated throughout experiments for various cutting conditions and materials. A guideline is proposed to achieve higher productivity and stable cut with a cusp-free cutting surface.

However, the productivity of turn-milling process is limited by the stability limits for each condition. In order to increase productivity, the stability limits can be increased by using special tools such as variable-helix, variable-pitch, serrated, and crest-cut tools, which are shown in Figure 1.7. Features of the milling tool such as the number of cutting teeth, helix angle, and shape of cutting edges strongly affect the process stability, and thus part quality and productivity. Special end mills can increase stability with the help of varying pitch and helix angles compared to standard end mills. The characteristics of variable-helix and variable-pitch tools on process stability and cutting forces have been discussed extensively in literature survey sections. This part of the thesis focuses on developing models to implement serrated and crest-cut tools in orthogonal turn-milling.

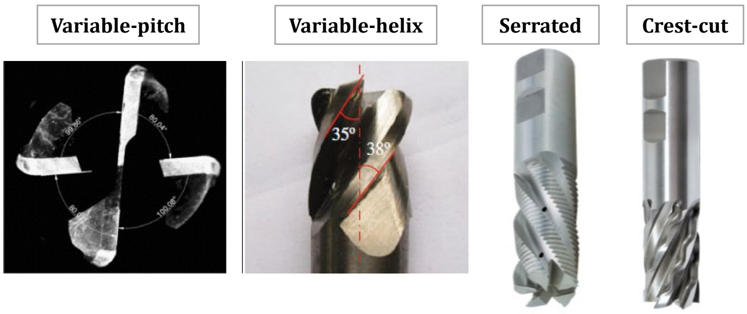

Figure 1.7: Four different types of special end mills.

The serrated tools offer lower cutting forces due to the discontinuous CWE along the tool axis because of the serration geometries on the cutting edges. This phenomenon significantly increases the process stability and decreases the cutting forces, torque, and power. Therefore, in roughing operations, i.e., in the machining of screw shafts, serrated tools can introduce superiorities in terms of cutting forces and process stability compared to standard end mills.

As another type of special end mill, crest-cut end mills have non-constant helix angles with harmonic variations along their axis, unlike variable helix tools with constant helix angles on each tooth. Considering the benefits proposed by variable pitch and helix tools in chatter suppression, crest-cut end mills encompass their effects simultaneously, suppressing chatter with better performance. Therefore, implementing crest-cut tools in turn-milling can offer a higher stable depth of cuts in machining the screw shafts and crankshafts where the flank milling is required.

In this regard, the mechanics model proposed for standard milling tools is extended to calculate the cutting forces resulting in orthogonal turn-milling using serrated and crest-cut tools. The models are experimentally validated for several conditions. Furthermore, the turn-milling stability model is also extended to calculate the specific distributed delays and CWE of crest-cut tools in orthogonal turn-milling. The stability lobes are estimated in discrete-time and frequency domains for the first time in the literature, and several cutting experiments validate the results.

In addition to turn-milling operations, the stability of crest-cut tools is investigated in thin-walled structures and compared to that of variable-pitch and regular end mills. The thin-walled structures like combustion casings are widely manufactured using the orthogonal turn-milling process. Therefore, the stability analysis on a simple thin-walled structure while 2D milling is the preliminary work to apply special tools in rotating thin-walled casings in turn-milling operation.

In this regard, the in-process workpiece (IPW) dynamics are calculated based on the determined cutting conditions. The tuned variable-pitch and crest-cut tools are designed according to the structural dynamics of the system. A stability map for the structure is generated based on IPW dynamics. The performance of each tool is investigated throughout the stability maps and is validated by experiments for different cutting strategies.

Based on the previously mentioned background, it is an undeniable fact that the tooling system (tool-holder-spindle assembly) and workpiece system (workpiece and clamping unit) have a deterministic role in the stability of the process. Therefore, it is essential to understand the effective parameters of structural dynamics of a machine tool. Although there are plenty of studies on predicting the tooltip dynamics according to different tool-holder assembly designs, in this part of the present thesis, the dynamics of a spindle are studied for improved rigidity. Spindle-bearing assembly is the most flexible component in machining centers, and its dynamics directly affect the performance of the machines. Spindle geometry (shaft geometry, bearing dimensions, etc.) and the location of the bearing and their configurations are the crucial parameters that determine the spindle dynamics. Therefore, the selection of the optimum design parameters is the key factor for the spindle design procedures. This study offers a design methodology for the spindle-bearing assembly for the optimized spindle dynamics. In this method, the spindle shaft is first modeled using the analytical solution of Timoshenko beam and receptance coupling methods. Then, bearing dynamics are included using the structural modification technique. Using the developed analytical model, the effect of each design parameter on spindle dynamics is analyzed. Simulations show that the proposed method and the sensitivity analysis can be efficiently used to select the optimum spindle-bearing assembly configuration. The workpiece dynamics is the next influential structure in the stability of the process. It is vital to determine the in-process workpiece dynamics of the flexible and slender workpiece during turn-milling operation. Since it is not possible to measure the workpiece dynamics during the process, it must be calculated analytically; however, the clamping stiffness affects the workpiece dynamic properties. Several analytical methods are proposed to predict the workpiece dynamics clamped on the rotating chuck. The predictions are validated through experiments.

2. LITERATURE SURVEY

The research on turn-milling began in the early 1990, and the researchers first focused on the tool wear and surface finish of hard-to-cut materials. Later, researchers began investigating the different aspects of this process, such as chip geometry and force predictions, CAM, stability analysis, and temperature predictions. The literature survey classifies the references according to the sections of the thesis.

2.1. Surface and Geometrical Errors in Turn-milling

As the first authors on the turn-milling process, Schulz et al. [4] conducted the co-axial turn-milling and reported the surface roughness of below 5µm for alloyed bearing steel. Later, the author conducted another experiment of co-axial turn-milling on hardened steel (>62HRC) using CBN cutting tools [5]. They achieved surface roughness below 10µm depending on the tool's feed rate and wear width. However, the radial depth of the cut was kept considerably low during the experiments. Choudhury et al. [6] were the next group who investigated the surface roughness by implementing non-eccentric orthogonal turn-milling on brass and mild-steel cylinders. The surface finish was measured for different tool rotational speeds and linear feed. They concluded that the surface roughness would decrease by 10 times by increasing the rotational speed and reducing the linear feed rate. Another experimental study was conducted by Choudhury et al. [7] four years later on the surface finish of mild steel workpiece by orthogonal turn-milling. They conducted an empirical analysis of non-eccentric orthogonal turn-milling for different cutter diameters, depth of cut, and workpiece rotational speed values. The main conclusions of this work are that increasing the depth of the cut will deteriorate the surface finish, while increasing the cutter diameter will enhance the surface finish. However, the workpiece speed will decrease the surface roughness until a limit (10 rpm) and then increase. The surface roughness values for these studies are below the maximum of 4µm.

Ekinovic et al. [8] conducted high-speed eccentric orthogonal turn-milling experiments on hardened and ductile steel and compared them to hard turning for equal MRR and axial feed. The cutting speed was high, but the radial and axial depth of cut was kept low. They obtained better surface roughness for turn-milling in all trials.

Experimental work was conducted by Cai et al. [9] investigating the effect of eccentricity on surface roughness. The authors stated that when the eccentricity is equal to the cutter radius, the effective cutting edge is maximum, and this will decrease the surface roughness. The same research group conducted another research work that focused on the effect of eccentricity by Uysal et al. [10] and Karaguzel et al. [11,12]. Both articles utilized the normal and wiper inserts and compared their effect on the surface finish of orthogonal turn-milling components of AISI 1050 steel. They concluded that the wiper inserts present better surface quality than standard inserts. However, the surface roughness has an ascending manner until a critical value and then decreases.

The first attempt to model the surface topology and roughness analytically was made by Yuan et al. [13]. The formulation for residual material left regarding tool minor edge geometry, nose radius, and residual height was modeled. Similar work was performed by Zhu et al. [14]on modeling the surface topology based on cutting parameters with experimental validations. In the case of tangential turn-milling, Savas and Ozay [15] were the first to perform experiments on this process. They investigated the effect of depth of cut, feed rate, and rotational speeds on surface roughness values for AISI 1040 steel. They obtained very low surface roughness below 1µm. The same team conducted two other research works on tangential turn-milling of two different workpiece materials and measured the surface roughness in the axial direction [16,17].

In another work focused on surface texture simulation, Funke et al. [18] developed a dexel-based MATLAB simulation that permits the prediction of surface texture generated by tangential turn-milling. They performed the simulations for several tool corner geometry and radii and compared them with the experimental results. The main purpose of this work was to increase the coefficient of static friction by inclined tool tangential turn-milling operation.

Karpuschewski et al. [19] studied the surface roughness of rolling bearings, hardened 100Cr6 workpiece with a minimum hardness of 58 HRC, machined by a tangential turn-milling process with an inclined B-axis angle and compared with hard turning and grinding. They conclude that tangential turn-milling meets their tribological needs and friction coefficient range better than grinding and turning.

Due to the kinematics of turn-milling process, geometric errors occur during on the cut surface. The magnitude of these errors depends on several parameters such as tool geometry, rotational speed ratio, diameter ratio, and eccentricity.

As a pioneer study, Schulz et al. [5] mentioned the existence of wavy and non-circular surfaces and gave eccentricity suggestions to avoid these defects. Later, Neagu et al. [20] investigated the cutting cinematics and tool functional geometry in detail using geometrical analysis considering the eccentricity. The authors concluded that orthogonal turn-milling is suitable for high productivity ranges, especially in roughing heavy shafts. Wang et al. [21] developed a mathematical model to evaluate the scallops left on the machined surface of orthogonal turn-milling using cutter-contact points.

In a comprehensive study, Karaguzel et al. [11,22] and Uysal et al. [10] discussed the cylindrical error and formation of the cusp in orthogonal turn-milling operations as a possible geometrical error. It is stated that the circularity error always happens due to the kinematic of the process. The cusp height formula was also developed depending on the eccentricity, tool and workpiece radius and rotational speed ratio and calculated for different feed and eccentricity values to find an optimum value for lower cusp height and higher MRR. As a geometrical error, Karpuschewski et al. [19] investigated the roundness error for tangential turn-milling components and compared it with hard turning and grinding. It is observed that despite the hard turning and grinding, which generated a polygon-shaped workpiece and oscillation in roundness, tangential turn-milling produced acceptable cylinders with considerably lower roundness error compared to other methods. Jiang et al. [23] developed an analytical model which simulates the scallops and textures formed by tangential turn-milling on machined parts based on the kinematic of the process. Berenji et al. [24] investigated the cusp formation in orthogonal turn-milling based on the analytical uncut chip geometry model. They developed an analytical model that relates eccentricity and stepover based on the engagement of the minor edge of the tool. They demonstrated that according to the proposed model, cups could be eliminated while the productivity can approximately be doubled. The model outcomes were validated through experiments.

2.2. Kinematics and Mechanics of Turn-milling

In addition to experimental work, many researchers studied turn-milling theoretically through modeling. As a first attempt, Filho [25] proposed an approach to model the chip geometry without considering the axial feed of the tool in orthogonal turn-milling for a specific engagement condition. A similar approach was followed by Karaguzel et al. [12] for a different and specific cutter-workpiece engagement condition without considering the effect of tool rotation, axial feed, and tool geometry. Zhu et al. [26] proposed a different approach to model the uncut chip geometry based on boundary surfaces mathematically. The chip model was verified by visual and analytical chip volume comparisons in experiments. Qui et al. [27] proposed an approach for modeling the chip geometry of round inserts during the orthogonal turn-milling process. This model was based on the kinematic of the process and geometry of the round inserted tool. The engagement model was evaluated by mapping the workpiece surface into grids along axial and circumferential directions. Yonglin et al. [28] also proposed a model for the prediction of the swept are in eccentric orthogonal turn-milling for inserted milling tools. The model was based on the sweeping kinematics of cutting-edge and the rotational workpiece. The model was limited to a specific range of eccentricities and not validated with any experimental method. Later, Comak et al. [29] analyzed and verified the cutting forces of orthogonal turn-milling in three dimensions. In this work, the chip geometry was extracted using the MACHPro® software package for side cutting edge only, and the experiments were performed for centric orthogonal turn-milling. Otalora-Ortega et al. [30] developed a more detailed approach for modeling the uncut chip thickness for centric orthogonal turn-milling. The authors proposed two different formulations for small and large depth of cut regimens by neglecting the effect of minor edge length for zero eccentricity conditions. Recently, Sun et al. [31] proposed a relatively complex and case-based approach to predict the engagement boundaries of uncut chip in orthogonal turn-milling without considering the minor edge geometry.

2.3. Dynamics and Stability of Turn-milling

As in any machining process, stability is an important factor in turn-milling operations for high-performance cutting and high part quality. As pioneer research works, Tobias et al [32] and Tlusty et al. [33] introduced the self-excited regenerative chip formation mechanism due to the relative vibrations between the flexible tool and workpiece, and proposed a stability solution in frequency domain. Later, Merrit [34] modeled the regeneration mechanism by a feedback control block, and employed Nyquist criterion to predict the stability limits. Tlusty et al. [35] and Tobias et al. [36] investigated the non-linear behavior of cutting in time domain when the tool lost contact due to excessive vibration amplitudes. Minis and Yanushevsky [37] modeled the dynamics of milling by two sets of coupled delayed differential equations with periodic coefficients. In their study, the effect of spindle speed was considered using Floquet Theory, and the stability was resolved using Nyquist Theory. For milling operations, Altintas and Budak [38] solved the stability in frequency domain analytically by averaging the time periodic directional factors. By using this solution technique, also known as zero order solution, it is possible to predict the stability limits in milling operations with high radial immersions in a rapid and accurate manner. Due to the time-varying nature of the cutting forces, taking only the average component to determine the directional factors may not provide a high level of accuracy. Stepan and Insperger [39,40] proposed a technique for discretizing system equations within the system's time period by applying a semi-discrete method. Basically, the semi-discretization method involves discretizing only the delayed states and estimating them with piecewise constant functions, while leaving the non-delayed terms unchanged.

There are very few studies in the development of a chatter stability model for turn-milling operations. Zhu et al. [41] performed a study on chatter prediction during turn-milling of a blade on a mill-turn machine tool by a ball end mill. The studies were focused on the 5-axis machining of a thin-walled blade on mill-turn rather than a turn-milling operation with a feed rate in the workpiece axis direction. Yan et al. [42] conducted a study on the stability prediction of the orthogonal turn-milling process. The mechanistic model was employed to evaluate the dynamic cutting forces. The chatter analysis was performed in the frequency domain with constant damping constant for tool and workpiece. The stability lobe diagram for this case was evaluated and compared for different workpiece-tool diameter ratios; however, the effect of the minor cutting edge of the tool and effect of other cutting parameters such as workpiece rotational speed and eccentricity was not stated.

In a more complete work by Comak et al. [43], the dynamic model for the orthogonal turn-milling process by an end mill was presented. In this study, the dynamic chip thickness in orthogonal turn-milling is considered with a time-varying delay which is periodic at tooth passing periods due to the simultaneous rotation of tool and workpiece. The time-varying delay is highly sensitive to tool and workpiece speeds and diameters. Several researchers have previously studied the effect of time-varying delay in different machining processes.

Insperger and Stepan [44] solved the stability of turning with varying spindle speed, which has varying time delays for different modulation frequencies and amplitudes, using the semi-discretization method. Faassen et al. [45] predicted the chatter in milling using the semi-discretization method by considering the trochoidal tool path model and periodic time-varying delay approach. In this study, the periodic time delay is calculated based on the feed motion of the tool. The authors concluded that the effect of varying time delay is more distinguishable at low radial immersion conditions and causes considerable differences between up-milling and down-milling conditions. In a similar approach, Long et al. [46] proposed a dynamic milling model with variable time delay and solved the stability of the system using the semi-discretization method. The effect of feed rate on 2D milling operation is investigated using a varying time delay model. Based on the proposed model, not much difference was seen between the stability lobes obtained with varying and constant time delays. Zhao and Balachandran [47] and Balachandran [48] employed a similar approach to predict the chatter in 2D milling. The nonlinear dynamics of the process studied. It is concluded that for high-immersion conditions using constant delay models is sufficient. However, the time-varying delay models must be used for low-immersion conditions since the difference between stability lobes increases as the feed rate increases.

In addition to time-varying and periodic delays, multiple delays have been studied in the literature on parallel machining operations and special tools. Budak et al. [49] and Azvar et al. [50] proposed a stability model for parallel turning operation based on multiple time delays. Budak et al. [51] modeled the parallel milling operation using a multiple delay approach. Due to the shared flexible workpiece between the turning and milling tools, their time delays are coupled and affect the regenerative chip thickness mechanism.

A literature review of multiple and distributed delays occurring when using special tools is presented in the following section.

2.4. Stability of Special Tools

There have been several studies on the mechanics and dynamics of special end mills and their benefits. Slavicek [52] analyzed the effects of irregular tooth pitch by extending Tlusty's chatter model [33] to cutters with non-constant pitch. In this study, the pitch selection criteria are defined. Based on the chatter frequency, the optimal pitch to improve cutting speed stability is determined. Based on the results, a specific pitch variation pattern may not increase stability at all speeds. Tlusty et al. [53,54] studied the effects of irregular-pitch end mills on the process dynamics in the following years. The employed methods are based on time domain simulations which are computationally costly. Based on the outcomes of these research works, milling tools with irregular pitch patterns were accepted as an alternative way to suppress chatter vibrations and increase the stability limit of milling processes. Shirase et al. [55] demonstrated that end mills with irregular pitch angles could reduce surface error. Altintas et al. [56] predicted the stability lobes for variable pitch cutters using the zero-order approximation by transforming the time-varying directional cutting constants into constants. The solution is based on numerical methods in the frequency domain. Budak [57,58] proposed an analytical method for the selection of the optimal pitch variation in designing variable pitch cutters for improved stability. An explicit formulation of the relation between the chatter stability limit and pitch angle variation is established in this method, leading to a simple equation for determining the optimal pitch angle. However, the variable-pitch cutters also introduce some limitations. First, when chatter and tooth passing frequencies are considered, regular pitch variation in variable pitch tools can only increase chatter stability in a limited spindle speed range. Moreover, if the tooth passing frequency is higher than the critical mode frequency, the optimum pitch variation increases drastically, resulting in irregular overloading of some edges and chip evacuation problems. On the other hand, the pitch value between other teeth becomes so small that it causes limitations in manufacturing such tools [59]. As an alternative, Suzuki et al. [60] proposed a robust optimal design methodology of variable pitch end mills with irregular pitch variation for enhanced absolute stability limit. Besides its advantages, the irregular pitch variation can cause unbalanced cutting forces and chip loads, leading to significant run outs and overloading. An accurate scheme for the optimal selection of pitch angles for maximized stability of variable pitch tools was introduced by Çomak and Budak [61] based on the previous approach by Budak [57].

Based on the advantages of variable-pitch cutters, many works were carried out on different types of special end mills, such as variable-helix, serrated, and crest-cut end mills. In the 2000s, serrated end mills were the focus of academia and industry because of their advantages in decreasing cutting forces in milling processes. Serrated tools, first proposed by Strasman [62,63], have wavy flutes that produce periodic variations in local radii and the lead angle. Because of the wavy edge shape, the serrated tools cannot be used in finishing operations. Merdol and Altintas [64] studied the mechanics and dynamics of serrated end mills with sinusoidal wave shapes on their clearance faces. The predictive cutting force model and stability model in the time domain are verified experimentally. It is deduced that the effectiveness of serrated tools on process stability depends on the feed per tooth value. Dombovari et al. [65] investigated the effects of serrations on cutting forces and the stability of the process. This study employed the semi-discretization method to predict the stability lobes for serrated tools with distributed delays. Recently, a chatter stability model for serrated tools in the frequency domain was proposed by Farahani et al. [66], which introduces lower computational time compared to time-based solutions. Tehranizadeh et al. [67,68] analyzed the mechanics and dynamics of milling operation with serrated end mills with different serration wave shapes, such as sinusoidal, trapezoidal, and circular. Serration shapes are optimized by considering cutting forces and stability limits. In another study, Bari et al. [69] present an improved chip thickness model for serrated end mills that considers the tooth's actual trochoidal path. Moreover, the model incorporates the effect of radial run-out on teeth. Dombovari and Stepan [70] modeled chatter stability of variable-helix end mills using the semi-discretization method and investigated the performance of these tools in different spindle speeds. Hayasaka et al. [71] proposed a method to design and optimize variable-helix end mills to suppress chatter vibration. The proposed method, which is applicable to tools with high helix angles, was verified experimentally. Turner et al. [72] used average helix values to establish an equivalent variable-pitch model for variable-helix tools. The optimum values for helix and pitch angles are obtained using evolutionary optimization algorithms. Variable-helix tools are further analyzed by Sims [73] using Laplace transformation by taking the multi-frequency and nonlinear cutting stiffness effects into account. However, these phenomena can adversely affect the accuracy of the stability solution, despite the variable helix tool's ability to enlarge the stable zone.

As an additional type of special end mill, crest-cut end mills are characterized by non-constant helix angles that harmonically change over their axis, as opposed to variable helix tools that have a constant helix angle on each tooth. Crest-cut end mills encompass the effects of variable-pitch and variable-helix tools simultaneously. However, unlike other special end mills, these tools are not widely known. Their application in the industry has been limited due to the low number of producers and a lack of guidance and instructions for their design and application. Due to the continuous variation in the regeneration delay caused by the periodic variations in helix and pitch angles along the cutting edges, crest-cut tools have the ability to improve the process stability substantially, provided that they are correctly designed. Nevertheless, there is very limited research on these tools, and there is no information available on how to design wave geometries. The stability of crest-cut tools was investigated by Dombovari et al. [74], employing the semi-discretization method using distributed delays for the first time in the literature. It is concluded that large stable lobes could be achieved using these tools at lower spindle speeds, while they lose this effect at higher speeds [70]. As a technical brief to this article, Sanz et al. [75] used the previous model for investigating different case studies without experimental validations. Gomez et al. [76] extracted the geometry of crest-cut end mills using a 3D scanner and predicted their dynamic behavior using time-domain simulations. In a recent study, Tehranizadeh et al. [77] proposed a novel and precise approach to analytically model the geometry of crest-cut tools. The cutting forces are calculated and verified experimentally based on the proposed model. The stability of crest-cut tools is predicted by employing the semi-discretization method. The authors proposed a procedure to select the optimal geometrical parameters of crest-cut tools for improved stability. The experimentally verified model showed that crest cut tools offers higher stability limits than standard and variable-pitch tools.

There is limited amount of work in literature which focus on the stability of special tools in machining thin-walled structures. Avoiding chatter vibrations in machining thin-walled structures made from hard-to-cut materials have always been the focus of researchers and engineers in academic and industry. Due to the low machinability of hard-to-cut materials, lower cutting speeds are preferred when machining these materials. As a result, deeper stability pockets which exist at high cutting speeds cannot be achieved. Variable pitch tools can be used at low cutting speeds to suppress chatter vibrations. However, due to the existence of multiple dominant modes and varying in-process workpiece dynamics (IPW), their use in milling thin-walled parts does not always provide a satisfactory solution for chatter suppression. Crest-cut tools, on the other hand, provide chatter suppression capability over a wider frequency and speed range [77], and can be highly effective for suppression of chatter in milling of thin-walled parts. In machining of thin-walled structures, workpiece dynamics have a substantial effect on the process stability. Thus, the stability analysis must include the mass removal effect, i.e., in-process workpiece (IPW) dynamics [78].

The varying dynamics of thin-walled structures are usually obtained using the finite element (FE) method at cutter locations considering the material removal. Bravo et al. [79] modeled the machined workpiece using FE analysis at each cutting depth along the height, while Thevenot et al. [80] obtained the stability diagrams for various cutter locations in the feed direction. For more complex part geometry and tool paths, Biermann et al. [81] coupled the FE model of the workpiece with time domain simulation to predict stable and unstable regions in the 5-axis milling of turbine blades. Budak et al. [78] predicted the IPW dynamics for 5-axis milling of blades using the structural modification technique, which was previously applied to plate-like structures by Alan et al. [82]. In this approach, the dynamics response of the machined workpiece is updated by adding the removed material in the opposite direction of the tool path using a structural modification technique. In a different method, Tuysuz et al. [83] obtained the IPW dynamics by replacing the removed mass with a fictitious substructure having opposite dynamics to the removed material.

2.5. Spindle Dynamics

Chatter is an important problem in machining operations, and chatter-free machining conditions can be determined using stability diagrams [38]. To determine the stability diagrams tool point Frequency response function (FRF), which reflects the dynamics of the whole spindle-holder-tool assembly at the tooltip, is required. Therefore, spindle dynamics directly affect the process stability and part quality.

Both spindle dynamics and tool point FRF can be obtained experimentally using impact testing [84]. However, performing impact testing for each holder-tool combination is not practical in production. Also, direct measurement does not always provide detailed information on the component dynamics of the assembly. Additionally, measurements can only be done on the existing systems, and thus cannot be used in spindle design optimization. Another important limitation in the experimental approach is the effect of operational conditions on spindle-bearing assembly dynamics. Under operational conditions, bearing stiffness decreases due to centrifugal forces and gyroscopic effects [85–87]. In addition, spindle dynamics also change with undercutting forces [88,89] and thermal effects in operation [87]. Thus, both spindle dynamics and tool point FRFs deviate from the dynamics at the machine's idle state, leading to inaccurate stability predictions at high-speed machining operations [90].

To alter these limitations, Cao and Altintas [86] modeled the spindle-holder-tool assembly using the Finite Element method and included the speed-dependent bearing dynamics in the model. Later Xiong et al. [91] and Movahhedy and Mosaddegh [92] modeled spindle-holder-tool assembly, including the gyroscopic effects, and showed the effect on both tool point FRFs and chatter stability. As an alternative, Schmitz et al. [93,94] proposed a receptance coupling technique for the tool point FRF prediction by coupling the analytically calculated holder-tool dynamics with the experimentally identified spindle dynamics. Later, Ertürk et al. [95] modeled the complete spindle-holder-tool assembly using the analytical solution of Timoshenko beam and receptance coupling technique and obtained the tool point FRF analytically. The main advantage of the analytical approach over the FEM is that it reduces the computational load considerably [95] and provides an efficient way for the design optimization of spindles.

Since the spindle-bearing assembly is the most flexible component in high-speed machining centers, its dynamics directly affect the performance of the machines. Therefore, the design of the spindles plays a crucial role in the productivity of machining centers. For that purpose, Ertürk et al. [96] analyzed the effect of spindle design parameters on both spindle tip and tool point FRFs using the analytical model. Cao et al. [97] proposed a design methodology for the spindles for improved productivity based on FEM.

In one of the current studies, Cao et al. [98] developed a dynamic model of the spindle in order to find the range of the fit clearance in the front and rear bearings, which can ensure rotational accuracy and meet the design requirements for the minimization of error motion. In another study, Wanga et al. [99], uses Genetic Algorithm to find out the best spindle speed variation scheme to maximize the sum of all critical axial cutting depths on the given interval of spindle speed. Although, they do not take the spindle structure into account, they mainly consider removing chatter from the process.

As most influential parameter in spindle design, speed-dependent dynamics of bearing has been extensively studied previously. Angular contact ball bearings (ACBB) can be used in high-speed rotors and have the advantage of being able to carry loads in both the axial and radial directions, thus they are used in spindles as well [85,100,101]. Angular contact ball bearings are unique since they have some inherent properties. As an example, since it can support only a load in one axial direction when used as an axial type, two or more are used symmetrically arranged, and it is known that the arrangement method predominantly affects the characteristics of the spindle [87,102]. In order to use it properly, an axial preload must be applied. In recent high-speed spindles, a constant preload can be applied regardless of heat generation or thermal expansion caused by it. Many methods are adopted in which the support point of one bearing is movable using a ball bush or sleeve [103].

The effect of bearing alignment direction on the dynamic characteristics of the spindle was demonstrated by Li and Shin [87]. For the past several decades, there have been many studies on the high-speed spindle system for machine tools to improve productivity and machining quality. This has been studied as Senda et al. [104] observed the protrusion according to the change of the rotational speed, whereas only approached it from the viewpoint of thermal expansion. Protrusion was also considered in another study [105], whereas it was also discussed in terms of displacement due to thermal deformation and compensation. Recently, it has been discussed in [106–108] that the bearing characteristics change due to the centrifugal force of the bearing itself or the gyroscopic effect can lead to protrusion. However, it is difficult to adequately explain the physical phenomenon inside the bearing by focusing on the change in the axial load. Bae et al. [109] presented a basic analysis using a commercial bearing analysis program, and it was confirmed that the protrusion occurred due to the rotational speed of the ring regardless of thermal expansion.

3. MECHANICS OF ORTHOGONAL TURN-MILLING OPERATION

3.1. Overview

Prediction of static cutting forces is the first step to investigating the characteristic of turn-milling operation for process planning and optimization purposes. The static cutting forces are used to calculate the cutting torque and power, which are critical for machine design, process planning, and high-performance cutting. In addition, the predictive model of cutting mechanics will be used to predict the stability of the process. For this purpose, a comprehensive model is required to precisely predict the uncut chip geometry, encompassing all the conditions and configurations of the process with compatibility of applying on different tool geometries. Some studies in the literature focused on predicting static cutting forces of orthogonal turn-milling operations for specific and limited configurations with sophisticated calculations for uncut chip geometry predictions. This chapter presents the cutting mechanics of the orthogonal turn-milling process to predict the static cutting forces, cutting torque, and power required for process planning and process dynamics. In this regard, firstly, the kinematics of the process is studied. Next, a mathematical model is presented to predict the instantaneous uncut chip geometry used for discretized static cutting force calculations. Based on the process kinematics, the allowable ranges of cutting parameters are discussed to avoid surface errors during the cutting operation. The cutter-workpiece engagement (CWE) is calculated for different tool offset, tool-workpiece rotational speed, and diameter ratios. Then the predictive cutting force model is confirmed by experiments.

3.2. Kinematics of Orthogonal Turn-milling

Turn-milling operation is a multi-axis machining process that can be defined as the combination of milling and turning processes in which, the tool and workpiece rotate simultaneously. In this regard, turn-milling can be categorized in orthogonal, co-axial, and tangential configurations. In this study, the orthogonal turn-milling operation is studied in detail, while the formulations for the other two configurations are discussed by Karagüzel et al. [22]. In orthogonal turn-milling, the tool follows a linear path along the workpiece axis ($-Z_w$ axis of the workpiece coordinate system (WCS)) as shown schematically in Figure 1. In addition, the cutter position can be changed in in X_w direction to adjust the axial depth of cut (a_p) and in Y_w to add eccentricity (tool axis offset e) to the process (See Figure 3.1). Note that in orthogonal turn-milling, there is no movement in the B-axis (rotation around Y-axis). Any alteration in workpiece/tool geometry, depth of cut, or eccentricity will change the side and minor edge's engagement boundaries, as shown in Figure 1. Since the mechanics and predictive force model of the process is based on the instantaneous CWE, the engagement of each edge must be calculated precisely by considering the geometrical and process parameters. In this section, the cutting geometry and process kinematics are defined and used to develop an accurate model for uncut chip geometry resulting from the cutter's side and minor edge.

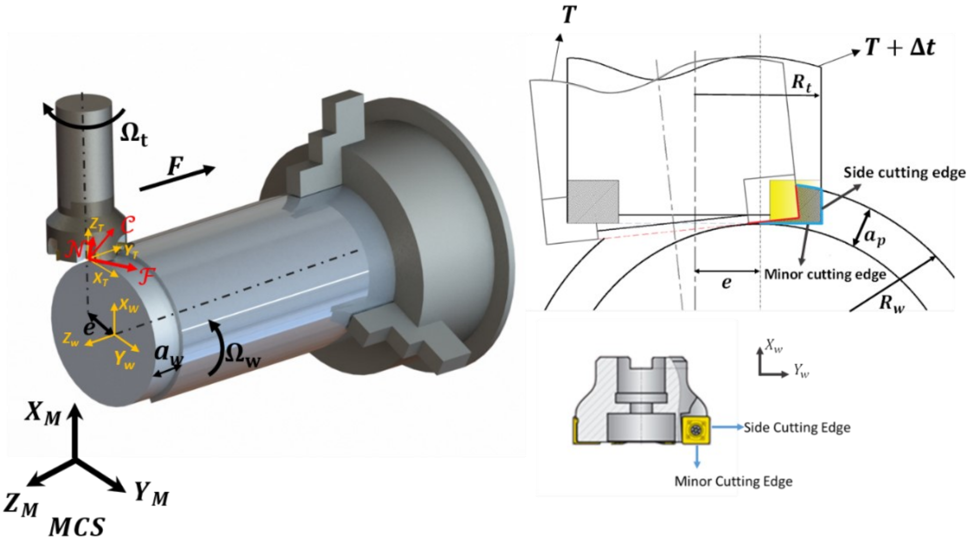

Figure 3.1. General schematic representation of orthogonal turn-milling operation.

Turn-milling operation is mainly performed on mill-turn multi-axis machining centers where the workpiece chuck and tool spindle can rotate independently. Although the turn-milling operation can be considered a 5-axis machining operation, implementation of the kinematics of the 5-axis operation and the addition of complexity of the C-axis in spatial coordinates adds extra infeasibility. However, the independent rotation of chuck and spindle on mill-turn machining centers introduces feasible and user-friendly programming.

In turn-milling operation, the cutter is rotating with rotational speed Ω_t (rev/min) and the workpiece is rotating at the speed of Ω_w (rev/min), simultaneously. Considering the stationary WCS, the tool is traveling a helical path due to the workpiece rotation and linear feed motion. This helical path is aligned to the surface feed direction of $\mathcal{FCN}$ coordinate system. In $\mathcal{FCN}$ coordinate system, $\mathcal{F}$ stands for feed direction, $\mathcal{C}$ represents the cross-feed direction, and $\mathcal{N}$ is the surface normal axis (See Figure 3.1). The rotational direction of this helical path depends on the rotational direction of the workpiece. Given that the tool's rotational direction is constant, changing the rotational direction of the workpiece merely without considering the eccentricity direction would cause undesired cutting due to the engagement of the uncut part with the minor edge of the tool and may cause excessive tool failure. In order to prevent such cases, it is suggested to perform the orthogonal turn-milling operation in two configurations, as shown in Figure 3.2. It is shown that, while the tool's rotation is kept clockwise and linear feed direction is similar in both cases, the rotational direction of the workpiece and eccentricity direction pairs, as shown below, defines the cutting type; up-milling or down-milling. Figure 3.2-a shows that if the workpiece rotates in a counter-clock-wise direction and the eccentricity direction is negative, the cutting type is up-milling (entry angle is zero, and exit angle is non-zero).

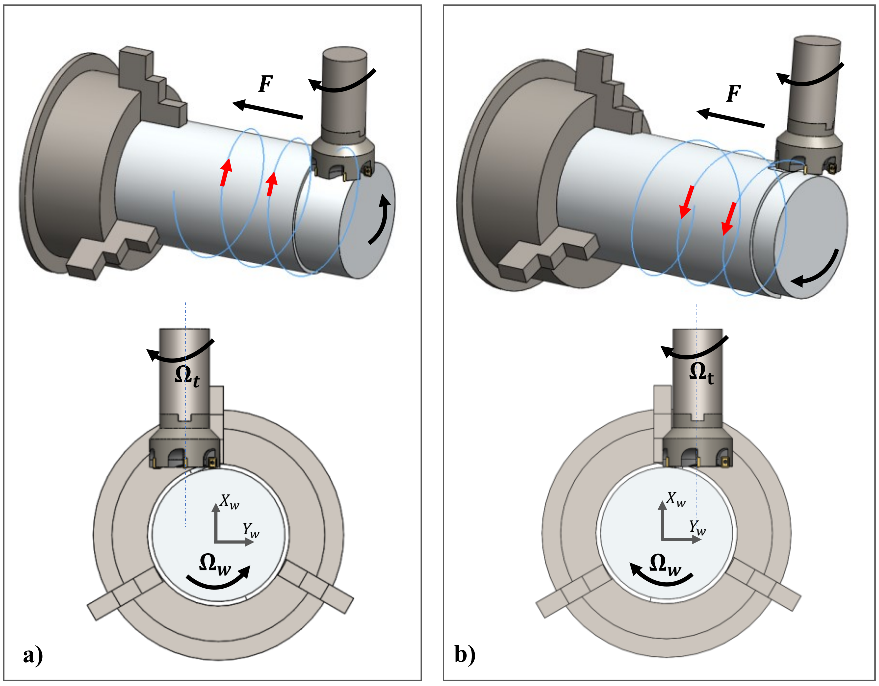

Figure 3.2. Orthogonal turn-milling configurations; a) up-milling, b) down-milling.

The down-milling case (entry angle is non-zero, and the exit angle is π) happens in the configuration shown in Figure 3.2-b where is workpiece rotation direction is clock-wise, and the eccentricity direction is in $+Y_w$ direction. In this study, the kinematics and chip geometry model are given according to the up-milling case, which is the most common configuration in turn-milling operations. However, the kinematic relations are identical in both cases, except for the direction of the tool's helical path and the entry/exit angles of the CWE.

As mentioned before, due to the rotational of the workpiece and linear motion of the tool in the feed direction, the tool follows a helical trajectory in stationary WCS. The helix angle of this helical trajectory can be defined as the angle between the stationary TCS and the $\mathcal{FCN}$, which is located at the tooltip.

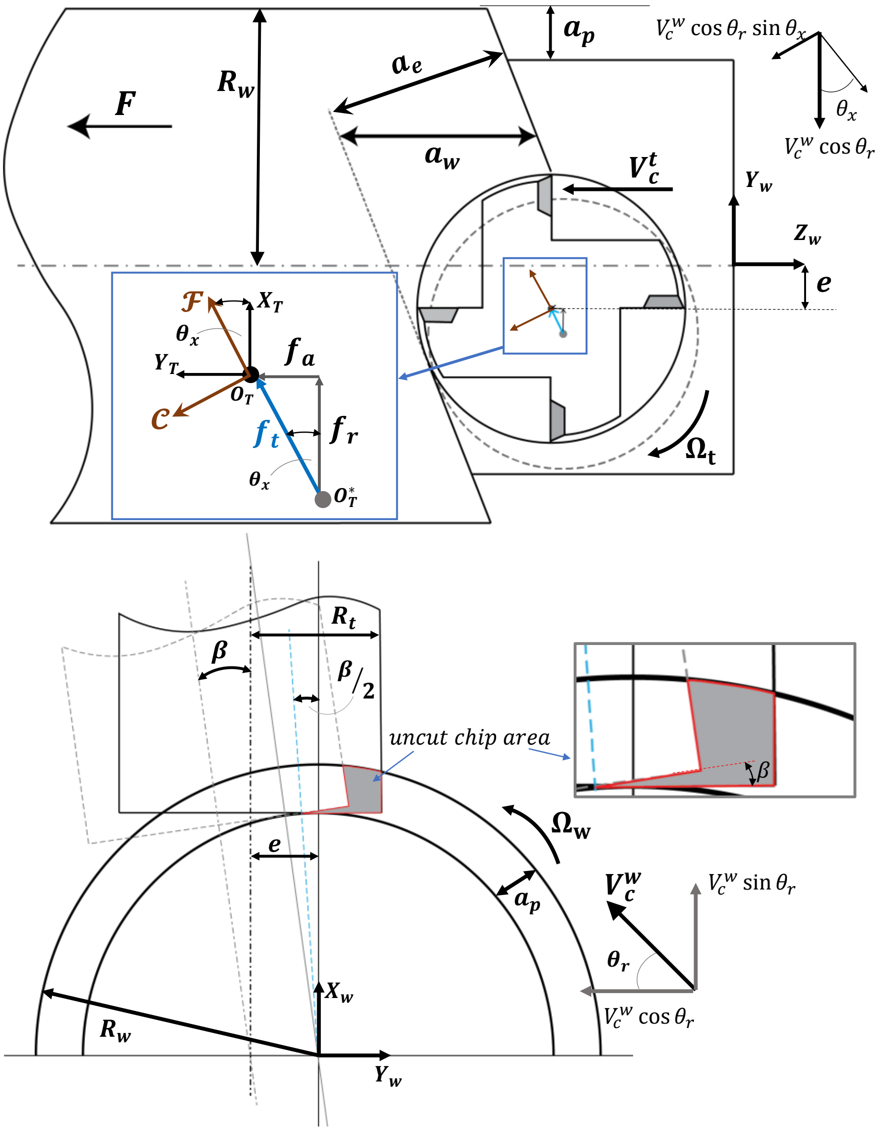

Figure 3.3. Schematics of cutting geometry

This angle is defined as below and illustrated schematically in Figure 3.3.

$$\theta_x = \tan^{-1}\left(\frac{a_w}{2\pi(R_w - a_p)}\right) \tag{3.1}$$

where R_w is the workpiece radius before cut, a_p is the nominal depth of cut, and a_w is the feed per workpiece revolution. Note that, since the process kinematics is based on the tooltip position, the machined part radius ($R_{w2} = R_w - a_p$) is used in Equation (3.1). As a result, not only the diameter of the unmachined part but also the depth of cut affects the helix angle of the helical trajectory of the tool. As shown in Figure 3.3, the radial depth of cut (step over) can be calculated as;

$$a_e = a_w . \cos\theta_x \tag{3.2}$$

Another important parameter in turn-milling kinematics is the angular displacement of the workpiece per tooth passing period (Δt) of the tool, which is shown by β in Figure 3.3 and defined in Equation (3.3).

$$\beta = \frac{2\pi\Omega_w}{\Omega_t N} \tag{3.3}$$

where N is the teeth number of the cutter. Based on the kinematics of the turn-milling, the angle between two surfaces generated by cutting two consecutive teeth and rotation of the workpiece simultaneously, equals to β (see Figure 3.3), which can be proven using geometric relations. The β angle is an important parameter in the definition of minor edge engagement. Note that, the β angle depends on the ratio of the rotational speeds of the cutter and workpiece $\left(\frac{\Omega_w}{\Omega_t}\right)$. As the cutter moves along the helical trajectory, the feed value in the helical direction (surface feed $\mathcal{F}$) can be divided into axial and radial feed vectors, as illustrated in Figure 3.3. The radial and axial feed vectors are the amounts of tool tip travel from point O_T^* to point O_T at the time interval of Δt at feed and cross-feed directions, respectively. The tool positions at time t and $t + \Delta t$ are shown schematically in Figure 3.4b. If the tool is discretized into m number of disk elements with the height of dz along its axis, it is seen that each discrete element within the nominal depth of cut (a_p) has different radial feed (f_r) values depending on its distance from tool tip, as depicted in Figure 3.4a. The distance of each element from the tooltip can is defined by $a(z) = m * dz$.

Hence, the elemental radial feed vector is a function of the distance of the associated element from the tooltip and can be calculated as follow;

$$f_r(z) = \beta.\left(\left(R_w - a_p\right) + a(z)\right) \tag{3.4}$$

The radial feed varies along the depth of cut and the magnitude of f_r increases as the distance from the tooltip (effective radius) increases (See Figure 3.4-a). On the other hand, the axial feed vector f_a is formed due to the linear motion of the tool along the workpiece axis.

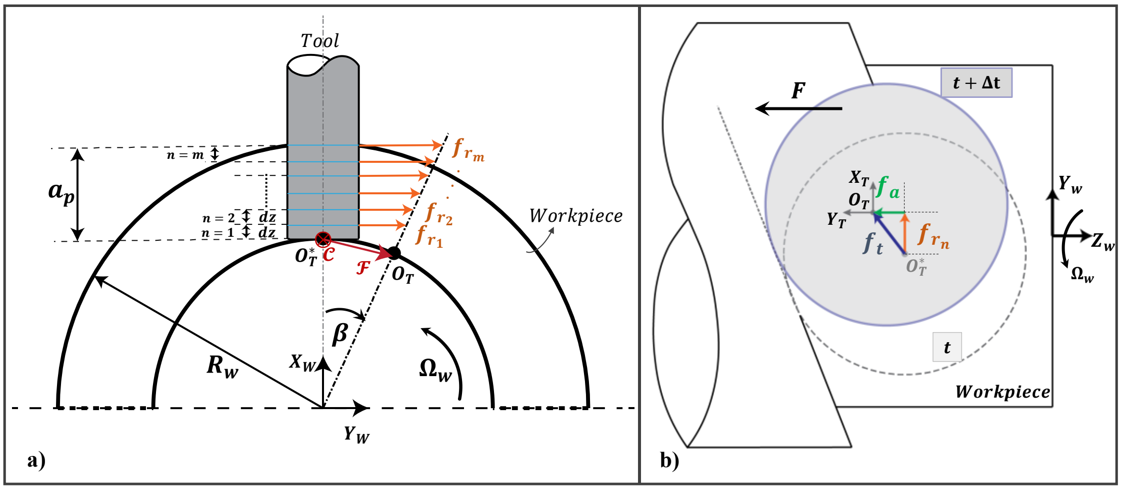

Figure 3.4: Definition of radial and axial feed vectors along with the axial depth of cut.

This vector is constant for all of the disc elements and can be calculated as below:

$$f_a = \frac{a_w \Omega_w}{\Omega_t N} \tag{3.5}$$

Note that both radial and axial feed vectors are formulated and defined at the tooth passing period. As a result, the resultant vector of these two gives the total feed at tooth passing period or the feed per tooth f_t $\left(\frac{mm}{rev.tooth}\right)$ on the helical direction for orthogonal turn-milling operation as follow;

$$f_t(z) = \sqrt{f_r(z)^2 + f_a^2} = \frac{2\pi\Omega_w}{\Omega_t N \cos(\theta_x)}\left(R_w - a_p + a(z)\right) \tag{3.6}$$

Finally, as shown in Figure 3.3, the tool rotates by β at stationary WCS at a tooth passing period. In other words, the Z_T axis of the tool has a β angle with surface normal $\mathcal{N}$. As a result, the feed vectors (f_t) at each disc elevation must be transferred into unit surface feed direction at $\mathcal{FCN}$. The feed vector can be calculated as:

$$\breve{f}_t(z) = f_t(z).\cos\beta \tag{3.7}$$

In orthogonal turn-milling operation, the linear feed $F\left(\frac{mm}{min}\right)$ along the Z_w direction is related to the feed per workpiece rotation and the rotational speed of the workpiece and can be formulated as follows;

$$F = \Omega_w a_w \tag{3.8}$$

As seen, the feed per tooth varies along with the nominal depth of cut. Further, based on its dependency on β the ratio of rotational speeds also affects the feed per tooth, and hence, the cutting mechanics are affected significantly. For this purpose, the parameter selection of orthogonal must be according to the precise calculation of kinematic parameters.

Finally, the simultaneous rotation of the tool and workpiece causes the overall cutting speed to vary in turn-milling operation. According to the kinematics illustrated in Figure 3.3, the linear speed vector resulted from the workpiece V_c^w varies based on the cutting angular position of the cutter since at each angular position, the effective workpiece radius is different. This variation is formulated by θ_r angle and formulated as below:

$$\theta_r = \tan\left(\frac{R_t\sin(\theta_x+\phi_i)}{R_w-a_p}\right) \tag{3.9}$$

As a result, the overall cutting speed resulting from the tool and workpiece rotations can be obtained using the equation below:

$$V_c = V_c^t + V_c^w\, cos(\theta_r)\, sin(\theta_x)\, sin(\phi_j) \tag{3.10}$$

where ϕ_i is the angular position of the edge at angular increment i. Equation (3.10) shows that the cutting speed varies in turn-milling due to the simultaneous rotation of the workpiece and tool. However, the effect of linear workpiece speed is negligible, and the cutting speed of the process can be calculated by the tools cutting speed V_c^t.

3.3. Geometric Model of Cutter-Workpiece Engagement

Modeling chip geometry in multi-axis machining plays a significant role in accurately predicting cutting mechanics and stability analysis. Although there are several methods for evaluating CWE using CAD or FE-based software packages that are costly and time-consuming, analytical models can introduce the fast and precise calculation of CWE with minimum error.

This section presents the cutter-workpiece engagement model of orthogonal turn-milling operation. In this study, the engagement model is presented for end mill type cutters and cylindrical workpieces. As a result of tool geometry and simultaneous rotation of cutter and workpiece, the minor edge of the tool is also engaged, despite peripheral milling operation. This phenomenon distinguishes the turn-milling cutting geometry, mechanics, and dynamics from 3-axis milling operations. In this regard, several studies dealt with turn-milling cutting mechanics previously. Karaguzel et al. and Filho [12,25] extracted the CWE by employing the simple CAD representation of the tool and workpiece. However, the effect of the minor edge was not included in the models, which excludes the different chip geometries and limitations caused by the minor edge length.

Similarly, Ortega et al. [30] used the same approach to evaluate the chip geometry and cutting forces without considering the eccentricity. Comak et al. [29] utilized the CAM and virtual machining software packages to assess the CWE in turn-milling operation required for cutting force calculations. In this section, the CWE occurs at both side edge, and the minor edge of the flat end mill is modeled based on basic cutting geometry and process kinematics. The current approach calculates the CWE analytically and gives an easy and simple understanding of it. This model can predict the uncut chip thickness in turn-milling operation while using crest-cut and serrated tools. The following subsections will discuss the tool's engagement boundaries for side and minor edges separately.

3.3.1. Side edge engagement model

In turn-milling operation, the side edge of the cutter experiences a chip removal process with variable depth of cut due to the simultaneous rotation of the cutter and the circular workpiece. Based on the geometry of the cutter and workpiece and the cutting parameters, the instantaneous depth of cut varies at each angular position of the tool within its immersion boundaries. The instantaneous depth of cut (chip height from tooltip) is formulated in Equation (3.11) [24].

$$a_i(\phi_j) = \sqrt{R_w^2 - \left(R_t \sin(\phi_j) - e\right)^2} - \left(Rw - a_p\right) \tag{3.11}$$

where ϕ_j is the angular position of tooth j within the immersion angles ($\phi_{st} \leq e \leq \phi_{ex}$), and e is the tool center offset (eccentricity) as depicted in Figure 3.3. In our previous work [24], the entry angle of tooth j was assumed equal to θ_x since the cutting geometry was modelled according to stationary TCS. In this chapter, the chip geometry will be discussed in $\mathcal{FCN}$ coordinate system in more detail.

Equation (3.11) shows that the uncut chip geometry has a varying depth of cut within CWE. However, if the CWE is divided into disk elements along the tool axis, each element has a different entry angle. Further, the variation of instantaneous chip thickness is also changing drastically by changing the tool/workpiece radius ratio, eccentricity, and even nominal depth of cut. Since the instantaneous depth of cut varies within the CWE, each elemental segment along the axial depth of cut will have specific entry and exit angles [29]. However, the entry and exit angle definition for each axial element can also be divided into two different categories based on the eccentricity.

i. If the eccentricity is in the range of $\mathbf{0} \leq \boldsymbol{e} \leq \boldsymbol{e_g}$.

The entry (start) angle (ϕ_{st}) for each disc element along the tool axis within the CWE is calculated as:

$$\phi_{st}(z) = \sin^{-1}\left(\frac{-u(z)}{R_t}\right)$$

$$u(z) = \sqrt{R_t^2 - \frac{1}{4}\left(f_a - f_r(z)\sqrt{\frac{4R_t^2}{f_a^2 + \left(f_r(z)\right)^2} - 1}\right)^2} \tag{3.12}$$

and exit angle (ϕ_{ex}) is:

$$\phi_{ex} = \cos^{-1}\left(\frac{a_e}{2R_t}\right) \tag{3.13}$$

The e_g is a critical eccentricity where the uncut chip geometry's definition changes and can be calculated as follows:

$$e_g = a_p\sqrt{2\frac{R_w}{a_p} - 1} + R_t \sin\left(\phi_{st}(0)\right) \tag{3.14}$$

Moreover, the parameter m defined in the eccentricity range will be defined geometrically in Section 3.3.2. The m is defined as:

$$m = \left(R_w - a_p\right).\frac{\beta}{2} \tag{3.15}$$

If the eccentricity is within case i, the entry and exit angle for each disc element n along the tool axis can be found by the formulas mentioned above. (See Figure 3.4).

ii. If the eccentricity is in the range of $\boldsymbol{e_g < e \leq e_{max}}$

Similarly, the entry angle for each disc segment along the tool can be calculated as:

$$\phi_{st}(z) = \sin^{-1}\left(\frac{e-\sqrt{2R_w\left(R_w-a_p+a(z)\right)-\left(R_w-a_p+a(z)\right)^2}}{R_t}\right) \tag{3.16}$$

The exit angle for this range is equal to case **i**. and can Equation (3.13) can be employed. Note that, e_{max} is the maximum value of eccentricity that can be defined in an orthogonal turn-milling operation and can be calculated as follows:

$$e_{max} = R_t - m \tag{3.17}$$

If eccentricity exceeds this value, the instantaneous depth of cut will be lower than the nominal value; hence, the material removal rate will decrease. The detailed simulation and discussion are presented in Section3.4.

3.3.2. Minor edge engagement model

As mentioned before, due to simultaneous rotation of workpiece and tool, the minor edge of the tool is also engaged during the material removal operation. The minor edge engagement plays a vital role in the surface quality of the cut part and cutting forces. As a result, having a precise model for minor edges is essential in the definition of cutting forces and parameter selection procedure. The chip formation by the minor cutting edge is based on a different cutting geometry than the side cutting edges of the tool.

Similarly, the uncut chip thickness varies at each angular position within the immersion boundaries, while the immersion boundaries depend on the tool offset value. In general, the cutting geometry of the minor edge and its cutting mechanics differ from the milling tool's side cutting edge. The schematic representation of the cutting geometry of the minor edge is represented in Figure 3.5. The following geometric model is true when tool offset is in the range $m \leq e \leq e_{max}$. It means that for tool offset values greater than e_{max} the minor edge of the tool will lose engagement and decrease the maximum engagement of the side edge.

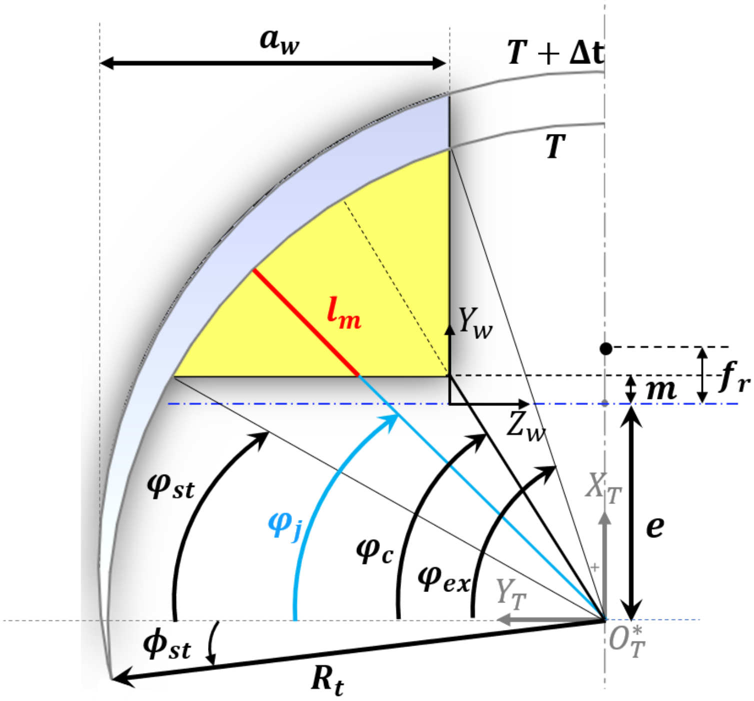

Figure 3.5: Schematic representation of chip geometry resulting from the minor edge.

Note that the minimum value for eccentricity equals m, as also seen in Section 3.3.1. This is because if the eccentricity is equal to zero, the minor edge will not cut at the vicinity of the tool center due to zero cutting speed. This issue must be taken into account while cutting with endmills since edges can be connected at the tool center. In contrast, the inserts have an offset from the tool center in most face milling tools, and zero eccentricity will not cause any problem. According to the cutting geometry of the minor edge, the entry angle for the immersion zone of the minor edge can be calculated by

$$\varphi_{st} = \sin^{-1}\left(\frac{e+m}{R_t}\right)$$

$$\varphi_{ex} = \begin{cases} \phi_{ex} & a_w \le R_t \\ \tan^{-1}\left(\dfrac{a_w - R_t}{e+m}\right) & a_w > R_t \end{cases} \tag{3.18}$$

The exit angle for minor edge (φ_{ex}) is equal to the exit angle of the side edge (ϕ_{ex}) when the a_w is equal to or smaller than the tool radius. As seen in Figure 3.5, the engagement length (l_m) of the minor edge changes within the immersion zone at each angular position of the minor edge. The engagement length is calculated based on the cutting geometry and defined as below:

$$l_m(\varphi_j) = \begin{cases} R_t - \frac{(e+m)}{\sin\varphi_j} & \varphi_{st} \le \varphi_j \le \varphi_c \\ \begin{cases} R_t - \frac{(R_t-a_w)}{\cos\varphi_j} & a_w \le R_t \\ \left|\frac{a_w-R_t}{\cos\varphi_j}\right| - \frac{(e+m)}{\sin\varphi_j} & a_w > R_t \end{cases} & \varphi_c < \varphi_j \le \varphi_{ex} \end{cases} \tag{3.19}$$

where φ_j is the immersion angle of the minor edge of tooth j within the immersion zone. In this equation, φ_c is the angle where the definition of engagement length is changed because of the uncut chip geometry and can be calculated as below:

$$\varphi_c = \begin{cases} \tan^{-1}\left(\frac{e+m}{R_t-a_w}\right) & a_w \le R_t \\ \frac{\pi}{2} + \sin^{-1}\left(\frac{a_w-R_t}{R_t}\right) & a_w > R_t \end{cases} \tag{3.20}$$

It is mentioned before that the region in cut with the minor edge is produced by the face formed by current tooth j and the face formed by previous tooth $j-1$, which has an angle of β due to the rotation of the workpiece. In other words, the angle between these two faces is equal to the rotation angle of the workpiece at the tooth passing period of the tool. The schematics of these two faces are given in Figure 3.6. As seen, although the angle between two faces is constant and equal to β at X_T direction, however, because of the geometry, the angle between two faces is different when the geometry is cut at the tool's angular position (φ_j). This locally varied angle is shown as β_l in Figure 3.6. This angle is important since it defines the maximum uncut chip thickness for the minor edge at any angular position. As a result, as the tool rotates, the minor edge of the tool experiences a specific engagement length and maximum uncut chip thickness at each angular position, where the uncut chip thickness varies along the engagement length. The elemental uncut chip thickness removed by the edge segment on the minor edge with the differential length of dl is formulated in Equation (3.21).

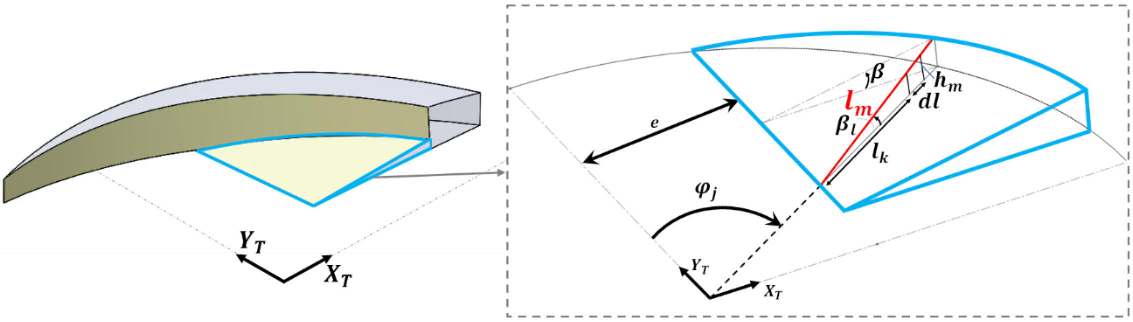

Figure 3.6: Schematic representation of minor edge geometry

$$h_m(\varphi_j, l_k) = l_k.\tan\left(\sin^{-1}\left(\frac{[R_t \sin(\varphi_j) - e - m]\tan\beta}{l_m(\varphi_j)}\right)\right) \quad \because l_k = k.dl \tag{3.21}$$

Note that the engagement length (l_m) is divided into infinitesimal elements with a length of dl. Therefore, the number of elements varies for each engagement length while the element length is constant. The parameter l_k is the distance of element $k, (1 \leq k \leq n)$ from the beginning of the engagement, where $n = \frac{l_m(\varphi_j)}{dl}$. In order to discuss the uncut chip geometry generated by minor edge, a case study is selected, and chip geometry is shown in Figure 3.7. The workpiece rotation per tooth period is $\beta = 2°$. The cross-section views of C1-C1 and C2-C2 parallel with X_T direction shows that the angle between the two faces is equal to β. However, as the tool rotates, the angle between two consecutive faces changes because of the geometrical relations. The cross-section views B1-B1, and B2-B2 shows the uncut chip cross-section view at two arbitrary angular positions of the cutting edge (See Figure 3.7). It is deduced that at each angular position, the angle between two consecutive faces is different, and the chip has a local angle of β_l. In other words, the maximum uncut chip thickness or minor edge is different at each angular position, and it varies along the engagement length ($l_m(\varphi_j)$). It is deduced that the minor edge experiences a different local maximum uncut chip thickness at each angular position with varying engagement lengths. This phenomenon will affect the cutting mechanics and dynamics drastically.

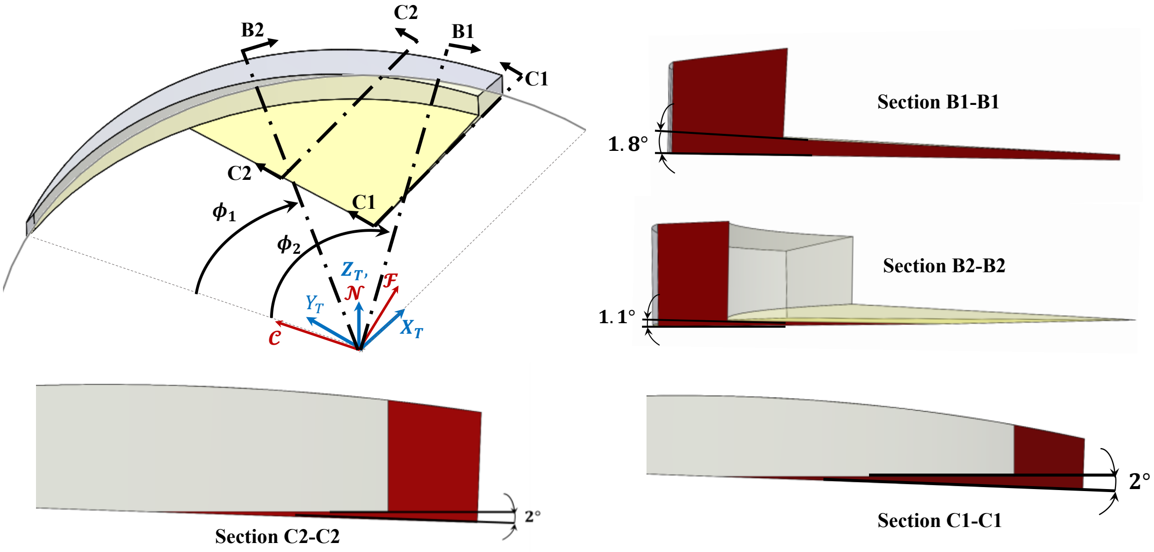

Figure 3.7: Different cross-section views for chip geometry in orthogonal turn-milling.

3.4. Effect of Cutting Parameters on the Chip Geometry

Based on the geometrical model given in previous sections, the uncut chip model of the orthogonal turn-milling operation can be simulated. Using the proposed uncut chip model, effect of different cutting parameters and tool/workpiece geometries on chip formation can be studied. From this point of view, the impact of these parameters on cutting mechanics, surface formation, and process stability can be studied. Note that the uncut chip geometrical model will be indirectly confirmed in the next sections using cutting force experiments and simulations. However, this section performs preliminary confirmation using the CAD model. The uncut chip height and chip boundaries generated by the side edge of the tool and the cutting boundaries and chip thickness generated by the minor edge are compared and confirmed in both mathematically simulated and CAD models in Figure 3.8. Note that the feed per tooth value in CAD simulation is exaggerated to have a better visualization; however, all the geometrical parameters are confirmed with the mathematical model. The uncut chip geometry simulations are shown in $\mathcal{FCN}$ coordinate system.

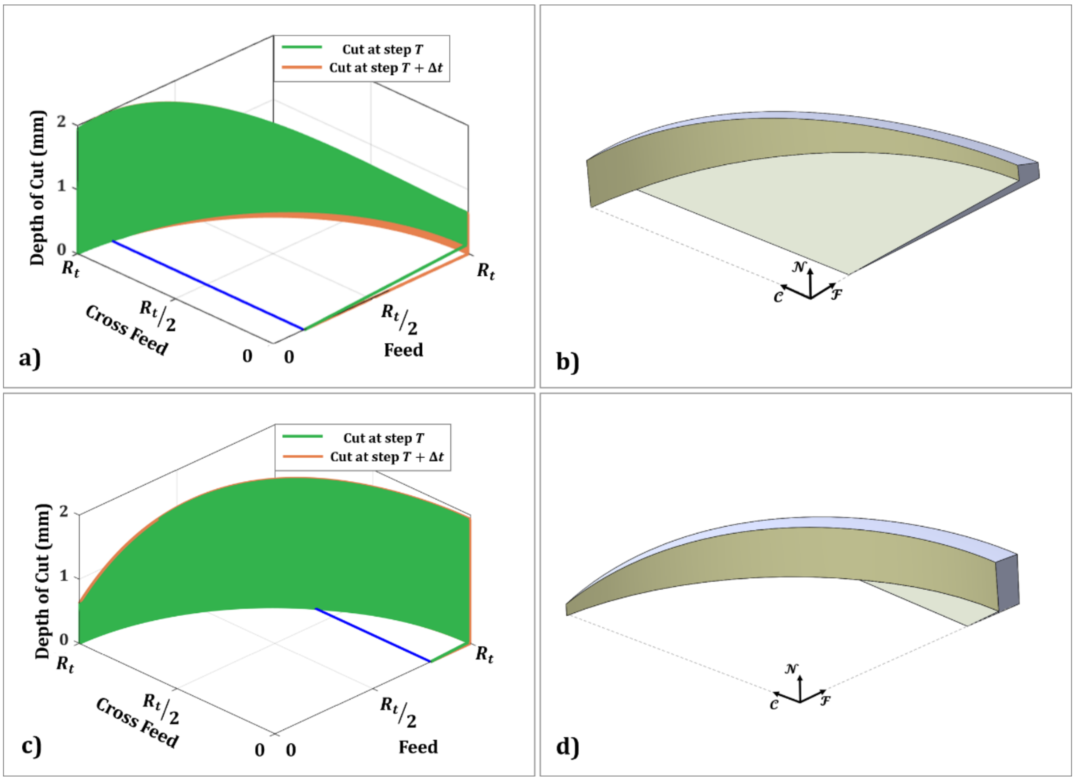

Figure 3.8: Chip geometry simulations for $D_t = 22\ mm, D_w = 60\ mm$, $a_p = 2\ mm$,

$a_e = 0.5D_t$, a) Analytical simulation $e = 2mm$, b) CAD simulation $e = 2mm$, c) Analytical simulation $e = 9\ mm$, d) CAD simulation $e = 9\ mm$

As mentioned in Section 3.3, the cutter and workpiece diameters affect the chip geometry. However, in turn-milling operation, the tool offset (eccentricity) is the most influential parameter which influences the CWE drastically. As seen in Figure 3.8, the variation in eccentricity changes the chip geometry of the side edge and the chip generated by the minor edge. This variation will affect the cutting mechanics and dynamics significantly.

In this regard, the engagement boundaries of the side edge are simulated to show the effect of eccentricity and tool radius on the chip formation caused by the side edge. The cutting parameters for the two cases are given in Table 3.1. The tool radii for Case 1 and Case 2 are different. In both cases, the radial immersion is 50% of the tool diameter. For each case, the chip geometry comparisons for various eccentricities values are depicted in Figure 3.9 and Figure 3.10.

As shown in Figure 3.9, the variation of depth of cut within the immersion boundary is different at different tool offset values. It is to be noted that the variation pattern is not similar for other workpiece and tool diameter ratio values $\left({}^{R_w}/_{R_t}\right)$.

Table 3.1: Cutting parameters for chip geometry comparisons for different eccentricities.

	$\mathrm{D_w}(mm)$	$\mathrm{D_t}(mm)$	$\mathrm{a_w}(mm)$	$\mathrm{a_p}(mm)$	${}^{\Omega_t}/_{\Omega_w}$
Case 1	160	32	16	3	200
Case 2	160	50	25	3	200

According to Equations (3.14) and (3.17), for Case 1, the critical eccentricity is $e_g = 20.8\,mm$ and the maximum allowable eccentricity is $e_{max} = 15.3\,mm$. As shown in Figure 3.9, when the tool offset exceeds e_{max} the axial depth of cut begins to decrease (the case $e = 20mm$) while the entry angle stays the same where the Equation (3.12) governs. Note that, eccentricity values above the e_{max} is not practical since the axial depth of cut is reducing which causes lower material removal rate and failure in the final part dimensions; however, in this example, it is discussed for comparison purposes.

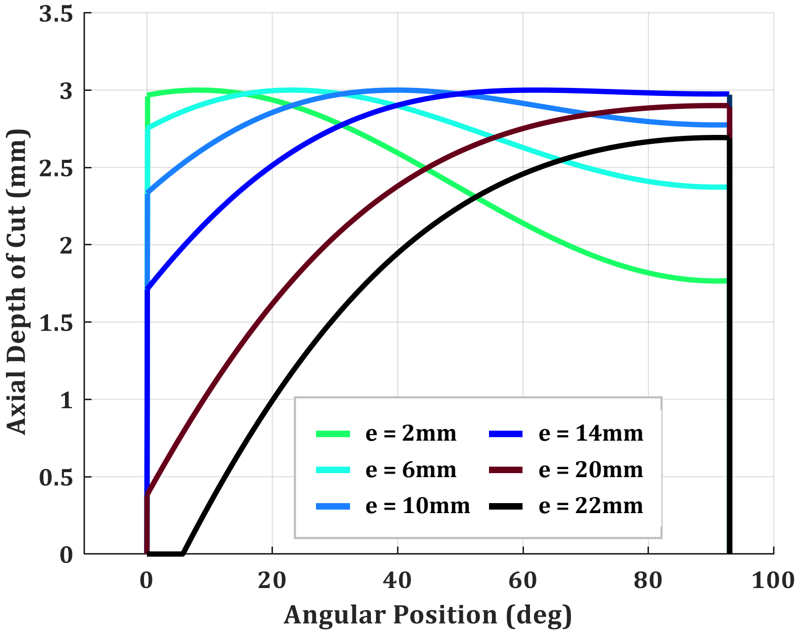

Figure 3.9: Chip boundary comparisons for Case 1 in Table 3.1.

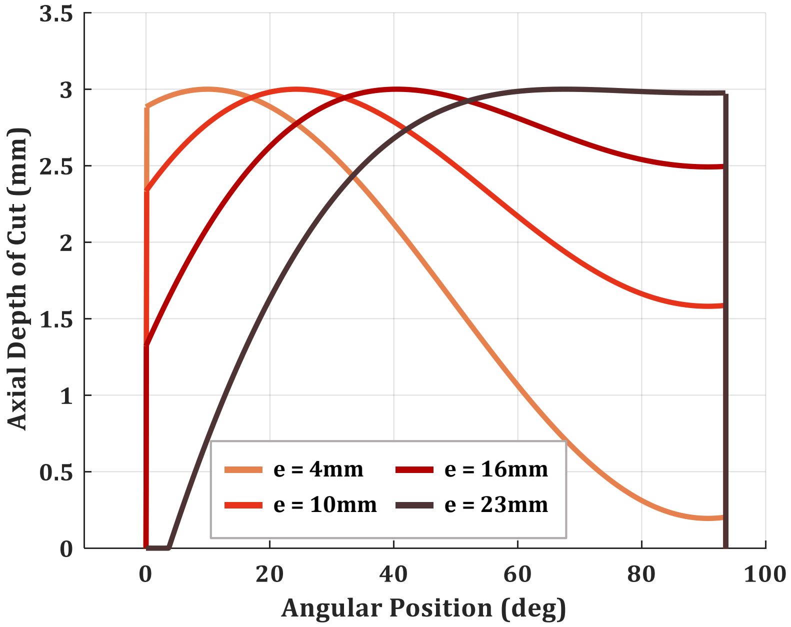

Figure 3.10: Chip boundary comparisons for Case 2 in Table 3.1.

For another workpiece and tool diameter ratio (Case 2), the e_g value could be smaller than e_{max} ($e_g < e_{max}$) which means that within the feasible range of tool offset ($e \leq e_{max}$), both formulation should be used for the calculation of entry immersion angle. In Case 2, since the tool diameter is increased, the critical tool offset is altered. For this case, the

$e_g = 20.5\,mm$ while the $e_{max} = 24.3\,mm$. The comparison simulation is also depicted in Figure 3.10. Equation (3.12) for the tool offset range $e_g \leq e \leq e_{max}$ Equation (3.16) must be employed. The simulations are CWE boundaries are depicted in $\mathcal{FCN}$ coordinate system.

It is shown that the allowable eccentricity depends on the ratio of workpiece and tool diameter ratio value. Next, the effect of the radial depth of cut on CWE of the side edge is studied. For this purpose, the cutting parameters of Case 2 in Table 3.1 are selected with $e = 2mm$ and two different radial depth of cut values. The 3D simulation of chip geometry in $\mathcal{FCN}$ coordinate system and corresponding 2D representation in $\mathcal{F} - \mathcal{N}$ view is given in Figure 3.11. According to Figure 3.11 (a), for the given eccentricity and radial depth of cut value, engagement of the side edge is limited to a specific angular position and is diminished after that specific angular position within the immersion angles, while the minor edge is in the cut. This is due to the geometrical condition caused by the tool-workpiece diameter ratio, radial depth of cut, and eccentricity values.

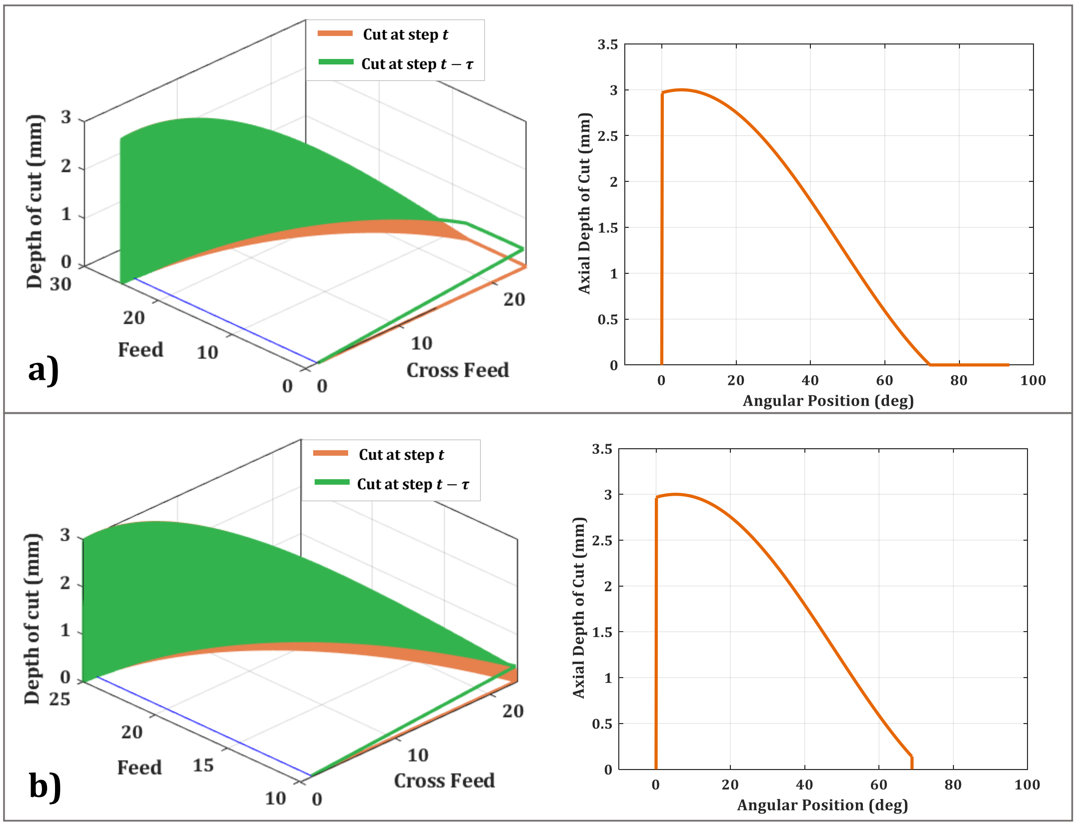

Figure 3.11: Chip geometry comparison with parameters in Table 3.1;

a) $e = 2mm$, $a_w = 25mm$, b) $e = 2mm$, $a_w = 15mm$

However, if the radial depth of cut is decreased (as shown in Figure 3.11 (b)), the side edge is kept engaged within the immersion boundary as well as the minor edge. The engagement loss of the side edge will cause surface defects due to the uncut material left on the machined part. It is shown that in orthogonal turn-milling, eccentricity is a critical parameter and cannot be determined randomly. In addition, it has a relationship with the radial depth of cut value, and the possible undesired chip geometries can be added or omitted by tuning the appropriate eccentricity and radial immersion values. The relationship between these two parameters is discussed in detail in terms of surface failures in the next section.

3.5. Surface Errors in Orthogonal Turn-Milling

The surface quality of the finished part is an important outcome of the machining processes. Unlike the conventional turning process, simultaneous rotation of tool and workpiece during turn-milling operation leads to surface errors such as circularity and cusp formation [12]. The circularity error is the difference between the desired workpiece cross-section (perfect circle) and the workpiece's polygon-shaped cross-section, which is caused by the simultaneous rotation of the workpiece and tool, which is described by Karagüzel et al [12]. The maximum circularity error is depicted in and can be calculated as follows;

$$e_{circ} = \left(R_w - a_p\right)\left(\frac{1}{\cos\left(\frac{\beta}{2}\right)} - 1\right) \tag{3.22}$$

where β is defined in Equation (3.3).

Similar to surface roughness in conventional turning, circularity error in turn-milling operation cannot be eliminated because of the intermittent nature of the process; however, it can be reduced by increasing the ratio of tool to workpiece spindle speeds. For this purpose, the spindle speed of the tool could be increased, which can cause excessive tool wear. As an alternative, the workpiece's spindle speed can be decreased, leading to lower productivity. As a result, the allowable circularity error must be calculated. The tradeoff between the surface quality, MRR, and machining cost must be considered at the process planning stage.

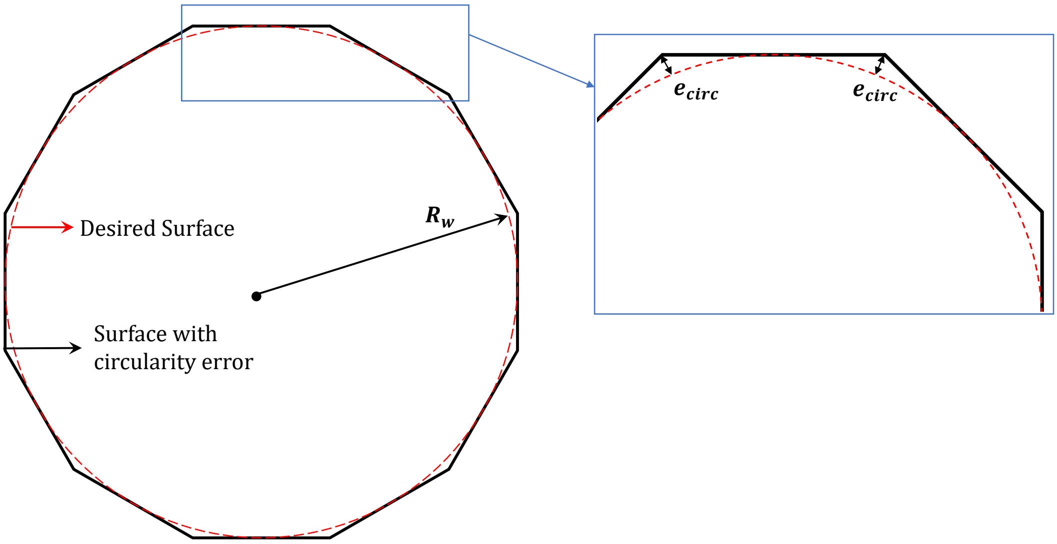

Figure 3.12: Definition of circularity error in orthogonal turn-milling.

Another important surface error that happens during orthogonal turn-milling operation is the cusp formation. Previously, Karagüzel et al. [12] introduced cusp generation and proposed a geometrical model for the calculation of cusp height. However, the tool geometry and the geometry of the minor edge on the tool were not considered. As mentioned in previous sections, the tool's minor edge significantly affects cutting mechanics, surface generation, and chip geometry. The engagement and contact of minor edge with the machined surface of the workpiece is the key element in the definition of the surface quality, chip formation, and hence, cutting forces.

As the tool follows a helical path along the workpiece axis, the minor edge is engaged in the chip removal process, and depending on the minor edge geometry; the surface form is generated. In most of the milling cutters used in 3-axis milling operations, the minor edge has an approach angle ($\alpha_m > 0$) to reduce the friction between the tool and the cut surface since the material removal process is done by the side cutting edge of the tool. Using such milling tools with minor edge approach angle (See Figure 3.13) in the orthogonal turn-milling process, cusp formation will be inevitable. As shown in Figure 3.13, due to the geometry of the minor edge, uncut material will be left between two consequent passes per workpiece rotation.

In order to eliminate cusp formation in orthogonal turn-milling operation, the first solution is to use milling tools with zero minor edge approach angle (α_m) as shown in Figure 3.13 (b). However, using such a tool will not solve the cusp formation phenomenon in orthogonal turn-milling process. Because of the complex kinematic of the process, based on the eccentricity and radial depth of cut, a cusp can still be formed because of the uncut material left between two consequent stepovers even if the approach angle is minor edge is zero.

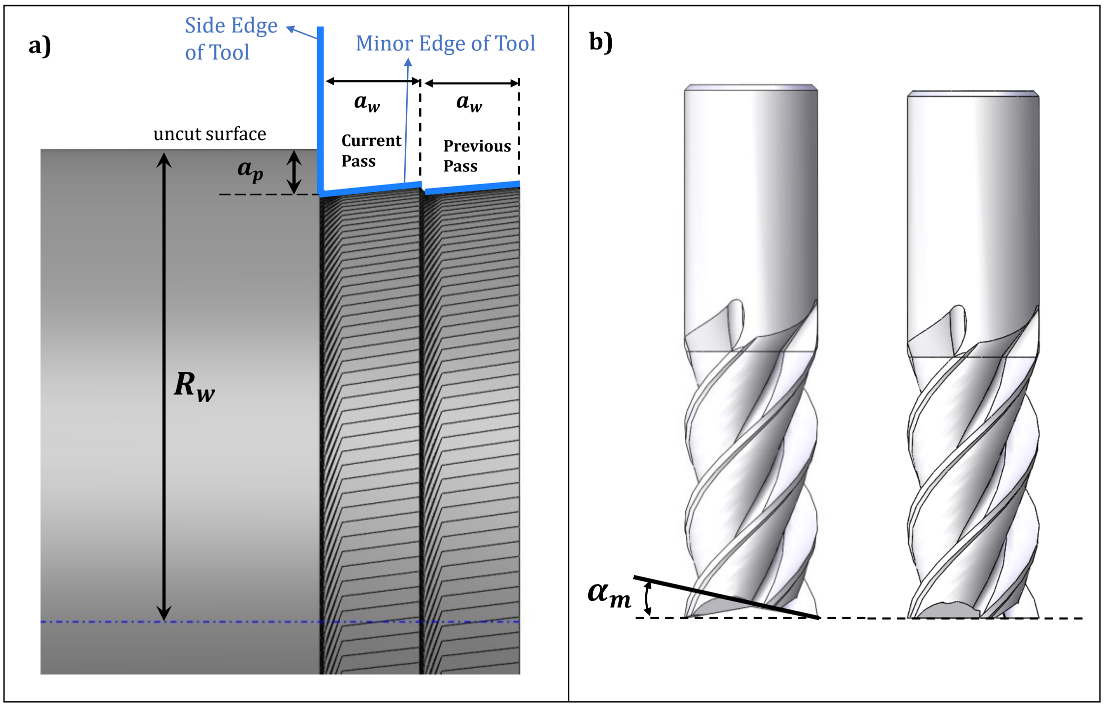

Figure 3.13: Cusp formation in orthogonal turn-milling process due to minor edge approach angle.

As mentioned before, the minor edge will experience a specific engagement length based on the eccentricity value. If the engagement length is not sufficient enough to wipe out the material left from the previous pass as the tool travels a_w in the workpiece axial direction at the time of one workpiece rotation, the cusp will be formed. In other words, if the feed per workpiece rotation (a_w) is greater than the length of which minor edge sweeps, the uncut material will be left between two consequent passes, named cusp. This phenomenon is illustrated in Figure 3.14.

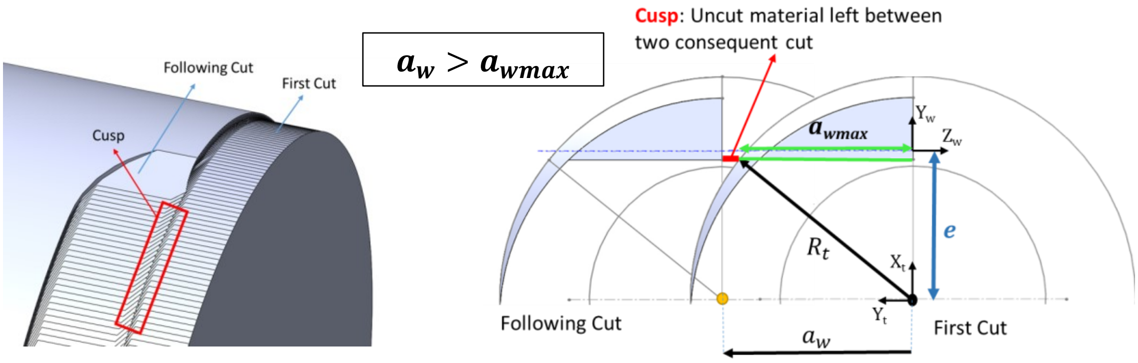

Figure 3.14: Formation of cusp in orthogonal turn-milling operation.

In order to prevent the cusp formation, the feed per workpiece revolution (a_w) must be smaller than the step over during the process. Alternatively, depending on the eccentricity value, there is a maximum allowable range (a_{wmax}) which the minor edge can wipe out all the material during the cut, and no uncut material will be left. Another important issue in this regard is the length of the minor edge l_t (or wiper edge length) which leads to different engagement at every eccentricity value. By considering all the mentioned parameters, the allowable feed per workpiece revolution a_{wmax} is modeled in Equation (3.23) based on the cutting geometry given in Figure 3.15. According to Equation (3.23), it is deduced that, unlike the conventional milling process, the stepover in the orthogonal turn-milling process cannot be chosen any arbitrary value smaller than tool diameter, and it depends on tool geometry and eccentricity value.

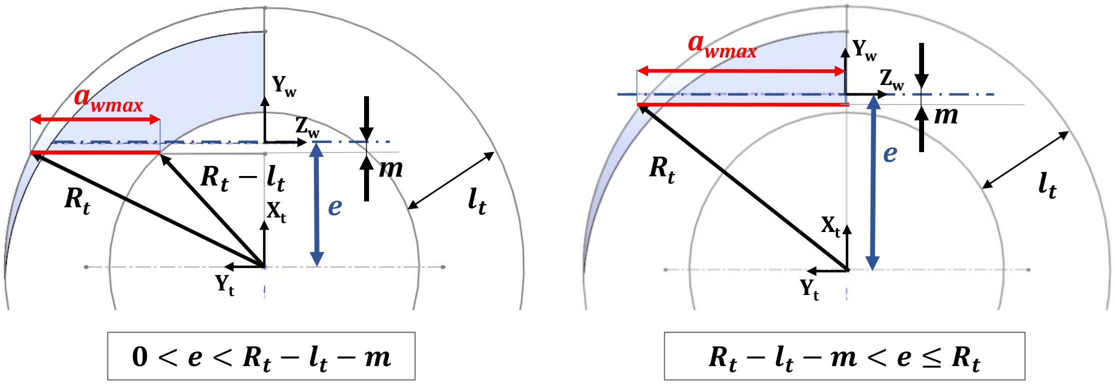

$0 < e < R_t - l_t - m$

$R_t - l_t - m < e \leq R_t$

Figure 3.15: Schematic representation of cutting geometry for calculation of a_{wmax}.

$$a_{wmax} = \begin{cases} l_t + m & e = 0 \\ \sqrt{R_t^2 - (e-m)^2} - \sqrt{(R_t - l_t)^2 - (e-m)^2} & 0 < e < R_t - l_t - m \\ 2\sqrt{2R_t l_t - l_t^2} & e = R_t - l_t - m \\ 2\sqrt{R_t^2 - (e-m)^2} & R_t - l_t - m < e \leq R_t \end{cases} \tag{3.23}$$

where $m = \frac{(R_w - a_p)\beta}{2}$ and l_t is the minor edge length.

According to the proposed model, the minor edge length defines the eccentricity ranges and hence, allowable radial depth of cut value and MRR. For better understanding, Equation (3.23) is illustrated in Figure 3.16.

It is deduced that, as the minor edge length increases the allowable feed per workpiece revolution (a_w) also increases. However, the maximum value of a_w which defines the radial depth of cut happens in a specific eccentricity which depends on minor edge length. As a result, if the tool has longer minor (wiper) edge length higher feed per workpiece values will be achieved which increases the MRR without sacrificing the surface quality. In this regard, employing the proposed model to select the proper eccentricity and feed per tooth value based on the tool diameter and minor edge length leads to higher productivity with error-free surface.

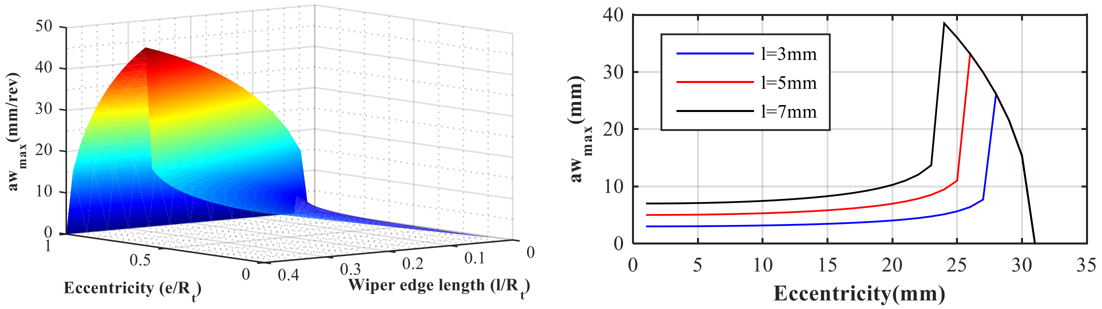

a) b)

Figure 3.16: Effect of minor edge length and eccentricity on allowable a_w, ($R_t = 31.5$)

3.5.1. Experimental verification

In this section, the orthogonal turn-milling operation is performed based on the parameters which are selected according to the model proposed in the previous section to investigate the surface profile. For this purpose, the orthogonal turn-milling experiments are performed on Mori Seiki NTX 2000 multi-tasking machine tool, as shown in Figure 3.17. The workpiece is stainless steel with 116 mm diameter, where a 63 mm diameter face-milling cutting tool with four inserts with minor edge length (l) is 12.7 mm, was used. During the experiments, the cutting speed and feed per tooth values were kept constant, equal to 200 m/min and 0.1 mm/rev/tooth, respectively. Two different experiments were conducted to show eccentricity's effect on productivity and surface quality. The parameters used in the experiments are given in Table 3.2.

Table 3.2: Cutting conditions for surface profile measurement experiments.

Exp. No:	n_t (rpm)	n_w (rpm)	a_w (mm/rev)	a_p (mm)	e (mm)
1	1000	1	20	0.5	15
2	1000	1	40	0.5	22

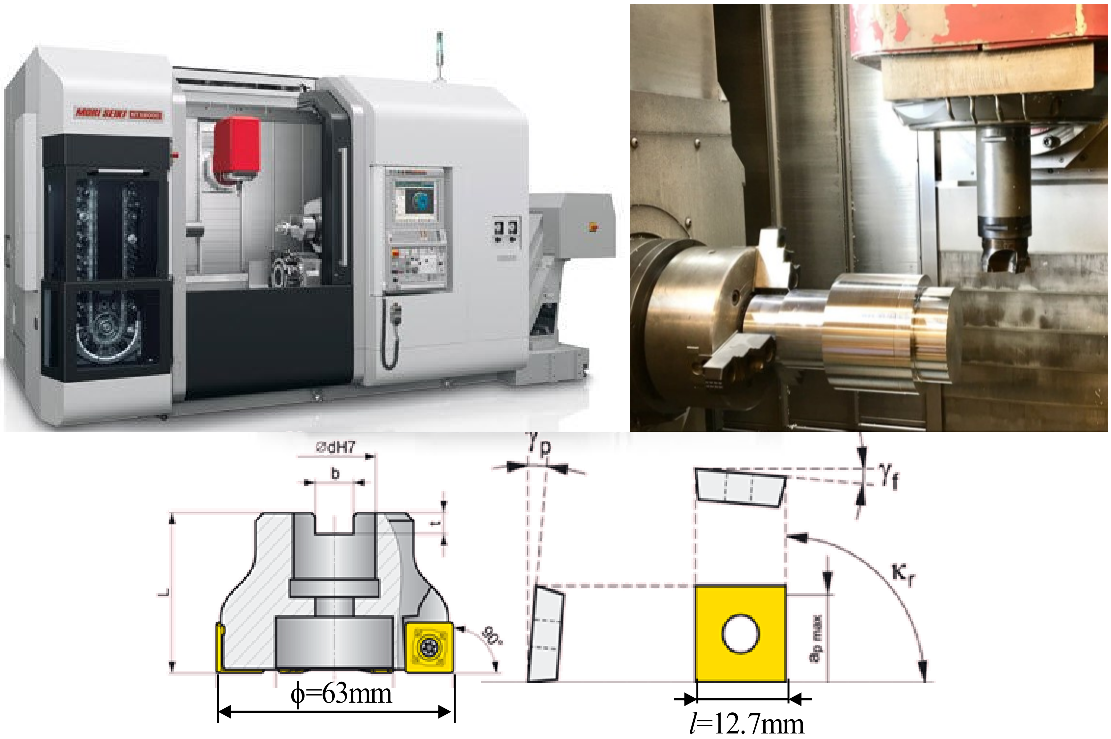

Figure 3.17: Experimental setup used for orthogonal turn-milling process.

The resulting workpiece surfaces are shown in Figure 3.18. While the maximum feed per workpiece revolution is $a_{wmax} = 16.2\frac{mm}{rev}$ for $e = 15$ mm in experiment 1, setting the a_w as 20 (mm/rev) which is higher than the allowable value, results in very poor surface quality with uncut material left on the surface (see Figure 3.18 (1)). On the other hand, for experiment 2 which eccentricity is $e = 22\,mm$ the allowable feed per workpiece is

$a_{wmax} = 45\frac{mm}{rev}$. In this case, better surface quality without uncut material is achieved at an even higher a_w value, as seen in Figure 3.18 (2). It is evident that since the eccentricity and radial depth of cut in experiment 2 are selected based on the proposed model in Section 3.5, the cusp formation is prevented while the MRR is doubled. That indicates using the procedure proposed in this study; one can select all the parameters in turn-milling and use them to program the machine tool by considering both surface quality and productivity. The parameter selection for better cutting performance also depends on other criteria such as the maximum torque capacity of the machine tool and process stability, which will be discussed in the following sections. The complete parameter selection guide will also be given the upcoming sections.

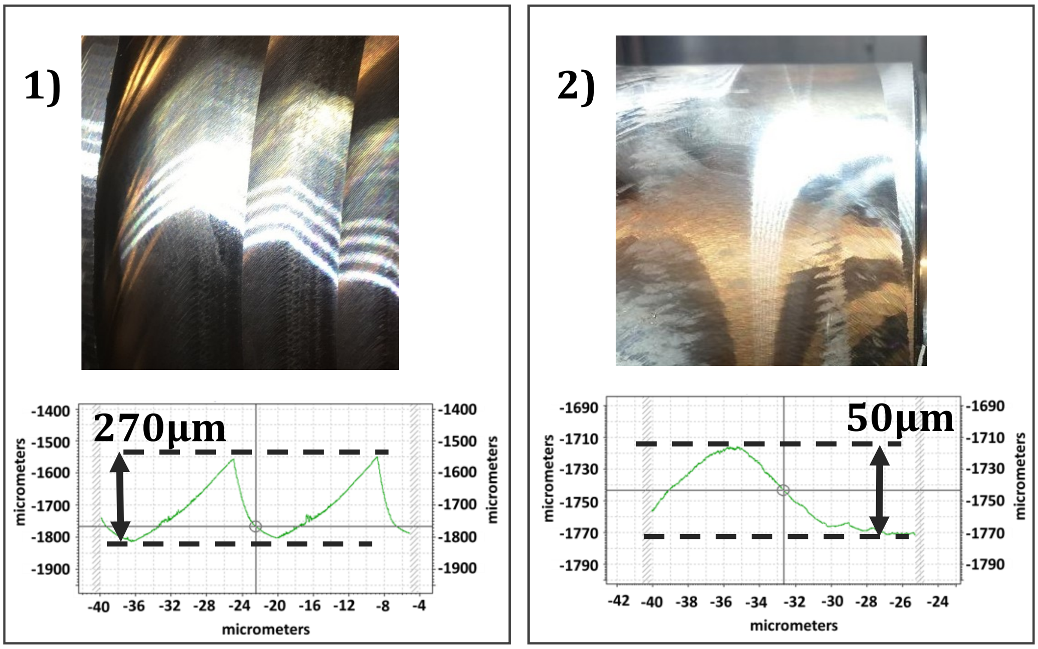

Figure 3.18: Surface profile measurements for conditions in Table 3.2.

3.6. Static Cutting Force Model in Orthogonal Turn-Milling

Based on the cutting geometry and kinematics, it is deduced that both the side edge and minor edge of the milling tool are engaged in cutting in orthogonal turn-milling operation. The CWE and uncut chip thickness are modeled for both cutting edges in Sections 3.2 and 3.3. Once the uncut chip geometry is evaluated, the static cutting forces can be computed using the well-known linear edge force model in the literature [110,111].

As shown in Figure 3.19, the side edge cutting of the tool is divided into infinitesimal small disc elements with a height dz and the minor edge is divided into segments with a width of dl. The differential cutting forces of the discrete cutting edges (side and minor) are calculated separately since the CWE and uncut chip thickness, and hence the cutting mechanics are different for each.

- Side cutting edge:

For a discrete element on the side cutting edge of tooth j^{th}, the differential cutting forces along tangential (t) , radial (r) and axial (a) directions can be written according to linear edge force model as follows [111];

$$\begin{aligned} dF_{t,j}^{s}(\phi_j, z) &= \left[\left(K_{tc}h_j\left(\phi_j(z)\right) + K_{te}\right)dz\right].g\left(\phi_j(z)\right).q\left(\phi_j(z), z\right) \\ dF_{r,j}^{s}(\phi_j, z) &= \left[\left(K_{rc}h_j\left(\phi_j(z)\right) + K_{re}\right)dz\right].g\left(\phi_j(z)\right).q\left(\phi_j(z), z\right) \\ dF_{a,j}^{s}(\phi_j, z) &= \left[\left(K_{ac}h_j\left(\phi_j(z)\right) + K_{ae}\right)dz\right].g\left(\phi_j(z)\right).q\left(\phi_j(z), z\right) \end{aligned} \tag{3.24}$$

where ϕ_j is the angular position of the element on the cutting edge of tooth j which is defined as;

$$\phi_j(z) = \phi + (j-1)\phi_p - \frac{\tan(\gamma_j)}{R_t}z \tag{3.25}$$

where ϕ is the angular increment of the reference tooth, z is the height of the element from the tooltip, γ_j is the helix angle of j^{th} tooth and ϕ_p is the pitch angle defined as $\phi_p = \frac{2\pi}{N}$ for regular milling tools with N number of teeth. The uncut chip thickness in Equation (3.24) can be calculated by;

$$h(\phi_j, z) = \breve{f}_t(z)\sin\left(\phi_j(z)\right) \tag{3.26}$$

where $\breve{f}_t(z)$ is defined in Equation (3.7). The $g\left(\phi_j(z)\right)$ and $q\left(\phi_j(z)\right)$ in Equation (3.24) are unit pulse functions that determine whether the disc element is within the CWE boundaries. The g function controls the angular position of the disc element if it is within the immersion boundary, and the q function determines whether the corresponding element is within the CWE boundaries at that specific angular position and height.

$$g\left(\phi_j(z)\right) = \begin{cases} 1, & \phi_{st}(z) \leq \phi_j(z) \leq \phi_{ex} \\ 0, & \phi_j(z) < \phi_{st} \mid \phi_j(z) > \phi_{ex} \end{cases}$$

$$q\left(\phi_j(z), z\right) = \begin{cases} 1, & 0 < z \leq a_i\left(\phi_j\right) \\ 0, & z > a_i\left(\phi_j\right) \end{cases} \tag{3.27}$$

In the linear edge force model, the cutting force coefficients (K_{tc}, K_{rc}, K_{ac}) and edge force coefficients (K_{te}, K_{re}, K_{ae}) are obtained by orthogonal-to-oblique transformation [110,111]. In this approach, the orthogonal cutting experiments are performed to calculate the orthogonal cutting parameters; shear stress (τ_s), shear angle (ϕ_s) and friction angle (β_s) at for cutter-workpiece pair. The orthogonal cutting tests are performed at different cutting speeds and feed rates, and rake angles (α_r) for that specific cutter-workpiece pair. As a result, the orthogonal cutting parameters will be a function of cutting speed, federate and rake angle. Then, the orthogonal database is transformed to the oblique plane using orthogonal-to-oblique transformation as defined in [111]. The cutting force coefficients in for oblique cutting conditions on the oblique plane are formulated as;

$$\begin{aligned} K_{tc} &= \frac{\tau_s}{\sin\phi_n \cos\gamma} \frac{\sin(\beta_n - \alpha_n)}{\sqrt{\cos^2(\phi_n + \beta_n - \alpha_n) + \tan^2\eta_c \sin^2\beta_n}} \\ K_{rc} &= \frac{\tau_s}{\sin\phi_n} \frac{\cos(\beta_n - \alpha_n) + \tan\gamma \tan\eta_c \sin\beta_n}{\sqrt{\cos^2(\phi_n + \beta_n - \alpha_n) + \tan^2\eta_c \sin^2\beta_n}} \\ K_{ac} &= \frac{\tau_s}{\sin\phi_n} \frac{\cos(\beta_n - \alpha_n)\tan\gamma + \tan\eta_c \sin\beta_n}{\sqrt{\cos^2(\phi_n + \beta_n - \alpha_n) + \tan^2\eta_c \sin^2\beta_n}} \end{aligned} \tag{3.28}$$

where ϕ_n, β_n, α_n, and η_c are the shear, friction, normal rake angle, and chip flow angles on the normal plane, respectively. According to the Stabler's rule [111–113] the angles on the normal plane are considered equal to the orthogonal cutting angles $\phi_n = \phi_s$, $\beta_n = \beta_s$, $\alpha_n = \alpha_r$, and the chip flow angle η_c is assumed to be equal to the oblique angle of the tool (γ). Note that, since the rake angle, helix (oblique) angle, cutting speed (V_c) and feed per tooth $(\breve{f}_t)$ values are constant along the tool axis for standard end mills, the cutting force coefficients for any element on the side cutting edge will be constant. The edge force coefficients are obtained by extrapolating the measured forces in orthogonal cutting experiments to zero chip thickness. Further details can be found in [111].

The differential cutting forces acting on the disc element at height z on the j^{th} tooth in rotating coordinates of (tra) can be transformed into TCS coordinate system using the transformation matrix given in Equation (3.29).

$$dF^s_{x,y,z}(\phi_j,z) = \begin{Bmatrix} dF^s_{x,j}(\phi_j,z) \\ dF^s_{y,j}(\phi_j,z) \\ dF^s_{z,j}(\phi_j,z) \end{Bmatrix}_{TCS} = \boldsymbol{T_S} \begin{Bmatrix} dF^s_{t,j}(\phi_j,z) \\ dF^s_{r,j}(\phi_j,z) \\ dF^s_{a,j}(\phi_j,z) \end{Bmatrix}$$

$$\boldsymbol{T_S} = \begin{bmatrix} -\cos\phi_j(z) & -\sin\phi_j(z) & 0 \\ \sin\phi_j(z) & -\cos\phi_j(z) & 0 \\ 0 & 0 & 1 \end{bmatrix} \tag{3.29}$$

Note that the T_S matrix is the transformation matrix only for the differential cutting forces acting on the side cutting edge of the tool. The total forces acting on the tool body generated by the side cutting edge can be calculated by integrating the differential cutting forces contributed by N number of teeth within the CWE boundaries [114]. The CWE boundaries for each tooth are defined by the immersion angles $\phi_{st}(z), \phi_{ex}(z)$ of each element and the axial engagement limit of element at each angular position $a_i(\phi_j)$. The total cutting forces contributed by all teeth within the CWE are calculated and summed to evaluate the instantaneous cutting forces at the angular position of ϕ imposed on the tool, which are generated by the side edge as follows;

$$F^s_p(\phi) = \sum_{j=1}^{N} \int_0^{a_i(\phi)} dF^s_p(\phi_j,z)dz, \quad p{:}\, x,y,z \tag{3.30}$$

The further details of the integration of differential cutting forces resulting from the side edge can be found in references [111,114] considering the fact that in orthogonal turn-milling process, the angular and axial engagement boundaries only differ from the conventional milling operation.

- Minor cutting edge:

The minor edge engagement is divided into infinitesimal segments with a length of dl. However, as mentioned in previous sections, the engagement length of the minor edge varies at every angular increment of φ_j. Therefore, the engagement limits and number of segments on the engagement length vary. For an arbitrary element with a length of dl the differential cutting forces in rotating coordinates can be written based on the linear edge force model as follows:

$$dF^m_{t,j}(\varphi_j,l_k) = [(K_{tc}(\varphi_j,l_k)\, h_{m,j}(\varphi_j,l_k) + K_{te})dl].g(\varphi_j) \tag{3.31}$$

$$dF^m_{f,j}(\varphi_j, l_k) = \left[\left(K_{rc}(\varphi_j, l_k)\, h_{m,j}(\varphi_j, l_k) + K_{re}\right)dl\right].\mathcal{g}(\varphi_j)$$

$$dF^m_{r,j}(\varphi_j, l_k) = \left[\left(K_{ac}(\varphi_j, l_k)\, h_{m,j}(\varphi_j, l_k) + K_{ae}\right)dl\right].\mathcal{g}(\varphi_j)$$

The angular position (φ_j) of the minor edge of the j^{th} tooth is defined by

$$\varphi_j = \phi + (j-1)\phi_p\,, \quad \phi_p = \frac{2\pi}{N} \tag{3.32}$$

Where the $\phi = \Omega_t t$ is the angular increment of the reference tooth from the Y_T axis, and l_k is the distance of the element from the beginning of the engagement $(l_k = k.dl)$. The uncut chip thickness $h_{m,j}(\varphi_j, l_k)$ is different for each element along the engagement length as defined and discussed in (3.21) in Section 3.3.2. The $\mathcal{g}(\varphi_j)$ is a binary function similar to Equation (3.27), is equal to one if the angular position of the minor edge of tooth j is between φ_{st} and φ_{ex}, and is equal to zero if the angular position is out of this boundary. Note that, unlike the side cutting edge, the discrete elements on the minor cutting edge have a different radius and hence, different cutting speed values. Since the varying cutting speeds affect the cutting force coefficients, the cutting force coefficients are written as a function of the radial distance of each element. The radial distance of discrete element k is $r_k(\varphi_j) = (k-0.5)dl + r_t(\varphi_j)$, where r_t is the offset distance of the insert from tool center and is equal to; $r_t(\varphi_j) = R_t - l_m(\varphi_j)$. Therefore, the cutting force and edge force coefficients for minor edge must be calculated according to the radial distance of the discrete element, minor edge rake, and oblique angle. The differential cutting forces acting on each element of the minor edge is resolved to TCS coordinates in $X_T Y_T Z_T$ frame using the transformation matrix given in Equation (3.33).

$$dF^m_{x,y,z}(\varphi_j, l_k) = \begin{Bmatrix} dF^m_{x,j}(\varphi_j, l_k) \\ dF^m_{y,j}(\varphi_j, l_k) \\ dF^m_{z,j}(\varphi_j, l_k) \end{Bmatrix}_{TCS} = \boldsymbol{T_M} \begin{Bmatrix} dF^m_{t,j}(\varphi_j, l_k) \\ dF^m_{f,j}(\varphi_j, l_k) \\ dF^m_{r,j}(\varphi_j, l_k) \end{Bmatrix}$$

$$\boldsymbol{T_M} = \begin{bmatrix} -\cos\varphi_j & \sin\varphi_j \sin\alpha_m & \sin\varphi_j \cos\alpha_m \\ \sin\varphi_j & \cos\varphi_j \sin\alpha_m & \cos\varphi_j \cos\alpha_m \\ 0 & \cos\alpha_m & -\sin\alpha_m \end{bmatrix} \tag{3.33}$$

Note that, the transformation matrix T_M is given for the general case where the milling tool has an approach angle of minor angle α_m (See Figure 3.13). However, it is previously mentioned that in order to prevent the cusp formation, it is recommended to use milling tools with zero minor edge approach angle $(\alpha_m = 0)$ for orthogonal turn-milling operations. The total cutting forces generated by the minor cutting edges of all contributed teeth can be calculated by integrating the discrete elements along the engagement length at the angular position of φ within the CWE as follows;

$$F_p^m(\varphi) = \sum_{j=1}^{N} \int_{l_{j,1}(\varphi_j)}^{l_{j,2}(\varphi_j)} dF_p^m(\varphi_j)dl, \quad p = x, y\, z \tag{3.34}$$

where $l_{j,1}(\varphi_j) = R_t - l_m(\varphi_j)$ and $l_{j,2}(\varphi_j) = R_t$ are the engagement boundary of minor edge at angular position of φ_j.

The total instantaneous cutting forces imposed on the tool body and produced by both side and minor cutting edges is obtained by the superposition of both forces in TCS coordinate system ($X_T Y_T Z_T$ frame) as follows;

$$\bar{F}_p(\phi) = F_p^s(\phi) + F_p^m(\phi), \qquad p = x, y, z \tag{3.35}$$

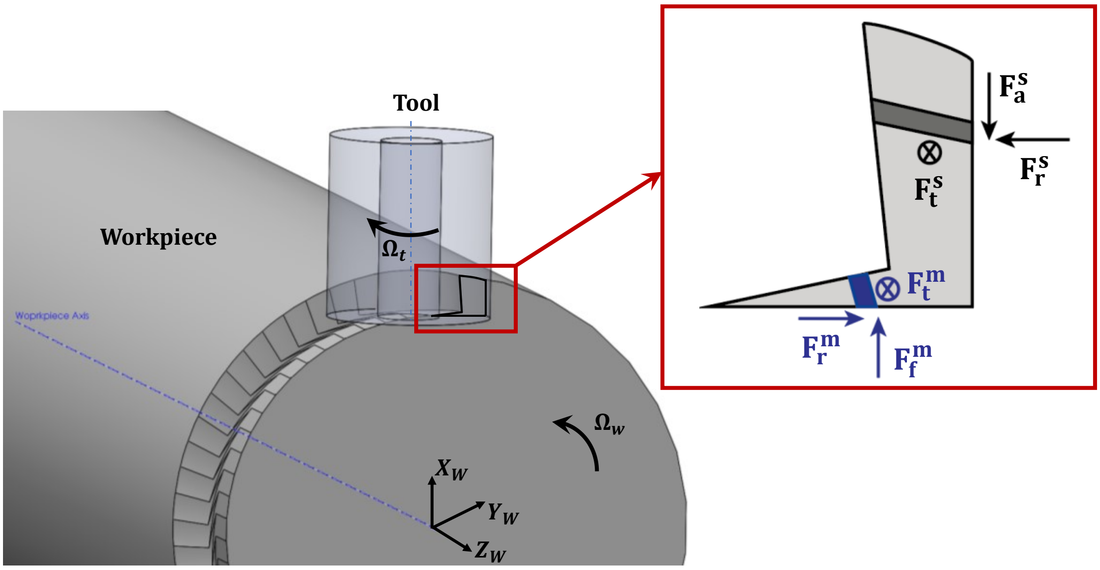

Figure 3.19: Representation of differential forces imposed on side and minor cutting edges in tangential, feed, and radial directions.

Note that the angular position ϕ in Equation (3.35) is an arbitrary angle. However, the unit pulse function for each cutting edge should be checked to make sure that ϕ is within the CWE and immersion angles.

As the cutting forces are calculated, spindles' torque and power requirements can also be calculated using the cutting forces. Unlike conventional milling operation, in turn-milling operation and tool spindle, the torque and power predictions must be considered at the process planning stage. The torque value imposed on the tool spindle T_t (N. m) and cutting power P_t (W) are calculated as below;

$$T_t(\phi) = R_t\left(\bar{F}_t^s(\phi) + \bar{F}_t^m(\phi)\right)$$
$$P_t(\phi) = \Omega_t T_t(\phi) \tag{3.36}$$

where R_t is tool radius, Ω_t is the tool spindle speed, $\bar{F}_t^s(\phi)$ and $\bar{F}_t^m(\phi)$ are the total tangential force imposed on the tool for all teeth within the CWE generated by side edge and minor edge, respectively.

The torque from the workpiece spindle T_w (N. m) and the corresponding power P_w (W) can also be calculated by;

$$T_w(\phi) = R_w \bar{F}_x(\phi)$$
$$P_w(\phi) = \Omega_w T_w(\phi) \tag{3.37}$$

where R_w is the workpiece radius, Ω_w is the workpiece spindle speed, and $\bar{F}_x(\phi)$ is the total cutting forces generated by both side and minor cutting edges in X_T direction, which is calculated in Equation (3.35).

3.7. Experimental Verification of Cutting Force Model

The proposed force model of the orthogonal turn-milling process has been verified in this section. The cutting force verifications are carried out on aluminum alloy Al7075-T6 cylindrical workpiece. Two different cutters are used for experiments, a solid carbide end mill and inserted milling tool, and the specifications are given as follows. The cutting forces are measured using Kistler 9123C rotary dynamometer, as seen in Figure 3.20. The cutting force data were collected using DAQ systems. The cutting force coefficients were calculated using orthogonal-to-oblique transformation from the orthogonal data for the given tool geometry and workpiece material using Equation (3.28). The orthogonal database for Aluminum alloy Al7075-T6 and uncoated WC tool are given in Appendix A: Orthogonal databases, Table A1.

The cutting experiments can be conducted on Mori Seiki NTX2000 CNC mill-turn (Figure 3.20a) and DMG Mori DMU monoblock75 (Figure 3.20b) machining centers. In the first experimental setup, as shown in Figure 3.20a, an additional extension must be added due to the difference in spindle adaptor interfaces. Due to the extension length, the tool tip experiences excessive runout. In order to eliminate the runout, the cutting force measurements are performed on DMG Mori DMU machining center, in which the spindle adaptor of the machine tool and spindle are both SK40.

In the first set of measurements, a WC standard end mill with four flutes, having 16mm diameter, 7˚ rake, and 38˚ helix angle, is selected. The minor edge has a rake angle of 5˚ and zero oblique angles. The cutting conditions are given in Table 3.3. Note that f_t is the nominal feed per tooth value at the tool tip; however, it varies along the tool axis because of the kinematics of the process (See Equation (3.6)). D_{w1} is the diameter of workpiece before cut. The cutting parameters for experimental verification of the cutting forces with a solid end mill are given in Table 3.3.

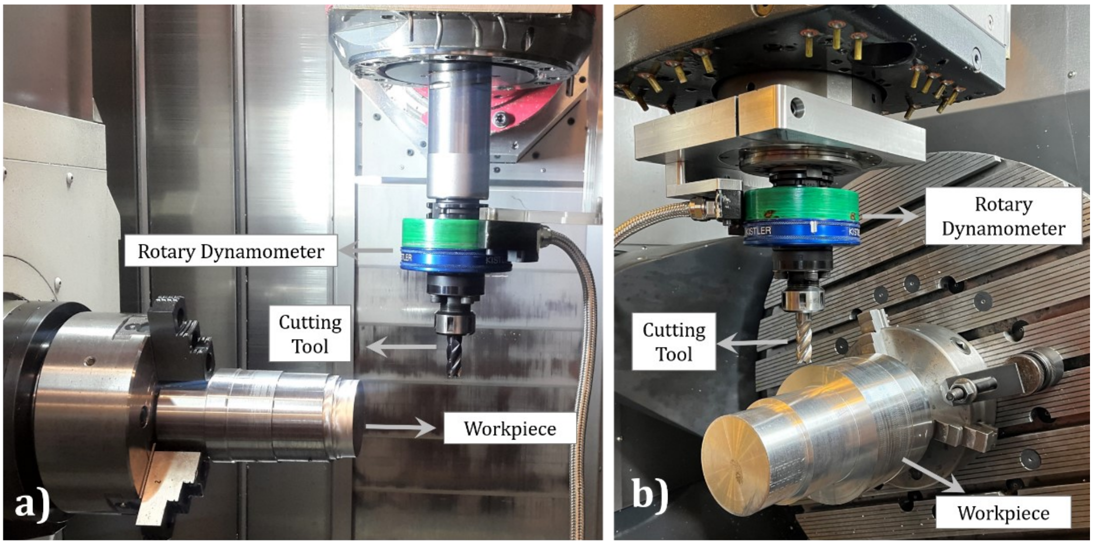

Figure 3.20: Experimental setup for cutting force measurement in orthogonal tur-milling a) Mori Seiki NTX 2000, b) DMG Mori DMU Monoblock 75.

Table 3.3: Cutting conditions for cutting force measurement experiments in turn-milling.

Exp.	Ω_t (rpm)	Ω_w (rpm)	e (mm)	f_t $mm/(rev.tooth)$	a_w (mm/rev)	a_p (mm)	F $(^{mm}/_{min})$	D_{w1} (mm)
1	3600	5	2	0.15	4	3.5	40	143
2	3600	5	5	0.15	4	3.5	40	143
3	3600	5	7	0.15	4	3.5	40	143
4	3600	10	5	0.31	4	3.5	40	143
5	3600	5	5	0.15	8	3.5	40	143

Exp. 1

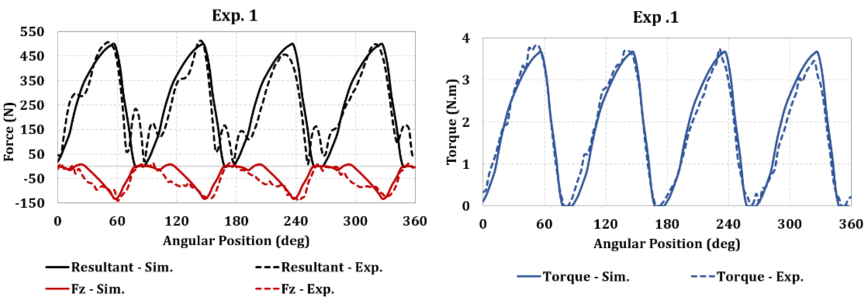

Exp. 2

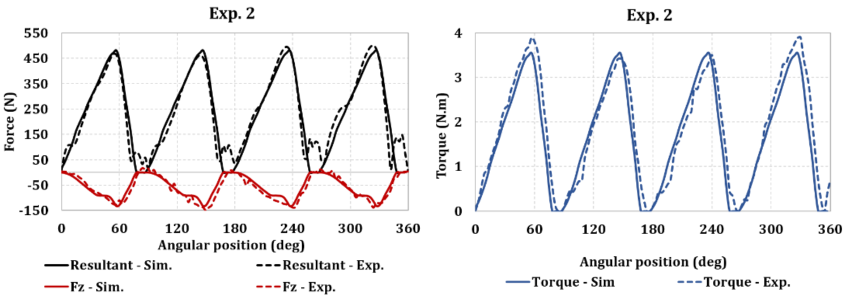

Exp. 3

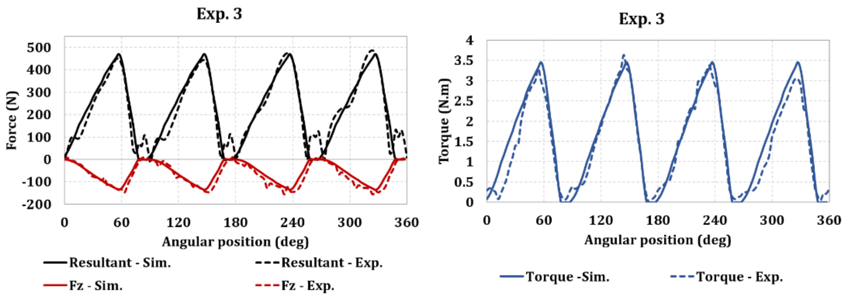

Exp. 4

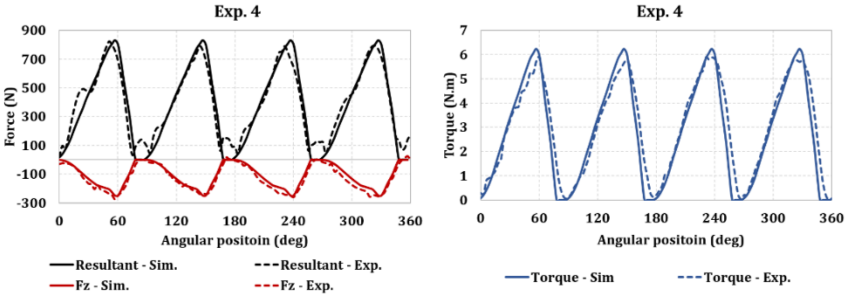

Exp. 5

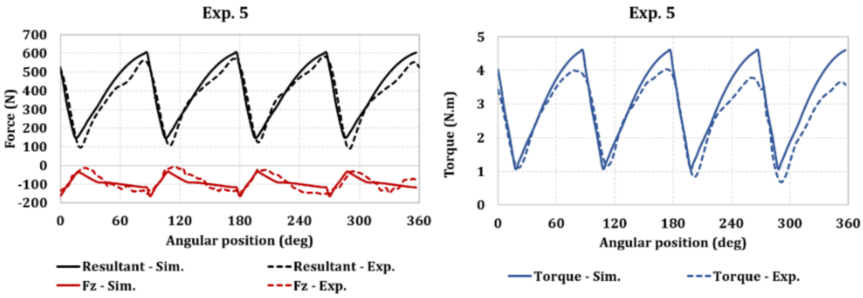

Figure 3.21: Verification of cutting forces in turn-milling with the standard tool for the given conditions in Table 3.3.

The simulation and experimental results are shown in Figure 3.21, comparing the resultant force, axial force, and tool torque. Exp1. – Exp3. are performed at different eccentricity values with similar other parameters. As expected, by increasing the eccentricity, the engagement of the minor edge is decreased, and hence the axial forces are reduced. In Exp.4, the workpiece rotational speed is increased, which causes an increase in nominal feed per tooth value. In order to keep the radial depth of cut similar to Exp.2, the linear feed value is increased. Moreover, in Exp.5, the effect of radial depth of cut is investigated by increasing the linear feed value and keeping the workpiece rotational speed similar to Exp.2.

It is seen that workpiece rotational speed has a major effect on the axial force magnitude. According to Figure 3.21, there is a good agreement between the cutting force simulations and experiments. The relatively high error occurs in Exp.4 and Exp.5, where the maximum cutting forces increased due to the increased workpiece rotational speed and radial depth of cut, respectively. The maximum error occurs in Exp.5 with 7.5% for resultant force and 12.5% for the torque values.

3.8. Analyzing Cutting Forces in Orthogonal Turn-Milling

According to the cutting force results given in the previous section, it is seen that while the eccentricity and radial depth of cut varies, the average axial force has a relatively smaller variation compared to resultant forces. Depending on the tool geometry, with the minor edge engagement increase, the axial forces resulted from the minor edge increase. According to equations (3.18) and (3.19), the engagement length of the minor edge can be changed by the radial depth of cut, eccentricity, and tool radius. In order to discuss the effect of these, maximum resultant force, maximum torque, and maximum axial cutting forces are plotted with respect to eccentricity and radial depth of cut. For this purpose, the simulations are performed for a case study for a roughing operation of a Ti4Al4V cylindrical part with 300 mm diameter, an indexable milling tool with 63 mm diameter, 8 cutting teeth, and 12.7 mm minor edge length. The axial depth of cut is determined as $a_p = 3mm$, with cutting speed $V_c = 60m/min$, and workpiece rotational speed is taken as $\Omega_w = 1\ rpm$. The insert grades are selected with respect to the feed per tooth and cutting speed.

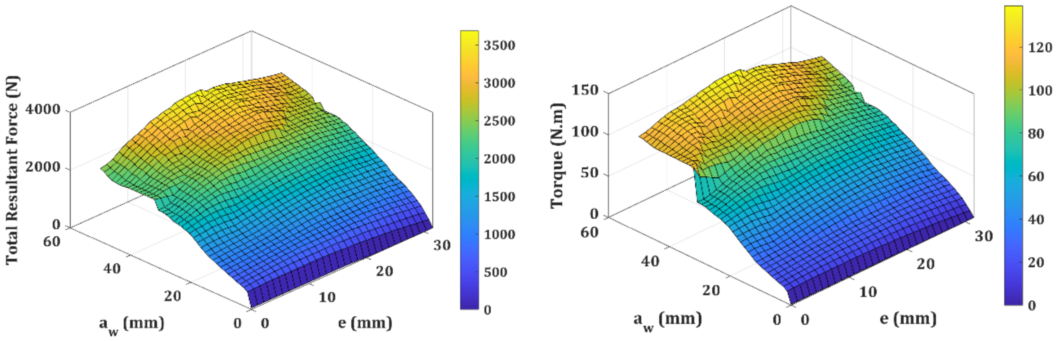

Figure 3.22: variation of resultant force and torque by eccentricity and radial depth of cut.

Figure 3.22 demonstrates the effect of eccentricity and feed per workpiece revolution on torque and resultant force. It is seen that the torque and resultant forces have an approximately linear relationship with the parameters. As the a_w increases the both torque and resultant force also increases linearly, similar to the conventional milling operation. Although the eccentricity also affects the torque and resultant force because of change in CWE (as seen in Figure 3.22), the magnitude of the variation is relatively small compared to the effect resulting by a_w. Therefore, it can be concluded that the resultant force and torque mostly depend on the radial depth of cut rather than eccentricity, and due to the linear relationship, there is no conflicting effect and hence, can be eliminated from the parameter selection procedure.

The total axial force in the tool axis direction (Z_T) in TCS (workpiece radial direction (X_W) in WCS) is plotted in Figure 3.23 with respect to eccentricity and feed per workpiece revolution (a_w). Since the direction of axial forces resulting from the minor edge and side edge are opposite (Figure 3.19), the direction of the total axial force changes depending on the CWE variation based on the eccentricity and a_w. In other words, as the engagement of the minor edge increases (depending on the eccentricity and stepover), the axial forces result from the minor edge in $-Z_T$ direction exceeds the axial forces generated from the side edge (in $+Z_T$ direction) and therefore, the total axial force is dominated by the axial force of the minor edge. Note that the total axial force distribution given in Figure 3.23 depends on the rake and oblique angle of the edges of the tool. Since higher axial forces (radial force in WCS) cause deflection on the slender flexible workpieces as well as on the thin-walled cylindrical parts causing dimensional errors [115,116], it is crucial to select the parameters that result in lower axial forces in the orthogonal turn-milling process. The simulations given in Figure 3.23 allow the selection of eccentricity and stepover combinations based on the desired range of the axial forces. In Figure 3.23, an arbitrary range in the vicinity of zero axial forces is colored specifically in green for better visualization and distinguishing.

One can select the eccentricity-stepover pair based on minimum axial force using the simulations in Figure 3.23; however, this is not a sufficient parameter selection criterion. According to the parameter selection procedure proposed by Berenji et al. [24], the allowable stepover is limited with respect to eccentricity to avoid cusp formation.

The authors showed that lower eccentricity values require a lower radial depth of cut to provide the sufficient engagement boundary for the minor edge to cut the material at two consequent rotations of the workpiece (stepovers). Therefore, the maximum stepover with respect to eccentricity for the tool and workpiece geometries used in this case study is plotted and merged with the total axial force distribution plot. It is proven that, for a specific eccentricity, the stepover values above the critical value, shown as a solid black line in Figure 3.23, cause cusp formation [24].

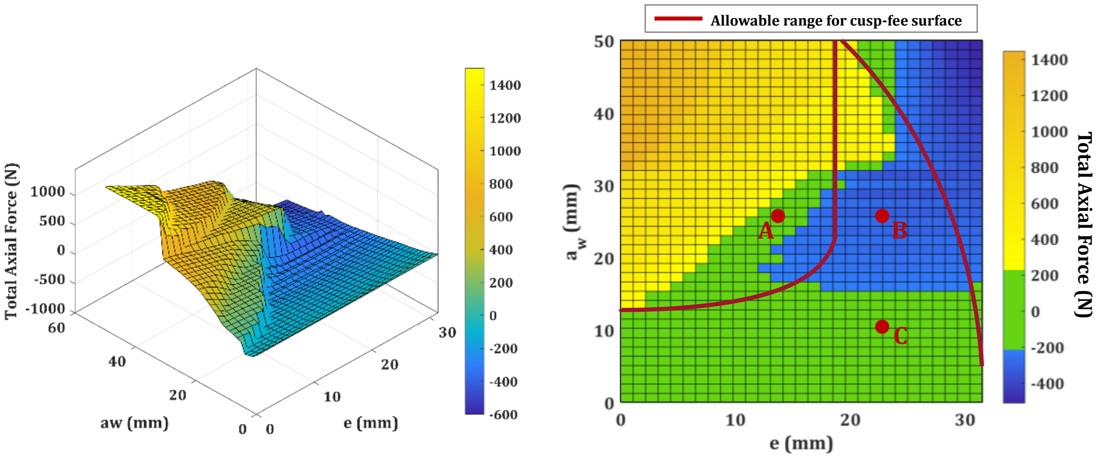

Figure 3.23: Total axial force variation by eccentricity and radial depth of cut.

This criterion limits the parameter selection based on axial force. It is deduced that although there are lower axial force regions (point A), the surface quality will be deteriorated due to cusp formation, which requires an additional operation. For similar MRR, Point B's parameters can be selected with a slight change in axial cutting forces. However, for the minimum axial force criterion, the parameters of Point C can be selected by sacrificing the MRR.

As a result, in orthogonal turn-milling in order to have better surface quality and control the exerted forces and torque values, process planning based on the simulation is required for efficient cutting, especially in the machining of hard-to-cut materials

3.9. Summary

This chapter presents detailed modeling of orthogonal turn-milling kinematics. The definition of cutting parameters such as feed per tooth, stepover, and feed rate are different from conventional machining operations. An analytical model is proposed for uncut chip geometry for both side and minor cutting edges of the milling tool during orthogonal turn-milling operation. The effect of eccentricity on chip geometry formed by the side edge and the minor edge is shown through simulations. Based on the proposed uncut chip model, the relation between the eccentricity and stepover is discussed, and its effect on surface quality is modeled. The experimental validations proved that using the proposed relation cusp-free surface and enhanced MRR can be achieved simultaneously.

The static cutting forces are calculated based on the proposed chip geometry and cutting parameter relations. The proposed mechanics model of orthogonal turn-milling is validated throughout experiments against different cases. Having validated the proposed model, a parameter solution discussion was made with the axial forces' objective. The total axial force variation with respect to eccentricity and stepover is presented to select suitable parameters to reduce axial forces while cutting slender and flexible parts.

4. DYNAMICS AND STABILITY OF TURN-MILLING OPERATION

4.1. Overview

Turn-milling operations require simultaneous rotation of tool and workpiece spindles and translational motion of tool spindle in three-dimensional Cartesian coordinates (X, Y, Z). In turn-milling operations, the workpiece is mounted on the chuck with constant rotational speed. The tool is mounted on the spindle with constant rotational speed and has three translational motions. The resulting kinematics of the orthogonal turn-milling operation cause a complex chip thickness, cutting forces, and hence, cutting dynamics compared to conventional milling and turning operations. In this regard, the uncut chip geometry generated by the side and minor cutting edges of the tool and the resulting cutting forces have been modeled and verified in Chapter 3. It is deduced that the parameter selection highly depends on the tool and workpiece geometry, process kinematics, and the uncut chip geometry, which influence the cutting mechanics, surface quality, and productivity.

Furthermore, the improper selection of cutting parameters such as workpiece and tool spindle speeds, cutting depth, eccentricity, and feed rate can cause self-excited, regenerative chatter vibrations, leading to poor surface finish and excessive cutting forces, tool and spindle failure. This chapter aims to develop a predictive model for the orthogonal turn-milling process stability to find chatter-free conditions to avoid costly trial experiments. The dynamic chip geometry and cutting forces are modeled based on the previous chapter's proposed process kinematics and mechanics models.

The dynamics of the orthogonal turn-milling process are modeled as a multi-degree freedom system having multi-dimensional chatter vibrations. In order to obtain the stability diagrams, the delayed-differential equations of the dynamic system are solved in discrete-time domain by considering the time-varying delay caused by the system’s kinematics. The results are compared with frequency domain solutions and validated on a turn-milling machining center for various conditions and materials.

4.2. Dynamic Chip and Cutting Forces in Orthogonal Turn-Milling Process

In orthogonal turn-milling operations, the uncut chip thickness on the side edge (h) and on the minor edge (h_m) are different due to the kinematics of chip generation during the process. The total uncut chip thickness imposed on each edge consists of static and dynamic parts [117]. The static part (h^s) corresponds to the constant feed movement of the tool and the dynamic part (h^d) is due to the self-excited displacements of the cutter and/or workpiece under the effect of the regeneration mechanism. Figure 4.1 shows the dynamic system in orthogonal turn-milling operations. In this system, the cutter and workpiece are assumed to be flexible, each with three degrees of freedom. It is assumed that the dynamic system experiences vibrations in two lateral (x, y) and axial (z) directions in TCS. As shown in Figure 4.1, due to the vibration of the cutter and workpiece, the tooth j of the cutter removes the modulated chip thickness left by the vibration marks of tooth $j-1$, in addition to the static chip load. The total chip thickness imposed on the side cutting edge of the tool can be written as:

$$h^d(\phi_j, z) = \Delta x \sin \phi_j(z) + \Delta y \cos \phi_j(z) + \check{f}_t \sin \phi_j(z) \tag{4.1}$$

Similarly, the total chip thickness, including the dynamic and static parts for minor edge, is formulated as follows;

$$h_m^d(\varphi_j, l_k) = \Delta z + h_m^s(\varphi_j, l_k) \tag{4.2}$$

Δx, Δy, and Δz are related to dynamic chip thickness and are defined as the relative displacements of the workpiece and cutter to each other in x, y, and z directions, respectively, and can be formulated as below:

$$\begin{aligned}
\Delta x &= \left[\left(x_c(t) - x_c(t-\tau)\right) - \left(x_w(t) - x_w(t-\tau)\right)\right] \\
\Delta y &= \left[\left(y_c(t) - y_c(t-\tau)\right) - \left(y_w(t) - y_w(t-\tau)\right)\right] \\
\Delta z &= \left[\left(z_c(t) - z_c(t-\tau)\right) - \left(z_w(t) - z_w(t-\tau)\right)\right]
\end{aligned} \tag{4.3}$$

where x_c, y_c and x_w, y_w and z_c, z_w are the cutter and workpiece displacements in the current tooth pass at time t in the x, y, and z directions at the specific angular position of tooth j at height z of side edge and length l of the minor edge. τ stands for the tooth passing period which is used to define the cutter and workpiece displacements left on the surface by the tooth $j-1$ at time $t-\tau$ at the same point. Hence, the delay of the system is equal to τ.

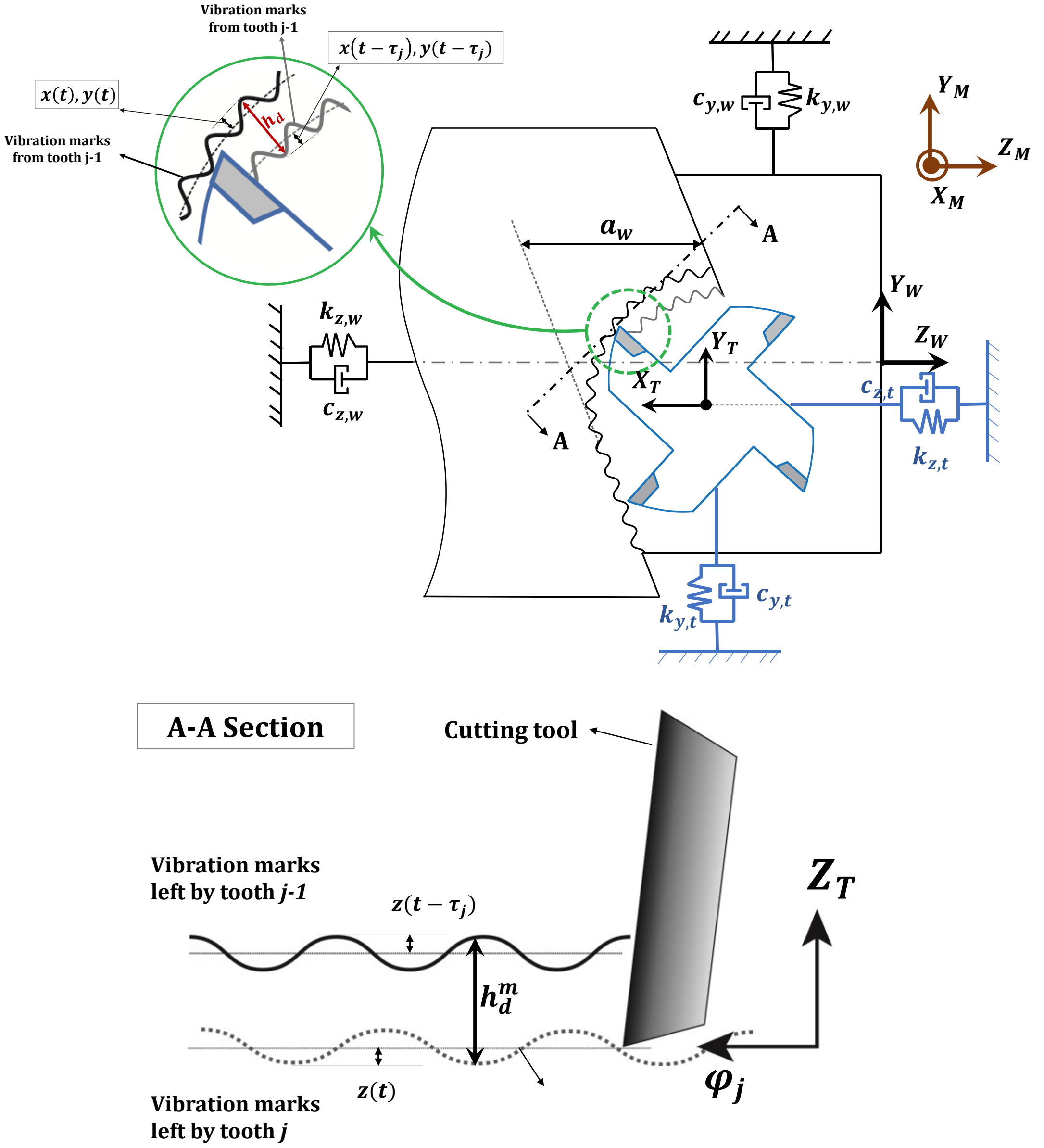

Figure 4.1. Dynamic chip generation.

The angular position of the discrete element on the side edge at height z on tooth j is $\phi_j(z) = \Omega_t t + j\phi_p - \frac{\tan\gamma_j}{R_t} z$, where Ω_t is the rotational speed of cutter (rad/s), $\phi_p = 2\pi/N$ is the constant pitch angle for standard milling tools and γ_j is the helix angle of the tooth j. The angular position of the minor edge is defined by $\varphi_j = \Omega_t t + j\phi_p$. The corresponding immersion boundaries for angular positions of each edge are given in Section 3. Note that in equations (4.1) and (4.2), the static chip load terms are $h^s =$

$\breve{f}_t \sin\phi_j(z)$ and $h_m^s(\varphi_j, l)$ are neglected in the stability analysis since they do not contribute to regenerative dynamic chip generation mechanisms.

Similar to the approach used in static cutting force calculation, the engagement lengths on the side and minor edges of the tool are divided into a number of small elements. The differential dynamic milling forces in $x, y,$ and z directions subjected to side cutting edge on tra coordinates are shown in Figure 4.1. The differential tangential ($dF_{t,j}^s$), radial ($dF_{r,j}^s$), and axial ($dF_{a,j}^s$) cutting forces exerted on the side cutting edge on tooth j for an infinitesimal axial element thickness of dz can be formulated as;

$$\begin{Bmatrix} dF_{t,j}^s(\phi_j, z) \\ dF_{r,j}^s(\phi_j, z) \\ dF_{a,j}^s(\phi_j, z) \end{Bmatrix}_d = \begin{Bmatrix} K_{tc} \\ K_{rc} \\ K_{ac} \end{Bmatrix} [\sin\phi_j \quad \cos\phi_j \quad 0] \begin{Bmatrix} \Delta x \\ \Delta y \\ \Delta z \end{Bmatrix} g\left(\phi_j(z)\right) q\left(\phi_j(z), z\right) dz \tag{4.4}$$

The K_{tc}, K_{rc} and K_{ac} are the tangential, radial, and axial cutting force coefficients, respectively, which are defined in Section 3.6 and Equation (3.28). Further, the function $g\left(\phi_j(z)\right)$ is unit pulse functions which determines whether the tooth is in cut or out of the cut, and similarly, $q\left(\phi_j(z), z\right)$ determines if the axial element is within the engagement boundaries. The detailed formulations are given in Section 3.6, Equation (3.27). The differential dynamic cutting forces in tra coordinates in Equation (4.4) can be resolved in the TCS coordinates by using the transformation matrix given in Equation (3.29). The differential cutting forces in tool coordinate system can be expressed as;

$$\begin{Bmatrix} dF_{x,j}^s(\phi_j, z) \\ dF_{y,j}^s(\phi_j, z) \\ dF_{z,j}^s(\phi_j, z) \end{Bmatrix}_d = \begin{bmatrix} -\cos\phi_j(z) & -\sin\phi_j(z) & 0 \\ \sin\phi_j(z) & -\cos\phi_j(z) & 0 \\ 0 & 0 & 1 \end{bmatrix} \begin{Bmatrix} dF_{t,j}^s(\phi_j, z) \\ dF_{r,j}^s(\phi_j, z) \\ dF_{a,j}^s(\phi_j, z) \end{Bmatrix}_d \tag{4.5}$$

The differential dynamic milling forces exerted on the side edge are integrated within the element i with a height of dz, for j^{th} flute as follows;

$$\left\{ F_{p_j}^s(i, \phi_j) \right\}_d = \int_{z_i}^{z_{i+1}} \left\{ dF_{p,j}^s(\phi_j, z) \right\}_d dz \,; \; p = x, y, z \tag{4.6}$$

The dynamic cutting forces for each infinitesimal element on the minor edge with a length of dl in radial distance from the tool center r_k, in tra coordinates can be formulated as

$$\begin{Bmatrix} dF_{t,j}^{m}(\varphi_j, l_k) \\ dF_{f,j}^{m}(\varphi_j, l_k) \\ dF_{r,j}^{m}(\varphi_j, l_k) \end{Bmatrix}_d = \begin{Bmatrix} K_{tc}(\varphi_j, l_k) \\ K_{rc}(\varphi_j, l_k) \\ K_{ac}(\varphi_j, l_k) \end{Bmatrix} [0\ 0\ 1] \begin{Bmatrix} \Delta x \\ \Delta y \\ \Delta z \end{Bmatrix} g(\varphi_j)\, dl \tag{4.7}$$

Note that the cutting force coefficients corresponding to each element along the minor edge are a function of the element's radial distance (l_k) and angular position (φ_j) because the cutting speed is different for each element. Moreover, the function $g(\varphi_j)$ is unit pulse function which determines if the element on the minor edge of tooth j at the angular position of φ_j is in cut or not.

The tangential, radial, and feed forces acting on each element on the minor edge can be transformed to TCS coordinates using the transformation given in Equation (3.33).

$$\begin{Bmatrix} dF_{x,j}^{m}(\varphi_j, l_k) \\ dF_{y,j}^{m}(\varphi_j, l_k) \\ dF_{z,j}^{m}(\varphi_j, l_k) \end{Bmatrix}_d = \begin{bmatrix} -\cos\varphi_j & 0 & \sin\varphi_j \\ \sin\varphi_j & 0 & \cos\varphi_j \\ 0 & 1 & 0 \end{bmatrix} \begin{Bmatrix} dF_{t,j}^{m}(\varphi_j, l_k) \\ dF_{f,j}^{m}(\varphi_j, l_k) \\ dF_{r,j}^{m}(\varphi_j, l_k) \end{Bmatrix}_d \tag{4.8}$$

As discussed in Section 3.5, the milling tools with minor edge approach angle would cause undesirable surface quality in orthogonal turn-milling operation. Therefore, stability analyses are performed for tools with $\alpha_m = 0$ (See Figure 3.13).

Note that, in this study, the eccentricity value is predefined in stability analysis. Hence, the engagement boundaries of the minor edge at each angular position are known (see Figure 3.6). As a result, the total dynamic cutting forces resulting from the regeneration in z direction subjected to the minor edge (Δz) at each angular position must be summed up with the dynamic cutting forces resulting from the element i by the regeneration in x, and y directions.

The total dynamic cutting forces on the minor edge of tooth j at the angular position of φ_j can be calculated by integration of all elements with length dl within the engagement boundary as:

$$\begin{aligned} F_{x,j}^{m}(\varphi) &= \int_{l_{j,1}(\varphi_j)}^{l_{j,2}(\varphi_j)} \left(-K_{tc}(\varphi_j, l_k)\cos\varphi_j - K_{rc}(\varphi_j, l_k)\sin\varphi_j\right) \Delta z\, g(\varphi_j)\, dl \\ F_{y,j}^{m}(\varphi) &= \int_{l_{j,1}(\varphi_j)}^{l_{j,2}(\varphi_j)} \left(-K_{tc}(\varphi_j, l_k)\sin\varphi_j - K_{rc}(\varphi_j, l_k)\cos\varphi_j\right) \Delta z\, g(\varphi_j)\, dl \end{aligned} \tag{4.9}$$

$$F_{z,j}^{m}(\varphi) = \int_{lj,1(\varphi_j)}^{lj,2(\varphi_j)} K_{fc}(\varphi_j, l_k)\Delta z\, g(\varphi_j)\, dl$$

where $l_{j,1}(\varphi_j)$ and $l_{j,2}(\varphi_j)$ are the engagement boundary of the minor edge at the angular position of φ_j (see Section 3.3.2).

The total dynamic forces in TCS can be obtained by the superposition of the dynamic forces generated from dynamic chip thicknesses exerted on both side and minor cutting edges of the tool (superposition of Equations (4.6) and (4.9)). The explicit form of dynamic cutting forces in x, y and z direction is show as follow;

$$\begin{aligned}
F_{x,j}(\phi, \varphi, n) = & \int_{z_n}^{z_{n+1}} \left(-K_{tc}\cos\phi_j - K_{fc}\sin\phi_j\right)\left(\Delta x \sin\phi_j \right.\\
& \left. + \Delta y \cos\phi_j\right) g\left(\phi_j(z)\right) q\left(\phi_j(z)\right)\, dz \\
& + \int_{lj,1(\varphi_j)}^{lj,2(\varphi_j)} \left(-K_{tc}(\varphi_j, l_k)\cos\varphi_j \right.\\
& \left. - K_{rc}(\varphi_j, l_k)\sin\varphi_j\right) \Delta z\, g(\varphi_j)\, dl \\
F_{y,j}(\phi, \varphi, n) = & \int_{z_n}^{z_{n+1}} \left(K_{tc}\sin\phi_j - K_{fc}\cos\phi_j\right)\left(\Delta x \sin\phi_j \right.\\
& \left. + \Delta y \cos\phi_j\right) g\left(\phi_j(z)\right) q\left(\phi_j(z)\right)\, dz \\
& + \int_{lj,1(\varphi_j)}^{lj,2(\varphi_j)} \left(-K_{tc}(\varphi_j, l_k)\sin\varphi_j \right.\\
& \left. - K_{rc}(\varphi_j, l_k)\cos\varphi_j\right) \Delta z\, g(\varphi_j)\, dl \\
F_{z,j}(\phi, \varphi, n) = & \int_{z_n}^{z_{n+1}} K_{ac}\,(\Delta x \sin\phi_j + \Delta y \cos\phi_j)\, g\left(\phi_j(z)\right) q\left(\phi_j(z)\right)\, dz \\
& - \int_{lj,1(\varphi_j)}^{lj,2(\varphi_j)} K_{fc}(\varphi_j, l_k)\Delta z\, g(\varphi_j)\, dl
\end{aligned} \tag{4.10}$$

Note that, since the cutting force coefficients of dynamic cutting forces generated by the minor edge vary along the engagement length, the integral cannot be executed explicitly. In other words, the cutting force coefficients related to the minor edge are functions of engagement length and angular position $\left(K_{pc}(\varphi_j, l_k)\right)$. As an alternative, the average cutting force coefficients along the engagement length at each angular position of φ_j can be used. Since the engagement length is different at each angular position, the average cutting force coefficients will only be a function of the rotation angle $\left(\bar{K}_{pc}(\varphi_j)\right)$. After the integration and expanding trigonometric formulations, equation (4.10) is simplified as follows;

$$
\begin{aligned}
F_{x,j}(\phi,\varphi,n) = & -\frac{1}{2}\Big[\big(K_{tc}\sin 2\phi_j + K_{rc}(1 \\
& - \cos 2\phi_j)\big)\,\Delta x^n\, g_j(t,z) q_j(t,z)\,\delta z \\
& + \big(K_{tc}(1+\cos 2\phi_j) + K_{rc}\sin 2\phi_j\big)\Delta y^n g_j(t,z) q_j(t,z)\,\delta z\Big] \\
& + \left(-\bar{K}_{tc}(\varphi_j)\cos\varphi_j - \bar{K}_{rc}(\varphi_j)\sin\varphi_j\right)\Delta z\, g(\varphi_j)\, l(\varphi_j) \\
F_{y,j}(\phi,\varphi,n) = & \frac{1}{2}\Big[\big(K_{tc}(1-\cos 2\phi_j) - K_{rc}\sin 2\phi_j\big)\Delta x^n\, g_j(t,z) q_j(t,z)\delta z \\
& + \Big(K_{tc}\sin 2\phi_j - K_{rc}\big(1+\cos 2\phi_j\big)\Big)\Delta y^n g_j(t,z) q_j(t,z)\delta z\Big] \\
& + \left(-\bar{K}_{tc}(\varphi_j)\sin\varphi_j - \bar{K}_{rc}(\varphi_j)\cos\varphi_j\right)\Delta z\, g(\varphi_j) l(\varphi_j) \\
dF_{z,j}(\phi,\varphi,n) = & K_{ac}\sin\phi_j\,\Delta x^n\, g_j(n) q_j(n)\delta z \\
& + K_{ac}\,\Delta y^n g_j(t,z) q_j(t,z)\,\delta z - \bar{K}_{fc}(\varphi_j)\Delta z\, g(\varphi_j)\, l(\varphi_j)
\end{aligned}
\tag{4.11}
$$

where $\delta z = z_{n+1} - z_n$, $z = n\delta z$, $g_j(z) = g\left(\phi_j(z)\right)$, $q_j(z) = q\left(\phi_j(z), z\right)$. Δx, Δy, and Δz are the elemental displacement of the cutter and workpiece for the considered axial element n on the side edge of flute j and the rotation angle of ϕ_j in the X_T, Y_T and Z_T directions, respectively. It is to be noted that $l(\varphi_j)$ is the total engagement length of the minor edge of j^{th} tooth at each angular position of φ_j which is previously defined in Equation (3.19). As a result, the differential dynamic cutting forces can be written in terms of directional coefficients as follows,

$$
\begin{Bmatrix} dF_{x,j}(t,z,l) \\ dF_{y,j}(t,z,l) \\ dF_{z,j}(t,z,l) \end{Bmatrix}_d = \begin{bmatrix} \alpha_{xx,j}(t,z) & \alpha_{xy,j}(t,z) & \alpha_{xz,j}(t,l) \\ \alpha_{yx,j}(t,z) & \alpha_{yy,j}(t,z) & \alpha_{yz,j}(t,l) \\ \alpha_{zx,j}(t,z) & \alpha_{zy,j}(t,z) & \alpha_{zz,j}(t,l) \end{bmatrix} \begin{Bmatrix} \Delta x(t) \\ \Delta y(t) \\ \Delta z(t) \end{Bmatrix}
\tag{4.12}
$$

$$
\therefore \left\{dF^n_{x,y,z}(t)\right\}_d = \left[DC_{j,z,n}(t)\right]\left\{\Delta_{x,y,z}(t)\right\}
$$

The directional force coefficients which relate the dynamic milling forces and the dynamic displacements at three directions are defined as;

$$
\begin{aligned}
&\alpha_{xx,jn}(t) = -\tfrac{1}{2}\left[K_{tc}\sin 2\phi_j + K_{fc}\left(1-\cos 2\phi_j\right)\right] g_j(z) q_j(z)\delta z \\
&\alpha_{xy,jn}(t) = -\tfrac{1}{2}\left[K_{tc}\left(1+\cos 2\phi_j\right) + K_{fc}\sin 2\phi_j\right] g_j(z) q_j(z)\delta z \\
&\alpha_{xz,jl}(t) = \left[-\overline{K}_{tc}\left(\varphi_j\right)\cos\varphi_j - \overline{K}_{rc}\left(\varphi_j\right)\sin\varphi_j\right] g\left(\varphi_j\right) l\left(\varphi_j\right) \\
&\alpha_{yx,jn}(t) = \tfrac{1}{2}\left[K_{tc}\left(1-\cos 2\phi_j\right) - K_{fc}\sin 2\phi_j\right] g_j(z) q_j(z)\delta z \\
&\alpha_{yy,jn}(t) = \tfrac{1}{2}\left[\sin 2\phi_j - K_{fc}\left(1+\cos 2\phi_j\right)\right] g_j(z) q_j(z)\delta z \\
&\alpha_{yz,jl}(t) = \left[-\overline{K}_{tc}\left(\varphi_j\right)\sin\varphi_j - \overline{K}_{rc}\left(\varphi_j\right)\cos\varphi_j\right] g\left(\varphi_j\right) l\left(\varphi_j\right) \\
&\alpha_{zx,jn}(t) = \left[K_{ac}\sin\phi_j\right] g_j(z) q_j(z)\delta z \\
&\alpha_{zy,jn}(t) = \left[K_{ac}\cos\phi_j\right] g_j(z) q_j(z)\delta z \\
&\alpha_{zz,jl}(t) = -\left[\overline{K}_{fc}\left(\varphi_j\right)\right] g\left(\varphi_j\right) l\left(\varphi_j\right)
\end{aligned}
\tag{4.13}
$$

The elemental directional coefficients of dynamic forces given in Equation (4.13) are time varying according to the angular position of the tooth j within the engagement boundaries. The directional coefficients will be used in stability analysis in the following section. In this study, similar to milling, the stability of the system is studied for different rotational speeds of the tool and axial depth of cuts. Since the feasible eccentricity range is limited due to surface generation aspects, it cannot be taken as a defining parameter in chatter stability. Therefore, the eccentricity which defines the engagement of minor edge will be identified prior to stability analysis based on process kinematics and surface quality considerations. As a result, whether the axial engagement of the tool at the side cutting edge is a_1 or a_2, the engagement and hence, the regenerative dynamic forces resulting from the minor edge are constant at similar eccentricity for both cases. In equation (4.12) the elemental regenerative forces resulting from the minor edge are integrated along the minor edge at time t, as follows;

$$
\left[DC_{j,z}(t)\right] = \begin{bmatrix} \alpha_{xx,jn}(t) & \alpha_{xy,jn}(t) & \int_{l=1}^{k}\alpha_{xz,jl}(t) \\ \alpha_{yx,jn}(t) & \alpha_{yy,jn}(t) & \int_{l=1}^{k}\alpha_{yz,jl}(t) \\ \alpha_{zx,jn}(t) & \alpha_{zy,jn}(t) & \int_{l=1}^{k}\alpha_{zz,jl}(t) \end{bmatrix} = \tag{4.14}
$$

$$\begin{bmatrix} \alpha_{xx,jn}(t) & \alpha_{xy,jn}(t) & \alpha_{xz,j}(t) \\ \alpha_{yx,jn}(t) & \alpha_{yy,jn}(t) & \alpha_{yz,j}(t) \\ \alpha_{zx,jn}(t) & \alpha_{zy,jn}(t) & \alpha_{zz,j}(t) \end{bmatrix}$$

$$\left\{F^n_{x,y,z}(t)\right\}_d = \left[DC_{j,n}(t)\right]\left\{\Delta_{x,y,z}\right\}$$

4.3. Varying Time Delay Model in Turn-Milling Process

According to the kinematics of the orthogonal turn-milling operation and the cutting geometry (See Section 3.3), it is shown that any discrete element on the tool axis experiences individual radial feed and angular displacement in a tooth passing period. This phenomenon affects the feed value of each element along the tool axis in static cutting force calculation. Similarly, the rotational motion of workpiece and the circular tool trajectory in turn-milling will affect the regeneration mechanism and formation of the dynamic chip thickness, and hence, dynamic forces.

Based on the process kinematics and cutting geometry of orthogonal turn-milling process, the simultaneous rotational motion of workpiece and tool produce a phase shift between the waves imprinted on the workpiece surface, resulting in a varying time delay in the regenerative chip formation mechanism. Çomak et al. [43] discretized the tool and workpiece rotational rigid body motion in Cartesian coordinate system and calculated the phase difference by using coordinated of the surface point generated by each tooth at each time interval. This study uses a quasi-static approach to evaluate the phase difference between the waves imprinted on the surface by the two subsequent teeth [46].

At discrete time instant i (i^{th} time interval Δt), the axial element z on j^{th} tooth leaves a surface point $P^0 = P_{i,j}$ at angular position $\phi^0 = \phi_{i,j}(z)$, as shown in Figure 4.2. As the workpiece rotates at a constant speed and the tool moves in a helical feed direction, after one tooth passing period (τ_0) at time instant $i + 1$, the next immediate tooth $j + 1$ arrives at point $P^1 = P_{i+1,j+1}$ at angular position $\phi^1 = \phi_{i+1,j+1}(z)$. However, the dynamic chip thickness and the corresponding delay must be calculated between the surface points in the static chip direction, which is shown as $\overline{P^0 P^*}$. The next immediate tooth $j + 1$ arrives at point P^* at angular position ϕ^* ($\phi^* \neq \phi_{i,j}$). Hence, there is a phase shift between the surface marks left by two subsequent teeth on current and previous modulations. This phase shift means that the time interval τ that tooth $j+1$ arrives at point P^* is different than the tooth passing period τ_0. The phase difference at time instant i is shown by α_i in Figure 4.2, and can be defined as;

$$\alpha_i = \phi^0 - \phi^* \tag{4.15}$$

At the time interval τ, the displacement of the tool due to workpiece rotational motion and linear feed is equal to $\frac{\tau}{\tau_0} f_t(z)$ where $f_t(z)$ is defined in Equation (3.6).

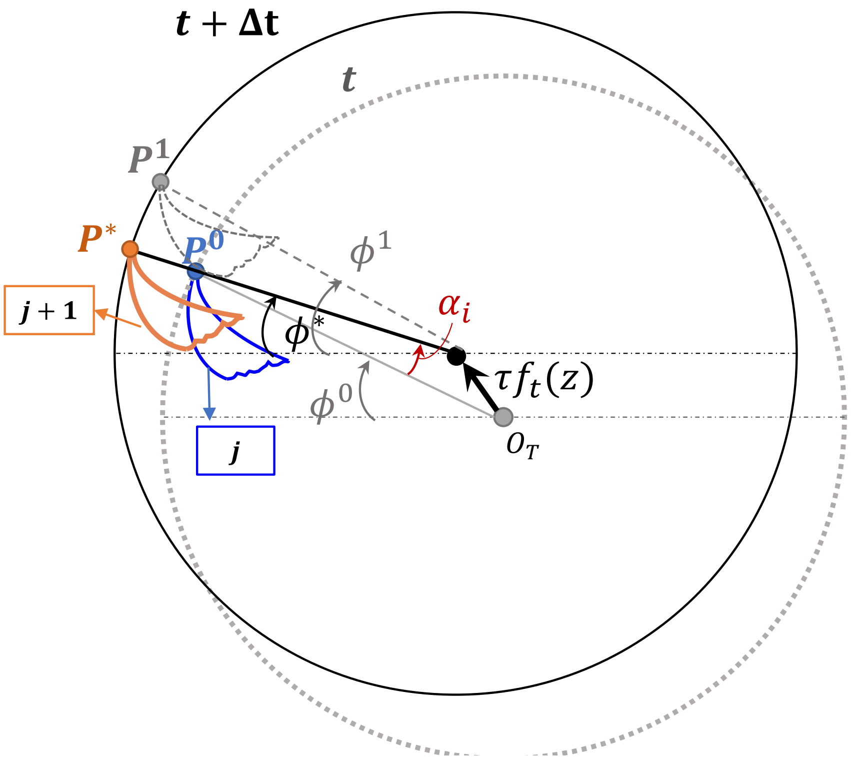

Figure 4.2. Phase difference representation.

By applying the trigonometrical relations (law of sines) stated in [46], the phase difference can be calculated as;

$$\alpha_i(z) = \frac{\frac{\tau}{\tau_0} f_t(z) \cos(\theta_x + \phi_i)}{R_t} \tag{4.16}$$

The total varying time delay in the regeneration mechanism ($\tau_{i,j}$) can be calculated by the superposition of the time delays contributed by the phase angle (α_i) and the nominal tooth passing period (τ_0) as follows;

$$\tau_{i,j}(z) = \tau_0 - \frac{\alpha_i}{\Omega_t} = \frac{2\pi}{N\Omega_t} - \frac{\tau f_t(z) \cos(\phi_i + \theta_x)}{\tau_0 R_t \Omega_t} \tag{4.17}$$

By combining Equation (3.6) and (4.17), it follows that;

$$\tau_{i,j}(z) = \frac{2\pi R_t \cos\theta_x}{N\left[\Omega_t R_t \cos\theta_x + \Omega_w \left(R_w - a_p + a(z)\right)\cos(\theta_x + \phi_i)\right]} \qquad (4.18)$$

According to Equation (4.18), it is deduced that the varying time delay resulting from the workpiece rotation depends on the spindle speed and radius of the workpiece and tool. As the workpiece speed increase, the phase difference at each angular increment increases, leading to a lower time delay. This phenomenon affects the regeneration mechanism and hence, the stability limits. Furthermore, since the feed values for each axial element along the tool are different due to the workpiece radius, the phase difference, and hence overall delay will vary along the tool engagement. It is also worth mentioning that, at similar workpiece and tool speeds, the time varying delay and its average are different for different workpiece diameters. Therefore, unlike conventional milling, where the time delay is constant and equal to the tooth passing period ($\tau = \tau_0$), in turn-milling process the time delay varies at each angular position of the tool (each time instant) caused by the rotational motion of the workpiece and is not equal to the tooth passing period ($\tau_{i,j} \neq \tau_0$). The time delays not only are distributed along the tool axis but also vary at each time instant within the engagement. This phenomenon brings more complexity to the solution of stability. Due to the time-marching nature of the semi-discretization method (SDM) [118] in discrete-time domain, it is the best solution method to capture the variations resulting from time-varying and distributed delays in orthogonal turn-milling stability. As a result, in turn-milling process, the varying time delay approach must be employed in order to include the effect of speed and radius ratios in stability diagram calculations.

The behavior of varying time delays for different conditions is investigated in the following diagrams. In Figure 4.3, the time delay values are normalized by the tooth passing period (τ_o) and depicted for different conditions. For case (a) in Figure 4.3, it is deduced that as the spindle speed ratio (r_s) decreases which means higher workpiece spindle speed the time delay variation is increasing which affect the stability of the process. The second comparison is depicted in Figure 4.3 (b) shows that as the ratio of tool and workpiece diameter decreases the variation of time delay will be close to tooth passing period [46].

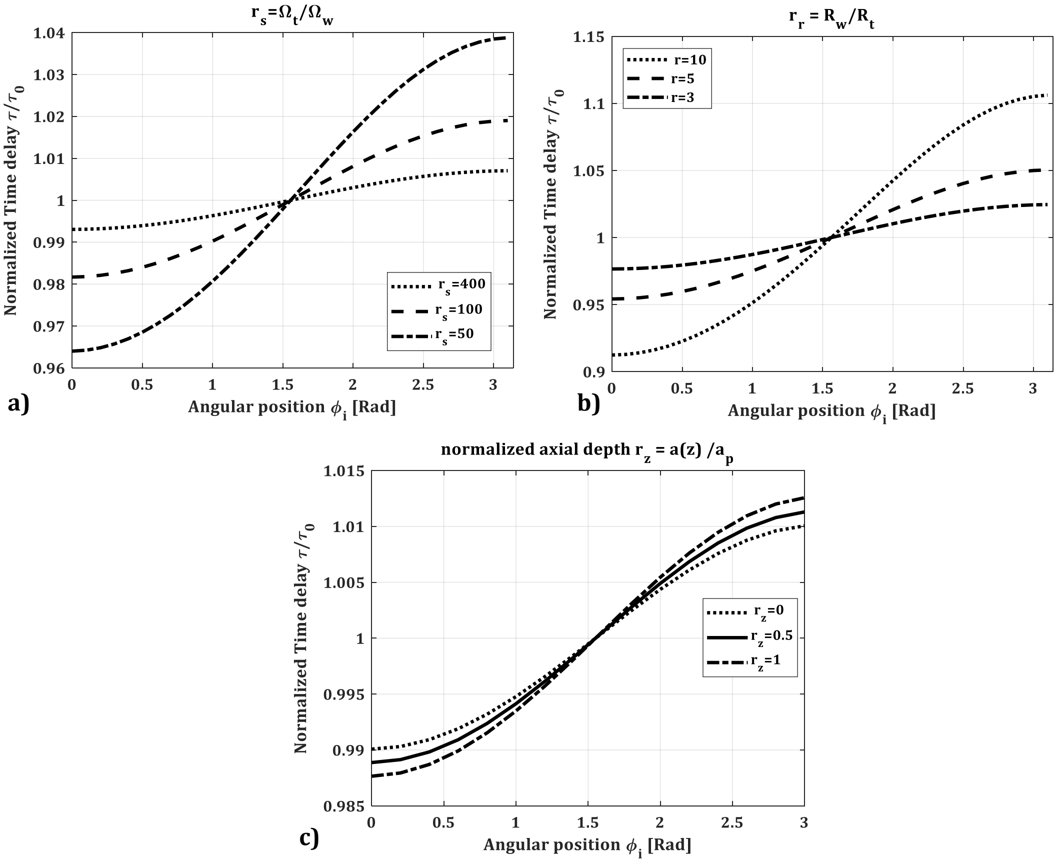

Figure 4.3. Comparison of time delay variation; a) for different speed ratio, b) different diameter ratio, c) different depth of cut

The third diagram shows the variation of delay amplitude along the depth of cut. It is shown that the variation amplitude is lowest at the tooltip ($r_z = 0$) compared to the axial element with $r_z = 1$. Based on the simulation given in Figure 4.3, if the workpiece spindle speed is slow, which is mainly used in machining of large-scale parts in turn-milling operations, the total time delay will be close to the tooth passing period, and the time delay will be approximately equal to that of the regular milling operation. However, for applications requiring lower cutting speeds (lower tool rotational speed), as the workpiece rotational speed increases, the time delay in turn-milling deviates from tooth passing period and the system's dynamics will be different from the regular milling operation.

4.4. Dynamics of Orthogonal Turn-Milling Process in Time Domain

During orthogonal turn-milling operation, the tool and workpiece can have flexibilities in all three dimensions, as shown in Figure 4.4.

The displacements $Q(s)$ caused by the cutting force $F(s)$ imposed on the structure can be expressed as follows;

$$\{Q_p(s)\}_{4v\times1} = \{\Phi_{\mathrm{p}}(s)\}_{4v\times4v}\{F_p(s)\}_{4v\times1} \quad p: t, w \tag{4.19}$$

where the subscript v represents the number of contact points along the engagement length of the flexible tool and flexible workpiece [119]. Depending on the turn-milling configuration, for both flexible tool and workpiece, if the contact area is large multiple contact points $(v > 1)$ can be used. However, if the depth of cut is small or the workpiece is rigid in tool's flexibility directions the lumped dynamics $(v = 1)$ approach is employed [43].

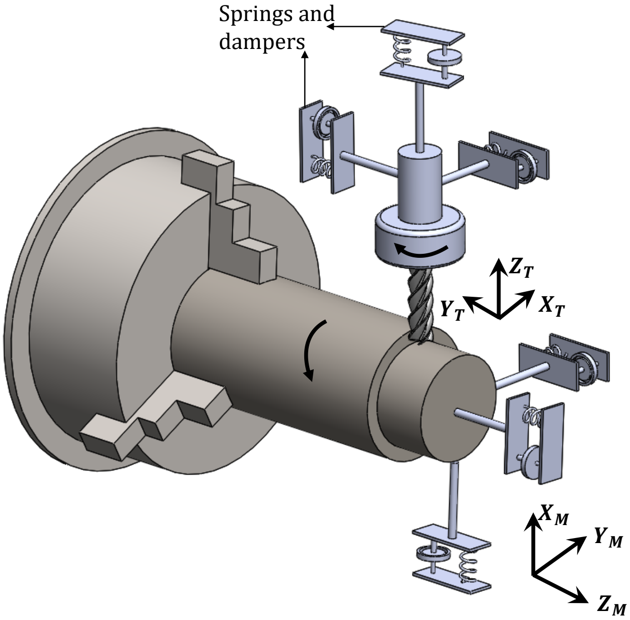

Figure 4.4: Structural flexibilities in orthogonal turn-milling operation.

Subscript p defines the equations that corresponds to tool (t) or workpiece (w). The Equation (4.19) with on contact point can be written for flexible tool and workpiece in three directions as follows;

$$\begin{Bmatrix} Q_x \\ Q_y \\ Q_z \end{Bmatrix}_p = \begin{bmatrix} \Phi_{xx} & \Phi_{xy} & \Phi_{xz} \\ \Phi_{yx} & \Phi_{yy} & \Phi_{yz} \\ \Phi_{zx} & \Phi_{zy} & \Phi_{zz} \end{bmatrix}_p \begin{Bmatrix} F_x \\ F_y \\ F_z \end{Bmatrix}_p, \quad p: t, w \tag{4.20}$$

The measured transfer functions are given as;

$$\Phi_p(s) = U_p\left(Is^2 + 2\bar{\zeta}_p\bar{\omega}_{n_p}s + \bar{\omega}_{n_p}^2\right)^{-1} U_p^T, \quad p: t, w \tag{4.21}$$

where $I_{(m_p \times m_p)}$ is identity matrix, $\bar{\omega}_{n_{p_{(m_p \times m_p)}}}$ is diagonal natural frequency, and $\bar{\zeta}_{p_{(m_p \times m_p)}}$ is damping ratio matrices for m_p number of identified flexible modes of the tool or workpiece. $U_{(3\times m_p)}$ is the mass normalized mode shape matrix of tool and workpiece at the cutting location as defined in Equation (4.22). The mode shape matrix and diagonal natural frequency and damping ratio matrices are given as follows:

$$U_p = \begin{bmatrix} \begin{Bmatrix} u_{x,1,p} \\ u_{y,1,p} \\ u_{z,1,p} \end{Bmatrix} & \begin{Bmatrix} u_{x,2,p} \\ u_{y,2,p} \\ u_{z,2,p} \end{Bmatrix} & \ldots & \begin{Bmatrix} u_{x,m,p} \\ u_{y,m,p} \\ u_{z,m,p} \end{Bmatrix} \end{bmatrix}_{3\times m_p}, \quad p: t, w$$

$$\bar{\omega}_{n_p} = \begin{bmatrix} \omega_{n_{x,p}} & 0 & 0 \\ 0 & \omega_{n_{y,p}} & 0 \\ 0 & 0 & \omega_{n_{z,p}} \end{bmatrix}_{m_p\times m_p}, p: t, w \tag{4.22}$$

$$\bar{\zeta}_p = \begin{bmatrix} \zeta_{x,p} & 0 & 0 \\ 0 & \zeta_{y,p} & 0 \\ 0 & 0 & \zeta_{z,p} \end{bmatrix}_{m_p\times m_p}, p: t, w$$

where each column is the mode shape vector representing the relative displacement of the cutting point in three directions in corresponding coordinate system, when the structure vibrates in the corresponding mode. The equation of motion of each structure can be converted into the time domain as:

$$\ddot{Q}_p(t) + 2\bar{\zeta}_p\bar{\omega}_{n_p}\dot{Q}(t) + \bar{\omega}_{n_p}^2 Q_p(t) = F_p \qquad p: t, w \tag{4.23}$$

It is to be noted that the dynamic displacements and dynamic forces are defined in TCS in the previous sections. The frequency response functions and the mode shapes evaluated for workpiece in MCS must be transformed into TCS. In orthogonal turn-milling case, the FRF of the workpiece in X_M direction in MCS is aligned with X_T in TCS, Y_M is aligned in X_T direction, and Z_M in Y_M direction, as shown in Figure 4.4.

The physical dynamic displacements can be transformed into modal space using the transformation given in [119]:

$$\{Q_p(t)\}_{(3\times 1)} = [U_p]_{(3\times m_p)}\{\Gamma_p(t)\}_{(m_p\times 1)} \tag{4.24}$$

where U_p is the mode shape vector of the structure and $\Gamma(t)$ is the modal displacement vector in modal space. By substituting the equation (4.24) into Equation (4.23) the equation of motion for tool and workpiece in time domain and modal space can be given as:

$$\begin{aligned}
&\ddot{\Gamma}_t(t) + 2\bar{\zeta}_t\overline{\omega_{n_t}}\dot{\Gamma}_t(t) + \overline{\omega_{n_t}}^2\Gamma_t(t) = U_t^T F^n(t) \\
&\ddot{\Gamma}_w(t) + 2\bar{\zeta}_w\overline{\omega_{n_w}}\dot{\Gamma}_w(t) + \overline{\omega_{n_w}}^2\Gamma_w(t) = -U_w^T F^n(t)
\end{aligned} \tag{4.25}$$

where U_t and U_w represent the mass normalized mode shape matrices of the tool and workpiece, respectively. Note that the cutting forces generated at the cutting zone between tool and workpiece act on both with the same magnitude but in the opposite direction [117], as given in Equation (4.25). The following equation can be obtained by unifying the explicit equations in Equation (4.25) into matrix form in modal space;

$$I\begin{Bmatrix}\ddot{\Gamma}_t(t)\\ \ddot{\Gamma}_w(t)\end{Bmatrix} + \begin{bmatrix}2\bar{\zeta}_t\overline{\omega_{n_t}} & 0\\ 0 & 2\bar{\zeta}_w\overline{\omega_{n_w}}\end{bmatrix}\begin{Bmatrix}\dot{\Gamma}_t(t)\\ \dot{\Gamma}_w(t)\end{Bmatrix} + \begin{bmatrix}\overline{\omega_{n_t}}^2 & 0\\ 0 & \overline{\omega_{n_w}}^2\end{bmatrix}\begin{Bmatrix}\Gamma_t(t)\\ \Gamma_w(t)\end{Bmatrix} = \begin{bmatrix}U_t^T\\ -U_w^T\end{bmatrix}F^n(t) \tag{4.26}$$

In Equation (4.26), it is required to define the elemental cutting forces in modal space. Therefore, the elemental cutting forces are given in Equation (4.12) must be transformed from physical to modal space. For this purpose, the relative displacement between the tool and workpiece in the time domain can be written as follows;

$$\{Q(t)\} = \{Q_t(t)\} - \{Q_w(t)\} \tag{4.27}$$

According to the dynamic chip calculation during regeneration mechanics in Equation (4.3), the dynamic displacement can be defined in TCS as follows;

$$D(t) = \begin{bmatrix}\Delta x\\ \Delta y\\ \Delta z\end{bmatrix} = \left[Q(t) - Q\left(t - \tau_{i,j}\right)\right] \tag{4.28}$$

where $\{Q(t)\}$ and $\left\{Q\left(t - \tau_{i,j}\right)\right\}$ are the relative displacements between tool and workpiece at the present time (t) and one delay period $(\tau_{i,j})$ before.

By substituting the Equations (4.27) and (4.28) into (4.24), the dynamic displacements can be obtained as follows;

$$D(t) = \left[\left(U_t\Gamma_t(t) - U_w\Gamma_w(t)\right) - \left(U_t\Gamma_t\left(t - \tau_{i,j}\right) - U_w\Gamma_w\left(t - \tau_{i,j}\right)\right)\right] \tag{4.29}$$

By substituting equation (4.29) into Equation (4.12), the following formulation can be obtained for the elemental dynamic cutting forces in modal space:

$$\{F^n(t)\} = [DC_j(t)]\left[\left(U_t\Gamma_t(t) - U_w\Gamma_w(t)\right) - \left(U_t\Gamma_t(t-\tau_{i,j}) - U_w\Gamma_w(t-\tau_{i,j})\right)\right] \tag{4.30}$$

where $[DC_j(t)]$ refers to the cutting force directional coefficients given in Equations (4.12) and (4.13). Combining the Equation (4.30) and (4.27) gives the generalized dynamics of turn-milling process in modal space as;

$$\begin{gathered} I\begin{Bmatrix}\ddot{\Gamma}_t(t)\\ \ddot{\Gamma}_w(t)\end{Bmatrix} + \begin{bmatrix}2\bar{\zeta}_t\overline{\omega_n}_t & 0\\ 0 & 2\bar{\zeta}_w\overline{\omega_n}_w\end{bmatrix}\begin{Bmatrix}\dot{\Gamma}_t(t)\\ \dot{\Gamma}_w(t)\end{Bmatrix} + \begin{bmatrix}\overline{\omega_n}_t^2 & 0\\ 0 & \overline{\omega_n}_w^2\end{bmatrix}\begin{Bmatrix}\Gamma_t(t)\\ \Gamma_w(t)\end{Bmatrix} = \\ \begin{bmatrix}U_t^T\\ -U_w^T\end{bmatrix}[DC_j(t)]\,[U_t - U_w]\left(\begin{Bmatrix}\Gamma_t(t)\\ \Gamma_w(t)\end{Bmatrix} - \begin{Bmatrix}\Gamma_t(t-\tau_{i,j})\\ \Gamma_w(t-\tau_{i,j})\end{Bmatrix}\right)\end{gathered} \tag{4.31}$$

Equation (4.31) represents the coupled equation of motion of tool and workpiece by taking the dynamic cutting forces that resulted during turn-milling operation into account.

4.5. Stability of Orthogonal Turn-Milling Process

In the previous sections, the dynamic chip thickness, dynamic forces, and the dynamic model of turn-milling are presented by taking the dynamics of the tool and workpiece into account. In order to solve the stability of orthogonal turn-milling dynamics, discrete-time domain and frequency domain approaches are proposed in this section. The results and comparisons of both approaches are discussed in Section 4.6.

4.5.1. Stability Analysis in Discrete-Time Domain

In this section, the stability of turn-milling process is studied using the Semi-discretization method (SDM) proposed by Insperger and Stepan [39]. This method allows the delayed differential equation to be discretized in discrete time intervals within a period by linearizing the time domain simulation of the vibrating system. This method discretizes the delayed terms within a period of the system only while keeping the non-delayed states unchanged. It has been shown in Section 4.3 that, unlike regular milling operation, the time delay varies in time during turn-milling operation. By integrating the varying time delay which is obtained in Equation (4.18) with the dynamic equation of motion of turn-milling process in modal space, the following formulation is obtained:

$$I\left\{\ddot{\bar{\Gamma}}(t)\right\} + [C]\left\{\dot{\bar{\Gamma}}(t)\right\} + [D]\{\bar{\Gamma}(t)\} = [FC]\left(\{\bar{\Gamma}(t)\} - \left\{\bar{\Gamma}\left(t - \tau_{i,j}(z)\right)\right\}\right),$$
$$\{\bar{\Gamma}(t)\} = \begin{Bmatrix} \Gamma_{\mathrm{t}}(t) \\ \Gamma_{\mathrm{w}}(t) \end{Bmatrix}_{M\times 1} \tag{4.32}$$

The coefficient matrices stated in Equation (4.32) are as follows:

$$[C] = \begin{bmatrix} 2\bar{\zeta}_t \overline{\omega_{n_t}} & 0 \\ 0 & 2\bar{\zeta}_w \overline{\omega_{n_w}} \end{bmatrix}_{M\times M} ; [D] = \begin{bmatrix} \overline{\omega_{n_t}}^2 & 0 \\ 0 & \overline{\omega_{n_w}}^2 \end{bmatrix}_{M\times M} ;$$
$$[FC(t)]_{M\times M} = \begin{bmatrix} U_t^T \\ -U_w^T \end{bmatrix} \left[DC_j(t,z)\right] [U_t \;\; -U_w] \;\; \therefore M = m_w + m_t \tag{4.33}$$

where m_t and m_w are the number of modes of tool and workpiece, respectively.

Note that, the varying time delay is periodic at the tooth passing period $\tau_{i,j} = \tau_{i,j}(t) = \tau_{i,j-1}(t + \tau_0)$. The subscript i refers to time instant, and subscript j refers to tooth number for each axial element. Note that, since the time delay varies in time within the cutting limits, depending on the delay resolution, several delays can be generated in the system [43]. In this regard, special milling tools such as variable-pitch, variable-helix, serrated, and crest-cut tools also introduce discrete and distributed time delays during the cutting due to their particular geometry, which affects the local pitch angle of each element [61,77,120,121]. While the time delay with a regular milling tool (equal-pitch) in milling operation is constant and is equal to the tooth passing period (τ_0), the time delay at each discrete interval ($i\Delta t$) and axial height (z) in turn-milling is different and time varying but periodic at tooth passing period. In order to apply semi-discretization, the principal period (rotational period) of the system T is divided into m discrete time intervals.

$$\Delta t = \frac{T}{m} \tag{4.34}$$

where m is an integer and known as the principal period resolution, and Δt is the time interval. The number of delays can be changed by the tool geometry, process kinematics, and process configurations. The delay resolution defines the number of discrete points within the delay as can be calculated as follows;

$$r_{i,j}(z) = int\left(\frac{\tau_{i,j}(z)}{\Delta t} + \frac{p}{2}\right) \tag{4.35}$$

where int denotes the integer-part function, and p is the order of the Lagrange polynomial for the approximation of the delayed term [118]. As stated in detail by Insperger and

Stepan [39,118], while other approaches of SDM approximate the delayed terms of the system by piecewise constant delays over each discretization step, higher-order methods approximate the delayed terms by higher-order polynomials of time t. In other words, in higher-order SDM, the time-periodic coefficients are approximated by piecewise constant ones, and the delayed terms are approximated by a linear combination of the corresponding discrete delayed values of the delayed state q, while the non-delayed terms are left in their original form. In this study, the updated first order semi-discretization method (SDM) is used where $p = 1$ in equation (4.35) [39].

Note that, since the time delay $\tau_{i,j}$ is varying at each discrete time interval in turn-milling, the period resolution m and delay resolution $r_{i,j}$ are not equal. However, since the principal delay is equal to tooth passing frequency in conventional milling, the delay resolution and period resolutions are equal. The number of unique delays (r) in the system with the particular delay label of $r_{i,j}$ is represented by N_D.

$$\begin{gathered} r = unique\left(r_{i,j}(z)\right)\ ;\ i = 1,\cdots,m\ ; j = 1,\cdots,N\ ; z = n.dz \\ N_D = size(r) \end{gathered} \tag{4.36}$$

In the semi-discretization method, the system period is divided into m time intervals (Δt), and over each interval, the delayed differential equation (DDE) is turned into an ordinary differential equation (ODE) which the analytical solution can be obtained. In this regard, the dynamic equations are represented in the state-space form a first order ODE by using the time-periodic coefficient matrices [39];

$$\{\dot{q}(t)\} = L(t)\{q(t)\} + B(t)\left\{q\left(t - \tau_{i,j}(z)\right)\right\} \tag{4.37}$$

where the coefficient matrices can be defined as

$$\begin{gathered} \{q(t)\} = \begin{Bmatrix} \bar{\Gamma}(t) \\ \dot{\bar{\Gamma}}(t) \end{Bmatrix};\ \ L(t) = \begin{bmatrix} 0 & I \\ [\overline{FC}(t)] - [D] & -[C] \end{bmatrix}_{2M\times 2M}; \\ B\ (t) = \begin{bmatrix} 0 & 0 \\ -[FC_r(t)] & 0 \end{bmatrix}_{2M\times 2M} \end{gathered} \tag{4.38}$$

$\{q(t)\}$ represents the modal states of the coupled tool-workpiece system at time t, which is defined by the modal displacements $\bar{\Gamma}(t)$ and modal velocities $\dot{\bar{\Gamma}}(t)$ of the coupled tool-workpiece system. The coefficient matrices $L(t)$ and $B(t)$ are periodic at tooth passing period. $\left\{q\left(t-\tau_{i,j}(z)\right)\right\}$ is the modal states with time-varying delays $\left(\tau_{i,j}(z)\right)$ which are periodic in the tooth passing period, as well. In equation (4.38), the coefficient matrix $B(t)$ consist of matrix $[FC_r(t)]$, in which, the directional coefficients are grouped according to their delay values based on their delay label. This is because matrix $B(t)$ is multiplied by the state vector that contains delayed states, and it only encompasses the directional coefficients of the elements with unique delays with label r.

$$[FC_r(t)] = \begin{bmatrix} U_t^T \\ -U_w^T \end{bmatrix} \left[\sum_{j=1}^{N} \int_0^{a_i} \left[DC_j(t,z)\right] dz \right] [U_t - U_w] \tag{4.39}$$

On the other hand, the matrix $[\overline{FC}(t)]$ in coefficient matrix $L(t)$ corresponds to the transient part of the equation, which is not affected by the delays. In other words, $[\overline{FC}(t)]$ has the contributions of all the directional coefficients active with the cut, regardless of their delay label, as follows;

$$[\overline{FC}(t)] = \sum_{r=1}^{N_D} [FC_r(t)] \tag{4.40}$$

where N_D is the number of unique delays contribute to the coupled system. The time-periodic coefficient matrices (L, R) and varying time delay $\left(\tau_{i,j}(z)\right)$ are averaged within each discrete time interval $\Delta t, t \in [t_i, t_{i+1})$ as given below;

$$L_i = \frac{1}{\Delta t} \int_{t_i}^{t_{i+1}} L(t)dt \;\; ; \;\; B_{i,r} = \frac{1}{\Delta t} \int_{t_i}^{t_{i+1}} R_r(t)dt \;\; ; \;\; \tau_{i,j} = \int_{t_i}^{t_{i+1}} \tau_j(z)dt \tag{4.41}$$

where $r = 1,2, \dots, N_D$. According to the theory of SDM, the delayed state is defined by the discretization steps. Having introduced the discretization steps (discrete points), the delayed states $\left\{q\left(t-\tau_{i,j}(z)\right)\right\}$ are approximated as a weighted sum of the two neighboring delayed states $q(t_{i-r})$ and $q(t_{i-r+1})$ as follows (See Figure 4.5);

$$q\left(t-\tau_{i,j}(z)\right) = \beta_{i,a}(t)\, q\left(t_{i-r_i}\right) + \beta_{i,b}(t)\, q\left(t_{i-r_i+1}\right) \tag{4.42}$$

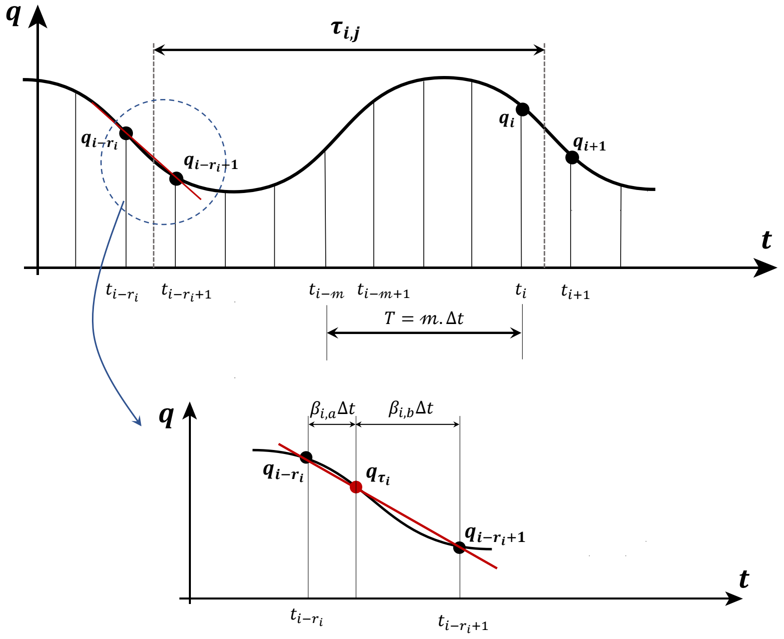

Figure 4.5: Approximation of the delayed states by time-varying weights using 1st order Lagrange polynomial approximation [39].

Note that, since the time delay $\tau_{i,j}$ varies within the time period of the system; hence the neighboring delays vary as well. Consequently, the weights are given in equation (4.42) also vary within the time period and can be calculated as;

$$\beta_{i,a}(t) = \frac{\tau_{i,j} + (i - r_i + 1)\Delta t - t}{\Delta t} \;;\; \beta_{i,b}(t) = \frac{t - (i - r_i)\Delta t - \tau_{i,j}}{\Delta t} \tag{4.43}$$

The discrete state weights hold the following conditions; $\beta_{a,b} = [0,1] \in \mathbb{R}$ and $\beta_{i,a} + \beta_{i,b} = 1$.

As a result, the state space equation (4.37) can be expressed as below for each discrete time interval $t \in [t_i, t_{i+1})$ for $i = 0,1,\cdots,m-1$;

$$\{\dot{q}(t_i)\} = L_i\{q(t_i)\} + \sum_{r_i=1}^{N_D} B_{i,r}\big[\beta_{b,i}\{q\big(t_{i-r_i}\} + \beta_{a,i}\{q\big(t_{i-r_i+1}\big)\}\big] \tag{4.44}$$

The solution over one discrete time step is;

$$\{q_{i+1}\} = P_i\{q_i\} + \sum_{r=1}^{N_D}\big(R_{r,i,b}\{q_{i-r}\} + R_{r,i,a}\{q_{i-r+1}\}\big) \tag{4.45}$$

where

$$
\begin{aligned}
P_i &= e^{L_i \Delta t} \\
R_{r,i,a} &= \int_0^{\Delta t} \frac{\tau_{i,j} - (r_i - 1)\Delta t - s}{\Delta t} e^{L_i(\Delta t - s)} ds B_{r,i} \\
R_{r,i,b} &= \int_0^{\Delta t} \frac{s - \tau_{i,j} + r_i \Delta t}{\Delta t} e^{L_i(\Delta t - s)} ds B_{r,i}
\end{aligned}
\tag{4.46}
$$

Assuming that the time periodic coefficient matrix L_i is invertible $(L_i L_i^{-1} = I)$, the equation (4.46) is calculated as;

$$
\begin{aligned}
R_{r,i,a} &= \left(L_i^{-1} + \frac{1}{\Delta t}\left(L_i^{-2} - \left(\tau_{i,j} - (r_i - 1)\Delta t\right) L_i^{-1} \right) \left(I - e^{L_i \Delta t}\right) \right) B_{r,i} \\
R_{r,i,b} &= \left(-L_i^{-1} + \frac{1}{\Delta t}\left(-L_i^{-2} + \left(\tau_{i,j} - r_i \Delta t\right) L_i^{-1} \right) \left(I - e^{L_i \Delta t}\right) \right) B_{r,i}
\end{aligned}
\tag{4.47}
$$

Or in a short form;

$$
\begin{aligned}
R_{r,i,a} &= \left(e^{L_i \Delta t} - I\right) L_i^{-1} B_{r,i} \beta_{a,i} \\
R_{r,i,b} &= \left(e^{L_i \Delta t} - I\right) L_i^{-1} B_{r,i} \beta_{b,i}
\end{aligned}
\tag{4.48}
$$

From equations (4.42) and (4.45), the discrete map for one discrete time interval can be written as;

$$
\{z_{i+1}\} = [G_i]\{z_i\} \tag{4.49}
$$

where

$$
z_i = [q_i \; q_{i-1} \cdots q_{i-r+1} \; q_{i-r}]^T \tag{4.50}
$$

is augmented state vector which encompasses the current state and states a delay before. The coefficient matrix G_i in equation (4.49) which links the states at time t to the next time interval $i+1$, reads;

$$
G_i = \left[\begin{array}{c|cccc}
P_i & 0 & \cdots & 0 & 0 \\ \hline
I & 0 & \cdots & 0 & 0 \\
0 & I & \cdots & 0 & 0 \\
\vdots & \vdots & \ddots & \vdots & \vdots \\
0 & 0 & \cdots & I & 0
\end{array}\right]
+ \sum_{r=1}^{N_D}
\begin{array}{c|ccccccccc}
 & 1 & & & r_i - 1 & r_i & & & r_{max} \\
 & \downarrow & & & \downarrow & \downarrow & & & \downarrow \\
0 & 0 & \cdots & 0 & R_{r,i,a} & R_{r,i,b} & 0 & \cdots & 0 \\ \hline
0 & 0 & \cdots & 0 & 0 & 0 & 0 & \cdots & 0 \\
0 & 0 & \cdots & 0 & 0 & 0 & 0 & \cdots & 0 \\
\vdots & \vdots & \ddots & \vdots & \vdots & \vdots & \vdots & \ddots & \vdots \\
0 & 0 & \cdots & 0 & 0 & 0 & 0 & \cdots & 0
\end{array}
\tag{4.51}
$$

According to equation (4.45), the matrices $R_{r,i,a}$ and $R_{r,i,b}$ are located at the $(r_i - 1)^{th}$

and $(r_i)^{th}$ columns and upper right block of the transition matrix, respectively.

Note that, the transition matrix must build according to the maximum number of unique delays of the system $\left(r_{max} = \max\left(r_{i,j}\right)\right)$, and the number of total degrees of freedom of the system (M) (See equation (4.33)). As a result, the dimensions of the augmented system are $(2Mr_{max} + 2M) \times (2Mr_{max} + 2M)$.

The stability of the system is solved by evaluating the eigenvalues of the monodromy (transition) matrix $[\mathbf{\Psi}]$ [39,118]. This matrix is formed by expressing the equation (4.49) at m number of intervals within the system's principal period T, as follows [39,118];

$$\{z_m\} = [\mathbf{\Psi}]\{z_0\} \ \because \ [\mathbf{\Psi}] = G_{m-1}G_{m-2} \cdots G_1 G_0 \tag{4.52}$$

The stability of the linear periodic system in equation (4.52) can be solved by Floquet theory [39]. According to Floquet theory, the linear periodic system will be unstable if the modulus of any of the characteristic multipliers (eigenvalues) (μ) of the monodromy matrix is greater than unity, unstable if the modulus is less than unity, and critically stable of the modulus is equal to unity [39,118].

$$|\mu[I] - [\mathbf{\Psi}]| = 0 \ \therefore \ |\mu| = \begin{cases} < 1 & \text{stable} \\ = 1 & \text{critically stable} \\ > 1 & \text{unstable} \end{cases} \tag{4.53}$$

In the semi-discretization method, the stability must be searched iteratively at different spindle speeds and depth of cuts to find the stability lobes. Note that, for larger period resolution m, the time interval Δt decreases, leading to higher accuracy of the solution, especially at lower spindle speeds where the vibration wavelength is small. However, for smaller time intervals, the number of maximum delay resolutions increases, causing matrices with larger dimensions and lower computational speed. Therefore, the period resolution must be selected carefully to avoid inaccurate stability lobe prediction or unnecessary computational costs.

4.5.2. Stability Analysis in Frequency Domain

In this section, the zero-order approximation (ZOA) method proposed by Budak and Altintas [117,122] for milling is used to model the stability of orthogonal turn-milling process in the frequency domain. The stability model is based on the dynamic chip thickness and dynamic milling forces given in Section 4.2 and the dynamics of orthogonal turn-milling introduced in Section 4.4.

In this method, the time-varying elemental directional coefficient matrix $\left[DC_{j,n}(t)\right]$ given in equations (4.12), (4.13), and (4.14) for n^{th} element on j^{th} tooth, which is periodic at spindle rotation frequency and varies within the immersion angles, expanded into the Fourier series [111,117]. The Fourier expansion series are given as follows;

$$\left[DC_{j,n}(t)\right] = \sum_{r=-\infty}^{+\infty}\left[DC_{j,n}^{r}\right]e^{ir\omega_t t}\ ,\ \left[DC_{j,n}^{r}\right] = \frac{1}{T}\int_0^T\left[DC_{j,n}(t)\right]e^{-ir\omega_t t}dt \tag{4.54}$$

where ω_t is tooth passing frequency, and T is tooth passing period. If the higher order of harmonics are considered ($r > 0$), the stability can be solved using the multi-frequency approach [117], which also has high computation time due to the long numerical calculations. Therefore, by using the zero-order term in the Fourier series, only the average component (constant term) of the Fourier series is retained (zero number of harmonics ($r = 0$)). By substituting $\omega_t t = N\theta$ the Fourier expansion can be written in the angular domain as the detailed calculations are given in [117].

$$\left[DC_{j,n}^{0}\right] = \frac{1}{2\pi}\int_{\theta_{st,j,n}}^{\theta_{ex,j,n}}\left[DC_{j,n}(\theta)\right]d\theta\ ;\theta = \phi_j, \varphi_j \tag{4.55}$$

In orthogonal turn-milling since the angular position and the immersion angles of the elements on the side edge and the minor edges are different, the zero-order Fourier expansion is taken according to their particular angular increment parameter (ϕ_j, φ_j). Definition of ϕ_j and φ_j are given in equations (3.25) and (3.32), respectively. By substituting the equation (4.14) into (4.55), we have;

$$\left[DC_{j,n}^{0}\right] = \frac{1}{2\pi}\begin{bmatrix} \int_{\phi_{st,jn}}^{\phi_{ex,jn}}\alpha_{xx,jn}(\phi)\,d\phi & \int_{\phi_{st,jn}}^{\phi_{ex,jn}}\alpha_{xy,jn}(\phi)d\phi & \int_{\varphi_{st,j}}^{\varphi_{ex,j}}\alpha_{xz,j}(\varphi)d\varphi \\ \int_{\phi_{st,jn}}^{\phi_{ex,jn}}\alpha_{yx,jn}(\phi)\,d\phi & \int_{\phi_{st,jn}}^{\phi_{ex,jn}}\alpha_{yy,jn}(\phi)d\phi & \int_{\varphi_{st,j}}^{\varphi_{ex,j}}\alpha_{yz,j}(\varphi)d\varphi \\ \int_{\phi_{st,jn}}^{\phi_{ex,jn}}\alpha_{zx,jn}(\phi)\,d\phi & \int_{\phi_{st,jn}}^{\phi_{ex,jn}}\alpha_{zy,jn}(\phi)\,d\phi & \int_{\varphi_{st,j}}^{\varphi_{ex,j}}\alpha_{zz,j}(\varphi)d\varphi \end{bmatrix} \tag{4.56}$$

$$\left[DC_{j,n}^{0}\right] = \frac{1}{2\pi}\begin{bmatrix} \alpha_{xx,jn}^{0}(\theta) & \alpha_{xy,jn}^{0}(\theta) & \alpha_{xz,j}^{0}(\theta) \\ \alpha_{yx,jn}^{0}(\theta) & \alpha_{yy,jn}^{0}(\theta) & \alpha_{yz,j}^{0}(\theta) \\ \alpha_{zx,jn}^{0}(\theta) & \alpha_{zy,jn}^{0}(\theta) & \alpha_{zz,j}^{0}(\theta) \end{bmatrix}\ ;\ \theta = \phi_j, \varphi_j$$

By substituting the equation (4.56) into (4.12), the elemental cutting forces can be calculated as;

$$\begin{Bmatrix} dF_x(t) \\ dF_y(t) \\ dF_z(t) \end{Bmatrix} = \left[DC_{j,n}^{0}\right] \begin{Bmatrix} \Delta \mathrm{x} \\ \Delta y \\ \Delta z \end{Bmatrix} \tag{4.57}$$

From equation (4.20) it is known that the displacements of the system in Laplace domain can be expressed as;

$$\begin{Bmatrix} \Delta \mathrm{x}(s) \\ \Delta \mathrm{y}(s) \\ \Delta \mathrm{z}(\mathrm{s}) \end{Bmatrix} = \begin{bmatrix} \Phi_{xx}(s) & \Phi_{xy}(s) & \Phi_{xz}(s) \\ \Phi_{yx}(s) & \Phi_{yy}(s) & \Phi_{yz}(s) \\ \Phi_{zx}(s) & \Phi_{zy}(s) & \Phi_{zz}(s) \end{bmatrix} \begin{Bmatrix} F_x(s) \\ F_y(s) \\ F_z(s) \end{Bmatrix} \tag{4.58}$$

where the elemental dynamic chip thickness vectors in time domain are defined in equation (4.3). The regenerative dynamic chip thickness in time domain in equation (4.3) is transformed in Laplace domain as follows;

$$\begin{Bmatrix} \Delta \mathrm{x}(s) \\ \Delta \mathrm{y}(s) \\ \Delta \mathrm{z}(\mathrm{s}) \end{Bmatrix}_{jn} = \left[1 - e^{-s\tau_j(z)}\right] \begin{Bmatrix} x(t) \\ y(t) \\ z(t) \end{Bmatrix} \tag{4.59}$$

Based on the dynamic chip thickness formulation and considering the equal but opposite direction force that occurred between tool and workpiece, the transfer function matrix in equation (4.58) can be written as the summation of the FRFs of the tool and workpiece [117].

$$\left[\Phi_{qq}\right] = \left[\Phi_{qq}\right]_t + \left[\Phi_{qq}\right]_w ; q = x, y, z \tag{4.60}$$

where t and w refer to tool and workpiece, respectively. Note that, in the ZOA frequency domain method, the time-varying characteristic of the delay in orthogonal turn-milling is neglected. However, in the formulations (See equation (4.59)), the general case is given. Time delay can be variable between subsequent teeth and along the cutting edge caused by edge geometry in special tools such as variable-pitch variable-helix, serrated, or crest-cut tools. Recently, Farahani et al. [66] and Bari et al. [123] employed the varying delay approach to predict the stability of serrated tools in the frequency domain by using the normalized average delay. In this section, the standard end mills with regular pitch variation are used, and the time delay for each tooth at the tooltip is equal to the tooth passing period ($\tau = T$). However, due to the kinematics of the turn-milling operation, the time delay also varies along the tool axis due to the increase in linear speed of workpiece. In addition, as given in equation (4.18), the delay varies at each instantaneous immersion angle (by time). In ZOA approach, the average time delay within the immersion boundary is considered for all the teeth for at each height z.

The delay term in this section is given in a general form of $\tau_j(z)$ to be able to include the delay variations at each tooth and elemental height. This type of delay distribution can be seen in special tools such as variable-helix, variable-pitch, serrated and crest-cut tools. For the case of standard tools employed in orthogonal turn-milling, the average delay within the immersion boundaries is equal for all the teeth at the tooltip. However, the average delay varies along the tool axis.

By substituting the equations (4.58) and (4.59) into equation (4.57) and switching from the Laplace domain to the frequency domain by considering $(s = i\omega_c)$, the elemental dynamic force equilibrium or orthogonal turn-milling with standard end mills gives;

$$\begin{Bmatrix} dF_x \\ dF_y \\ dF_z \end{Bmatrix} e^{i\omega_c t} = \left[1 - e^{-i\omega_c \tau_j(z)}\right]\left[DC_{j,n}^{0}\right][\Phi(\mathrm{i}\omega_\mathrm{c})] \begin{Bmatrix} dF_x \\ dF_y \\ dF_z \end{Bmatrix} e^{i\omega_c t} \tag{4.61}$$

Equation (4.61) gives the elemental dynamic cutting forces of n^{th} axial element on side edge on j^{th} tooth in addition to the forces generated from the minor edge by the tooth j. As mentioned previously, the engagement of the minor edge, which is defined by the stepover and eccentricity, is established prior to stability analysis concerning surface quality and part accuracy. Therefore, the dynamic cutting forces resulting from the minor edge are constant regardless of the number of elements (depth of cut) at the side edge. In order to obtain the stability limit (critical depth of cut on side edge) all the elements in the cut have to be coupled and considered simultaneously. In this regard, it is proposed to sum the elemental dynamic forces acting on each element on the side edge to evaluate the total lumped dynamic cutting forces in $x, y,$ and z directions [124,125]. Furthermore, elemental forces contributed by all teeth within the cutting boundary must be considered in stability calculations. The lumped dynamic cutting forces acting on the side edges of all teeth are added to the dynamic cutting forces acting on the minor cutting edges of all teeth. By writing the equation (4.61) for all elements and summing up, the zero-order dynamic model of turn-milling can be written as;

$$\begin{Bmatrix} dF_x \\ dF_y \\ dF_z \end{Bmatrix} e^{i\omega_c t} = \left[1 - e^{-i\omega_c \tau_j(z)}\right]\left[[A_1] + [A_2]\right][\Phi(\mathrm{i}\omega_\mathrm{c})] \begin{Bmatrix} dF_x \\ dF_y \\ dF_z \end{Bmatrix} e^{i\omega_c t} \tag{4.62}$$

where $[A_1]$ is the summation of dynamic forces of all axial elements on side edges of all contributed teeth as follows;

$$[A_1] = \sum_{j=1}^{N}\sum_{n=1}^{m}\frac{1}{2\pi}\begin{bmatrix}\alpha^0_{xx,jn}(\phi) & \alpha^0_{xy,jn}(\phi) & 0\\ \alpha^0_{yx,jn}(\phi) & \alpha^0_{yy,jn}(\phi) & 0\\ \alpha^0_{zx,jn}(\phi) & \alpha^0_{zy,jn}(\phi) & 0\end{bmatrix} \tag{4.63}$$

where m is the number of axial elements. $[A_2]$ refers to the dynamic forces resulted from the minor edges of all contributed teeth;

$$[A_2] = \sum_{j=1}^{N}\frac{1}{2\pi}\begin{bmatrix}0 & 0 & \alpha^0_{xz,j}(\varphi)\\ 0 & 0 & \alpha^0_{yz,j}(\varphi)\\ 0 & 0 & \alpha^0_{zz,j}(\varphi)\end{bmatrix} \tag{4.64}$$

As a result, the characteristic equation of the dynamics of the turn-milling in frequency domain can be written as:

$$\mathbb{E}(\omega_c) = \det\Big[[I] - \big[1 - e^{-i\omega_c\tau_j(z)}\big]\big[[A_1] + [A_2]\big][\Phi(\mathrm{i}\omega_c)]\Big] \tag{4.65}$$

As a result, in order to find the critically stable depth of cut where the system begins to vibration at chatter frequency of ω_c, it is required to solve the roots of the characteristic equation in the equation [38]. If Λ is expressed as follows;

$$\Lambda = \Big[[I] - \big[1 - e^{-i\omega_c\tau_j(z)}\big]\big[[A_1] + [A_2]\big]\Big] \tag{4.66}$$

Then the roots of the characteristic equation can be found as;

$$\mathbb{E}(\omega_c) = 0 \ \rightarrow \det\big[[I] - \Lambda[\Phi(\mathrm{i}\omega_c)]\big] = 0 \tag{4.67}$$

Since the system may have multiple and distributed delays, and due to the mathematical limitations that directional coefficient matrices introduce, derivation of an explicit and analytical solution for the critical stable depth of cut a_{lim} from Λ, using the eigenvalue problem (as given in for milling operation with regular tools [38,117]) is not possible [123]. Instead, the Nyquist stability criterion is used to identify the critical stable depth of cut a_{lim} at different tool rotational speeds. In this method, at a fixed tool's rotational speed (Ω_t) and stepover (a_w), the axial depth of cut is increased by elements δz until the critical stable depth of cut is achieved [56]. Note that, in this method, the workpiece rotational speed and eccentricity are also fixed for each iteration. In the Nyquist stability criterion, the Nyquist plot of the characteristic equation $\big(\mathbb{E}(\omega_c)\big)$ is mapped onto a complex plane for a range of frequencies encompassing the tool's and workpiece's natural frequencies.

The system is unstable if any root of the characteristic equation creates a clockwise encirclement of the origin on the complex plane. The details of the solution procedure of the Nyquist stability criterion are given in Appendix B: Nyquist Stability Criterion.

4.6. Simulation and Experimental Verifications of Stability Model

The proposed chatter stability models in discrete-time and frequency domains are verified through experiments in this section. The orthogonal turn-milling experiments were verified using different tools and workpiece materials in different cutting conditions. The experiments were performed on Mori Seiki NTX 2000 mill-turn machining center. The confirmation experiments are performed for three cases with different tools and workpiece flexibility, material, and dimensions.

- **Case 1:**

In the first case, the tool has a significant flexible structural dynamic compared to the workpiece. The experimental turn-milling set-up using an end mill is shown in Figure 4.6. The chatter identification is performed using both sound measurement and surface quality inspection.

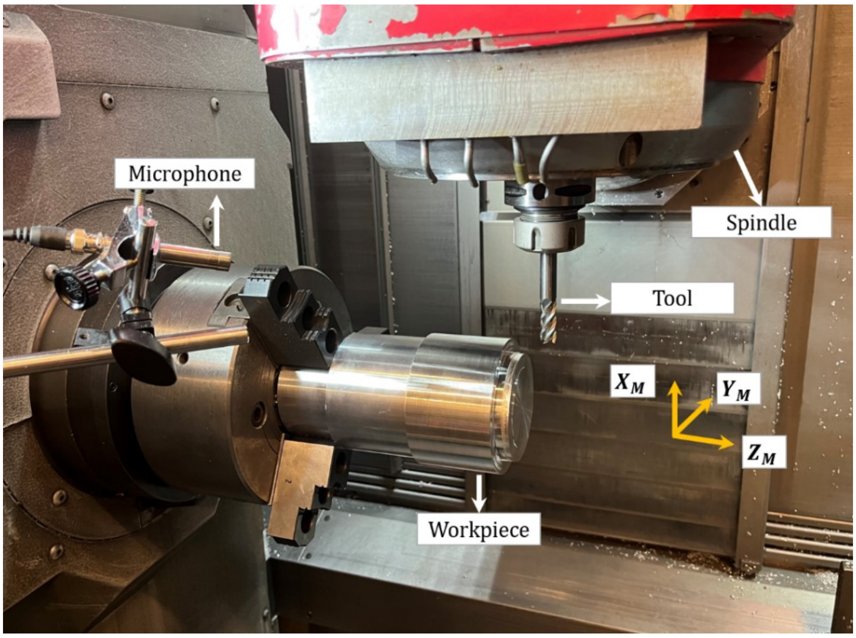

Figure 4.6: Experimental set-up for chatter identification in orthogonal turn-milling cutting tests.

The workpiece is Aluminum alloy Al7075 with 114 mm diameter and 200 mm length. The employed tool is a four-fluted WC regular end mill with 12 mm diameter, 70 mm stick out, 8° rake, and 38° helix angles. The cutting force coefficients for the above-mentioned tool-workpiece material pair are given in Appendix A: Orthogonal databases.

The tool and workpiece FRFs are measured by impact test using a modal hammer and miniature accelerometer, as shown in Figure 4.7. The accelerometer shown in Figure 4.7 is PCB 352A73, and the modal hammer is Endevco model 2301. The modal parameters and the FRF plots in the frequency domain are given in Figure 4.8 and Table 4.1, respectively.

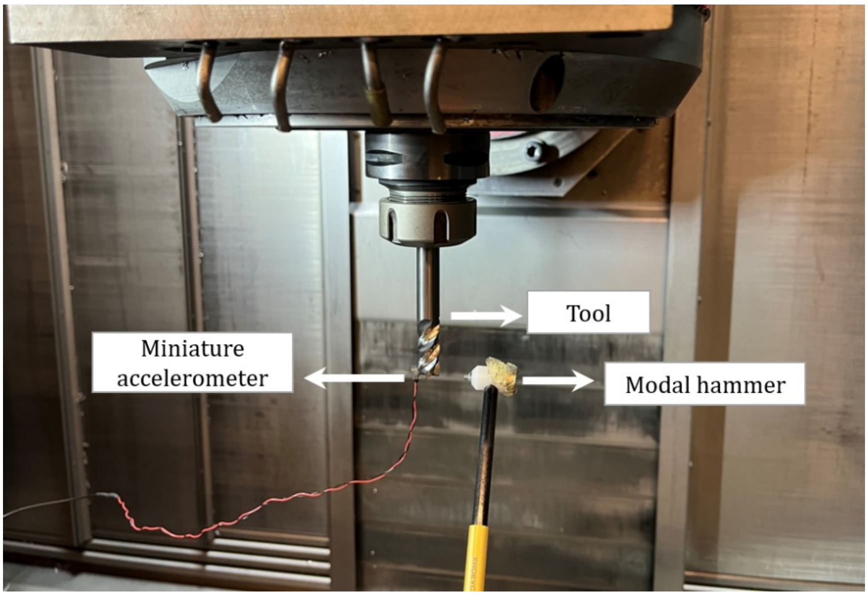

Figure 4.7: Impact testing experimental set-up for Case 1.

The modal analysis and the modal parameter identifications were conducted using CutPro® [126]. Note that, as mentioned in Section 4.4 and illustrated in Figure 4.4, the measured FRFs of the workpiece in MCS must be transformed into TCS to be used in the stability model.

In the present section, the given directions for both the tool and workpiece are transformed to TCS for simplicity. The tool is considered rigid in Z_T direction. The stability lobe diagrams for orthogonal turn-milling are calculated using semi-discretization (SDM) and zero-order approximation (ZOA) methods as stated in Sections 4.5.1 and 4.5.2 for the given tool and workpiece FRF and cutting force coefficient in this section and illustrated in Figure 4.9. It is seen that there is a close agreement between the stability lobes calculated by SDM and ZOA methods.

Table 4.1. Modal parameters of tool and workpiece for Case 1.

	Direction	Modes	Frequency (Hz)	Damping (%)	Modal Stiffness (N/m)
Tool	X_T	1	1015	3.38	4.66e7
		2	2073	2.74	3.29e6
	Y_T	1	1037	3.9	3.14e7
		2	2057	1.29	2.63e6
Workpiece	X_T	1	253.23	4.57	5.16e7
		2	349	2.82	5.41e7
		3	620	3.08	1.69e8
	Y_T	1	1853.5	0.97	1.46e9
	Z_T	1	243	4.09	5.89e7
		2	321.6	4.59	9.33e7
		3	555	2.3	1.26e8

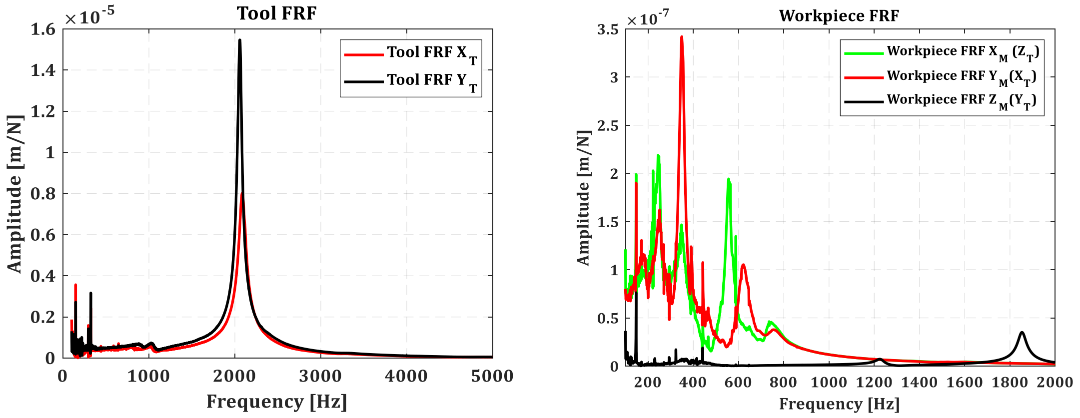

Figure 4.8: Tool and workpiece FRFs for set-up in Case 1.

In order to validate the proposed model and the resulting stability diagrams, several cutting tests at different tool spindle speeds and depth of cuts are performed, as shown in Figure

4.9. During the test, the workpiece spindle speed was constant at $\Omega_w = 5$ rpm and the eccentricity was $e = 2$ mm. During the tests, the sound signals were acquired using G.R.A.S. 40AO microphone. Based on the sound spectrum using Fast Fourier Transformation (FFT) of the acquired sound signal and the visual inspections of the cut surface by an optical camera, the tests were categorized as stable, unstable, and marginally stable.

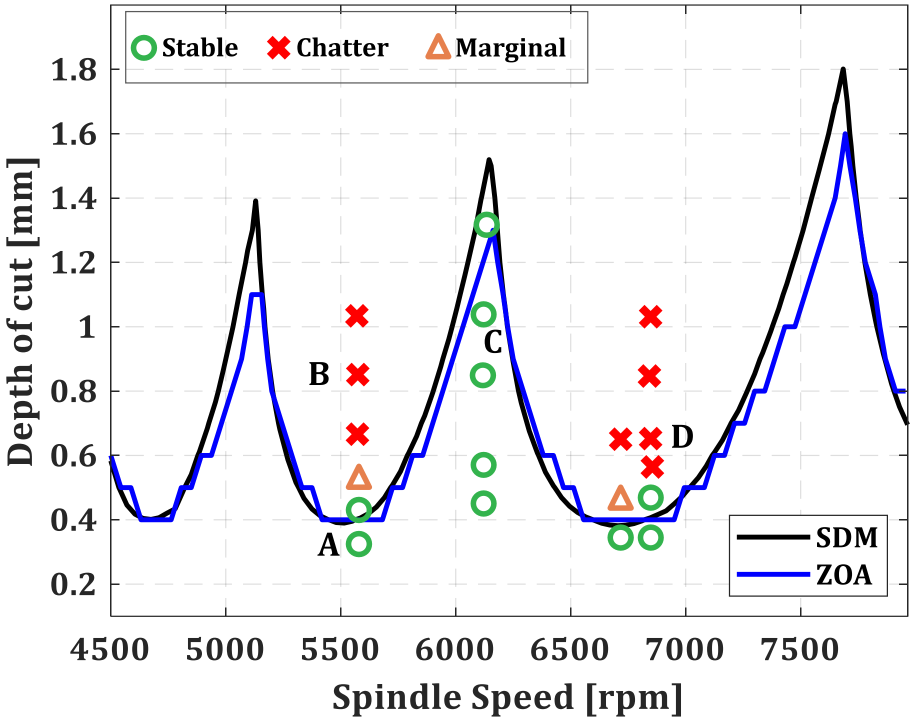

Figure 4.9: Stability diagram for Case 1 with $\Omega_w = 5\, rpm$, and $e = 2\, mm$.

If the FFT of the sound signal was dominated by the spindle or tooth passing frequency and/or its harmonics, the test was classified as a stable cut. The chatter case or unstable cut is classified when the spectrum of the sound signal is dominated by frequencies close to one of the system's natural frequencies or its harmonics other than the tooth passing and its harmonics.

The cases in which the chatter is not entirely developed and the FFT of the sound encompasses both tooth passing frequency and its harmonics as well as the chatter frequencies with relatively close amplitudes, are classified as marginally stable as transition regions from stable cut to chatter. In Figure 4.10, the tooth passing frequency is shown by ω_T, its n^{th} harmonic by ω_{Tn}, and the chatter frequency by ω_c. According to the sound spectrum and the cut surface photos given in Figure 4.10, it is evident that test A is stable since only the first harmonic of tooth passing frequency of 370 Hz (at 5600 rpm) is dominant in its sound FFT.

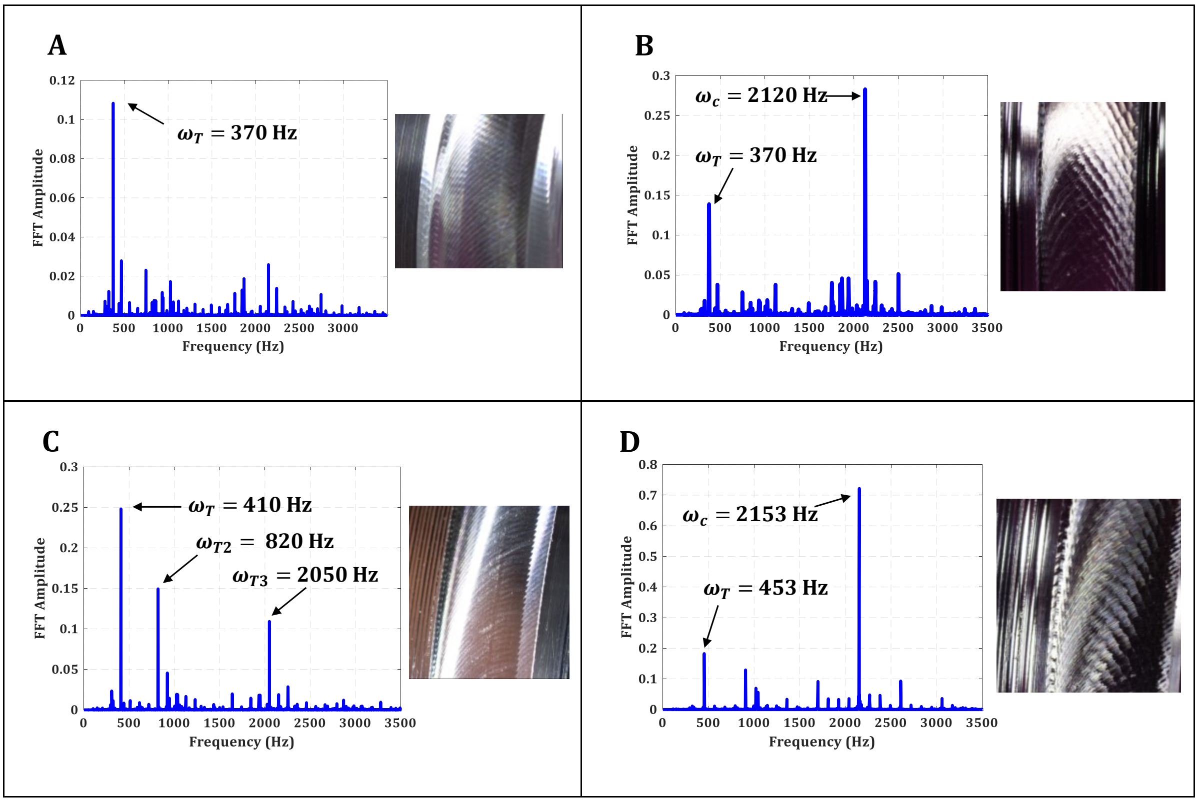

Figure 4.10: Sound spectrums and surface photos for stable and unstable points.

Similarly, test C is also classified as stable since its sound spectrum consists of the tooth passing frequency of 410 Hz (at 6150 rpm) and its next two harmonics. On the other hand, as seen in sound FFTs of tests B and D, the dominant frequency peak, i.e., the chatter frequency (ω_C), is close to the most flexible mode of the system, which is the tool's second mode in this set-up (See Figure 4.8 and Table 4.1). Furthermore, according to the surface photos, the chatter marks are visible on the machined surfaces for tests B and D. Based on these justifications, tests B and D can be classified as unstable (chatter), which is consistent with the predictions.

While the stability lobes are validated for Case 1 with an eccentricity of 2 mm, the stability lobe comparison for the maximum eccentricity for the tool with a 12 mm diameter is illustrated in Figure 4.11.

As seen in Figure 4.11, while the absolute stability limit is 0.4 mm for $e = 2$ mm, it increases by 0.1 mm as the eccentricity is increased to $e = 6$ mm. It is to be mentioned that, the validation tests were also performed for the case $e = 6$ mm.

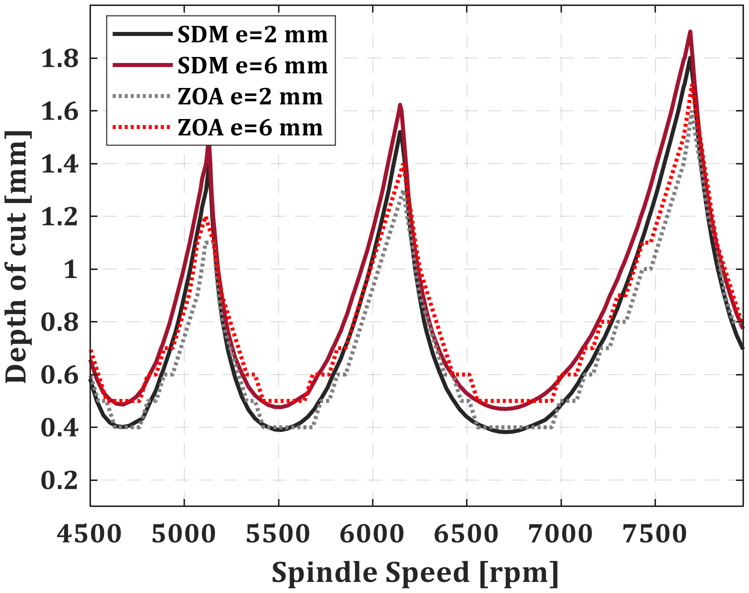

Figure 4.11: Stability comparison for conditions in Case 1 at two different eccentricities.

However, since the absolute stability limit difference is small and considering the marginally stable cases at the vicinity of absolute stability limits, the validation experiments are similar to the one given for the case of $e = 2$ mm. The negligible variation of stability lobes and absolute stability limits between these two conditions is due to the small tool diameter in this case and hence, shorter engagement of the minor edge. On the other, since the workpiece diameter to tool diameter ratio is considerably high, the uncut chip volume variation is low (See Section 3.4). It is previously mentioned that, as the diameter ratio increases, the orthogonal turn-milling mechanics and dynamics become more similar to the milling process. It is due to the fact that, as the diameter ratio is high, which means that the tool radius is much smaller than the workpiece ratio, eccentricity variation ($e_{max} \cong R_t$) does not result in considerable uncut chip geometry alteration.

- **Case 2:**

In previous cases, the employed tools were standard end mills in which the minor edge length is near the tool radius or slightly shorter than the tool radius. According to the discussions in Section 3.5 regarding the model for allowable stepover for different eccentricities given in equation (3.23) and the corresponding simulation in Figure 3.16, it is deduced that for tools with a long minor edge (such as end mills) there is no limitation for stepover at various eccentricities. In other words, the stepover can be selected as any value while eccentricity is between $m \leq e \leq R_t - m$ (See Section 3.3.2). However, turn-milling is mostly performed for roughing operations using face-milling tools where the minor edges on the inserts are smaller than the tool radius, and there is an offset distance between the insert and tool center. In this case, the proposed model in Section 3.5 and given in equation (3.23) must be used to select the proper eccentricity and stepover pair to prevent cusp formation, threaded surface, and undesired uncut chip geometry.

In this regard, the proposed stability model for orthogonal turn-milling is validated using a four-fluted face milling tool. The milling tool is Ceratizit A491.50.R.04-09 with a diameter of 50 mm, and a cutting edge angle of 90˚ (zero minor edge approach angle). The employed inserts are SNHU-type inserts with $l_t = 9.1$ mm cutting edge length and suitable coating for steel machining. The experimental setup is shown in Figure 4.12.

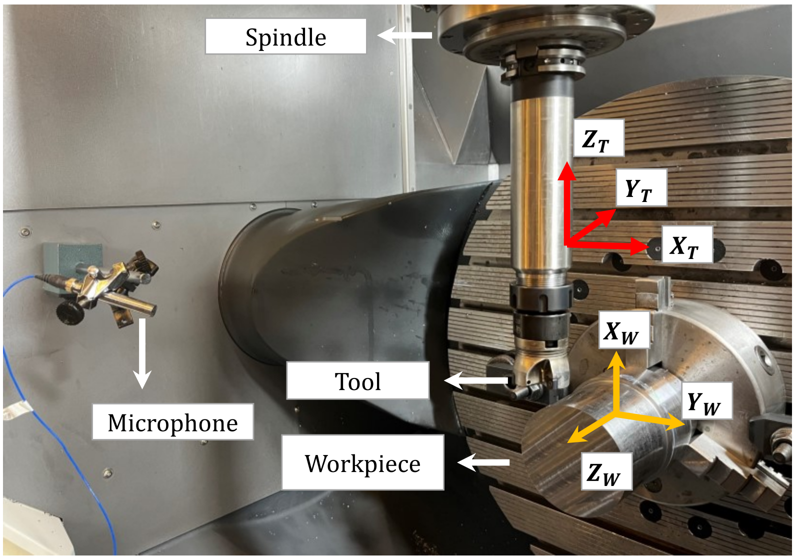

Figure 4.12: Experimental set-up for Case 2.

In Case 2, it is aimed to simulate the stability of a flexible face milling tool during orthogonal turn-milling. This situation can happen in machining a large-scale crankshaft where a longer tool holder is required for turn-milling the main journals. In this regard, a Haimer 40.326.32 tool holder with an overhang length of 200 mm is selected. The workpiece material is AISI 1045, with an initial diameter of 100 mm and 130 mm length from the clamping surface. The orthogonal data for the tool and material pair is given in Appendix A: Orthogonal databases. Due to the availability of the holder, the experiments were performed on DMG Mori DMU75 5-axis machine tool.

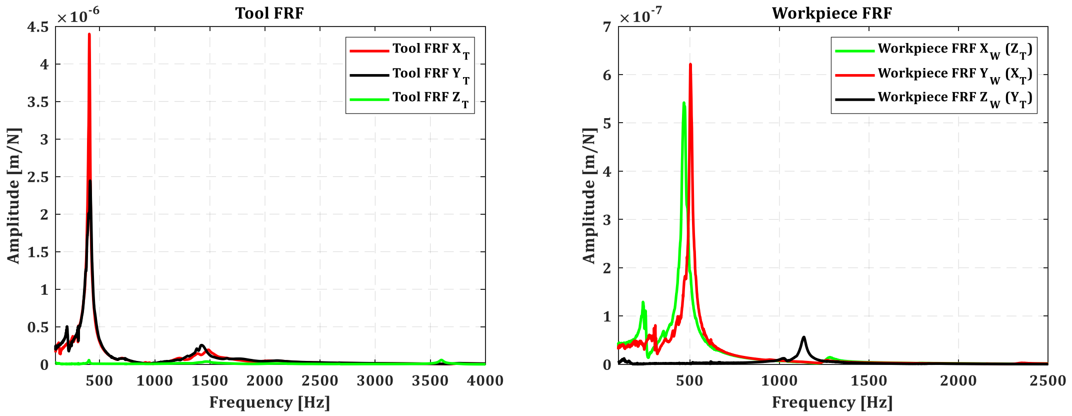

Figure 4.13: Measured FRFs of tool and workpiece employed in experiments of Case 2.

Table 4.2: Modal parameters of tool and workpiece employed in Case 2.

	Direction	Modes	Frequency (Hz)	Damping (%)	Modal Stiffness (N/m)
Tool	X_T	1	259	1.51	4.32e8
		2	404	2.19	5.56e6
		3	1488	1.38	1.32e8
	Y_T	1	297	0.12	2.46e9
		2	415	3.63	5.82e6
		3	1501	1.29	1.22e8
Workpiece	$X_w(Z_T)$	1	240	1.88	2.08e8
		2	468	2.44	3.688e7
	$Y_W(X_T)$	1	279	3.78	4.95e8
		2	505	1.85	4.82e7
	$Z_W(Y_T)$	1	1134	1.15	7.41e8

Note that, since the orthogonal turn-milling operation is performed in a 5-axis machining center and the machine coordinates are different from a mill-turn center, for compatibility with the previously-mentioned formulations, the stationary workpiece coordinate system is given, which corresponds to the MCS in mill-turn center in Figure 4.12. For this configuration, the measured FRFs and the modal parameters for the workpiece and tool are given in Figure 4.13 and Table 4.2, respectively.

According to discussions presented in Section 3.5, for a face milling tool with a minor edge length of $l_t = 9.1$ mm in which there is an offset distance between the tool center and inserts, the allowable stepover (a_w) and eccentricity must be selected using equation (3.23). The allowable stepover with respect to the eccentricity for the given tool in Case 2 is illustrated in Figure 4.14. In order to investigate the stability of the system given in Case 2, three points are selected, as shown in Figure 4.14. Points A and B are selected to demonstrate the effect of eccentricity on tool engagement and stability limit.

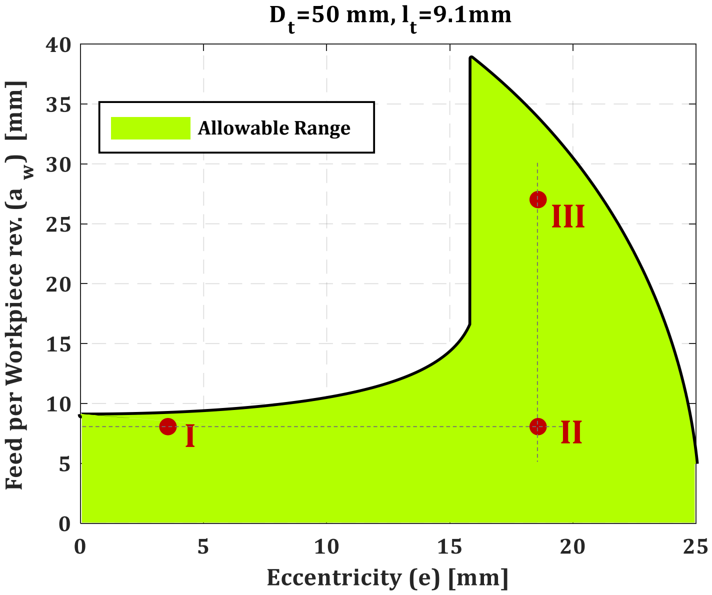

Figure 4.14: Allowable feed per workpiece revolution (stepover) with respect to eccentricity for the tool employed in Case 2.

Point C is selected to investigate the stability at higher stepover values. This is important as in orthogonal turn-milling, in order to achieve comparable MRR with the conventional turning process, higher stepover (a_w) must be selected. Both conditions I and II have the stepover value of $a_{w_{I,II}} = 8$ mm (16% of D_t). The eccentricity of condition I is $e_I = 4$ mm, and for condition II is $e_{II} = 19$ mm. The corresponding stability diagrams for both points I and II are illustrated in Figure 4.15. Based on the cutting inserts' allowable feed per tooth values, the workpiece spindle speed is selected as $\Omega_w = 5$ rpm. The stability lobes are simulated in a tool spindle speed range that fits in the allowable cutting speed range of the given inserts. Based on the simulated stability lobes, cutting tests have been performed at different tool spindle speeds and depth of cuts to validate the simulated stability diagrams at conditions I and II shown in Figure 4.14. The chatter detection was performed through sound spectrum and surface quality analyses.

As seen in Figure 4.15, the stability simulations are presented using ZOA and SD methods. According to the results, it is seen that both simulations have a good and close agreement. All the simulations were run on a PC having Intel ® Core ™ i7 4.0 GHz Central Processing Unit (CPU) and 16 GB of Random Access Memory (RAM). For both methods, the axial element height is $dz = 0.1$ mm and spindle speed interval is $ds = 5$ rpm during iteration. While the period resolution is taken as $m = 240$ in semi-discretization method, the frequency resolution in the Nyquist stability criterion approach is taken as 1 Hz. For the given conditions above, the SDM simulation takes about ~ 2 hours, and the ZOA method using the Nyquist stability criterion takes approximately ~5 minutes to achieve the simulation results illustrated in Figure 4.15.

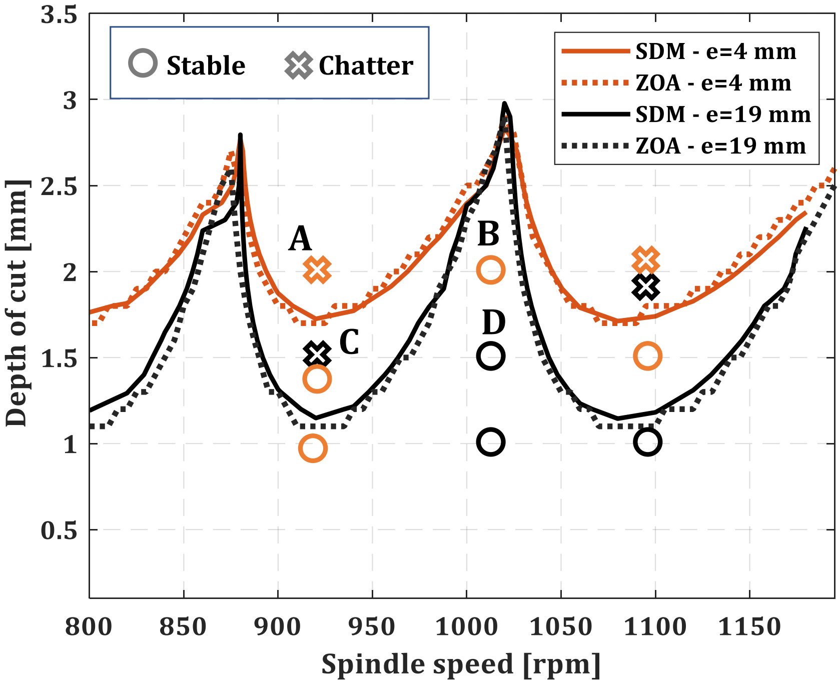

Figure 4.15: Stability diagrams and validations for Case 2 at two different eccentricities. (Conditions I and II in Figure 4.14).

Based on the simulation times and the discussions given in Section 4.3, the simulation time increases if the delay variation is high, and hence, the dimensions of matrices are larger due to the high number of unique delays. Therefore, if the spindle ratio (Ω_t/Ω_w)

is high (very low workpiece spindle speed compared to tools rotational speed), and the tool is a regular tool with equal pitch angles; the time delay varies neither by the time-varying nature of the process nor by the tool geometry, and the computational time is relatively lower. Moreover, the ZOA approach proposed in this study is more computationally efficient than the SDM.

The stable and unstable cases in Figure 4.15 are indicated as circles and cross marks, respectively, with colors corresponding to stability diagrams. According to the experimental verifications, chatter is observed at point A while the tool spindle speed is 930 rpm, at 2 mm depth of cut, and eccentricity is 4 mm. The chatter frequency of $\omega_c =$ 418 Hz is visible at vicinity of the most flexible mode of the system, which is the tool's natural frequency in this case (see Figure 4.16). The tooth passing frequency of $\omega_T = 62$ Hz and its harmonics are also visible in sound spectrum.

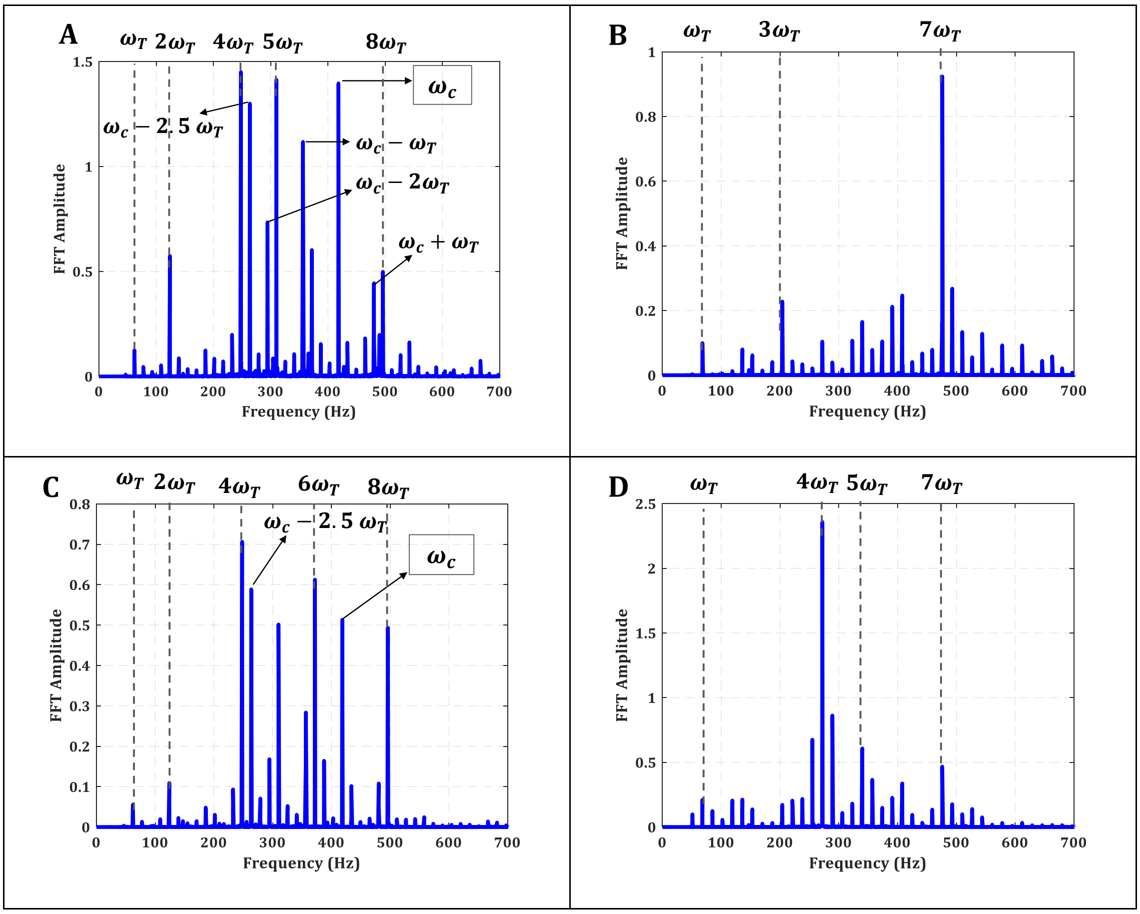

Figure 4.16: Sound Spectrum of the chatter experiments for Case 2.

However, the peak amplitude of the chatter frequency and its combination with tooth passing frequency ($\omega_c^* = \omega_c \pm k\omega_T, k = 0, 1,2, \cdots, k$) are higher than the ω_T and close to its higher harmonics (Figure 4.16A). A similar phenomenon is seen in Point C, as shown in Figure 4.16. The cutting test is performed at $\Omega_t = 930$ rpm, $a_p = 1.5$ mm with $e = 19$ mm eccentricity. As expected, the system chattered at 418 Hz, although the peak amplitudes of the tooth passing frequencies are approximately close to that of chatter frequencies. The chatter frequencies at different spindle speeds are illustrated in Figure 4.18.The sound spectrums of experiments B and D are given in Figure 4.16. The experiments were performed at $\Omega_t = 1020$ rpm at two different depths of cuts and eccentricities. Both spectrums show only tooth passing frequency with higher harmonics visible. According to the chatter frequency plot in Figure 4.18, for the current system, at a rotational speed of 1020 rpm, the corresponding frequency must be around 432 Hz, while no FFT peaks were observed at the related sound spectrums of experiments B and D around 432 Hz.

Furthermore, the chatter and stable conditions are verified by inspection of the cut surface. The surface samples for stable and unstable cases are shown in Figure 4.17.

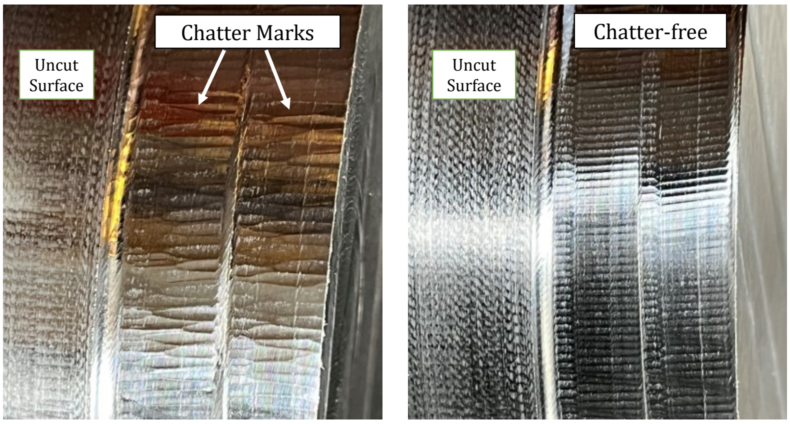

Figure 4.17: A sample surface photo for chatter (left) and chatter-free (right) conditions.

The chatter marks on the surface of the workpiece reveal that the chatter occurred at point A, as shown in Figure 4.17 left, while by increasing the spindle speed to 1020 rpm at an eccentricity of 4mm, the chatter marks disappear because of a stable cut.

The stability lobes are simulated using ZOA and SDM approaches for the eccentricity and stepover values of condition III indicated in Figure 4.14. It is seen that, similar to conventional milling operation, as the stepover (feed per workpiece revolution) increases, the absolute stability limit decreases. Despite the lower absolute stability limit of condition III, the MRR is slightly higher than both conditions I and II due to the higher stepover.

Considering the stable depth of cuts inside the stability pockets, $a_p = 2$ mm is achievable as a stable cutting while the step over is $a_w = 8$ mm (conditions I and II). On the other hand, at condition III, where the stepover is $a_w = 25$ mm, the maximum stable depth of cut is 0.8 mm.

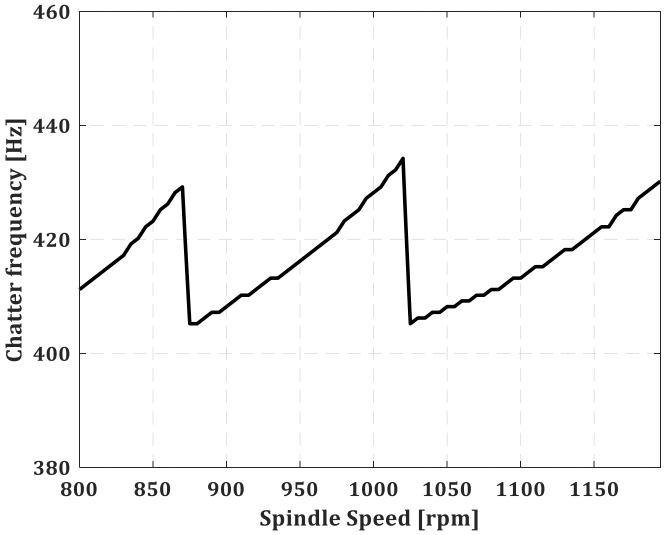

Figure 4.18. Chatter frequencies at different spindle speeds for Case 2.

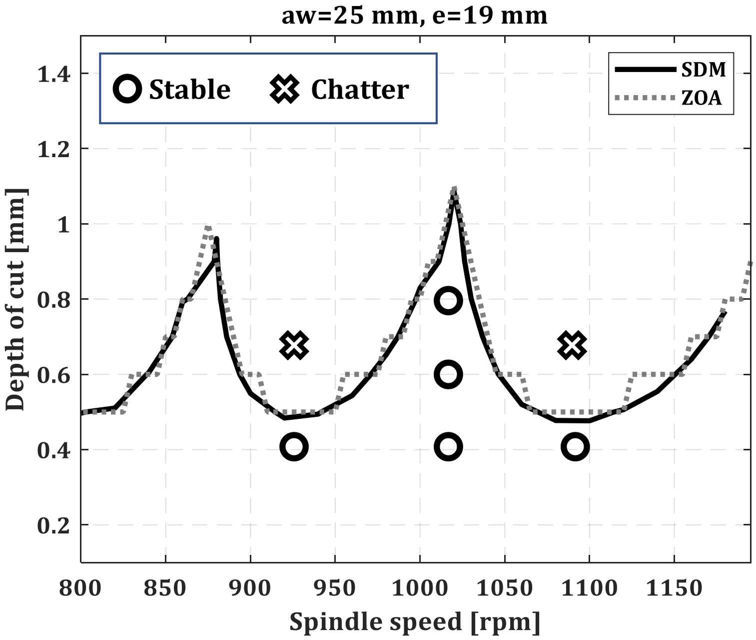

Figure 4.19: Stability lobes and validations for the system in Case 2, condition III in Figure 4.14.

However, by comparing the MRR of I, II, and III, it is deduced that due to the higher stepover of condition III, its MRR is 25% higher than conditions I and II. As a result, it is favorable to select condition III in orthogonal turn-milling in terms of productivity and machining cost.

4.7. Effect of Process Parameters on Stability of Orthogonal Turn-milling

Due to the simultaneous rotation of tool and workpiece in orthogonal turn-milling, which leads to simultaneous engagement of both minor and side cutting edges of the milling tool, additional parameters compared to conventional milling and turning are included in the process kinematics, mechanics, and dynamics. The effect and significance of these additional parameters are discussed in Section3 in terms of surface quality and cutting forces. However, these parameters are needed to be analyzed from process dynamics and chatter stability points of view. In the previous section, the effect of eccentricity is shown through simulations and validated by cutting experiments. Although some conclusions regarding the effect of eccentricity and stepover on process stability can be drawn by comparing the stability lobes in points I, II, and III shown in Figure 4.14, it is difficult to predict the stability behavior of the system at each combination of e and a_w. This is due to the fact that the stability of orthogonal turn-milling mainly depends on the chip load and the amount of force produced by the engagement. The chip volume and the CWE engagement do not follow a linear relationship based on eccentricity or engagement length of the minor edge. The CWE and uncut chip geometry show different results at a particular eccentricity but different tool and workpiece diameter combinations.

It is believed that at the process planning stage, based on the dynamics properties and the allowable ranges of eccentricity and stepover, the absolute stability limit of the system must be evaluated, as shown in Figure 4.20. Note that, Figure 4.20 is generated at a constant spindle speed of $\Omega_t = 930$ rpm to obtain the absolute stability limit of the system at the given speed. Therefore, based on the cutting strategy, one can select the proper eccentricity and stepover according to Figure 4.20, aiming stable depth of cut with cusp-free surface quality. Furthermore, after selecting the chatter-free condition, the axial forces during stable cutting must be selected and considered using the graph in Figure 3.23.

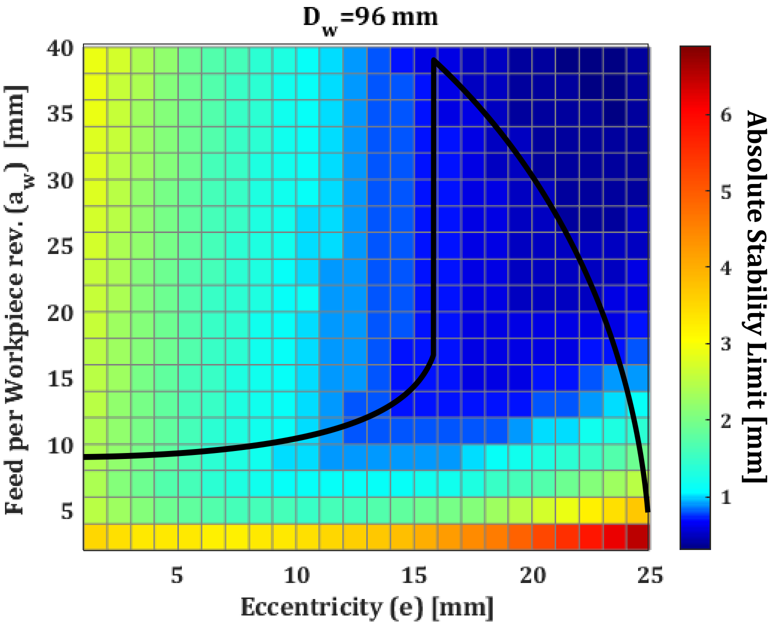

Figure 4.20: Absolute stability limit map for Case 2 at the allowable range of eccentricity and stepover.

Another important parameter that affects the orthogonal turn-milling process stability is the workpiece rotational speed. As discussed in Section 4.3 and the simulations given in Figure 4.3, by increasing the rotational speed of the workpiece (decreasing the ratio of $r_s = \Omega_t/\Omega_w$) the phase shift between the surface marks left by two subsequent teeth on current and previous modulations increases. This phenomenon causes the time-varying delay in orthogonal turn-milling, affecting stability behavior. Due to varying time delays within the engagement boundaries and distributed delays along the tool axis within the CWE, the semi-discretization method can capture the impact of variable delays on process stability [40,65].

As seen in Figure 4.21, increasing the workpiece rotational speed shifts the stability lobe toward lower tool speeds due to the alteration in time delay [43,46].

It is known that a higher rotational speed of the workpiece increases the MRR by increasing the linear feed rate. At the same time, the feed per tooth value both at side and minor cutting edges will be increased drastically, which must be considered in terms of cutting tool or insert feasibility at the resulted feed values. In addition, it is seen that the stability lobes are also shifted toward lower speeds which may cause unstable cutting without considering the effect of spindle speed [43].

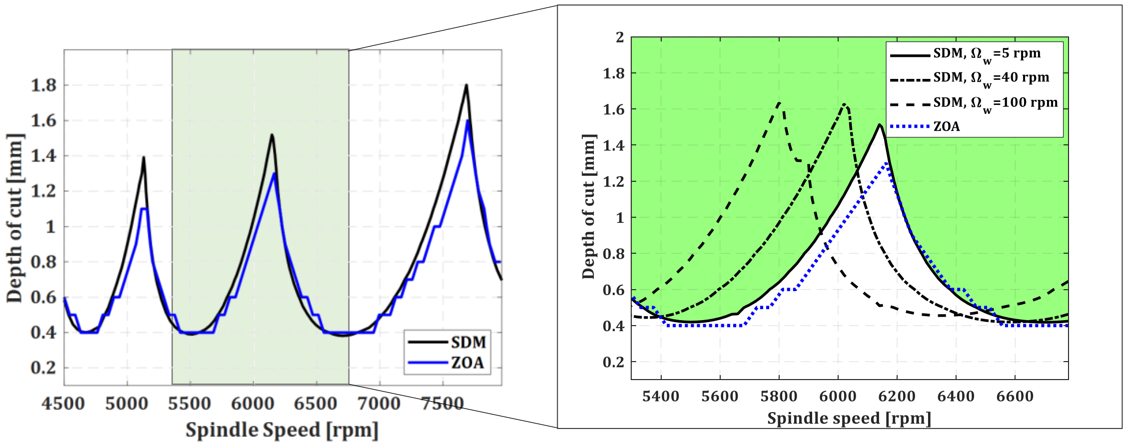

Figure 4.21: Effect of delay variation caused by workpiece rotational speed on stability lobes.

4.8. Summary

In this chapter dynamic and stability model of orthogonal turn-milling process is presented. The dynamic chip thickness and dynamic cutting forces are modeled as a function of vibrations between the tool and workpiece imposed on both side and minor edges of the tool in three directions. The time delay which alters the regeneration mechanism is modeled based on the kinematics of the process. It is shown that, due to the kinematics of the orthogonal turn-milling process, the tool experiences different time delays along its axis. Furthermore, the workpiece rotational speed alters the regenerative dynamic chip formation mechanism by altering the resulted time delay. Based on the obtained varying time delay, the stability of orthogonal turn-milling process is solved in discrete-time, and frequency domains using semi-discretization and zero-order approximation approaches, respectively. The proposed stability solutions are validated by experiments using standard end mills and face milling tools. The simulations discuss and represent the effects of different parameters such as workpiece rotational speed and eccentricity, considering their feasibility.

5. IMPLEMENTATION OF SPECIAL TOOLS IN TURN-MILLING

5.1. Overview

The previous sections present detailed predictive models for the mechanics and dynamics of the orthogonal turn-milling process using standard milling tools. However, special (irregular) end mills with irregular pitch and/or helix angles have been a focus of interest both in industry and academia for decades. It has been previously proved that milling tools with nonconstant pitch and/or helix angles can suppress chatter during machining and enhance productivity, especially when machining hard-to-cut materials [61,73,127]. In addition to variable-pitch and variable-helix tools with straight cutting edge geometry, serrated and crest-cut tools are also categorized as special end mills. Unlike standard end mills, special geometries (serration geometries or wavy shapes) along the cutting edges of serrated and crest-cut tools result in significant enhancements in process mechanics and stability [77,120]. Different types of special tools are shown in

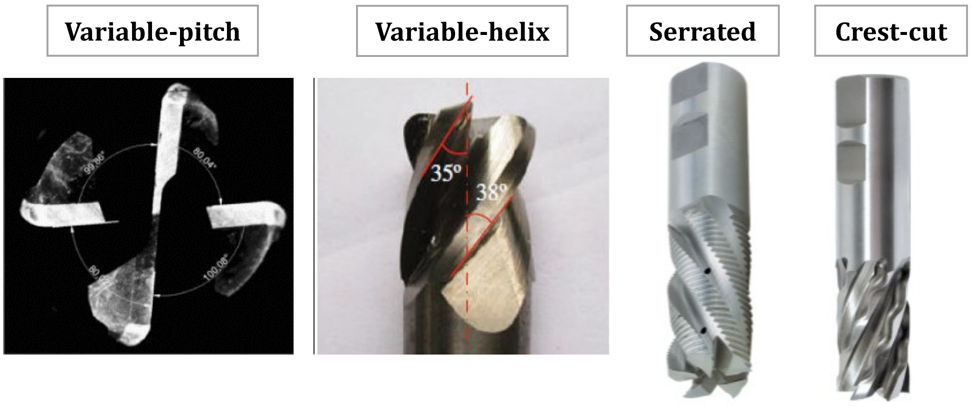

Figure 5.1. Different types of special tools.

In this regard, the serrated and crest-cut tools are implemented in orthogonal turn-milling operations to investigate their effect on cutting forces and process stability. Firstly, the mechanics of both tools during orthogonal turn-milling is discussed and validated through experiments. Next, the stability of crest-cut tools in orthogonal turn-milling is discussed based on the previous findings.

5.2. Mechanics of Special Tools in Turn-milling

5.2.1. Serrated Tools

Due to the existence of serrations, the chip load distribution along the engagement varies in serrated tools leading to higher stability and lower cutting forces in roughing operations. The performance of a serrated tool depends on the serrations' geometry, the serration profile's amplitude, and phase shift between the profiles [65,120]. Optimized geometry of serration profiles can lead to higher stability limits due to the disturbance in the regenerative mechanism provided by distributed varying time delays, irregular chip thicknesses, and missed-cut effects [68,123]. As a result, it is important to use serrated tools in turn-milling operations to achieve higher performance. The proposed uncut chip model for orthogonal turn-milling can be adaptable for special geometry end mills such as serrated tools. This section presents the uncut chip thickness of serrated tools and the kinematics of orthogonal turn-milling. For serrated cylindrical end mills, the angular position of axial element i of tooth j is defined as:

$$\phi_{ij} = p_t(j) - \frac{\tan(\gamma_j)}{R_t} z + \phi_j \tag{5.1}$$

where ϕ_j is the angular increment of reference tooth j, γ_j is the helix angle of the tooth j^{th}. $p_t(j)$ is the angular position of the tooth j with respect to the first edge, provided that the angular position of the first tooth as the reference tooth is assumed to be zero and can be calculated by;

$$p_t(j) = \sum_{u=1}^{j-1} p_u \tag{5.2}$$

where p_u is the pitch angle of the tooth u. It is obvious that the variable helix and variable pitch tools can also be modeled using a similar approach. In order to determine the uncut chip area, the tool-workpiece interference areas for each axial element are calculated based on the model proposed by Tehranizadeh et al. [68]. In the elemental chip area calculation of serrated tools in turn-milling operation, it is considered that the differential areas are not intersecting, and the chip area direction makes the chip thickness perpendicular to the element's edge.

While integrating the serrated tools chip geometry model, due to the workpiece's rotation, the workpiece's surface shape, which is generated by the previous teeth on the side cutting edge of the tool, is affected by the feed per tooth at each axial element. In order to calculate the uncut chip area, the workpiece surface must be calculated for each axial element (i) and angular position of tooth j as follows;

$$W(i, j, \phi_j) = \max\left\{\begin{matrix} 0 \\ \min\left\{R_{im} + \frac{2(k\pi n_w)}{n_t N \cos(\beta)\cos(\theta_x)} \cdot \left(R_w - a_p + i.dz\right)\right\}\end{matrix}\right\} \tag{5.3}$$

$$m = \begin{Bmatrix} k - j & if\ k - j > 0 \\ k - j + M & if\ k - j \le 0 \end{Bmatrix} \therefore k = 1,2, \dots, N$$

where R_{im} is the local radius of the element which is different for each axial element due to the wavy flank face of the serrated tools. The local radius definition depends on the serration wave type, such as sinusoidal, circular, or trapezoidal, as shown in Figure 5.2 [68]. The geometrical parameters of each serration type are specific, and hence, the geometrical relations of the local radius R_{im} (which is a tool geometry property) is specific for each serration type and can be found in [68] in detail.

The uncut chip thickness (the area between the tool and workpiece) for each axial element at each angular position depends on the serration type (R_{ij} is different for each serration type) is calculated by;

$$h(i, j, \phi_{ij}) = R_{ij} - W(i, j, \phi_{ij}) \tag{5.4}$$

Further geometrical operations are performed in order to avoid the intersection of the chip areas as defined by Tehranizadeh et al. [68]. The evaluated uncut chip thickness in equation (5.4) is substituted with equation (3.26) for cutting force calculations. The engagement of axial elements is updated at each angular position according to the engagement boundary given in equation (3.11).

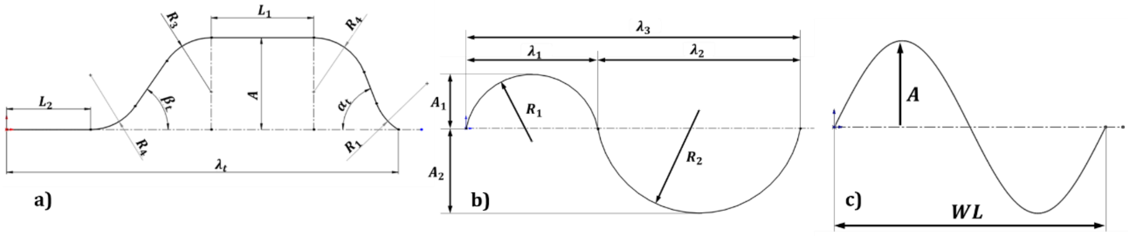

Figure 5.2: Parameter definition for different serration type; a) trapezoidal, b) circular, c) sinusoidal

Note that calculation of the instantaneous depth of cut and entry and exit angle of each axial element on serrated tools in turn-milling is performed by substituting the equation (5.1) into equations (3.12) and (3.13), respectively. Furthermore, the transformation of the elemental forces in tra coordinate system into TCS are performed according to the axial and angular immersion angles of the serrated tool, which the formulations are adopted from [64,68]. Finally, the cutting forces resulting from the tool's serrated side edge and the tool's minor edge are summed according to the mechanics of turn-milling given in Section 3.

The proposed force model of the orthogonal turn-milling process has been verified in this section. The cutting experiments are on Mori Seiki NTX2000 CNC mill-turn. The cutting force verifications are carried out on aluminum alloy Al7075-T6 cylindrical workpiece and two types of solid WC end mills; standard and serrated end mills. The tool parameters are given in Table 5.1. The schematic representation of the parameters for trapezoidal serration waves is given in Figure 5.2(a). The cutting forces are measured using Kistler 9123C rotary dynamometer, as shown in Figure 5.3.

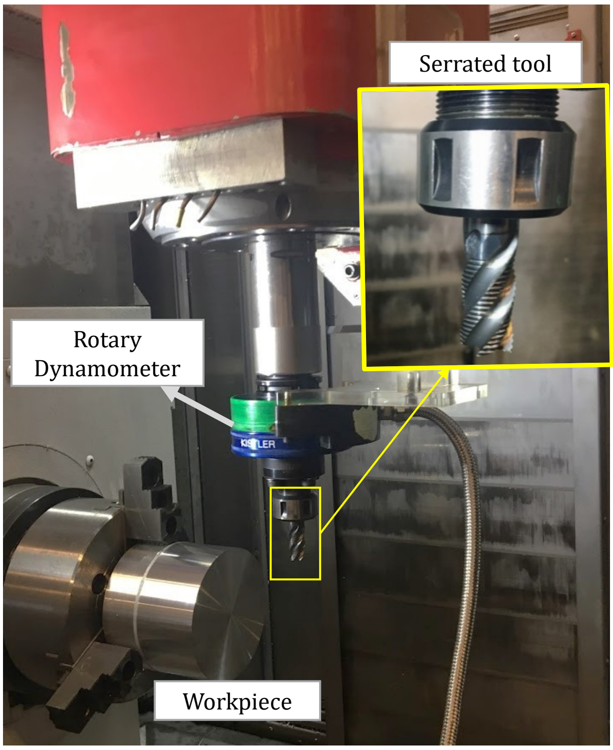

Figure 5.3: Cutting force measurement set-up for orthogonal turn-milling using serrated tools.

Table 5.1: Serrated tool geometrical parameters

Tool Type	Diameter (mm)	Cutting angles of side edge	Cutting angles of minor edge	Serration type	Serration parameters (mm)
Standard	16	$\alpha_s = 11°$ $\gamma_s = 38°$	$\alpha_m = 3°$ $\gamma_m = 0$	-	-
Serrated	16	$\alpha_s = 5°$ $\gamma_s = 38°$	$\alpha_m = 5°$ $\gamma_m = 0$	Trapezoidal	L_1=0.7, L_2=0.3, A=0.5, $\alpha_t = \beta_t = 30°$, $R_1 = R_2 = R_3 = R_4$ =0.3

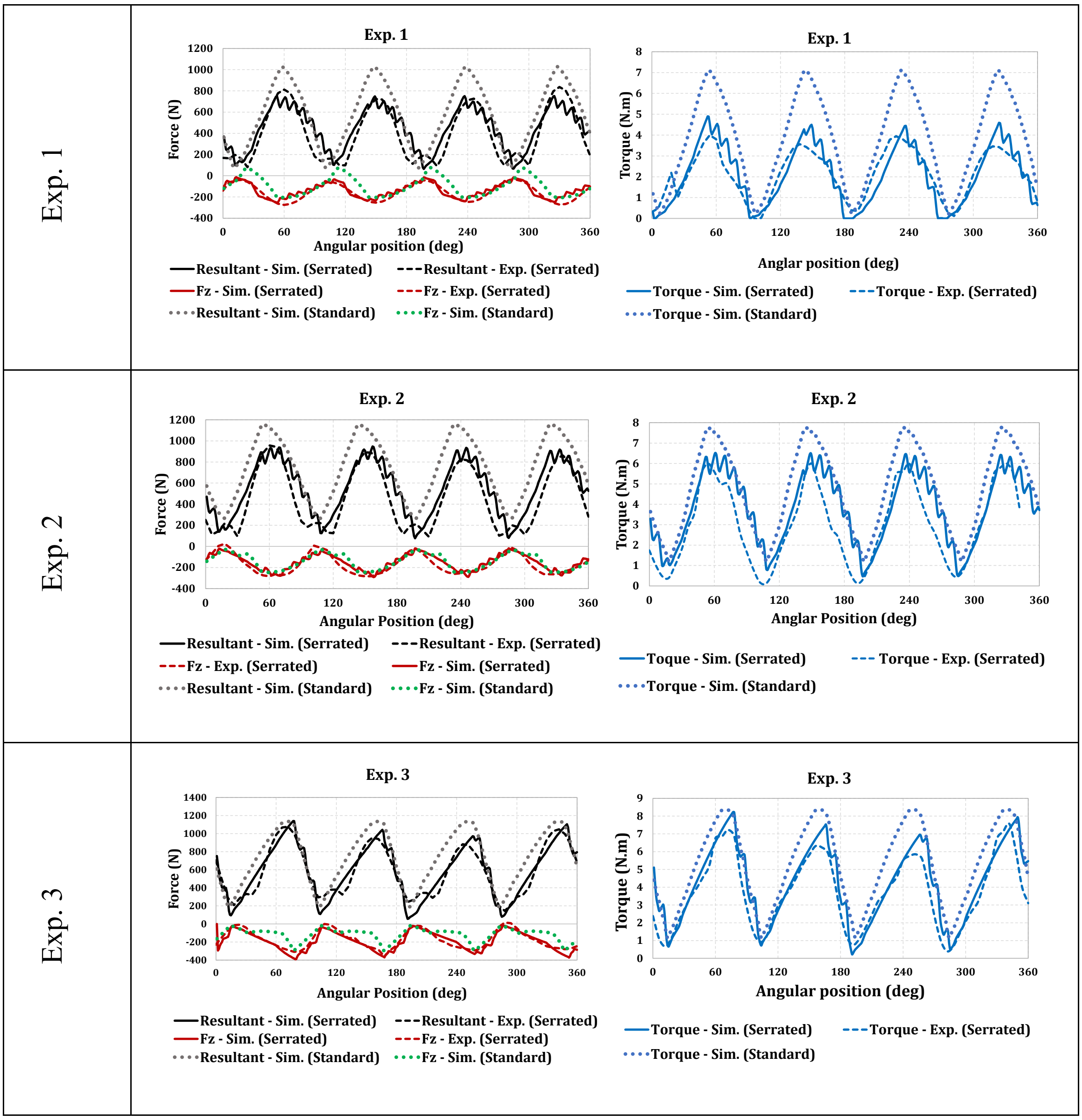

Figure 5.4: Verification of cutting forces in turn-milling with standard tool for the given conditions in Table 5.2.

Table 5.2: Cutting conditions for cutting force measurement experiments of serrated tool in turn-milling.

Exp.	Ω_t (rpm)	Ω_w (rpm)	e (mm)	f_t $mm/(rev.tooth)$	a_w (mm/rev)	a_p (mm)	F $(^{mm}/_{min})$	D_{w1} (mm)
1	3979	8	2	0.14	3	10	24	102
2	3979	8	4	0.17	3	10	24	122
3	3979	8	4	0.19	6	5	48	132

The cutting force confirmation for serrated end mills in orthogonal turn-milling is given in Figure 5.4. The cutting parameters for the experiments and simulations are listed in Table 5.2. The cutting force simulations with the same cutting parameters for standard end mills with similar geometrical parameters (See Table 5.1) are presented in Figure 5.4.

It is shown that the proposed model can predict the cutting forces and torque values for serrated tools in orthogonal turn-milling operation in good agreement. The difference between the simulation and experimental results for axial forces is negligible. It is evident that using the serrated end mills decreases the resultant force and torque due to the reduction in effective contact length along with the cutting depth [64]. According to the results in Figure 5.4, the serration geometry of the tools affected the resultant forces and torque more than the axial forces. As a result, the application of serrated tools will increase the stability limits significantly not only due to the decrease in the cutting forces but also by disturbing the regeneration in dynamic chip formation, leading to a substantial increase in MRR during roughing with turn-milling [64,68].

5.2.2. Crest-cut tools

Crest-cut end mills have sinusoidal wavy rake faces leading to varying local helix angles along the cutting edges. In addition, the sinusoidal wave on each tooth has a phase shift with the subsequent tooth’s wave, resulting in a varying local pitch angle along the cutting edges between consecutive teeth (Figure 5.5c). Crest-cut tools are shown in Figure 5.5.

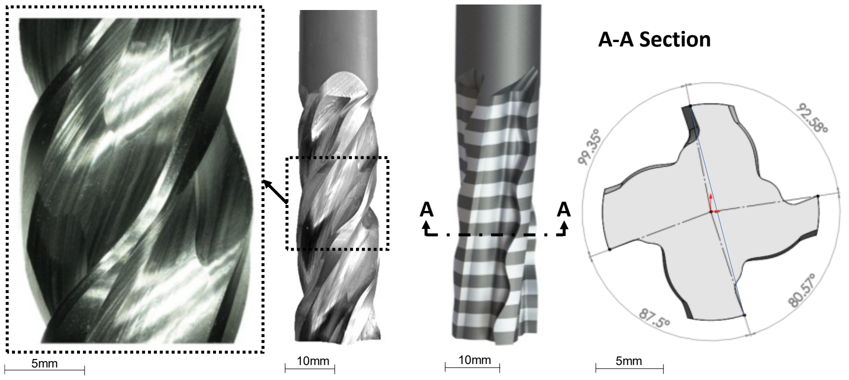

(a) (b) (c)

Figure 5.5: Crest-cut tools, (a) detailed view of wavy edges, (b) Discretized representation of tool along its axis, (c) Representation of varying pitch angles on a sample axial element [77].

In order to calculate the cutting forces using crest-cut end mills, the tool geometry must be primarily modeled to obtain the uncut chip thickness. For this purpose, similar to regular tools, the crest-cut tools are discretized into m number of disc elements, as shown in Figure 5.5b. This is required since each tooth's local pitch, helix, and oblique angle on each disc element is different. The detailed and profound definition of the tool geometry and local helix angles are defined by Tehranizadeh et al. [77]. In this study, the geometric formulations of the crest-cut tools are not included and adopted from [77]. Using the geometrical model of crest-cut tools, the angular position of each point $\left(\bar{\varphi}_{n,j}\right)$ in polar coordinate can be obtained. n refers to number of an element along tools axis on j^{th} tooth. Therefore, the local pitch angle at n^{th} disc element between the j^{th} and $(j+1)^{th}$ teeth is calculated by;

$$\Delta\bar{\varphi}_j(z) = \bar{\varphi}_{n,j+1} - \bar{\varphi}_{n,j} \tag{5.5}$$

Note that some parameters may be represented with different notations in order to have consistency with the previous sections.

The local pitch variation along the tool axis for standard, variable-pitch, and crest-cut tools is depicted in Figure 5.6b. The unfolded view of the cutting edges in Figure 5.6a shows the local pitch angle of two points at an elevation z_n on j^{th} and $(j+1)^{th}$ teeth. It is seen that, because of the wavy edge shape, the local pitch angles on the crest-cut tool are too different from the ones on standard or even variable-pitch tools. In Figure 5.6, A_j stands for wave amplitude, λ_j for wavelength, and γ_j for helix angle on tooth j.

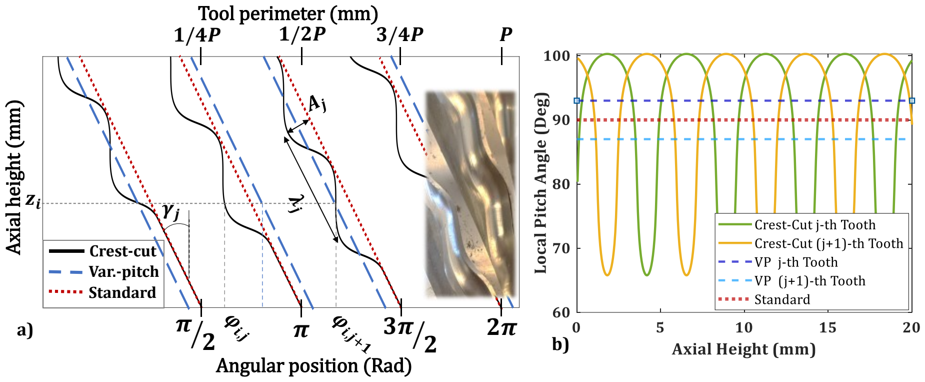

Figure 5.6: Representation of pitch variation for three different tool types; a) Unfolded comparison of chip variation and cutting edges for three tool types, b) representation of local pitch variation of each tool along its axis [128].

Considering that the angular position of the tool within a full revolution is ϕ, the angular position of element n on j^{th} tooth can be defined as;

$$\phi_{n,j} = \phi + \bar{\varphi}_{n,j} \tag{5.6}$$

The first step of adopting crest-cut tools in orthogonal turn-milling is the calculation of uncut chip thickness. Based on the uncut chip thickness definition in orthogonal turn-milling given in Section3.3 and the uncut chip thickness definitions explained in [77], the feed per tooth value for crest-cut tools during orthogonal turn-milling is achieved as;

$$f_{t_j}(z) = \frac{(\bar{\varphi}_{n,j+1} - \bar{\varphi}_{n,j})}{\Omega_t \cos(\theta_x)\cos(\beta)} \, \Omega_w \big(R_w - a_p + a(z)\big) \tag{5.7}$$

where $a(z)$ is the elevation of disc n from the tooltip $(a(z) = n * dz)$. $f_{n,j}$ represent the amount of feed that each disc element on tooth j travels during a tooth passing period. It is to be noted that the effect of rotational speed ratio on feed per tooth value is also true for crest-cut tools. However, contrary to standard tools, the amount of increase of feed per tooth for each tooth is different because of varying local pitch angles between consecutive teeth. According to the explanations given in Section 3.2, by transforming the feed per tooth vector to $\mathcal{FCN}$ coordinate system, the uncut chip thickness at each angular position of the tool can be calculated by;

$$h_{n,j}(\phi_{n,j}) = f_{t_j}(z).\cos\beta.\sin(\phi_{n,j}) \tag{5.8}$$

Note that, to find the immersion boundaries using crest-cut tools, the formulation given in Section 3.3.1 is sufficient. These formulations provide the overall boundaries of the engagement of the workpiece and the tool. However, due to the wavy edge shape on crest-cut tools and varying local helix and pitch angles, the engagement of each disc element will be different. This phenomenon is controlled by the binary function $g(\phi_{n,j})$ which is equal to 1 when the disc element n on j^{th} tooth is in cut $(\phi_{st} \leq \phi_{n,j} \leq \phi_{ex})$, and is equal to 0 otherwise. The instantaneous depth of cut at each angular position can be calculated by substituting the angular position of the first disc element on each tooth (equation (5.6)) into equation (3.11) ;

$$a_i(\phi_{0,j}) = \sqrt{R_w^2 - \left(R_t \sin(\phi_{0,j}) - e\right)^2} - \left(Rw - a_p\right) \tag{5.9}$$

Note that the mechanics of minor edges in crest-cut tools are identical to that of standard tools. However, in order to achieve better surface quality, the approach angles must be zero $(\alpha_m = 0)$. The cutting force calculations are performed using the formulations given in Section 3.6. The elemental forces for each disc element at each tooth are calculated according to its varying chip load and engagement. Then the exerted forces on the side edge and minor edge are summed to obtain the total cutting forces at each angular position according to its engagement boundaries.

The proposed cutting force model for crest-cut tool implementation is validated through experiments. The experiments were conducted on Mori Seiki NTX 2000 mill-turn machining center. The tool employed in experiments is an uncoated WC crest-cut end mill manufactured by Karcan® cutting tool company. The geometric parameters of the crest-cut tool are listed in Table 5.3. The wave shapes are identical at every tooth with a $\frac{\pi}{2}\ rad$ shift, successively.

Table 5.3: Parameters of the crest-cut tool used in experiments.

Tool Dia. (D_t) (mm)	No. of flutes (N)	Nominal helix angle (γ_j) (deg)	Pitch angle distribution (deg)	Wave Shape (mm)
12	4	38	83-97-83-97	$\lambda_j = 0.25, A_j = 4$

The workpiece material is Al7075-T6 alloy with a 90 mm diameter. The cutting force simulations and experiments are performed at the conditions given in Table 5.4. The resulted cutting forces during experiments were measured using Kistler 9123C rotary dynamometer. The orthogonal database for the tool-workpiece pair used in orthogonal-to-oblique transformation is given in Appendix A: Orthogonal databases. Note that, since the local helix (oblique) angle of each element varies along the tool axis, the cutting force coefficients are updated for each axial disc element based on the particular oblique angle and instantaneous feed per tooth during force predictions.

Table 5.4: Cutting parameters for cutting force experiments in turn-milling with crest-cut tools.

Exp.	Ω_t (rpm)	Ω_w (rpm)	e (mm)	f_t $mm/(rev.tooth)$	a_w (mm/rev)	a_p (mm)	F $(^{mm}/_{min})$	D_{w1} (mm)
1	4770	9	4	0.1	3	10	27	90
2	4770	15	4	0.17	3	10	45	90
3	4770	9	4	0.1	6	10	54	90
4	4770	9	2	0.1	1.5	10	13.5	90

As seen in Figure 5.7, there is an acceptable agreement between the force predictions and measurements. According to the simulation and measurement results, it is seen that, unlike conventional mill tools, the resulted forces from crest-cut tools are distorted due to the presence of wave edges on the side cutting edges of the tool. The phase shift between the waves on each edge creates a different chip thickness for each axial element on each tool. Moreover, each axial element on each tooth has particular immersion angles (entry and exit angles). Therefore, unlike standard tools, the resulted cutting forces are non-periodic in all feed, cross-feed, and axial directions. This phenomenon is also confirmed by Tehranizadeh et al. [77] during three-axis milling by crest-cut tools.

In addition, by comparing the cutting force results for crest-cut tools in Figure 5.7, for serrated tools in Figure 5.4, and standard end mills in Figure 3.21, it is deduced that crest-cut tools produce smoother cutting forces in the axial direction (F_z). This phenomenon can decrease the harmonic excitations in axial direction where the workpiece is flexible in the axial direction of the tool.

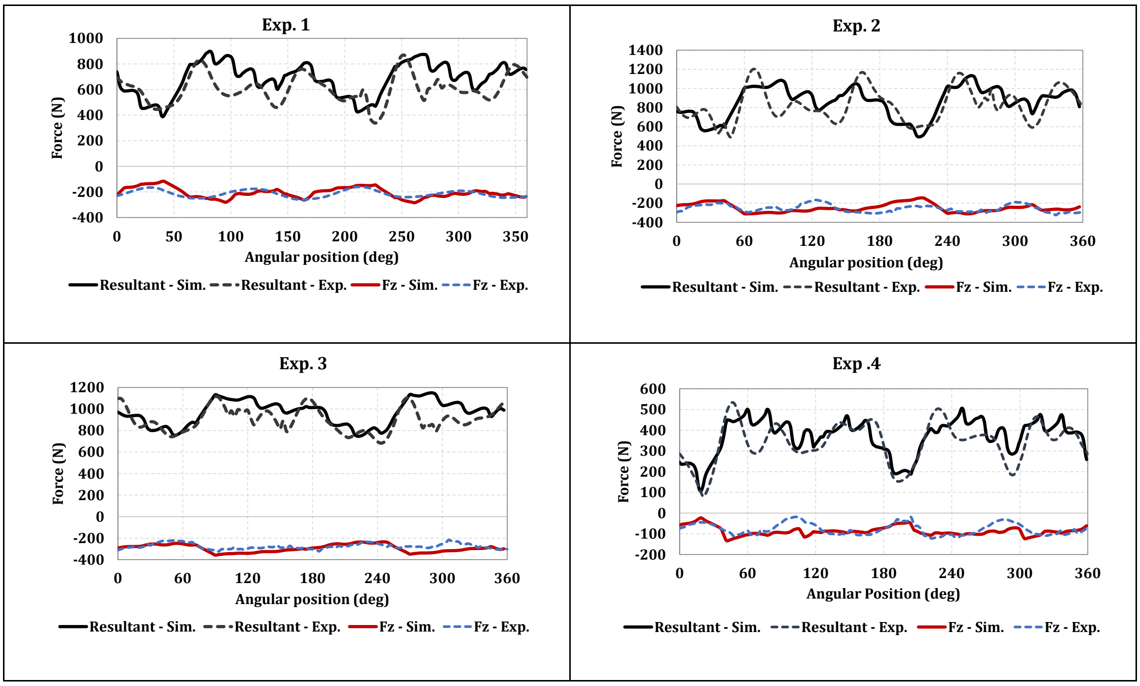

Figure 5.7: Verification of cutting forces in turn-milling with crest-cut tool for the given conditions Table 5.4.

5.3. Stability of Special Tools in Turn-milling

After validating the predicted cutting forces generated by crest-cut tools in orthogonal turn-milling operation in Section 5.2, the stability model of the process can be developed. While implementing the special tools like serrated, crest-cut, etc., the dynamics of the process do not change, and the model given in Section 4.4 governs. Due to the wavy shape on the cutting edges, the engagement boundaries along the tool axis change for each tooth by employing crest-cut tools. This leads to unequal chip thickness distribution along the cutting edges for each tooth. In addition, the variation in engagement boundaries of teeth at a specific height causes a varying delay between the subsequent teeth. This delay variation is also distributed along the tool axis due to the phase shift between the waves on each tooth [74,77]. The variation in engagement boundaries is discussed in Section 5.2.2. As a result, in order to implement the crest-cut tool in the orthogonal turn-milling model, it needs to calculate the varying and distributed time delay caused by both tool geometry and process kinematics. Next, the stability of the crest-cut tools in orthogonal turn-milling is solved in discrete-time and frequency domains, which are described in Sections 4.5.1 and 4.5.2, respectively.

5.3.1. Calculation of time delay in crest-cut tools used in orthogonal turn-milling

Given that, the local pitch angle varies for each disc element along the tool axis between the consecutive teeth, the constant tooth passing period governing in standard tools does not hold for every element in crest-cut tools. Therefore, the period between the engagement of j^{th} and $(j+1)^{th}$ teeth on n^{th} element $(z = n.dz)$, depends on the local pitch angle between these teeth $\left(\Delta\bar{\varphi}_j(z)\right)$ and rotational speed of tool (Ω_t), which can be calculated as;

$$\tau_0(n,j) = \frac{\Delta\bar{\varphi}_j(z)}{\Omega_t} \tag{5.10}$$

In order to add the effect of rotation of the workpiece and calculate the varying time delay in orthogonal turn-milling using crest-cut tools, equations (5.10) and (5.5) must be combined with (4.17) as given below;

$$\tau_{i,j}(z) = \tau_0(n,j) - \frac{\alpha_i}{\Omega_t} = \frac{\Delta\bar{\varphi}_j(z)}{\Omega_t} - \frac{\tau f_{t_j}(z)\cos(\phi_i+\theta_x)}{\tau_0(n,j)R_t\Omega_t} \tag{5.11}$$

By substituting equation (5.7) into equation (5.12), the varying time delay of n^{th} element at height $(z = n.z)$ on j^{th} tooth of a crest-cut tool used turn-milling operation can be obtained as follows;

$$\tau_{i,j}(z) = \frac{\Delta\bar{\varphi}_j(z)R_t\cos\theta_x}{\Omega_t R_t \cos\theta_x + \Omega_w\left(R_w - a_p + a(z)\right)\cos(\theta_x+\phi_i)} \tag{5.12}$$

As discussed in Section 4.3, the workpiece rotation will decrease the delay, particularly for each element along the tool axis. As a result, the effect of different parameters such as speed and diameter ratios of tool and workpiece on varying delay in crest-cut tools are similar to that of the standard tool, as shown in Figure 4.3.

5.3.2. Stability solutions

Having updated the cutter-workpiece engagement boundaries (entry and exit angles, instantaneous depth of cut, and the varying time delay for crest-cut tools in turn-milling, one can solve the process stability using the explanations and models given in Section 4. One of the solution methods for this problem is the semi-discrete time marching method which is described in Section 4.5.1. The stability lobes can be obtained by substituting the delay formulation obtained for crest-cut tools in equation (5.12) in SDM model in Section 4.5.1. However, as discussed previously, semi-discrete time marching methods are computationally costly and time-consuming. As an alternative to reduce the computational cost, the ZOA method in the frequency domain is employed to simulate the stability lobes for orthogonal turn-milling operation using crest-cut tools.

In orthogonal turn-milling using crest-cut tools, the time delay is different for each axial disc element on each tooth caused by varying local pitch angles. For instance, for a four-fluted crest cut tool with 12 mm diameter, a nominal helix angle of 38˚, the nominal pitch angle of 90˚, and wave properties of $\lambda_j = 6\text{mm}$, $A_j = 1$ mm, the local pitch variation along the tool axis for each tooth is illustrated in Figure 5.8. For a disc element at level $z = 2$ mm, the pitch angle distribution for each tooth is $\Delta\bar{\varphi}_1 = 100°$, $\Delta\bar{\varphi}_2 = 94.5°$, $\Delta\bar{\varphi}_3 = 66.8°$, $\Delta\bar{\varphi}_4 = 98.7°$. An illustration of a discrete element and local pitch angle distribution is given in Figure 5.5.

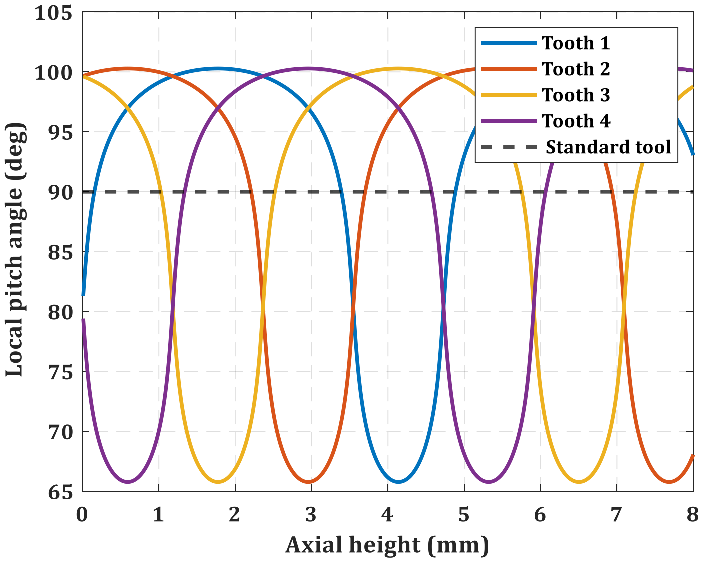

Figure 5.8: Local pitch angle variation for each tooth on crest-cut tool ($\lambda_j = 6\text{mm}$, $A_j = 1$ mm) vs. the standard tool.

As a result, at a constant rotational speed, the time delay of each tooth of this disc element is different and proportional to the corresponding pitch angle. Moreover, according to equation (5.12), this delay varies at each instantaneous angular position. The varying time delay of each tooth of the above-mentioned tool at a rotational speed of 1000 rpm is shown in Figure 5.9.

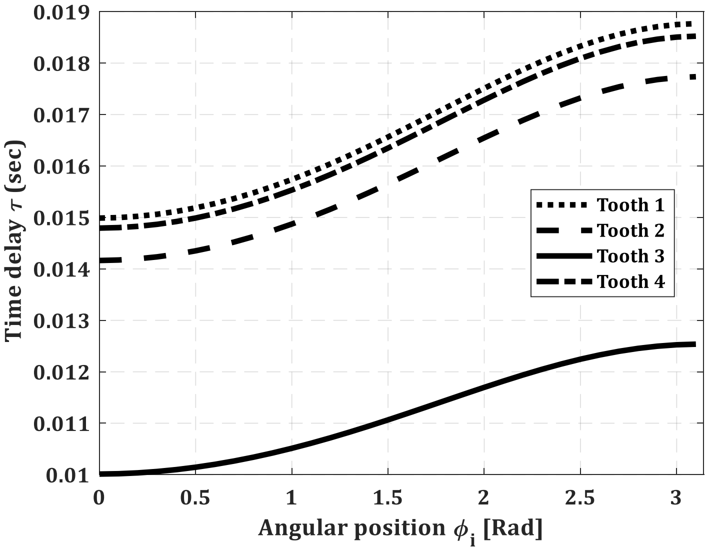

Figure 5.9: Delay variation of different teeth of the crest-cut tool at level $z = 2$ mm.

Since it is not possible to consider the time-varying delay in the ZOA method, the average value of the delay for each tooth at each disc element within the engagement boundary is considered. According to Figure 5.9, the average time delays of each tooth at $z = 2$ mm are; $\tau_1(2) = 0.0168$ sec, $\tau_2(2) = 0.0158$ sec, $\tau_3(2) = 0.0112$ sec, $\tau_4(2) = 0.0166$ sec. Therefore, each tooth of a disc element has a specific averaged-delay value denoted by $\tau_j(z)$.

Based on the discussions made in Section 4.5.2, the zero-order dynamics model of orthogonal turn-milling with crest-cut tools in the frequency domain becomes;

$$\mathbb{E}(\omega_c) = \det\left[[I] - \left[1 - e^{-i\omega_c\tau_j(z)}\right]\left[[A_1] + [A_2]\right][\Phi(\mathrm{i}\omega_c)]\right] \tag{5.13}$$

where $[A_1]$ and $[A_2]$ are the summation of zero-order Fourier transform of the time-varying directional coefficients for all teeth and levels, corresponding to side and minor cutting edges, respectively.

$$[A_1] = \sum_{j=1}^{N}\sum_{n=1}^{m}\frac{1}{2\pi}\begin{bmatrix}\alpha_{xx,jn}^{0}(\phi) & \alpha_{xy,jn}^{0}(\phi) & 0\\ \alpha_{yx,jn}^{0}(\phi) & \alpha_{yy,jn}^{0}(\phi) & 0\\ \alpha_{zx,jn}^{0}(\phi) & \alpha_{zy,jn}^{0}(\phi) & 0\end{bmatrix}$$

$$[A_2] = \sum_{j=1}^{N}\frac{1}{2\pi}\begin{bmatrix}0 & 0 & \alpha_{xz,j}^{0}(\varphi)\\ 0 & 0 & \alpha_{yz,j}^{0}(\varphi)\\ 0 & 0 & \alpha_{zz,j}^{0}(\varphi)\end{bmatrix} \tag{5.14}$$

Due to the existence of multiple time delays $\tau_j(z)$ cased by varying pitch angles along the tool axis at each tooth, there is no explicit solution for the characteristic equation to obtain the stable critical depth of cut, as proposed in [38]. In order to find the critical stable depth of cut at a fixed tool speed, the axial depth of cut is increased by increments of dz, and the stability is detected by Nyquist stability criterion (See Appendix B: Nyquist Stability Criterion).

The simulations are performed based on the FRF measurements of the tool and workpiece using an impact test. For this purpose, a crest-cut tool produced by Karcan® cutting tool company is clamped on a Mori Seiki NTX 2000 mill-turn machining center. The stability limits are compared between crest-cut and standard tools for comparison purposes. The geometric parameters of the tools are given in Table 5.5.

Table 5.5: The geometric parameters of the tools.

Tool Type	Tool Dia. (D_t) (mm)	No. of flutes (N)	Nominal helix angle (γ_j) (deg)	Pitch angle distribution (deg)	Wave Shape (mm)
Crest-cut (CC)	12	4	38	90-90-90-90	$\lambda_j = 1, A_j = 6$
Standard (ST)	12	4	38	90-90-90-90	--

The tools are clamped with a stick-out length of 55 mm, and clamping torque of 140 N.m. The modal parameters of the tools are given below:

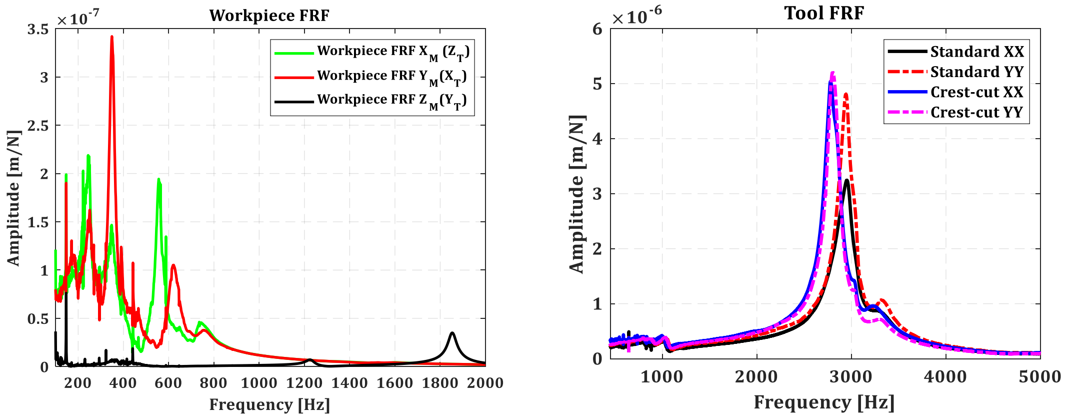

Figure 5.10: FRF measurements of the workpiece and the tools (in Table 5.5) used in this section.

The workpiece is Al7075-T6 workpiece with 114 mm diameter clamped on the chuck, as shown in Figure 4.6. According to Figure 5.10, it is seen that the FRFs of the workpiece are 10 times more rigid than the tool. The modal parameters of the workpiece are given in Table 4.1, since the identical workpiece is used for both experiments. The modal parameters acquired from the FRFs for the standard and crest-cut tools (Figure 5.10) are listed in Table 5.6.

Table 5.6: Modal parameters of the standard and crest-cut tools.

Tool	Direction	Frequency (Hz)	Damping (%)	Modal Stiffness (N/m)
Crest-cut (CC)	XX	2801	2.29	4.32e6
	YY	2809	2.05	4.75e6
Standard (ST)	XX	2933	3.12	5.21e6
	YY	2941	2.04	5.06e6

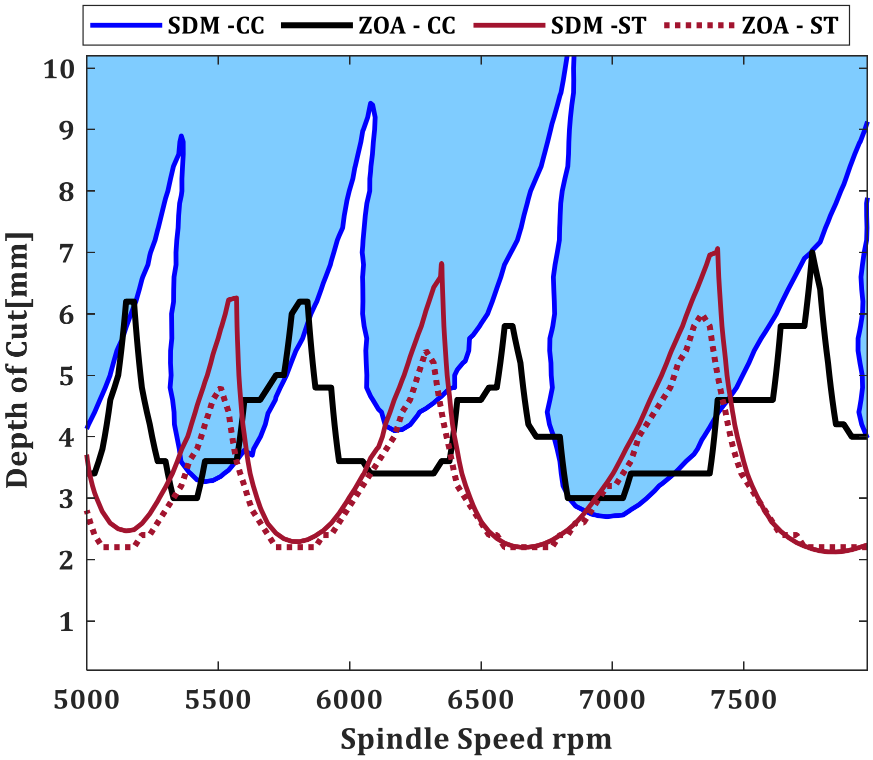

Figure 5.11: Stability lobe comparison of crest-cut (CC) and standard (ST) milling tools listed in Table 6.1 with modal parameters listed in Table 6.2. $a_w = 10\% \ D_t$, $\Omega_w = 5$ rpm, $e = 16\% \ D_t$

Based on the FRF measurements of the tools and their geometrical parameters, the stability lobes are predicted in discrete-time and frequency domains. The cutting force coefficients used in stability predictions are given in Appendix A: Orthogonal databases for the uncoated WC tools and Al7075-T6 workpiece material. The stability lobes are simulated for step over of $a_w = 0.1D_t$, workpiece speed $\Omega_w = 5$ rpm, and eccentricity of $e = 16\%D_t$.

According to Figure 5.11, it is seen that using crest-cut tools, the absolute stability limits are increased in comparison to that of the standard end mills, which is previously reported and confirmed by Tehranizadeh et al. [77]. Furthermore, there is good agreement between the stability lobes using SDM and ZOA approaches. The slight deviation between the SDM and ZOA simulations for crest-cut tools is caused by the existence of distributed delays along each edge. Since the delays are average within the engagement boundaries which are specific for each element, the ZOA approach shows lower accuracy. However, the location of lobes and the absolute stability limits between the two methods is in an acceptable error range. The accuracy can be increased by increasing the frequency resolution and step for spindle speed and depth of cut iterations, which leads to higher computational costs. For all the simulations given in Figure 5.11, the iteration interval for spindle speed is 30 rpm, and for depth of cut, the interval is 0.1 mm. The period resolution in SDM is 180, and the frequency interval in the ZOA method is 1 Hz. The simulation time for the crest-cut tool using SDM takes approximately 110 minutes, while using the ZOA approach reduces the simulation time to 16 minutes. The simulation time for a standard tool using SDM is about 78 minutes, and using ZOA is 13 minutes, approximately. It is evident that using the ZOA approach decreases the simulation time and hence, computational cost drastically. It is observed that using crest-cut tools and adding multiple delays into the solution increase the simulation time compared to standard tools.

According to the stability lobes in Figure 5.11, there is an additional lobe within the speed range of 5000-8000 rpm [129]. By considering the chatter frequency representation in Figure 5.12, it is deduced that there is an added lobe effect around 6500 rpm. Although there is a slight shift between the crest-cut and standard tool simulation because of the difference in their natural frequencies, the existence of chatter frequencies at the corresponding speeds confirms the phenomenon.

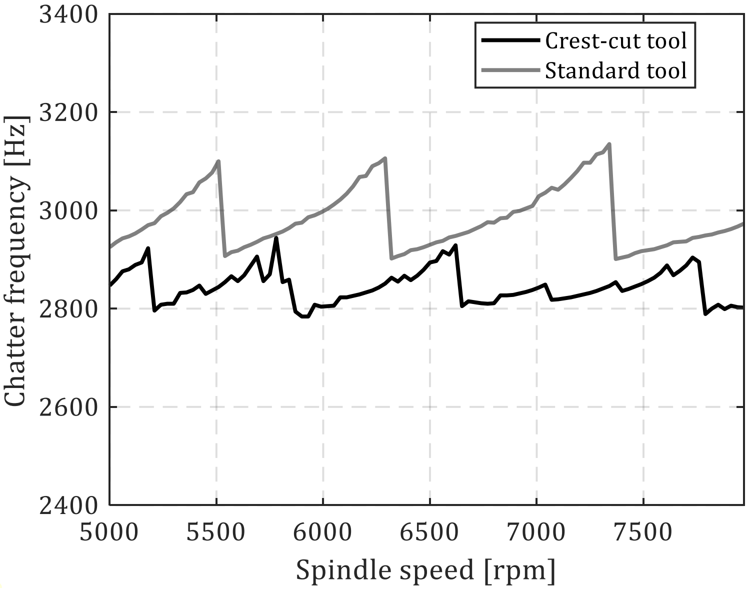

Figure 5.12: Chatter frequency vs. spindle speed for the stability diagrams in Figure 5.11.

Since the radial immersion is low $(16\%\ D_t)$The process is highly intermittent. Therefore, the periodic cutting forces and the directional coefficients regarding angular positions become narrow (semi-impulse). While expanding intermittent types of forces into the Fourier series, higher harmonics are included. Therefore, the chatter frequency is influenced by the higher number of harmonics. In other words, the higher number of harmonics of the directional coefficients associated with tooth passing frequency is included in the chatter frequency of the system. In low-immersion cases, a higher number of harmonics of tooth passing frequency contributes to chatter is called flip bifurcation [130,131]. In flip bifurcation, in the cutting force spectrum, the harmonic of tooth passing frequency $k\omega_T$, and the half of tooth passing frequency as well as its odd harmonics $(2k+1)\frac{\omega_T}{2}$ can be observed (k is an integer). As the spindle speed varies, the tooth passing frequency changes, and so does its harmonics. The higher harmonics of the tooth passing frequency shift the transfer function to higher frequencies. When the transfer function of higher harmonics coincides with the transfer function associated with the system's natural frequency, the stability solution is affected, and chatter frequency is observed near the natural frequency. Therefore, while scanning the possible chatter frequencies, the transfer functions with harmonics of the tooth passing frequency in the vicinity of the natural mode frequency fold to the region of natural frequency. Hence, if the frequency of the harmonic lies in the frequency region of $(1-\zeta)\omega_n \leq \omega_c \leq (1+\zeta)\omega_n$ flip bifurcation occurs [129].

In our case study, the simulations do not see the flip bifurcation frequencies and the added lobe for the standard tool. This is due to the fact that the radial immersion, large helix angle, and pitch angle variation affect the periodicity of the cutting forces and directional coefficients. Flip bifurcations mostly happen in highly intermittent cases. In this regard, due to the intermittent engagement of crest-cut tools caused by wavy edge shapes, large number of imposed delays, and highly varying pitch angles along the tool axis, the cutting forces become nonperiodic and more intermittent at low immersions compared to a standard tool. Therefore, added lobes exhibit at rotational speeds where the harmonics of tooth passing frequency is near to the natural mode.

In our case study given in Figure 5.11, at 6170 rpm, the tooth passing frequency is $\omega_T = 411.3$ Hz. Therefore, the 7th harmonic of tooth passing frequency is in the region of natural mode $\Phi(k\omega_T) \rightarrow \Phi(\omega_c)\,, k = 7$. Therefore, the 7th harmonic with 2879 Hz, which is within the above-mentioned frequency region, is the flip bifurcation chatter frequency. This value can be validated in Figure 5.12, while the chatter frequency of the standard tool at a speed of 6170 rpm is much higher than that of the crest-cut tool.

It is to be noted that the experimental validation for chatter tests is missing in this section. The highly stable cuts are observed at a larger depth of cuts at the predicted unstable region. This is believed that the straight portion of crest-cut tools increases the process of damping even at higher speeds. The small clearance angle of $(\gamma_1 = 2°, \gamma_2 = 8°)$ of the straight portion is the most important reason that causes process damping [132]. Furthermore, a high rate of tool wear has been observed during the chatter experiments, which shows a considerable immersion of the flank face of the tool. Further experimental investigation and process damping analysis will be the future research direction in this regard.

5.4. Summary

In this chapter, the predictive model for mechanics of the orthogonal turn-milling process is updated to be able to predict the cutting forces while cutting with serrated and crest-cut tools. The uncut chip geometry and cutter-workpiece engagement model in orthogonal turn-milling are updated specifically for serrated and crest-cut tools. The calculated cutting forces are verified with experiments using a rotary dynamometer for different cutting parameters. Next, stability of crest-cut tools in turn-milling operation is predicted. The varying time delay in orthogonal turn-milling is combined with the distributed delay resulting from the wavy edge geometry of crest-cut tools. The stability problem using variable time delays is solved using the semi-discretization method. Moreover, the stability of turn-milling with crest-cut tools is solved in the frequency domain for the first time in the literature. The resulting stability lobes for crest-cut tools are compared to standard tools and discussed.

6. APPLICATION OF SPECIAL TOOLS IN THIN-WALLED STRUCTURES

6.1. Overview

Having seen the advantages of crest-cut tools in milling and turn-milling in previous section, it is aimed to investigate the stability and performance of these tools in more challenging conditions like machining of thin-walled structures with hard-to-cut materials. A simple thin-walled structure is selected as a preliminary study before complex structures such as turbine blades or thin-walled tubes. It is known that lower cutting speeds are preferred when machining these materials due to the low machinability of hard-to-cut materials. As a result, deeper stability pockets that exist at high cutting speeds cannot be achieved. Variable pitch tools can be used at low cutting speeds to suppress chatter vibrations [133]. However, due to the existence of multiple dominant modes and varying IPW dynamics, their use in milling thin-walled parts does not always provide a satisfactory solution for chatter suppression. Crest-cut tools, on the other hand, provide chatter suppression capability over a wider frequency and speed range [77] and can be highly effective for suppressing chatter in milling thin-walled parts. This superior capability of crest-cut tools is due to their special geometry, which has to be designed considering important modes and IPW dynamics of thin-walled structures. Therefore, crest-cut end mills are proposed as a solution for improving the stability of the process in milling thin-walled structures. In this study, the varying IPW dynamics of thin-walled plates are modeled using FE, considering the element removal. For the first time in the literature, a stability map of the whole plate is generated for different tool geometries based on the IPW dynamics. According to the obtained stability map of each tool, different cutting strategies are explored, surface finish quality maps are derived, and compared in terms of cycle time and chatter-free surface area. The proposed simulations are validated through experiments. Both simulations and experiments confirm the superiority of crest-cut tools over variable-pitch and standard end mills, and the results show that these tools can be utilized as a robust solution against changes in IPW dynamics of thin-walled parts.

6.2. In-Process Dynamics of Thin-Walled Structures

As structures become more flexible or thinner, the effect of removed material during machining becomes more prominent, leading to significant variation in IPW dynamics and, therefore, stability limits. This section presents the procedure used for modelling material removal in thin-walled structures through FE analysis. In the implemented approach, the dependency of the IPW dynamics prediction procedure on the stability limits, and thus iterations and long simulation time, are eliminated. For this purpose, the unmachined flexible plate is meshed using 3D cubes with an element size of 0.6 mm. The elements from the meshed structure are removed, similar to the mass removal during the machining cycle (See Figure 6.1). The in-process FRFs are obtained at five different CLs along the feed direction (U) for each elemental depth along the plate height (V). Note that the element height in Figure 1 is exaggerated for better visualization.

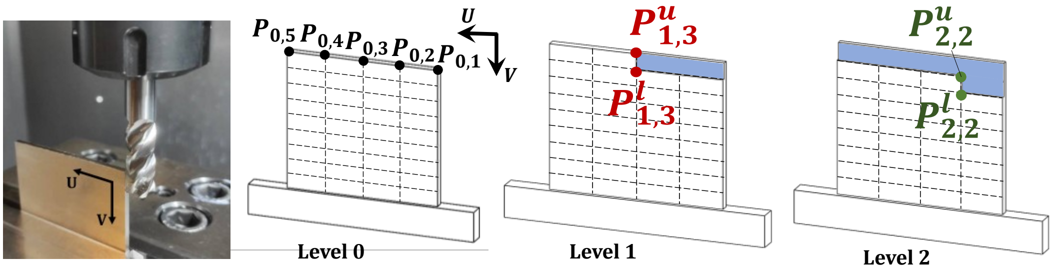

Figure 6.1: Illustration of element removal and FRF calculation points.

Points $P_{v,u}$ in Figure 6.1 represent IPW FRF identification points on the plate. The points $P_{0,u}$ are the FRF identification points on the tip of the uncut plate, Level 0. The next FRF identification locations are one element lower (Level 1), which are identified by removing the elements at that level which are shown as $P_{1,u}$. Since the material is removed at each step, the FRFs of the points with the same coordinates from the previous step are updated. For instance, at point $P_{1,2}$, two FRFs are identified, upper limit and lower limits. The lower limit $P^l_{1,2}$is the FRF of current state, and the upper limit $P^u_{1,2}$ is the updated FRF of point $P_{0,2}$ which has the same coordinate. The same procedure is repeated for Level 2 by removing the elements in Level 1. Similarly, the FRF of point $P^l_{1,2}$ is updated as $P^u_{2,2}$ to include the effect of material removal (See Figure 6.1). This procedure helps to identify the IPW FRF of any CL located between the upper and lower limits using interpolation.

Figure 6.2 shows the natural frequency and peak amplitude of each point on the plate for the first and second modes by updating the FRFs due to the material removal effect for a Ti6Al4V plate with the dimension of 40×65×3 mm. In the following simulations, the element size is kept equal to a radial depth of cut (0.6mm) to prevent excessive simulation time in FE analysis.

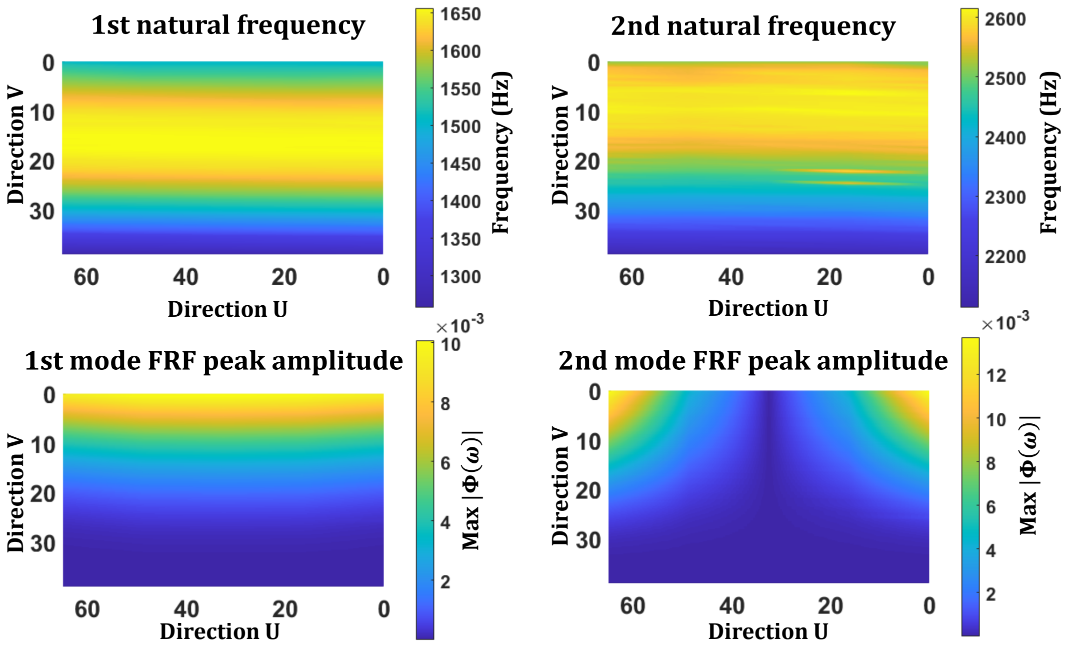

Figure 6.2. Variation of IPW dynamics; a) First, and b) Second natural frequency; c) First, and d) Second mode FRF peak amplitudes.

According to the results in Figure 6.2, both the plate's natural frequency and IPW FRFs vary drastically for both modes along the plate length and height directions, requiring multi-mode stability analysis. This scheme helps identify the FRF of any CL on the plate for evaluating stability limit considering the material removal effect. Note that, the damping ratios employed in simulations are identified from hammer tests at different plate locations considering the IPW dynamics scheme. In Figure 6.3, experimental and FE results at two points and levels on the plate are presented. In Figure 6.3 (a), measurements and predictions at two points (corner and middle) along the feed direction at the tip of the uncut plate are illustrated. Figure 6.3 (b) shows the results for the same corresponding points in the feed direction at level 54 (27mm in plate depth from the free end) after the material is removed up to this level. The maximum difference between predicted and simulated natural frequencies is less than 4%.

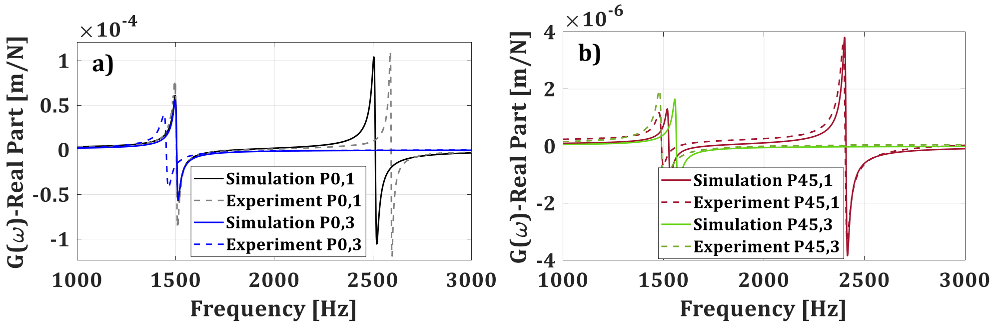

Figure 6.3. Validation of IPW dynamics at different levels.

6.3. Design Procedure of Special End Mills

The variable-pitch and crest-cut tools offer a significant possibility to attain high stability limits by tuning their geometry to a certain spindle speed [57,61,77]. In this study, the geometry of the tools is optimized considering the desired spindle speed of 2123 rpm (corresponds to 80m/min for 12mm tool diameter (D_t)). Two different variable-pitch tools with alternating pitch variations are designed to suppress chatter for each mode of the plate with the method presented in [57].

$$\Delta P = \pi \frac{\Omega_{\mathrm{t}}^{*}}{\omega_c} \qquad for\ even\ N$$

$$\Delta P = \pi \frac{\Omega_{\mathrm{t}}^{*}}{\omega_c} \frac{N \pm 1}{N} \qquad for\ odd\ N \qquad (6.1)$$

where Ω_{t}^{*} is spindle speed (rps), ω_c is chatter frequency, and N is the number of teeth. In order to consider the changes in chatter frequency due to the presence of pitch variation, an iterative method presented by Comak et al. [61] is used to find optimum pitch angles. According to the natural frequencies of the part and the desired spindle speed (2123 rpm), VP1 and VP2 tools (Table 6.1) are selected to suppress chatter. These tools are designed considering the average value of the first and second modes of the plate in its most flexible zone (0-20 mm in the V direction), 1590Hz, and 2550Hz, respectively. The presence of multi modes with varying frequencies due to IPW dynamics causes different chatter frequencies at different cutting points on the part. As variable pitch end mills are designed for a target chatter frequency and spindle speed, they lose their effectiveness in machining of thin-walled parts.

On the other hand, crest-cut end mills can suppress chatter in wider frequencies and speed ranges due to the wavy edges resulting in continuous pitch variations in the cutting zone. In order to determine the optimum crest-cut wave shape for a target spindle speed, the procedure presented in [77] is applied. The simulations are performed considering the average value of the first mode of the plate in its most flexible zone (0-20 mm in the V direction). However, as crest-cut tools introduce multiple delays, their effectiveness is not limited to the specified frequency as they can perform effectively in wider ranges. Figure 6.4 shows that the crest-cut tool (CC in Table 6.1) with 1mm edge wave amplitude (A) and 6mm edge wavelength (λ) shows superior stability at 2123 rpm.

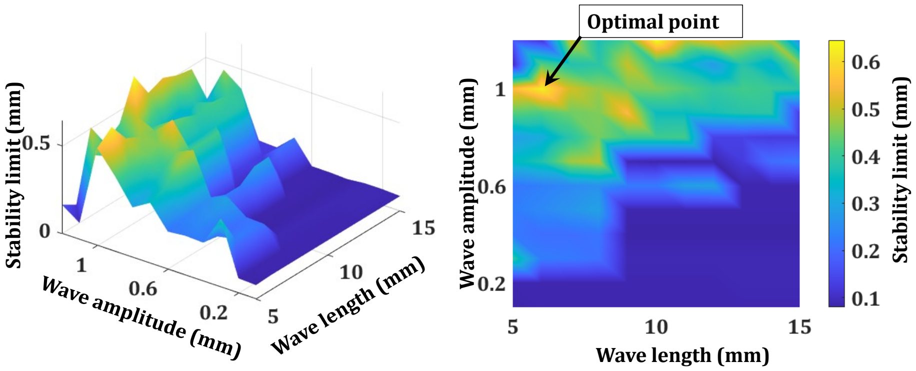

Figure 6.4: Stability of crest-cut end mill with different shapes at 2123 rpm.

Table 6.1: Geometrical parameters of end mills.

Type	D_t	N	γ_s	Pitch	A	λ
ST	12 mm	4	38°	[90°-90°-90°-90°]	-	-
CC				[90°-90°-90°-90°]	1mm	6mm
VP1				[88°-92°-88°-92°]	-	-
VP2				[88.75°-91.25°-88.75°-91.25]	-	-

6.4. Machining Stability of Thin-Walled Parts Using Special End Mills

After the tools are designed considering the frequency ranges for different modes of the plate, the stability limits are calculated using the semi-discretization method (SDM) [70,77].

Using SDM, each point's stability limit along the tool path is obtained according to the varying IPW dynamics described in Section 6.2. The resulting stability limits varying in feed (*U*) and plate depth (*V*) are illustrated for different tool types in Figure 6.5. Note that each tool's stability limits corresponding to 80m/min are calculated. According to Figure 6.5, it is seen that the crest-cut tools represent the best stability performance when compared to the other tools since the low-stable-depth region (red) is narrow and the high-stable-depth region (blue) is considerably large. Further, the variation of stability limits in feed direction is negligible since crest-cut tools can suppress chatter in a more comprehensive range of frequencies [77]. The stability limits for the VP1 tool at the middle of the plate are higher compared to the edges, as expected since this tool was designed to suppress chatter around the first bending mode of the plate. VP2 was tuned according to the chatter frequencies in the vicinity of the second mode of the plate. However, the stability is limited by the first mode of the plate, and thus the changes in the feed direction are not significant. As expected, the worst stability map with considerably low stability limits belongs to the standard tool.

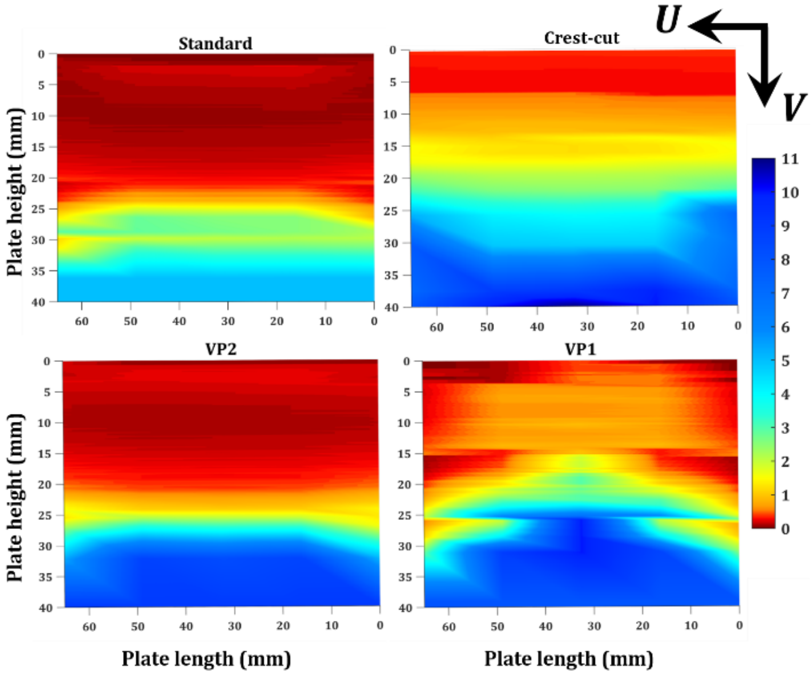

Figure 6.5. The stability limit distribution on plate considering IPW dynamics.

Once the stability maps are evaluated (Figure 6.5), several cutting strategies can be applied. These strategies involve different schemes of selecting the step down based on the stability maps. The most conservative strategy (STG1) has varying stepdown using the minimum stability limit of each pass. In the second strategy (STG2), the stepdown is chosen as the average of the stability limit in the feed direction (*U*), which also varies along the plate height. The third strategy (STG3) uses a constant stepdown for the whole plate based on the average of all stability limits evaluated in feed (*U*) and axial (*V*) directions. In STG4, the plate is divided into constant zones of 5 mm height, where the stepdown is taken as the average stability limit within that zone. In STG5, the stepdown value for all tools is defined according to that of the crest-cut tool to evaluate their performance. Finally, in STG6, the plate is divided into constant stepdown values, the most practical cutting strategy used with all tools. In order to evaluate the strategies in terms of productivity, the number of passes (NP) is calculated according to the stepdown value of each case.

Table 6.2: The number of passes and chatter-free area percentages.

	Standard		**Crest-cut**		**VP1**		**VP2**	
	NP	CFAP	NP	CFAP	NP	CFAP	NP	CFAP
STG1	258	100	57	100	159	100	146	100
STG2	212	36	55	87	49	44	134	58
STG3	204	57	43	69	68	63	164	56
STG4	202	37	53	65	46	37	130	52
STG5	57	11	57	100	57	31	57	36
STG6	100	47	100	83	100	70	100	52

Here, the Relative Stability Index (RSI), the ratio of the local stability limit at a point to the stepdown value, is used to represent the chatter condition related to the surface finish quality (SFQ). Then, the SFQ map is obtained based on the local RSI values over the workpiece surface, where darkening in color represents the transition from a stable to an unstable condition. For instance, the SFQ map for STG5 is shown in Figure 6.6. Furthermore, based on the SFQ map, the chatter-free area percentages (CFAP) are calculated using the image intensity histogram method as listed in Table 6.2. Low values of CFAP mean higher workpiece area with poor surface finish requiring further processing such as polishing. From Table 6.2, it can be clearly seen that STG1 results in the highest machining time since the most conservative depth of cut is used to generate a completely chatter-free surface. Nevertheless, the crest-cut tool's productivity is five times higher than the standard and three times higher than the variable-pitch tools in STG1. STG2 offers a significant decrease in machining time for VP1 due to the severe variations of the stability limit along the feed direction (See Figure 6.5). Since variable stepdown can be time-consuming in CAM programming, a constant stepdown, which is the average of all point stability limits is used in STG3. While a slight improvement is seen with standard and VP1 tools, the relative improvement with the crest-cut tool is lower compared to the previous strategies due to the averaging effect. In STG4, due to the averaging effect, the CFAP is lower when compared to the other strategies. In STG5, the performance of all tools is compared in terms of stability limits with the crest-cut tool, which shows superior performance in all strategies.

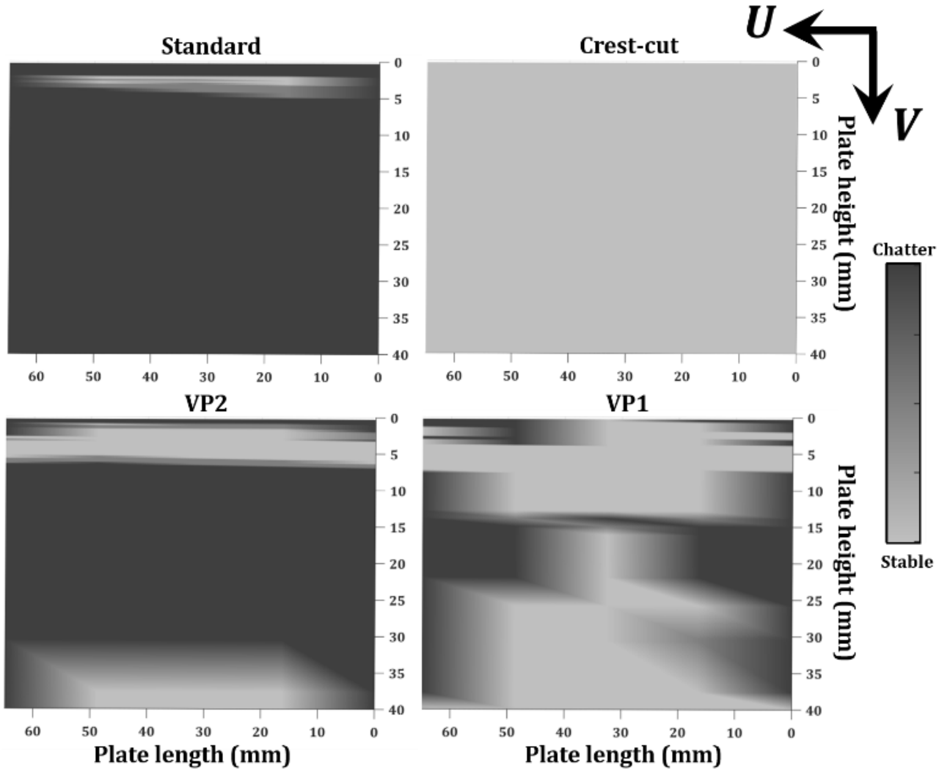

Figure 6.6. Surface finish quality map predictions for STG5.

Figure 6.6 shows that, while the crest-cut tool shows a fully chatter-free surface as expected, other tools produce a drastically poor surface finish as they cannot compete with the high stability limits of the crest-cut tool. In many cases, during industrial applications, a constant stepdown is used in many cases for CAM programming convenience. This constant stepdown value is usually selected based on the programmer's experience and tool-proving test results. This issue is considered in STG6, where a constant stepdown value of 0.4 mm is used all around the part. The SFQ maps together with the actual machined surfaces for this strategy are shown in Figure 6.7. According to the maps, the crest-cut tool offers higher CFAP compared to the other tools. As also illustrated in Figure 6.7, there is a good agreement between the SFQ maps and the surface finish obtained in the milling tests. The darker areas in the SFQ map represent a very poor surface finish, whereas the points in the light-colored areas indicate a much better surface finish. According to the results, the area with chatter marks is distributed on 50% and 17% of plate height for VP1 and crest-cut tools, respectively. This means crest-cut tools require lower time for additional processing to remove the chatter area.

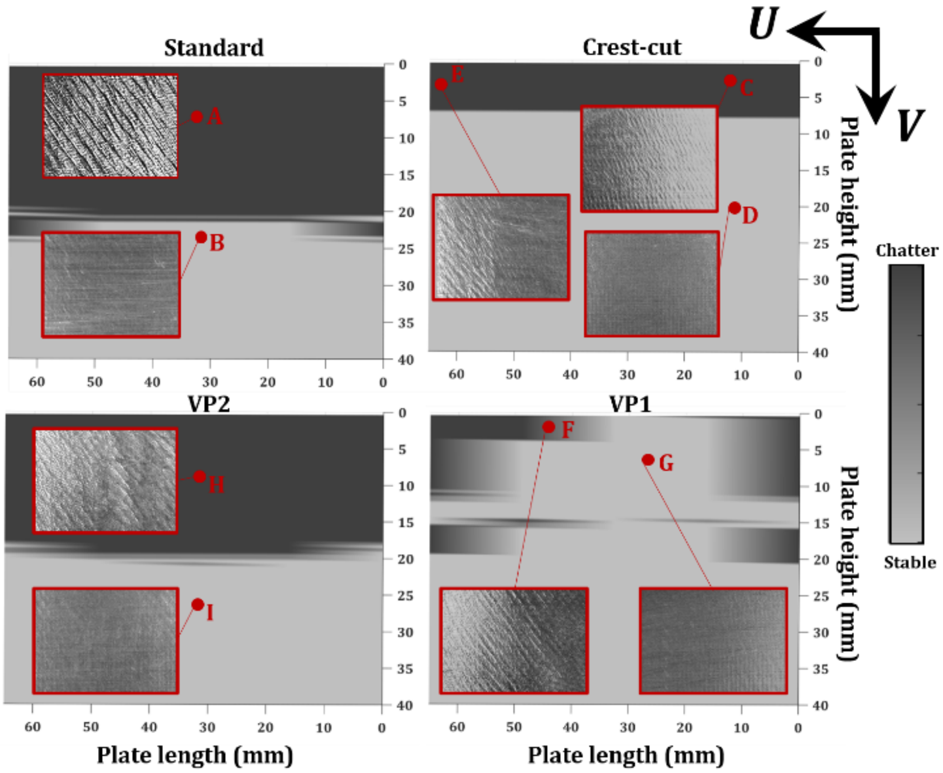

Figure 6.7: Surface finish quality maps for STG6 and verifications.

6.5. Summary

In this chapter, the simulations and experiments show the effectiveness of crest-cut tools compared to variable-pitch tools in machining thin-walled structures. The in-process workpiece dynamics are calculated using the FE method. The material removal effect is simulated by removing elements in the cut direction, and the FRFs are updated for any cutter location on the part surface. Based on the workpiece dynamics, the tuned variable-pitch and crest-cut tools are selected according to their stability limits. The surface finish quality maps are obtained and compared for 5 different cutting strategies with different stepdown values. It is deduced that crest-cut tools improve performance since the chatter-free area percentage is higher than standard and variable pitch tools in all the strategies.

7. EFFECT MACHINE TOOL DYNAMICS ON CUTTING STABILITY

7.1. Overview

The most influential and effective factor in the determination of the stability of a system is the dynamics of the tool and workpiece. Identifying each component's frequency response function (FRF) is vital to understanding how each component reacts to the exciting forces. However, a tool is usually clamped to the spindle with a tool holder in a machining system. As a result, the frequency response function at the tooltip is influenced by the tool-holder-spindle assembly. In addition, in turn-milling operation, the workpiece is also clamped to a chuck-spindle assembly. Hence, the spindle and its structural dynamic properties influence the dynamics of the tool and workpiece drastically. The main components of a regular spindle can be listed as; a shaft supported by some sets of bearings, rotor and stator, housing, cooling system, and drawbar system. Each component will affect the performance and feasibility of the spindle in different aspects like dynamics, thermal growth, speed limitations, and dimensions.

A predictive model for spindle dynamics allows the designers and engineering to develop a high-performance spindle according to different operational conditions like high rotational speeds and various types of loadings. The identification of dynamic properties of a shaft-bearing system is previously performed by Özşahin et al. [134] through modal testing. However, the identified dynamic properties are regardless of the bearing location and specifications.

This chapter presents an analytical approach to predicting the spindle tip and tooltip dynamics by implementing the bearing dynamics model into the spindle-shaft model based on receptance coupling. The dynamics of the assembly are investigated at different speeds and preloading conditions through simulations and verified with the experiments. The sensitivity analysis is performed for the machine tool spindle for improved rigidity and cutting stability. In addition, the dynamics of the clamped workpiece are also modeled using inverse receptance coupling to identify the contact dynamics. The proposed results are verified via experiments.

7.2. Predictive Model for Spindle Dynamics

7.2.1. Speed-dependent bearing dynamics model

In this section, a modified bearing model is presented considering the rotational speed effects and the centrifugal force effect of the inner ring proposed by de Mul [135] for angular contact ball bearing (ACBB). This model is an improved version of Harris's model [85,136], which facilitates analytical calculations.

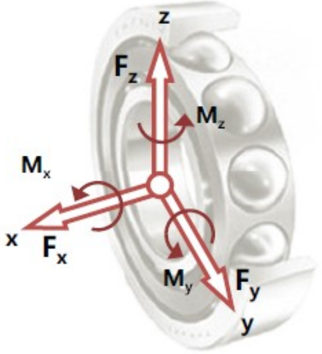

Figure 7.1: Forces and moments in a cartesian coordinate system for angular contact ball bearing [137].

The coordinate system representation to model the dynamic characteristics of an ACBB is given in Figure 7.1. The bearing stiffness is calculated based on the displacement against the external force and moment with respect to the center point of the inner ring of the bearing. The relationship between linear forces and moments (shown in Figure 8.1) and the translational and rotational displacements are modeled through coupling components. Such a coupling component appears mainly due to the contact angle between the balls and inner and outer rings of ACBB. Depending on the bearing arrangements, these components have the most important influence on the characteristic variations [87].

Figure 7.2. demonstrates a free-body diagram expressing the contact reaction force and the centrifugal force by the inner and outer rings and the friction force applied to the contact point due to the gyroscopic moment for an arbitrary rotating element.

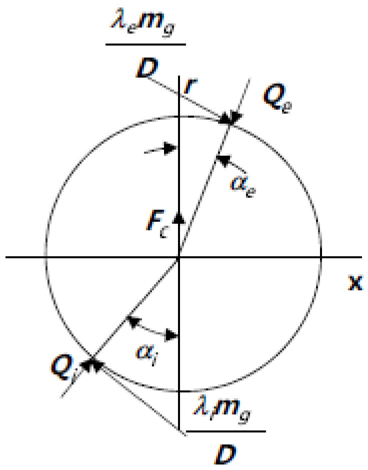

Figure 7.2: Contact, centrifugal, and friction forces acting on a ball [137].

In Figure 7.2., the coordinates x and r represent the axial and radial directions, respectively. In addition, Q_i and Q_e are the contact forces between the inner and outer rings, and α_i and α_e stand for the contact angles for the inner and outer rings, respectively. The centrifugal force F_C of the ball is expressed as follows.

$$F_C = \frac{1}{2} m_b d_m \omega_b^2 \tag{7.1}$$

In equation (7.1), m_b, d_m, and ω_b are the balls' mass, bearing pitch diameter, and rotational speed, respectively. Also, the gyroscopic moment m_g can be obtained by the following equation.

$$m_g = \frac{1}{10} m_b D^2 \omega_b \omega_r \sin(\beta_b) \tag{7.2}$$

Here, D is the diameter of the ball, and ω_r and β_b are the ball's speed and the angle between the ball's rotation axis and the bearing axis, respectively.

The contact force between the ball and the inner and outer rings is assumed as follows from the Hertzian contact theory.

$$Q_i = K_i \delta_i^{1.5}, Q_e = K_e \delta_e^{1.5} \tag{7.3}$$

Here, δ_i and δ_e stand for the amount of deformation between the inner ring and the ball and the outer ring and the ball, respectively, and K_i and K_e are the corresponding load-displacement proportional coefficients, which can be determined using the Hertzian contact ratio calculated from the bearing radius of curvature. The following equilibrium equation can be obtained from the free-body diagram in Figure 7.2.

$$Q_i\cos(\alpha_i) - Q_e\cos(\alpha_e) + F_c - \frac{m_g}{D}(\lambda_i\sin(\alpha_i) - \lambda_e\sin(\alpha_e)) = 0$$
$$Q_i\sin(\alpha_i) - Q_e\sin(\alpha_e) - \frac{m_g}{D}(\lambda_i\cos(\alpha_i) - \lambda_e\cos(\alpha_e)) = 0 \qquad (7.4)$$

where λ_i and λ_e represent the support ratios of the inner and outer rings to the gyroscopic moment. In a high-speed spindle, the contact force applied to the outer ring is relatively high; thus, it can be assumed that the outer race control mode is a rolling motion based on the outer ring, leaving $\lambda_e = 2$, otherwise $\lambda_i = \lambda_e = 1$.

The equilibrium equation for the entire bearing in the global coordinate system can be written as follows [137];

$$\{F\} + \sum_{j=1}^{Z}\left[T_\psi\right]_j^T\{Q_i\}_j = 0 \qquad (7.5)$$

Here, Z is the number of balls, $\{F\}$ is an external force vector applied to the bearing, and $\{Q_i\}_j$ is a vector obtained from the contact force between the j^{th} rotating element and the inner ring in the *x* coordinate direction. Furthermore, $\left[T_\psi\right]_j^T$ is a transformation matrix between the coordinates center of the inner ring curvature radius and the global coordinates. Both equations (7.4) and (7.5) are non-linear, and solved as a set of equations to obtain the stiffness matrix.

The bearing stiffness matrix is obtained from equation (7.5) as follows [137];

$$K = \left[\frac{\partial\{F\}}{\partial\{\delta\}}\right] = -\sum_{j=1}^{Z}\left[T_\psi\right]_j^T\left[\frac{\partial\{Q_i\}_j}{\partial\{u\}}\right]\left[T_\psi\right]_j \qquad (7.6)$$

where,

$$\{F\} = \left\{F_x,\ F_y,\ F_z,\ M_x,\ M_y\right\}^T$$
$$\{\delta\} = \left\{\delta_x,\ \delta_y,\ \delta_z,\ \gamma_x,\ \gamma_y\right\}^T \qquad (7.7)$$

Force matrix $\{F\}$ in equation (7.6) consists of the contact forces between the rotating elements and the inner ring associated with the transformation matrix. Therefore, the resultant stiffness matrix can be easily calculated using all imposed forces and resulting translational and rotational displacements, as given in equations (7.6) and (7.7).

Based on the theories mentioned earlier, a speed-dependent bearing dynamics model program has been developed by our project partner Prof. Seon Wook Hong’s research group at Kumoh National Institute of Technology in South Korea. By employing this program, Hong et al. [137] presented the influence of the ACBB on high-speed spindle dynamics using the bearing model and finite element method (FEM). Next, the provided program by our partner was integrated with the spindle dynamics model given in Section 7.2.2. Therefore, a predictive model is developed for the calculation of speed-dependent spindle dynamics.

The program is able to calculate bearing stiffness values under different preload values and different geometric parameters of bearing, as listed in Table 7.1. All the parameters that are effective in calculating the speed-dependent stiffness matrix of a bearing are given in Table 7.1 and illustrated in Figure 7.3.

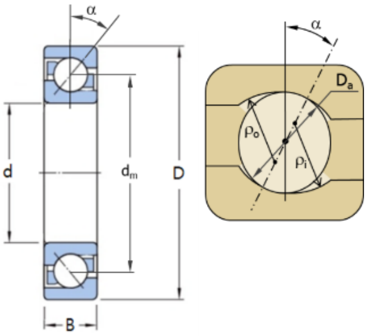

Figure 7.3: Geometric parameters of an ACBB.

Table 7.1: Bearing parameters definition.

B	Width
D	Outer Ring Diameter
d	Inner Ring Diameter
d_m	Pitch Diameter
D_a	Ball Diameter
α	Initial Contact Angle
$f_i\ (2r_i/D_a)$	Inner Curvature Ratio
$f_o\ (2r_o/D_a)$	Outer Curvature Ratio
Z	Number of Balls

The developed model provides all translational and rotational stiffness values and the cross-coupled stiffness values as given in equation (7.8).

$$[K] = \begin{bmatrix} k_{xx} & k_{xy} & k_{xz} & k_{x\theta_x} & k_{x\theta_y} \\ k_{yx} & k_{yy} & k_{yz} & k_{y\theta_x} & k_{y\theta_y} \\ k_{zx} & k_{zy} & k_{zz} & k_{z\theta_x} & k_{z\theta_y} \\ k_{\theta_x x} & k_{\theta_x y} & k_{\theta_x z} & k_{\theta_x \theta_x} & k_{\theta_x \theta_y} \\ k_{\theta_y x} & k_{\theta_y y} & k_{\theta_y z} & k_{\theta_y \theta_x} & k_{\theta_y \theta_y} \end{bmatrix} \tag{7.8}$$

In equation (7.8), the diagonal elements of the stiffness matrix are required and used in the analytical spindle dynamics model and FE model. The stiffness matrix components in equation (7.8)depend on the axial and radial preload magnitudes. Shin et al. [87] showed that these four stiffness terms ($k_{x\theta_y}$, $k_{\theta_y x}$, $k_{\theta_x y}$, $k_{y\theta_x}$) are the only dominant off-diagonal terms if there is no external radial load and only axial preload is applied. Similarly, in all the analysis in our studies the radial preload is not applied into our design. For zero radial preload, the following components of the stiffness matrix becomes negligible in bearing matrix calculation, and hence can be considered as zero [87,135,138].

$$\begin{gathered} k_{xy} = k_{xz} = k_{x\theta_x} = k_{yx} = k_{y\theta_y} = k_{yz} = k_{zx} = k_{zy} = k_{z\theta_x} = k_{z\theta_y} = k_{\theta_x x} = \\ k_{\theta_x z} = k_{\theta_x \theta_y} = k_{\theta_y y} = k_{\theta_y z} = k_{\theta_y \theta_x} = 0 \end{gathered} \tag{7.9}$$

Depending on the bearings' arrangement, the cross-coupling components' sign changes [87]. As a result, in our case study, for angular contact ball bearing without the radial preloading, the diagonal and off-diagonal components of the stiffness matrix have real values and will be included in the simulations. However, the main dynamic characteristic of the bearing is based on the diagonal terms and translational and rotational stiffness components. In this regard, bearing stiffness values are simulated with respect to important varying inputs such as rotational speeds and preload to understand their effect on bearing stiffness and hence, system dynamics. Figure 7.4 shows the effect of rotational speed on the radial, axial and rotational stiffness for a case study bearing with constant preload. For the simulations in Figure 7.4 and Figure 7.5, SKF 7009 CE/HCP4BGV275 bearing with 250N axial preload at zero rpm rotational speed is selected as a case study. It is seen that higher speed decreases the radial stiffness drastically while having a slight effect on the axial stiffness. On the other hand, the rotational (moment) stiffness decreases until a specific speed increases gradually. Increasing rotational speed decreases the relative axial displacement between the inner and outer rings for the bearing under constant pressure preload. Moreover, the contact angle between the ball and the inner ring is increased, and the contact angle between the ball and the outer ring is reduced. As a result, bearing stiffness decreases as the rotational speed increases [107].

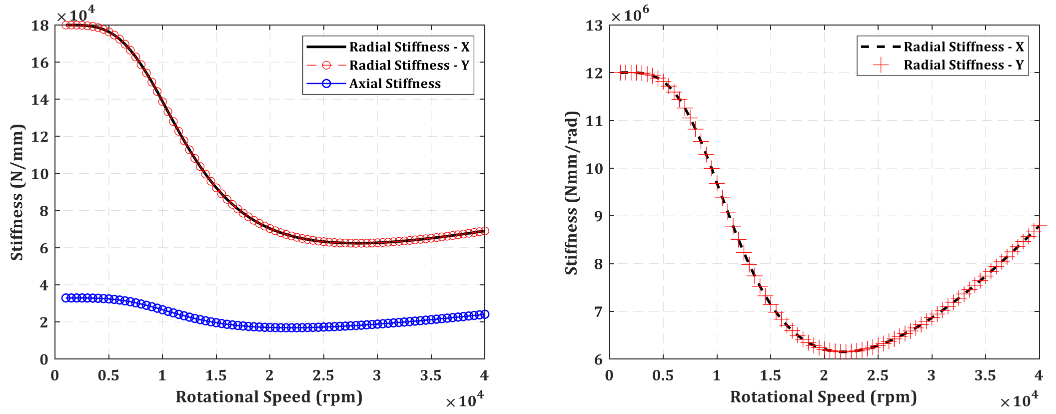

Figure 7.4: Simulation of translational and rotational stiffness with respect to rotational speed.

Figure 7.5 shows the effect of axial preload on the radial and moment stiffnesses. It is deduced that increasing the axial preload will increase the bearing stiffness; however, it has been previously proved that the generated heat will also be increased by preload, which is a deteriorating parameter in bearing performance and life [139,140].

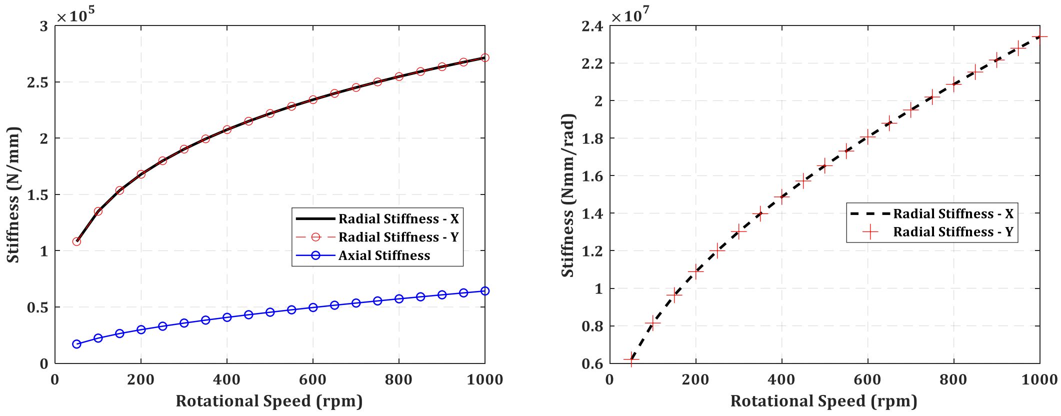

Figure 7.5: Simulation of translational and rotational stiffness with respect to axial preload.

7.2.2. Analytical Modeling of the Shaft-Bearing Assembly in a Spindle

In order to develop the fully analytical model for the spindle shaft-bearing assembly, the shaft is divided into subcomponents where the dynamics of each component are calculated using the analytical solution of the Timoshenko beam, and the subcomponents are coupled using the receptance coupling method to evaluate the dynamics of the whole structure. In this regard, the receptance functions of a subcomponent at the free-free condition at endpoints (points 1 and 2, as shown in Figure 7.6) are derived using the analytical solution of Timoshenko beam theory. The receptance functions relate the transverse displacements and bending rotations at points 1 and 2 with the forces and moments applied at the corresponding points.

Figure 7.6: Uniform subcomponent beam with free-free end conditions

The transverse displacement $w(x,t)$ and bending rotation $\psi(x,t)$ equations of a uniform beam due to harmonically applied force from Timoshenko beam solution are obtained as a function of mass-normalized eigenfunctions of transverse displacement $\phi_r(x)$ and bending rotation $\varphi_r(x)$ [95]. The receptance functions that relate the transverse displacements and harmonic forces are denoted as $\overline{H}_{jk}$ and the receptance functions that give information between the bending rotation and harmonic forces are shown as $\overline{N}_{jk}$, and defined as:

$$\overline{H}_{jk} = \frac{f_k}{y_j}, \overline{N}_{jk} = \frac{f_k}{\theta_j} \tag{7.10}$$

where y and θ represent the linear and angular displacements at point j, respectively. f_k is the harmonic force applied at point k and is defined as;

$$f_k = F_0 e^{i\omega t} \tag{7.11}$$

Similarly, the receptance functions which relate the transverse and rotational displacements at point j with the harmonic moment at point k are defined as;

$$\overline{L}_{jk} = \frac{m_k}{y_j}, \overline{P}_{jk} = \frac{m_k}{\theta_j} \tag{7.12}$$

Where m_k is the harmonic moment applied on point k and can be defined as:

$$m_k = M_0 e^{i\omega t} \tag{7.13}$$

Assuming that the structural damping of the component has the loss factor of $\bar{\gamma}$, the receptance functions can be defined as a function of transverse and bending eigenfunctions in frequency domains as follows;

$$\bar{H}_{jk} = \sum_{r=0}^{\infty} \frac{\phi_r(x_j)\phi_r(x_k)}{(1+i\bar{\gamma})\omega_r^2-\omega^2} \tag{7.14}$$

$$\bar{N}_{jk} = \sum_{r=0}^{\infty} \frac{\varphi_r(x_j)\phi_r(x_k)}{(1+i\bar{\gamma})\omega_r^2-\omega^2} \tag{7.15}$$

$$\bar{L}_{jk} = \sum_{r=0}^{\infty} \frac{\phi_r(x_j)\varphi_r(x_k)}{(1+i\bar{\gamma})\omega_r^2-\omega^2} \tag{7.16}$$

$$\bar{P}_{jk} = \sum_{r=0}^{\infty} \frac{\varphi_r(x_j)\varphi_r(x_k)}{(1+i\bar{\gamma})\omega_r^2-\omega^2} \tag{7.17}$$

Considering the subcomponent in Figure 7.7, $j = 1,2$ and $k = 1,2$.

The above-mentioned receptance functions must be evaluated for endpoints of a single segment for the sufficient number of modes. In order to obtain the FRFs of the multi-segment beam, the receptance functions of the segments at free-free conditions must be s coupled.

Considering a beam C with two segments, A and B, as shown in Figure 7.7, the receptance matrices for each subsegment can be written as follows:

$$[A] = \begin{bmatrix} [A_{11}] & [A_{12}] \\ [A_{21}] & [A_{22}] \end{bmatrix}, [B] = \begin{bmatrix} [B_{11}] & [B_{12}] \\ [B_{21}] & [B_{22}] \end{bmatrix} \tag{7.18}$$

Where each submatrix includes the receptance functions of the corresponding segment at endpoints as follows;

$$[A_{ij}] = \begin{bmatrix} \bar{H}_{jk}^A & \bar{L}_{jk}^A \\ \bar{N}_{jk}^A & \bar{P}_{jk}^A \end{bmatrix}, [B_{ij}] = \begin{bmatrix} \bar{H}_{jk}^B & \bar{L}_{jk}^B \\ \bar{N}_{jk}^B & \bar{P}_{jk}^B \end{bmatrix} \therefore j,k = 1,2 \tag{7.19}$$

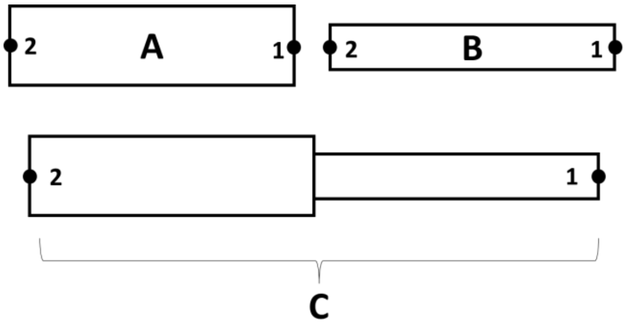

Figure 7.7: Rigid coupling of two uniform beams.

By holding the individual displacement-force and displacement-moment equilibriums for beam segments A and B by taking the continuity and combability relations at the connection point, the receptance matrix of the beam C by coupling the receptance matrices of segments A and B can be written as follows [141];

$$\begin{aligned}
[C_{11}] &= [A_{11}] - [A_{12}]\big[[A_{22}] + [B_{11}]\big]^{-1}[A_{21}] \\
[C_{12}] &= [A_{12}]\big[[A_{22}] + [B_{11}]\big]^{-1}[B_{12}] \\
[C_{21}] &= [B_{21}]\big[[A_{22}] + [B_{11}]\big]^{-1}[A_{21}] \\
[C_{22}] &= [B_{22}] - [B_{21}]\big[[A_{22}] + [B_{11}]\big]^{-1}[B_{12}]
\end{aligned} \tag{7.20}$$

Considering a spindle shaft with segments that have different diameters and lengths, one can calculate the FRF of the shaft at endpoints under free-free conditions. However, the spindle shaft is supported by the bearings at certain bearing locations and has contact with the specific element. This implies that the bearing can be coupled with the spindle shaft as springs and dampers (See Figure 7.8).

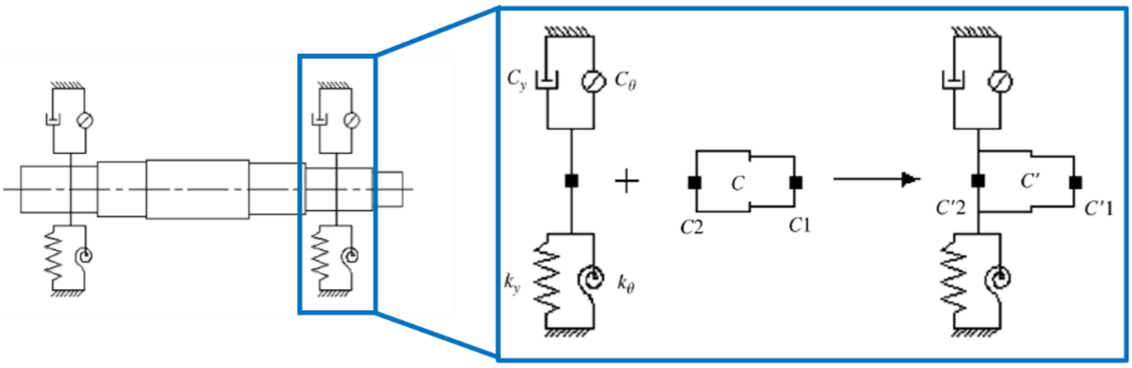

Figure 7.8: Coupling bearings with shaft receptance using structural modification.

It is to be noted that the receptance coupling allows the computation of endpoint receptances only. Hence, the effect of bearing dynamics must be imposed on the system dynamics by including the receptance of the endpoint of the segment in which the bearing is located (See Figure 7.8).

The dynamics of bearings are coupled with the shaft dynamics using the structural modification technique proposed by Özgüven [142]. In this method, the unmodified system's receptance matrix and the modification's properties (bearing stiffness and damping) are coupled using the displacement-excitation equilibriums. According to Equations (7.18), (7.19), and (7.20) the receptance of the two-segment beam C is obtained as follows;

$$[C] = \begin{bmatrix} H_{C1C1} & L_{C1C1} & H_{C1C2} & L_{C1C2} \\ N_{C1C1} & P_{C1C1} & N_{C1C2} & P_{C1C2} \\ H_{C2C1} & L_{C2C1} & H_{C2C2} & L_{C2C2} \\ N_{C2C1} & P_{C2C1} & N_{C2C2} & P_{C2C2} \end{bmatrix} \tag{7.21}$$

In order to apply the structural modification, the equation (7.21) must be rearranged in the following manner;

$$[\Gamma_C] = \begin{bmatrix} H_{C1C1} & H_{C1C2} & L_{C1C1} & L_{C1C2} \\ H_{C2C1} & H_{C2C2} & L_{C2C1} & L_{C2C2} \\ N_{C1C1} & N_{C1C2} & P_{C1C1} & P_{C1C2} \\ N_{C2C1} & N_{C2C2} & P_{C2C1} & P_{C2C2} \end{bmatrix} \tag{7.22}$$

Let $[\mathcal{D}]$ be the dynamic structural modification matrix that includes the rotational, translational, and rotational-translational cross stiffness and damping information of the corresponding bearings.

$$[\mathcal{D}] = \begin{bmatrix} 0 & 0 & 0 & 0 \\ 0 & K_y & 0 & K_{y\theta} \\ 0 & 0 & 0 & 0 \\ 0 & K_{\theta y} & 0 & K_\theta \end{bmatrix} \tag{7.23}$$

where;

$$\begin{aligned} K_y &= k_y + i\omega c_y \\ K_\theta &= k_\theta + i\omega c_\theta \end{aligned} \tag{7.24}$$

K_y and K_θ are the translational and rotational complex stiffness expressions, respectively. The parameters k_y and k_θ are the translational and rotational stiffness values, respectively, which are obtained by the speed-dependent bearing stiffness model presented in Section 7.2. c_y and c_θ are the translational and rotational damping coefficients, respectively, which are obtained from calibration with experimental measurements.

In structural modification technique, the translational stiffness k_y is replaced by the radial stiffnesses k_{xx}, k_{yy} $\left[\frac{N}{m}\right]$ obtained by the model given in Section 7.2.1. This parameter modifies the H_{C2C2} term in the receptance matrix of the shaft segment, which is the transfer function for harmonic force and radial displacement. Further, rotational stiffness k_θ in modification matrix $[\mathcal{D}]$ is replaced by the calculated moment stiffnesses $k_{\theta_x\theta_x}, k_{\theta_y\theta_y}$ $\left[\frac{N.m}{rad}\right]$ discussed in Section 7.2.1. This term modifies the P_{C2C2} receptance relates the harmonic moment and the bending rotation of the corresponding shaft.

In order to increase the accuracy of our simulations, the cross-stiffness parameters, which are appeared as off-diagonal stiffness values in equation (7.8), are also considered. The off-diagonal (cross) stiffness parameters obtained from the bearing model are substituted by the $K_{y\theta}$ components in modification matrix $[\mathcal{D}]$ to modify the receptance functions N_{C2C2} and L_{C2C2}. Note that, as described previously, these functions relate the harmonic radial forces and moment rotations and harmonic moments with radial displacements, respectively. The corresponding damping coefficients for translational and rotational modification terms in equation (7.24) are calibrated with the experimental data in terms of the peak amplitudes of the modes. Further, the signs of the off-diagonal terms for front and rear bearings are different. Since the configuration of the existing spindle is "double O-configuration," the off-diagonal terms for front bearings, which are positive bearings, are negative. The off-diagonal terms are positive for rear bearings (negative bearings) [87]. Note that the negative and positive configuration of the bearings on the spindle depends on the shaft-bearing coordinate systems, contact angle directions, and locations on the shaft. (See reference [87]). Having formed the modification matrix based on the bearing dynamics, the receptance matrix of the modified system (Γ_C') by integrating the analytically obtained bearing stiffnesses can be calculated by;

$$[\Gamma_C'] = \left[[I] + [\Gamma_C].[\mathcal{D}]\right]^{-1}.[\Gamma_C] \tag{7.25}$$

The FRF of the modified structure can be drawn from the $\left[\Gamma_C'^{11}\right]$ which represents the relation between the harmonic excitation force and the translational displacements. After the application of the procedure as mentioned earlier for the first bearing, the dynamic of the other segments can be coupled to the present segment (in which the first bearing is mounted) using receptance coupling until the segment in which the other bearing is connected. The structural modification is applied for each segment that the bearing is connected to, and then the next shaft segment is coupled to the endpoint of the modified segment. This procedure continues until all the segments of the spindle shaft is coupled, and the overall shaft-bearing system is modeled.

7.2.3. Experimental Verification

The experimental results for FRF measurements are provided by our project partner using the existing spindle in their laboratory. The FRF measurements are performed on the spindle shaft tip using the proper impact hammer and accelerometer, as shown in Figure 7.9 schematically.

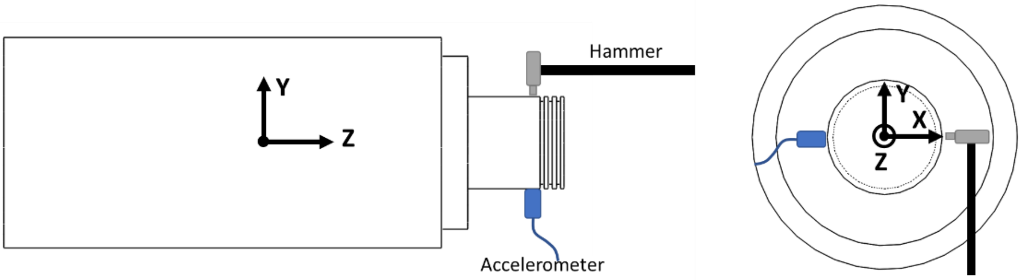

Figure 7.9. Schematic representation of FRF measurement setup.

In order to simulate the FRF of the existing spindle, the CAD assembly model of the whole spindle as well as the CAD model of the shaft and bearing specifications are provided by our partner.

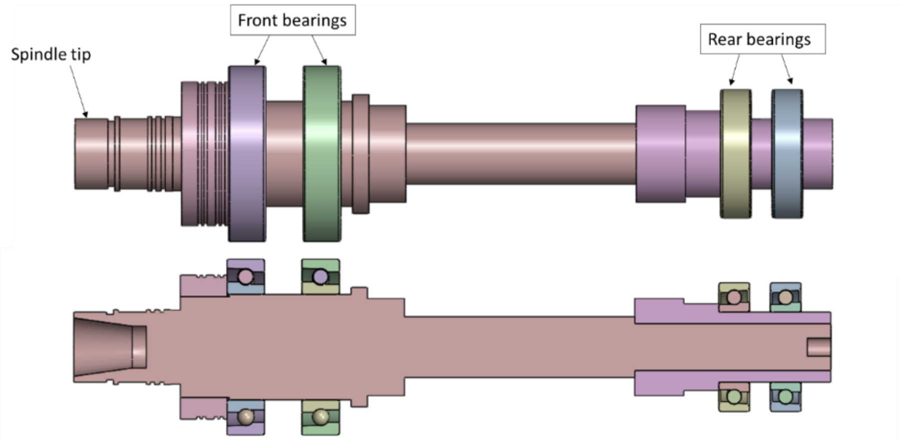

Figure 7.10: CAD model of the spindle-bearing system.

The shaft dynamics are modeled by applying receptances coupling techniques by dividing the shaft into segments with specific diameters, as explained in detail in Section 1.3. The bearings dynamic effect is added by applying the structural modification method. The dimensions of the shaft segments are given in Table 7.2. Note that segment number starts from the shaft tip and segment 1 corresponds to the first segment on the spindle shaft tip. The front bearings are located on segments 6 and 8, and the rear bearings are on segments 15 and 17, as shown in Table 7.2. The spindle shaft is made of alloyed steel with Elastic modulus $E = 210\ GPa$, density $\rho = 7810 \frac{kg}{m^3}$, and Poisson ratio $\nu = 0.3$.

Table 7.2: Dimensions of the spindle shaft.

Spindle shaft dimensions

Segment number	1	2	3	4	5	6	7	8	9	10	11	12	13	14	15	16	17	18
Length (mm)	12.5	12.5	6	14.5	20	16	16	16	5	7	15.8	98.4	21	15	13	9	13	12.8
Outer Diameter (mm)	30	30	30	32	61.5	45	55	45	45	51	41.5	26	41.5	37	30	40	30	30
Inner Diameter (mm)	25.02	22	18	0	0	0	0	0	0	0	0	0	0	0	0	0	0	8

The properties of the bearings used in the existing spindle are provided by our project partner, and listed in Table 7.3.

Table 7.3: Properties of the bearings in the existing spindle of Partner 2.

	Ball Dia. (mm)	Pitch Dia. (mm)	Outer Dia. (mm)	Bore Dia. (mm)	Width (mm)	Contact Angle (deg)	Inner Curvature ratio	Outer Curvature ratio	Number of Balls.	Axial Preload (N)	Ball material
Front Bearings	7.14	60	75	45	16	15	0.54	0.53	21	158	Ceramic
Rear Bearings	6.35	42.5	55	30	13	15	0.53	0.53	17	158	Ceramic

After entering the bearing properties and the shaft dimensions into the integrated program, the bearing translational and rotational stiffnesses are calculated and are coupled with the shaft dynamics. The resulted bearing stiffness values are given in Table 7.4.

Table 7.4: Calculated bearing stiffness and identified damping coefficients for idle state.

	Translational Stiffness (N/.m)	Rotational Stiffness (N.m/rad)	Cross rotational-translational stiffness (N/rad)	Translational damping coefficient (N.s/rad)	Rotational damping coefficient (N.m.s/rad)
Front Bearings	1.95e8	14941	-1.6716e6	650	1.8
Rear bearings	1.62e8	6563	1.006e6	400	1

The damping coefficients are calibrated according to the experimental results and listed in Table 7.4. The final simulations and the experimental results are compared in Figure 7.11. As seen in Figure 7.11, the first dominant mode with the highest FRF peak amplitude is taken into account. It is seen that the experimental results, the natural frequencies of the first mode have 8% deviation for X and Y directions. The error between the X and Y direction can be due to the clamping condition of the whole spindle, spindle housing, and other fastening parts mounted on the spindle. According to Figure 7.11, it is deduced that the experimental and simulation results are in good agreement in terms of first natural frequency. The is a 15% error in the second natural frequency between the simulation and experimental results. However, since the first mode is dominant, the effect of the second mode on overall spindle rigidity is negligible. To investigate the effect of rotational speed on spindle dynamics, the tip point FRF of the spindle-bearing assembly is calculated at various spindle speeds using the analytical model and speed-dependent bearing model.

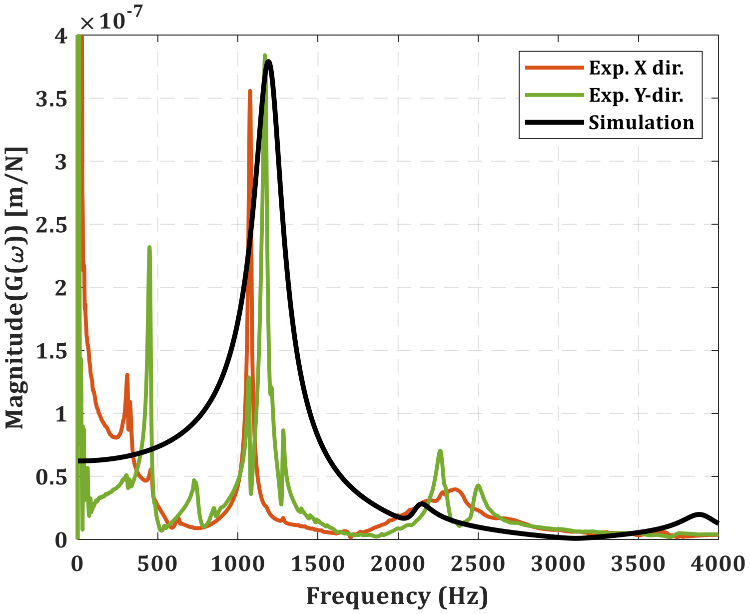

Figure 7.11: Comparison of the experimental and simulation results of FRFs at idle state.

The simulations are performed for the bearings and shaft geometry of the existing spindle, which is indicated in Table 7.2 and Table 7.3. In this approach, the fully-analytical angular-contact bearing stiffness matrix model is integrated with the above-mentioned receptance coupling and structural modification model to evaluate the speed-dependent frequency response functions. Figure 7.12 shows the variation of FRF of the spindle tip concerning the rotational speed. It has been previously shown that the rotational speed will decrease the bearing stiffnesses. This is evident in the magnitude variation of the first mode and its natural frequency, as shown in Figure 7.12. Higher rotational speeds decrease the overall bearing stiffnesses, increasing the FRF magnitude and decreasing the first natural frequency.

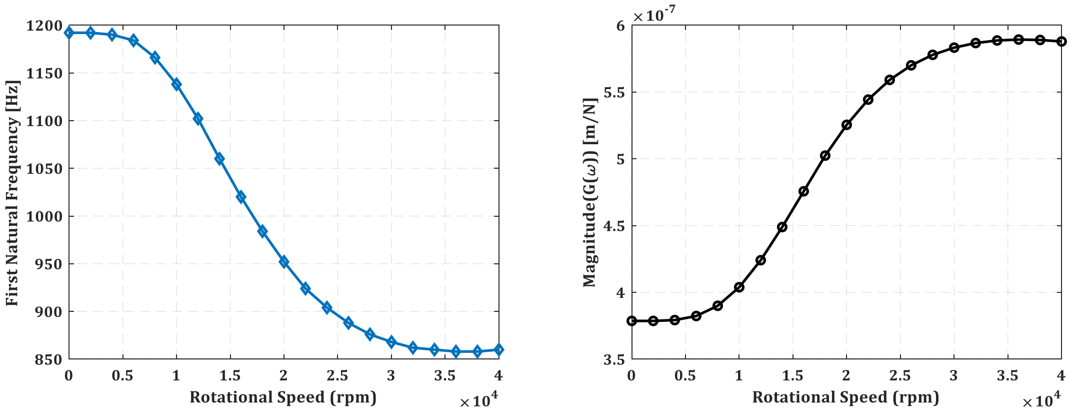

Figure 7.12: Variation of first mode frequency and FRF amplitude for different rotational speed using the analytical approach.

In order to identify the effect of the rotational speed on spindle FRF, the FRF measurements are performed on the spindle shaft tip after a sufficient time of rotation at the specific speed, as listed in Table 7.5. Firstly, the spindle FRF is measured at an idle state (Condition 1). Then for each condition spindle is rotated at the defined operation time. The spindle operated at each condition for approximately 5 minutes, allowing the spindle bearings to reach stable thermal conditions. At the end of each operation, the spindle stopped, and the FRF measurements were performed on the shaft tip.

Table 7.5: Conditions for speed variation experiments.

Condition	Operation Time (min)	Rotational speed (rpm)
1	Approx. 5 mins	0
2	Approx. 5 mins	5000
3	Approx. 5 mins	10000
4	Approx. 5 mins	15000
5	Approx. 5 mins	20000

The experiments are performed by the project partner and results are depicted in Figure 7.13. For idle state (zero speed), the comparison between the experiments and the simulations are quite similar, as depicted in Figure 7.11. For other rotational speeds, the comparisons are given in Figure 7.14. It is seen that up to 10K rpm, there is a small different between the experimental and simulation results, which can be neglected.

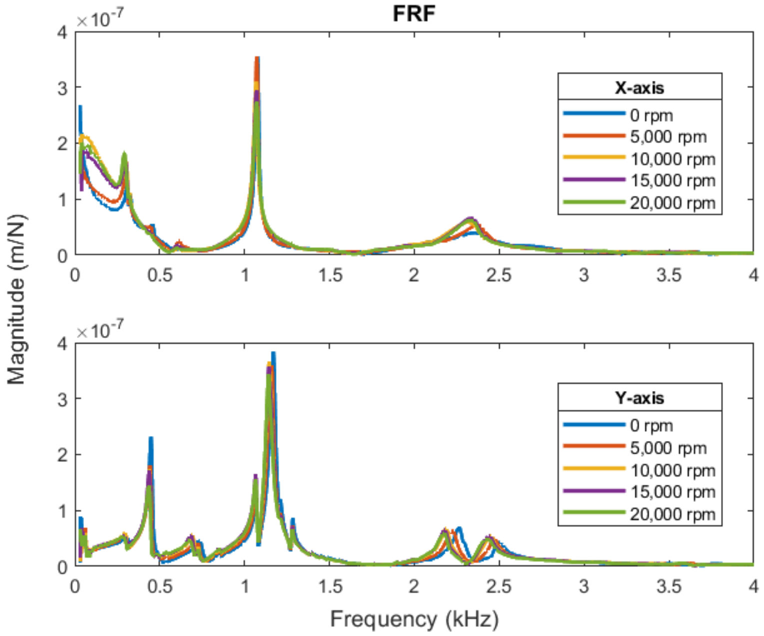

Figure 7.13: FRF measurements at different rotational speeds.

However, despite the simulation results in which the bearing stiffness and natural frequencies are decreasing at higher speeds, experimental results show that by increasing rotational speed, bearing stiffnesses are increased, leading to a decrease in peak FRF amplitudes. This phenomenon could be because the simulations consider the in-situ dynamics of the rotating bearing. For FRF measurements, the spindle is stopped, and the measurements are performed on a stationary shaft. In other words, the friction, gyroscopic forces, and contact angles of the bearing are affected drastically by the rotational speed increase, which affects the bearing and shaft dynamics. However, in the present experiments, the spindle is rotated at a certain amount of operational time to provide sufficient time for the thermal stability of the bearings. According to the experimental results in Figure 7.13, it is seen that the frequency change is not significant, but despite the simulation results, the FRF peak amplitude is decreasing. This conclusion can be drawn that the only reason for FRF reduction is the decrease in the damping coefficient.

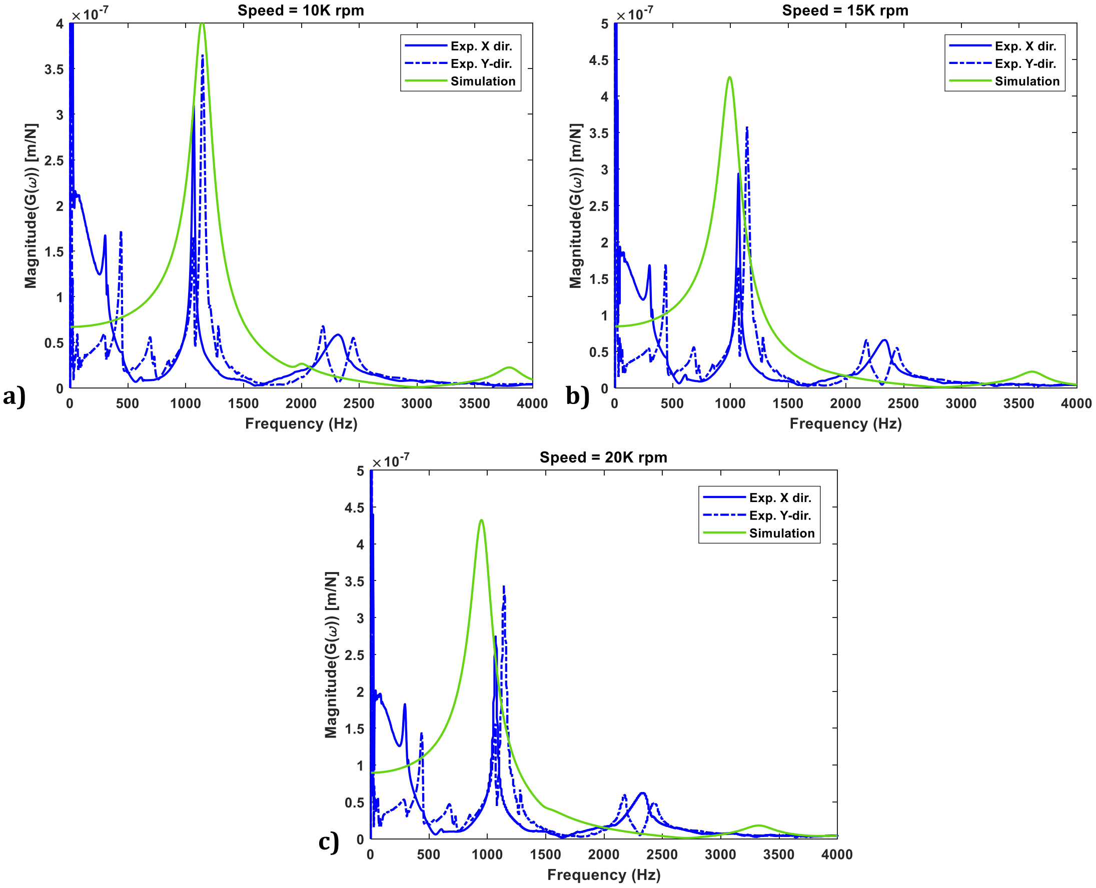

Figure 7.14: Comparison of experimental and simulation FRFs at different rotational speeds. a) at 10K rpm, b) at 15K rpm, c) at 20K rpm

7.2.4. Sensitivity Analyses of Spindle Parameters

Spindle dynamic performance is affected by several parameters. Variations in any of these parameters produce notable changes in the FRF peak magnitudes and natural frequencies of the structure, which are critical indicators of dynamic performance.

The analyses are based on the coupled-fully-analytical shaft-bearing model in Sections 7.2.1 and 7.2.2. Although the rigidity of a spindle can be affected by bearings' specifications, this study only focuses on the parameters regarding the shaft-bearing assembly, regardless of the bearings' specifications in Table 7.1. For this analysis, two important parameters are shortlisted for sensitivity checks owing to their potential benefits in terms of structural rigidity.

7.2.4.1. Bearing Locations

This section aims to investigate the effect of spindle locations on spindle and tool point

FRFs, as well as chatter stability of the process. This study is performed by varying the location of the bearing pairs on the spindle shaft with respect to shaft tip and shaft end (Figure 7.15). In this part, in a real spindle is considered as a case study adopted from [88]. The original dimensions of the shaft are given in Table 7.6 and illustrated schematically in Figure 7.15

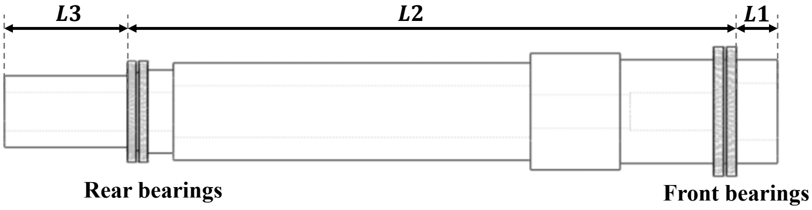

Figure 7.15: Schematics of the spindle and bearings.

Different spindle designs are studied by varying the $L1$ and $L3$ which correspond to the front and rear bearing set locations measured from the shaft tip and end, respectively. Note that, for the given spindle the front bearings are located on segments 2 and 3 and the rare bearings are located on segments 10 and 11.

Table 7.6: Spindle dimensions with sub-segments

Segment No.	Length (mm)	Outer Diameter (mm)	Inner Diameter (mm)
1	32	80	45
2	8	80	40
3	8	80	35
4	22	80	30
5	45	80	30
6	8	80	27
7	70	90	27
8	279	75	41
9	20	64	31
10	8	60	31
11	8	60	31
12	66	55	31

Although the bearing set locations can be varied in a limited amount because of the space limitations on the shaft, their impact on FRF is important in terms of process stability and, thus, productivity. According to the allowable ranges that the spindle design dictates, 30 different cases are examined, and the respective FRFs are calculated. The most extreme cases are chosen, and the corresponding FRFs are depicted in Figure 7.16. The spindle design dimensions for these cases are given in Table 7.7. From simulation results, it can be concluded that the peak spindle tip FRF decreases, i.e., its rigidity increases, when both bearing sets are close to the spindle tip. On the contrary, the most flexible case is obtained when both bearing sets are close to the spindle shaft end. The closer bearing sets to the spindle tip reduces the amplitude of the vibration response at the spindle shaft tip, resulting in a more rigid structure and lower FRF peak. Other combinations result in FRFs between ones for Case 1 and Case 2.

Table 7.7 Spindle design dimensions for the most extreme cases.

	L1 (mm)	L2 (mm)	L3 (mm)
Case 1	22	404	146
Case 2	62	464	46

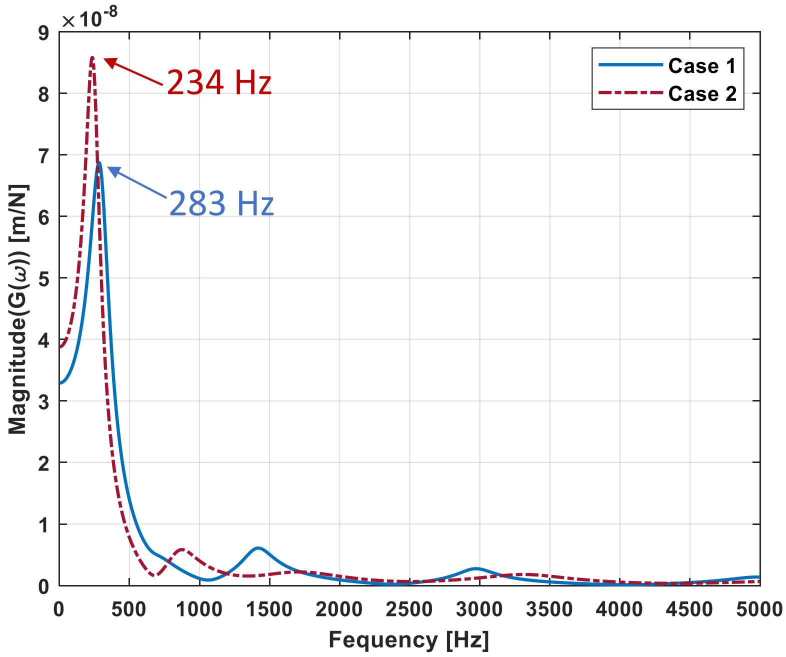

Figure 7.16: Calculated spindle tip FRFs for two different spindle designs in Table 7.7.

In order to have a better understanding of the effect of spindle dynamics on the machining stability and productivity, the tooltip FRFs for both cases have been obtained by coupling the tool-holder-spindle FRFs. The FRFs of the tool and holder is obtained using receptance coupling as mentioned in 7.2.2. Furthermore, the elastic coupling at the tool-holder and holder-spindle interfaces is also performed using the receptance coupling approach as described in [94,96]. Note that the tooltip FRFs for the given spindle were confirmed by Ozsahin [88] by identifying the bearing dynamics and contact dynamics using hammer tests and error minimization techniques and given in Appendix C: Tool-holder Dimensions and Dynamic properties. The tool and holder dimension identified contact parameters at the spindle-holder and holder-tool interface, and the identified bearing dynamic for this case study are given in Appendix C: Tool-holder Dimensions and Dynamic properties. As it can be seen from the FRFs given for both cases, The third mode, which is dominated by the tool, is not affected by the spindle design.

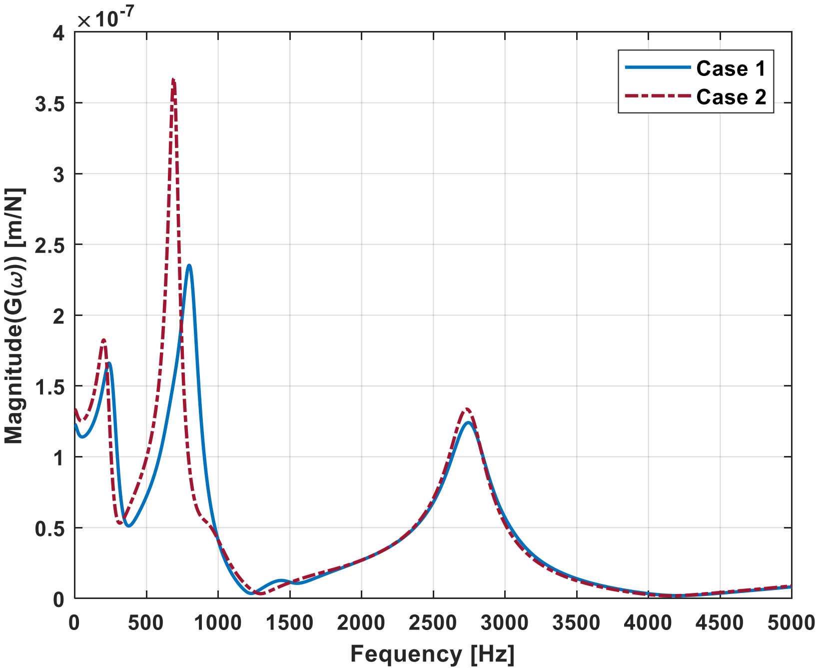

Figure 7.17: Calculated tool point FRFs for the two different spindle designs.

On the other hand, the first and the second modes are significantly affected by the spindle design as they are related to the spindle and the holder, respectively. The stability diagrams are calculated and compared based on the given tooltip FRFs for each case. It is shown that different spindle dynamics cause a drastic change in the stability diagrams, as shown in Figure 7.18.

It can be deduced that by keeping the tool and holder assembly identical, a spindle design with flexible dynamics decreases the stability limit. As shown in Figure 7.18, the peak and absolute limits are significantly reduced for case 2 due to flexible spindle dynamics.

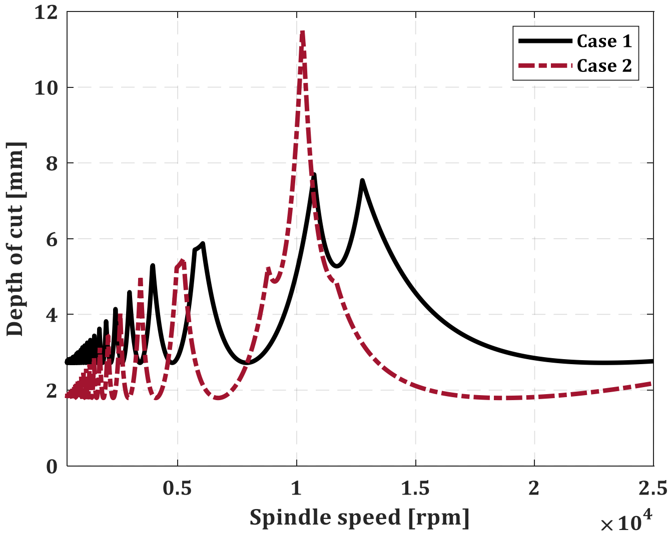

Figure 7.18: Stability diagrams based on the tool point FRFs of each case in Table 7.7.

7.2.4.2. Tail Length

The “tail” in a spindle refers to the length from the rare earing to the shaft end (indicated as L_3 in Figure 7.15. In this part, spindle dimensions given in 7.2.3 is taken as the case study. Considering that the bearing locations are in the most rigid condition, the structural analysis was performed by varying the tail length. The sensitivity check of the tail length was initially performed by introducing small variations of 10 mm. However, these failed to yield discernible results, indicating that small changes in the tail length are insignificant in terms of dynamics and rigidity. Figure 7.19 shows the various simulations run for larger variations in the tail length. The base value of the tail may be taken as 10mm. Several simulations are performed for comparison purposes. The results may be split into below 70 mm and above 70 mm. For tail lengths shorter than 70 mm, it is observed that the spindle becomes more rigid as peak FRFs slightly decrease while the natural frequencies remain approximately the same. After 70 mm, the second mode shows splitting tendencies as a third peak appears between the previous two.

It is observed that the peak FRF shows a decreasing trend with increasing tail length. At a tail length of approximately 80 mm, the mode splitting phenomenon is observed at the first mode. Initially, the two new peaks appear at a reduced magnitude. As the tail length is further increased to 90 mm, one of the peaks rises sharply. This observation indicates that there is the favorable region for the tail length where the mode splitting phenomenon can be exploited to improve dynamic performance. As a result, considering the amplitude of both peaks of the first mode, it is seen that the tail length of 86 mm is the most rigid case in terms of the average of the splitted modes peaks. Figure 7.15 shows that the first mode splits into two peaks, the higher of which is 25% less in magnitude than the peak for the original tail length.

The variation in each parameter is decided based on practical reasons such as physical limitations of the assembly, product availability, and intuition.

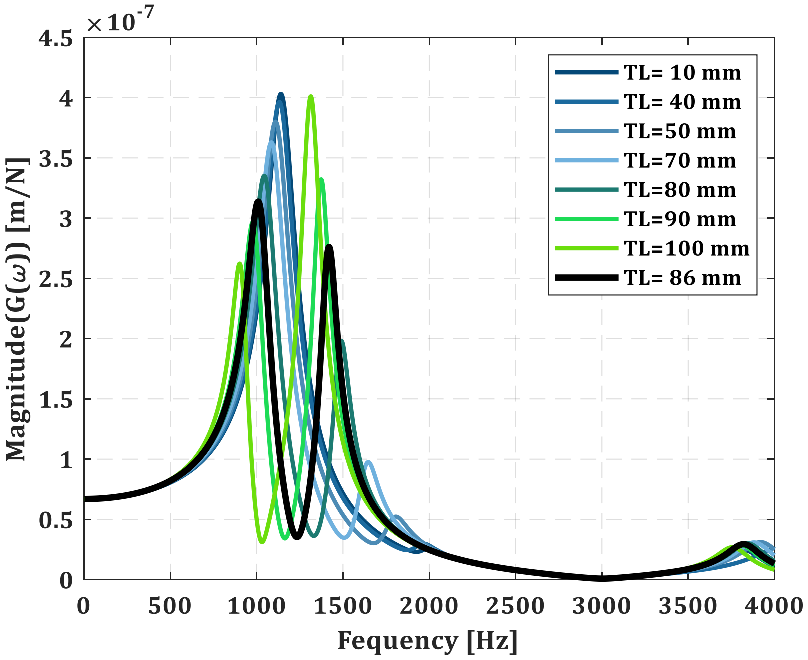

Figure 7.19: Spindle tip FRFs for different tail length.

7.3. Workpiece Dynamics

As another key factor in the stability of the process, workpiece dynamics must be identified precisely in order to have an accurate stability prediction. While the dynamics of a tool and spindle remain constant during the process, workpiece dynamics alter due to the material removal effect. As the tool removes the material from the rotating workpiece. The volume hence the mass of the workpiece, changes continuously. Therefore, the dynamic response of the workpiece may vary continuously during the operations. This variation also changes along the workpiece. This phenomenon is more effective in slender and flexible geometries. Based on the dimensions of the workpiece, its dynamics can be as flexible as or much more flexible than the tool-holder-spindle assembly. When the workpiece is clamped on the chuck, it can either be supported by the tailstock at the free end or not, leading to different boundary conditions. In both cases, workpiece dynamics and corresponding mode shapes exhibit different behaviors, affecting process stability.

Since it is not feasible and convenient to measure the in-process workpiece dynamics during the cutting operation at each set-up, analytical approaches must be used to calculate the FRFs.

In this chapter, in order to calculate the workpiece dynamics, receptance coupling [143] to predict the workpiece dynamics. As mentioned in Section 7.2.2, the workpiece is divided into subcomponents where the dynamics of each component are obtained using the analytical solution of the Timoshenko beam (See Figure 7.7). Similar to the receptance coupling of the subcomponents of the shaft explained in Section 7.2.2, each subcomponent of the workpiece with a specific length and diameter is coupled as illustrated in Figure 7.20. By coupling beams of different diameters and lengths together, the receptance matrices of main components of the shaft can be calculated as given in equation (7.20). Obviously, the multi-segment components built this way will have free–free boundary conditions. However, the workpiece as a beam is clamped to the chuck. This implies adding dynamics of the chuck to the workpiece at the contact locations as springs and dampers. Similar to the shaft modeling, the dynamics of the contact point between the workpiece and chuck are included in the system by using the Structural Modification approach [142].

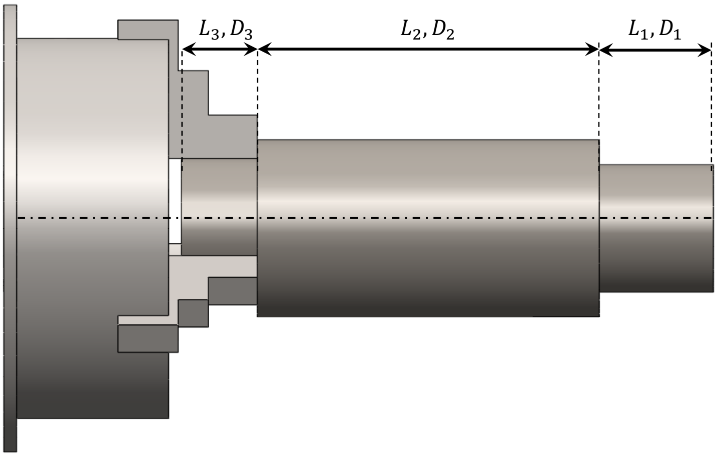

Figure 7.20: subcomponents of a clamped workpiece.

Since the receptance coupling method allows the computation of end point receptances only, the clamping length (L_3) (contact interface between the workpiece and jaws) is divided into two substructures, as shown in Figure 7.21. As a result, in the cylindrical workpiece shown in Figure 7.20, we have four effective segments instead of a three-segmented beam. However, unlike structural modification in spindle-shaft assembly, in this approach, the rotational stiffness, rotational complex damping, and the corresponding cross terms (off-diagonal) terms are eliminated since the moment effect is neglected. As a result, after rearrangement of the receptance matrix of the coupled segments I and II illustrated in Figure 7.21, the structural modification matrix, which includes the translational stiffness and damping information of the contact, can be written as follows;

$$[\mathcal{D}] = \begin{bmatrix} 0 & 0 & 0 & 0 \\ 0 & K_y & 0 & 0 \\ 0 & 0 & 0 & 0 \\ 0 & 0 & 0 & 0 \end{bmatrix} \tag{7.26}$$

where $K_y = ky + i\omega c_y$ is the translational complex stiffness expression, representing the stiffness and damping at the workpiece-jaw interface.

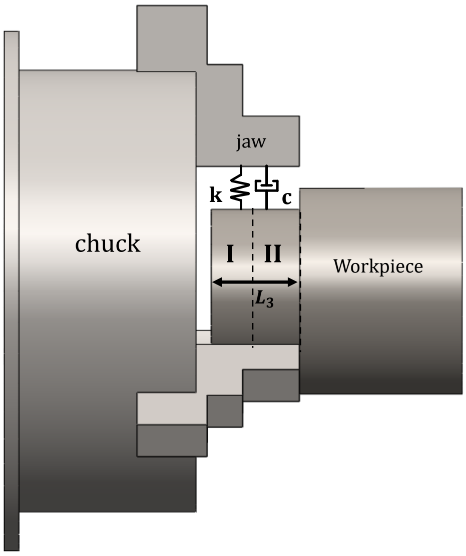

Figure 7.21: Addition of contact dynamics to the system by structural modification.

The modified receptance matrix of substructure 3 can be calculates by

$$[\Gamma_C'] = \left[[I] + [\Gamma_C].[\mathcal{D}]\right]^{-1}.[\Gamma_C] \tag{7.27}$$

where $[\Gamma_C]$ is the receptance matrix of coupled segments I and II of substructure 3. Having obtained all the end point FRFs of a single segment beam by using sufficient number of modes in the summation term for each segment, one might now couple the required number of free–free beams (substructures 1 and 2) to form the desired multi-segment beam and find the endpoint FRFs of the workpiece at its tip using equation (7.20) [143].

Once the contact mechanics at jaws-workpiece interfaces are identified, one can identify the in-process workpiece dynamics during material removal operation by only updating the diameter and length of segments 1 and 2. Note that the workpiece in Figure 7.21 is drawn for a simple case. However, more segments can be defined and coupled for tool paths with several lengths and diameters.

The contact stiffness and damping identification are performed by error minimization technique between the simulation and FRF measurement. For this purpose, first, a dummy workpiece with a relatively short length is clamped to the chuck, and the FRF measurements from the workpiece tip are conducted at X_M and Y_M directions. Then the FRF of the dummy workpiece is calculated using the receptance coupling method. The contact stiffness and damping at contact stiffness are found iteratively by minimizing the error between simulated and measured FRFs. Note that, in this approach, it is assumed that the clamping pressure of the hydraulic chuck is constant at each set-up. Furthermore, the contact dynamics for each material are unique, and as the material of the workpiece changes, the contact dynamic identification procedure should be repeated.

A cylindrical part is selected as a dummy workpiece with Al7075-T6 Aluminum alloy with 60 mm in diameter and 116 mm in length. The clamping length is 40 mm. The material properties of the dummy workpiece are given in Table 7.8.

Table 7.8: Material properties of Al7075-T6.

Density $\left[\frac{kg}{m^3}\right]$	Young Modulus $[GPa]$	Poisson Ratio	Loss Factor
2710	71.6	0.33	0.0002

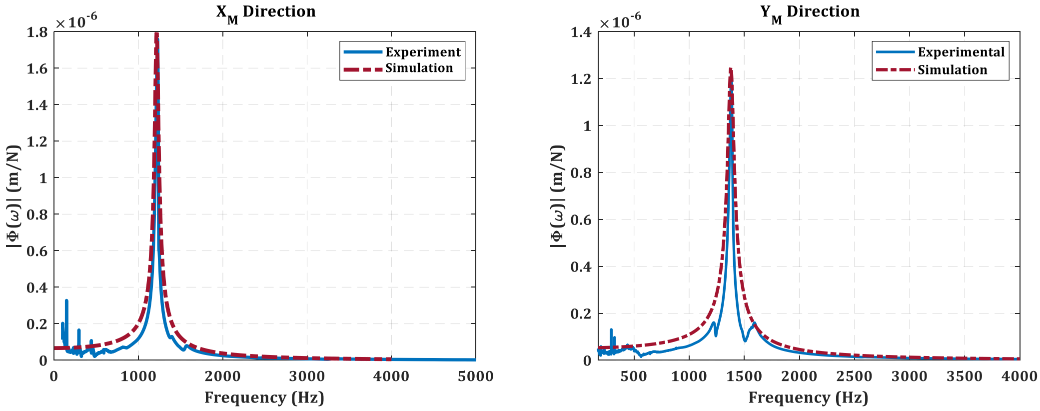

Figure 7.22: Identified FRF simulations using error minimization in X and Y directions.

After performing the identification procedure which runs several iterations to minimize the error between natural frequency and peak magnitude of the dominant mode of the simulation and measurement, the identified contact translational stiffness and damping in both directions are given as follows;

Table 7.9: Identified contact stiffness and damping at jaws-workpiece interface.

	Translational stiffness $[N/m]$	Translational damping $[N.s/m]$
X_M Direction	1.112e9	6493
Y_M Direction	1.5341e9	9593

The natural frequency of the system at X_M direction is 1223 Hz, and in Y_M direction is 1376 Hz. Another workpiece with similar material but different dimensions will be simulated to confirm the identified contact dynamics. The simulations will be compared with the experimental measurements. For this purpose, a workpiece with the dimension represented in Figure 7.23 is used as a case study. The resulted simulations and experiments are shown in Figure 7.24.

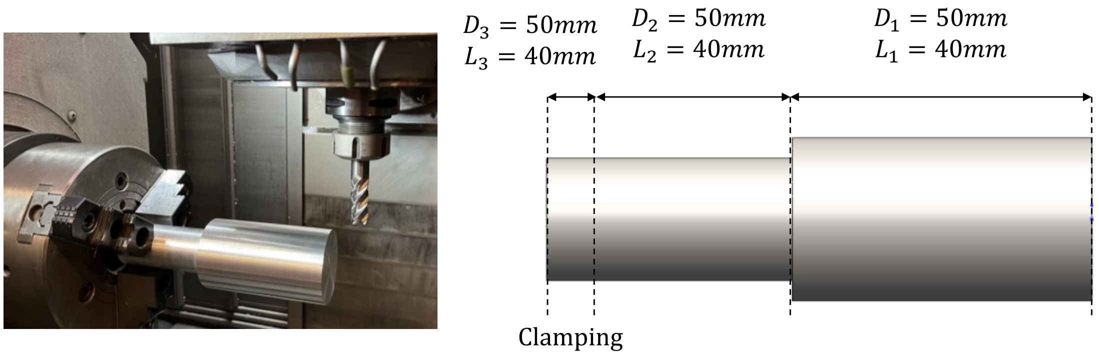

Figure 7.23: Dimensions of the tested part.

According to the simulation results, it is deduced that the predicted natural frequency values in both directions are in agreement. However, there is approximately 35% difference in FRF magnitudes of X_M direction and 50% difference in FRF magnitude in Y_M direction. In other words, the identified stiffness value affects the natural frequency with high accuracy. However, the translational damping which affects the FRF magnitude is identified with low accuracy. This can be caused by the clamping pressure variation at different part diameters, which needs to be investigated more. In addition, including rotational stiffness and damping may increase the accuracy of predictions but may increase the computational time. This issue also needs to be investigated more deeply. While there are other methods for the prediction of part dynamics, such as FEM, analytical Euler-Bernoulli, and inverse receptacle coupling, further research is needed to compare each method's accuracy and computational time when the effect of contact dynamics is included.

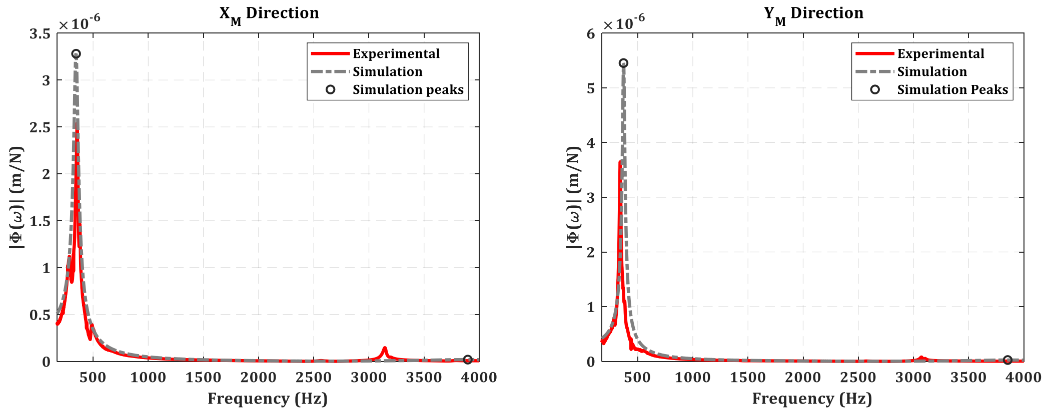

Figure 7.24: Comparison of predicted and simulation results of the part.

7.4. Summary

This chapter presents a dynamic model for predicting the frequency response of spindle and workpiece systems. The stability of a process drastically depends on the dynamic responses of the spindle-holder-tool assembly and the workpiece dynamics.

In this regard, a predictive model for bearing dynamics is presented. The frequency response function of the spindle shaft was also modeled using the receptance coupling method. By coupling the dynamics of bearing and shaft, the dynamic response of the spindle shaft tip is predicted and compared with experiments. Regarding rigidity, effective parameters such as bearing locations and tail length are analyzed.

Finally, the workpiece dynamics and the contact stiffness at the clamping interface are modeled using the receptance coupling method. The predictions are compared to experimental measurements.

8. CONCLUSIONS AND FUTURE WORKS

8.1. Conclusions and contributions

The contributions of the present thesis can be categorized under four main topics: mechanics of turn-milling, stability of turn-milling, stability of special tools, and structural dynamics of machine tools.

8.1.1. Mechanics of turn-milling

Exact chip geometry and mechanics of orthogonal turn-milling operation are presented. Based on the proposed model, cutting force predictions for standard and serrated end mills are presented and validated with experiments. It is shown that due to the simultaneous rotation of tool and workpiece, the cutter-workpiece engagement is relatively complex and additional cutting parameters are involved. As a result, the effect of each parameter on uncut chip geometry and cutting forces is different compared to conventional turning or milling. Therefore, it is vital to understand the process kinematics and mechanics in detail to achieve correct process planning as well as proper surface quality, low energy consumption, and high productivity. In this regard, specific contributions and conclusions drawn from this study are listed as follows;

- Due to simultaneous rotation of tools and workpiece, both the side and minor cutting edges of the tool are engaged during the chip removal operation. This causes a significant change in cutting forces in feed, cross-feed, and axial directions, which is important for process planning in terms of process mechanics and dynamics.

- The ratio of the tool over workpiece rotational speeds affects the uncut chip thicknesses generated by the side and minor cutting edges of the tool. As the ratio decreases, the uncut chip thickness and hence, cutting forces and torque increase.

- Eccentricity drastically affects the uncut chip geometry resulting from the side edge. The instantaneous depth of cut varies within the engagement boundaries, and the variation trend depends on the eccentricity. After a particular eccentricity value, the engagement of the side edge decreases, leading to lower MRR.

- The eccentricity alters the engagement boundaries of the minor edge. As the eccentricity increase, the engagement of the minor edge decreases. The part accuracy will be decreased for eccentricity values when the minor edge is not engaged, leading to smaller CWE and lower MRR.

- Parameter selection in turn-milling is more difficult owing to the existence of additional and special kinematic and geometric conditions due to special kinematics of the process resulted by simultaneously rotating tool and workpiece.

- The relation between eccentricity and stepover was modeled based on tool and cutting geometry. The effect of proper selection of these parameters on the surface quality is demonstrated experimentally. It is shown that a slight change in the eccentricity has a strong impact on the surface finish in turn-milling. However, using the proposed model, productivity can be doubled without sacrificing the surface quality.

- The ratio of the tool over workpiece diameters influences the uncut chip geometry as well as feed per tooth value. For constant tool radius and rotational speed ratios, the maximum feed per tooth value also increases as the workpiece radius increases.

- While eccentricity has a negligible effect on the torque and resultant force in orthogonal turn-milling, stepover affects drastically. On the other hand, both stepover and eccentricity significantly affect the axial force. Based on the combination of eccentricity and stepover, the axial force magnitude and direction can be altered drastically, which is a critical factor in the accuracy of flexible or thin-walled parts.

- A parameter selection procedure is proposed to select the proper eccentricity and stepover pair while considering the axial force magnitude and direction, surface quality with cusp prevention, and productivity. Minor edge length defines the allowable range for eccentricity and stepover and hence, the magnitude of the axial force for a specific pair of eccentricity and stepover. Higher productivities with lower axial forces are achievable for a longer minor edge.

The proposed model for cutting mechanics is confirmed for standard end mills, and the influential parameters on part accuracy, productivity, and cutting energy are discussed. This study's outcomes are significant for the development of new research possibilities in turn-milling and the implementation of high-performance.

8.1.2. Dynamics and Chatter Stability of Turn-milling

The dynamics of orthogonal turn-milling in three dimensions are modeled and studied for the first time in the literature. The dynamic chip thickness in feed, cross-feed, and axial directions resulting from the side and minor edges of the tool are modeled, and corresponding directional coefficients are formulated for the first time in the literature. The machine tool's structural dynamics are defined in modal space and coupled with the tool's and workpiece's dynamic displacements. The varying time delay caused by workpiece rotation is modeled using a novel approach. The stability of turn-milling process is solved through coupled time-varying delayed differential equation by the semi-discretization method in the discrete-time domain. The effect of varying time delays on process stability at different workpiece speeds is demonstrated. Moreover, the stability of turn-milling in the frequency domain is solved for the first time in the literature. The main contributions and conclusions of this chapter are listed as follows;

- The simultaneous workpiece and tool rotational motion produces a phase shift between the waves imprinted on the workpiece surface, resulting in a varying time delay within the engagement boundaries in the regenerative chip formation mechanism. This time delay depends on the ratio of tool and workpiece speeds, the ratio of tool and workpiece diameters, number of teeth, and axial depth of cut.
- Since the linear speed varies along the workpiece diameter, the time delay at each axial element along the tool is different. Therefore, a varying delay is distributed along the tool's axis even in turn-milling with standard tools. The delay at the tooltip is the minimum.
- As the ratio of the workpiece to tool diameters ($r_r = R_w/R_t$) increases, the time delay also decreases since the amount of phase shift at the tooth passing period is

higher due to the larger workpiece radius.

- Increase in workpiece speed (decrease in $r_s = \Omega_t/\Omega_w$), also increase the phase shift, leading to a larger phase shift, and lower time required for the current tooth to reach the surface point on the modulation left by the previous tooth, hence lower time delay.
- The stability prediction simulated in time and frequency domains showed good agreement with chatter experiments. It is seen that for the cases with a very large speed ratio (r_s) (low workpiece speed), and relatively small tool diameter in which the effect of the minor edge is negligible, the stability lobes are close to the milling process. The variation in eccentricity affects the stability lobes slightly while using end mills in turn-milling. The variation in absolute stability limit is due to the change in CWE resulting from eccentricity alteration.
- The effect of eccentricity becomes more significant in turn-milling with inserted tools. Due to the existence of offset distance between the tool center and inserts, the eccentricity and stepover must be selected according to the minor edge length and tool radius. Otherwise, cusps will be formed on the machined surface, and undesired uncut chip geometries can be formed, leading to excessive forces.
- An increase in eccentricity alters the absolute stability limit drastically because of the change in CWE of both side and minor cutting edges. Furthermore, due to the variation of chip distribution resulting from the side edge, the overall resultant and axial forces change, affecting stability limits.
- It is previously reported that lower eccentricities result in higher MRR and better surface roughness. In this study, it is also experimentally verified that lower eccentricities lead to higher absolute stability limits and hence, higher productivity. However, the allowable stepover for lower eccentricities is limited.
- As expected, larger radial immersions decrease the absolute stability limits. However, by selecting the proper stable depth of cuts inside the lobes, higher MRR can be achieved despite the lower absolute depth of cut compared to low eccentricity cases.
- High workpiece rotational speeds affect the regeneration system in turn-milling because of the smaller time delay, leading to a shift in stability lobes toward lower tool speeds. Neglecting the effect of varying time delay at different workpiece speeds and the lobe shifting phenomenon may cause chatter vibrations and hence,

tool and workpiece failure.

- The ZOA method exhibits approximately 20 times lower computational time in all conditions than SDM. Considering the negligible discrepancies, using the ZOA approach in predicting stability lobes in turn-milling is preferable.

The stability model of turn-milling operation for standard milling tools with regular geometry is presented. The proposed model and results are essential to be considered at the process planning stage to avoid poor surface quality, part accuracy, tool failure, and low MRR.

8.1.3. Mechanics and Dynamics of Special Tools

Special tools are implemented in the turn-milling process. The mechanics and dynamics of serrated and crest-cut tools are investigated during turn-milling operation. The mechanics of turn-milling is upgraded to be able to adopt the particular CWE and uncut chip thicknesses for serrated and crest-cut tools. The varying time-delay model of turn-milling is also upgraded to calculate the distributed time delays along with the crest-cut tools during turn-milling operation. While the system's stability is solved with SDM, the ZOA method is used to calculate the stability of crest-cut tools for the first time in the literature. Some findings are listed as follows;

- The application of serrated tools decreases the cutting forces and torque due to a reduction in engagement distribution along with the cutting depth due to the serrated edge geometry. The serrated tools cause a reduction in forces in feed and cross-feed directions more than in axial direction.

- Turn-milling forces resulting from crest-cut tools are predicted and confirmed with experimental results for the first time in the literature. Accurate cutting force predictions are obtained considering cutter-workpiece engagement and local cutting force coefficients. Unlike standard milling tools, crest-cut end mills produce non-periodic cutting forces.
- Crest-cut tools produce significantly smooth axial cutting forces, which may be beneficial in machining thin-walled pockets.

- Due to the local pitch and helix angle variation along the axis of crest-cut tools, the entry and exit angles and the time delay are different for each element on each tooth. Therefore, at any axial level, the average delay for each tooth is different.
- Since it is required to use average time delay for ZOA, the error between stability lobes calculated by SDM and ZOA increased.
- Considering that the computation time for crest-cut tools is higher than the standard tools for both methods due to the higher number of delays, the ZOA method stills offers a shorter computation time than SDM.
- Due to the high number of distributed delays imposed by crest-cut tools on the dynamic system, the regeneration mechanism is disturbed, leading to higher absolute stability limits.
- The wavy edge shapes on crest-cut tools increase the intermittence nature of engagement due to the varying delay and local pitch angles. Therefore, especially in lower-immersion engagements, the higher harmonics of the cutting forces can be dominant, leading to flip bifurcation type of instability. As a result of higher harmonics, added lobes were seen in the stability diagram of crest-cut tools, which are significantly helpful in achieving higher productivity.
- Crest-cut tools also offer significant improvements in machining thin-walled structures. Surface finish quality maps show that the crest-cut tool has superior performance considering the surface quality and productivity. Variable pitch tools may suppress chatter in one of the plate modes. Still, they lose their effectiveness on different cutter-location points due to frequency variations of multiple modes under mass removal effects. On the other hand, crest-cut tools provide much higher stability limits in a wide frequency range with high robustness against frequency variation.
- While calculating the stability of thin-walled structures, it is essential to include in-process workpiece dynamics to obtain precise predictions.

Crest-cut tools exhibit superior advantages compared to standard and variable-pitch tools in terms of process stability and productivity.

8.1.4. Structural Dynamics of Machine Tools

As the main contributors to process dynamics and stability, having a predictive model for dynamics of the spindle and workpiece systems is vital. Although the dynamic of the workpiece and spindle-holder-tool assembly can be performed throughout experimental impact hammer testing before the process, the in-process identification of their dynamic behavior is impossible. In order to model the spindle under operational conditions at different speeds, a predictive model is proposed. In this model, the dynamic model of the bearings is coupled with the analytic shaft's dynamic model based on receptance coupling. Moreover, the workpiece dynamics were also modeled using a similar approach. The conclusions are given as follows;

- The translational and rotational stiffnesses of the bearings have a decreasing manner as the speed increases. However, they increase as the preload increases.
- During the validation of our model with experiments, it is observed that including the cross-stiffness (off-diagonal terms) significantly increases predictions' accuracy.
- As the rotational speed increases, the system's natural frequency decreases, and the system becomes more flexible due to the reduction in stiffness. However, if the other parameters like thermal effects are included, this trend could be altered.
- In a typical spindle, as the location of both bearing sets become closer to the shaft tip, the system will have more rigidity and hence, more stability.
- The tail length of the spindle has an optimum length that exhibits lower FRF peak amplitude as well as divided modes. The mass-damper effect of the shaft tail improves the spindle rigidity; hence, less chatter vibrations and more productivity can be achieved.
- In-process workpiece dynamics using receptance coupling show a good agreement between experiments in terms of natural frequency. However, the required contact damping varies from part to part at each set-up.

8.2. Future Research Directions

Based on the presented mathematical models and the experimental validations, this thesis's outcomes can be considered a validated foundation for future advanced research in turn-milling technology. Although the proposed models can predict the process mechanics and dynamics, several aspects can still be investigated. The further research potentials in turn-milling, special tool technologies, and structural dynamics are listed as follows;

- Effects of minor edge geometrical parameters, such as hone radius, oblique angle, clearance, etc., on surface quality, cutting temperature, and process damping can be studied.
- The surface integrity of parts with hard-to-cut material machined using orthogonal turn-milling and conventional turning can be examined and compared. The residual stresses on the machine part can be obtained. The effect of eccentricity and tool geometry can be influential during process planning and optimization to achieve higher accuracy.
- A parameter optimization study can be carried out to investigate the best parameters in turn-milling highly flexible parts such as long shafts or thin-walled tubes to achieve improved productivity and surface quality and lower dimensional errors.
- A specific tool for orthogonal turn-milling can be designed considering the minor and side edge parameters for reduced cutting forces and improved productivity.
- The in-process workpiece dynamics of highly flexible parts can be considered in the stability model of turn-milling. The varying stability limit can be added to the global optimization problem as an additional constraint.
- Based on the calculated cutting forces, the temperature model must be investigated. The temperature model can be used either in predicting tool wear or predicting residual stresses. This study will help to fully benefit from turn-milling technology’s advantages over conventional turning operations.
- Special tools like crest-cut and serrated tools can also be implemented in other turn-milling configurations such as tangential and co-axial to investigate the surface quality and stability.
- Process damping of special tools in turn-milling by considering the damping effect

of both side and minor edges can be studied to benefit from its impact in machining hard-to-cut materials.

- The thermal model of the spindle can be combined with the proposed model to capture the effect of generated heat on spindle dynamics. The optimized spindle design can be obtained by considering the dynamic and temperature model at the same time.

APPENDICES

Appendix A: Orthogonal databases

- **Al7075-T6 Alloy**

Table A1: Orthogonal parameters for Al7075-T6

Orthogonal parameters	$\tau'_s = 297.1 + 1.1\alpha_n$ $\beta'_n = 18.8 + 6.7h + 0.0076V_c + 0.26\alpha_n$ $\phi'_s = 24.2 + 36.7h + 0.005V_c + 0.3\alpha_n$
Edge Force Coefficients	$K_{te} = 23.4\frac{N}{mm}, K_{re} = 35.2\frac{N}{mm}$

where τ'_s is shear stress (MPa), β'_n is friction angle (deg), ϕ'_s shear angle (deg), α_n is rake angle (deg), h is feed (mm), V_c is cutting speed (m/min), K_{te} is edge force coefficient in tangential, and K_{re} is edge force coefficient in radial direction.

- **AISI 1045 steel**

Table A2: Orthogonal parameters for AISI 1045

Orthogonal parameters	$\tau'_s = st(1) * \exp(V_c * st(2)) + st(3) * h$ $\beta'_n = f(1) * \exp(V_c * f(2)) + f(3) * h$ $\phi'_s = sa(1) * \exp(V_c * sa(2)) + sa(3) * \exp(h^{sa(4)})$ $f = [33.753, -0.00123, -7.33]$ $sa = [10.342, 0.001236, 10.912, 0.35]$ $st = [524.95, 0.0005302, -21.72]$
Edge Force Coefficients	$K_{te} = 35\frac{N}{mm}, K_{re} = 42\frac{N}{mm}$

where τ'_s is shear stress (MPa), β'_n is friction angle (deg), ϕ'_s shear angle (deg), α_n is rake angle (deg), h is feed (mm), V_c is cutting speed (m/min), K_{te} is edge force coefficient in tangential, and K_{re} is edge force coefficient in radial direction.

Appendix B: Nyquist Stability Criterion

Considering a characteristic equation in general form of $CH(s) = \det[I + (J + Je^{-st} + Js)\Phi(s)] = 0$, $\Lambda(s) = (J + Je^{-st} + Js)$, the stability analysis can be performed by analyzing its Nyquist plot. Poles of the characteristic equation $CH(s)$ are the poles of the structure (Φ) which are all stable. Any unstable zero of the characteristic equation $CH(s)$ creates a clockwise encirclement of the origin of complex plane by Nyquist mapping of the characteristic equation. Unstable zeros of the characteristic equation are unstable poles of the system, as the characteristic equation appears in the denominator of the input-output transfer functions in the closed loop system.

Therefore, it is sufficient to count the encirclements for mapping of the positive imaginary axis. This is equivalent to replacing s with $j\omega$ where ω is a nonnegative real number. It can be seen that $\Lambda(j\omega)$ forms a spiral shape with varying diameter; the circling is mostly due to the phase contribution of the complex exponential term.

$$e^{-iT\omega} = \cos(T\omega) - i\sin(T\omega)$$

Nyquist plot of two stable and unstable time delay systems with similar transfer functions are plotted in

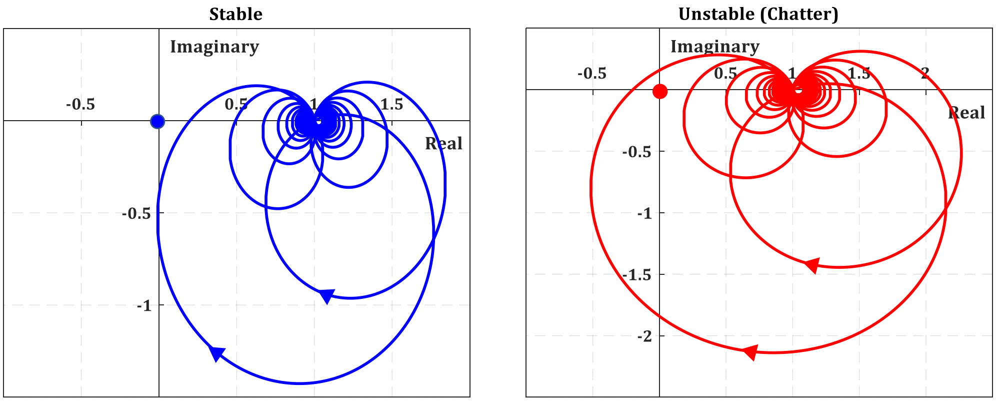

Stable

Unstable (Chatter)

Figure B1: Nyquist plots in complex plane for stable and unstable cases.

Although Nyquist contour is a continuous path, it is drawn using discrete frequencies on a digital computer. In addition, the frequency response function of the system $(\Phi(\omega))$ is also measured or simulated as a function of discrete frequencies. Therefore, the Nyquist contour is determined as a set of points. The frequency resolution is important to determine correct stable or unstable cases. Lower frequency resolutions may result in incorrect results. The unstable case in Figure B1 is plotted with lower frequency resolution. It is seen that, with lower frequency resolution, the Nyquist contour does not encircle the origin and the plot implies a stable condition. However, it is in fact an unstable condition.

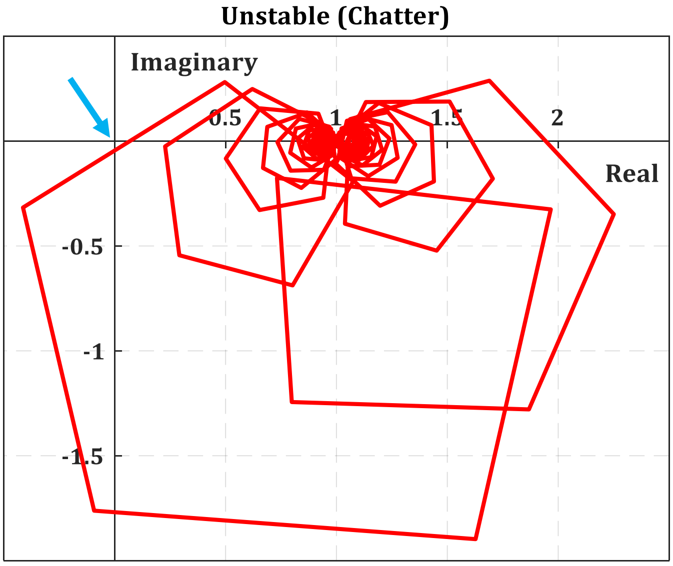

Figure B2: Similar condition in Figure B1 with lower frequency resolution.

In order to detect stable or unstable conditions, the following algorithm is applied:

1. Select a range of frequency to be swept that covers the flexible modes of the system with reasonable resolution $\omega_{min} \leq \delta\omega \leq \omega_{max}$.
2. Set the counter ($n = 1$), and calculate $CH0 = CH(i\omega_n)$
3. While $\omega_n < \omega_{max}$ do the following steps:

   Calculate $CH1 = CH(i\omega_{n+1})$

   a. If $CH0$ is in the third quadrant of complex plane $(\mathrm{Re}(CH0) < 0, \mathrm{Im}(CH0) < 0)$, while $CH1$ is in second quadrant $(Re(CH1) < 0, IM(CH1) \geq 0)$. The contour crosses the negative real axis (encircles the origin) and the condition is unstable.

   b. If $CH0$ is in the third quadrant and $CH1$ is in the first quadrant, calculate the approximate intersection point with the real axis using the two consecutive points in each quadrant. A line interpolation can be used between these points. If the intersection point with real axis has a negative part, then go to the step 4.

4. End.

Appendix C: Tool-holder Dimensions and Dynamic properties

Table C1: Holder segments and dimensions [88].

Segment No.	Length (mm)	Outer Diameter (mm)	Inner Diameter (mm)
1	26	63	21
2	34	50	21
3	24.5	50	25
4	17	44.5	25
5	6	63.5	25
6	3	56	25
7	6	63.5	25

Table C2: Tool segment dimensions [88].

Segment No.	Length (mm)	Outer Diameter (mm)	Inner Diameter (mm)
1	20	16	0
2	25	20	0

Table C3: Contact parameters at the spindle-holder and holder-tool interfaces [88].

	Translational Stiffness	Rotational Stiffness	Translational Damping	Rotational Damping

	(N/m)	(N.m/rad)	(N.s/m)	(N.m.s/rad)
Spindle - holder interface	12.6×10^{7}	1×10^{6}	50	170
Holder - tool interface	8×10^{7}	1.5×10^{6}	100	100

Table C4: Dynamic properties of bearings [88].

	Translational Stiffness (N/m)	Rotational Stiffness (N.m/rad)	Translational Damping (N.s/m)	Rotational Damping (N.m.s/rad)
Front bearing	$1.45\text{x}10^{6}$	$3.83\text{x}10^{6}$	3500	10
Rear bearing	$1.02\text{x}10^{8}$	$1.5\text{x}10^{6}$	1000	10

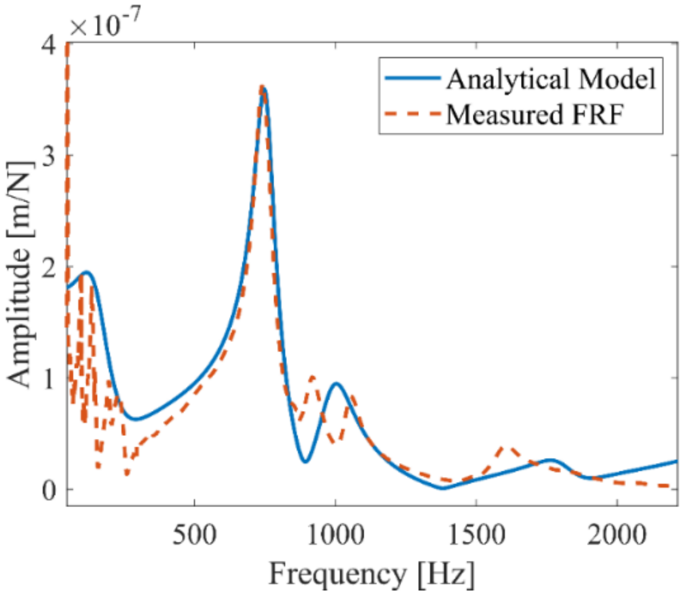

Figure C1: Calculated and measured tool point FRFs at idle state of the machine [88].

REFERENCES

[1] M. Mori, A. Hansel, M. Fujishima, Machine Tool BT - CIRP Encyclopedia of Production Engineering, in: L. Laperrière, G. Reinhart (Eds.), Springer Berlin Heidelberg, Berlin, Heidelberg, 2014: pp. 792–801. https://doi.org/10.1007/978-3-642-20617-7_6533.

[2] K.R. Berenji, M.E. Kara, E. Budak, Investigating High Productivity Conditions for Turn-Milling in Comparison to Conventional Turning, Procedia CIRP. 77 (2018) 259–262.

[3] W. Xin, D. Wenfeng, Z. Biao, A review on machining technology of aero-engine casings, J. Adv. Manuf. Sci. Technol. 2 (2022) 2022011.

[4] H. Schulz, G. Spur, High speed turn-milling—a new precision manufacturing technology for the machining of rotationally symmetrical workpieces, CIRP Ann. Technol. 39 (1990) 107–109.

[5] H. Schulz, T. Kneisel, Turn-milling of hardened steel-an alternative to turning, CIRP Ann. 43 (1994) 93–96.

[6] S.K. Choudhury, K.S. Mangrulkar, Investigation of orthogonal turn-milling for the machining of rotationally symmetrical work pieces, J. Mater. Process. Technol. 99 (2000) 120–128.

[7] S.K. Choudhury, J.B. Bajpai, Investigation in orthogonal turn-milling towards better surface finish, J. Mater. Process. Technol. 170 (2005) 487–493.

[8] S. Ekinović, E. Begović, A. Silajdžija, Comparison of machined surface quality obtained by high-speed machining and conventional turning, Mach. Sci. Technol. 11 (2007) 531–551.

[9] Y.L. Cai, C. Huang, J.Y. Li, Experimental study of cutter wear based on turn-milling, in: Appl. Mech. Mater., Trans Tech Publ, 2012: pp. 538–541.

[10] E. Uysal, U. Karaguzel, E. Budak, M. Bakkal, Investigating eccentricity effects in turn-milling operations, Procedia CIRP. 14 (2014) 176–181.

[11] U. Karaguzel, E. Uysal, E. Budak, M. Bakkal, Effects of tool axis offset in turn-milling process, J. Mater. Process. Technol. 231 (2016) 239–247.

[12] U. Karagüzel, E. Uysal, E. Budak, M. Bakkal, Analytical modeling of turn-milling process geometry, kinematics and mechanics, Int. J. Mach. Tools Manuf. 91 (2015) 24–33.

[13] S.M. Yuan, W.W. Zheng, The surface roughness modeling on turn-milling process and analysis of influencing factors, in: Appl. Mech. Mater., Trans Tech Publ, 2012: pp. 1614–1620.

[14] L. Zhu, H. Li, W. Wang, Research on rotary surface topography by orthogonal turn-milling, Int. J. Adv. Manuf. Technol. 69 (2013) 2279–2292.

[15] V. Savas, C. Ozay, Analysis of the surface roughness of tangential turn-milling for machining with end milling cutter, J. Mater. Process. Technol. 186 (2007) 279–

283.

[16] V. Savas, C. Ozay, The optimization of the surface roughness in the process of tangential turn-milling using genetic algorithm, Int. J. Adv. Manuf. Technol. 37 (2008) 335–340.

[17] V. Savas, C. Ozay, H. Ballikaya, Experimental investigation of cutting parameters in machining of 100Cr6 with tangential turn-milling method, Adv. Manuf. 4 (2016) 97–104.

[18] R. Funke, A. Schubert, Increase of the coefficient of static friction using turn-milling with an inclined milling spindle, Procedia CIRP. 45 (2016) 83–86.

[19] B. Karpuschewski, C. Döbberthin, K. Risse, L. Deters, Analysis of the textured surface of tangential turn-milling, Mater. Perform. Charact. 6 (2017) 182–194.

[20] C. Neagu, M. Gheorghe, A. Dumitrescu, Fundamentals on face milling processing of straight shafts, J. Mater. Process. Technol. 166 (2005) 337–344.

[21] W. Wang, F.Y. Peng, R. Yan, X.Y. Duan, Iso-scallop Toolpath Generation for Orthogonal Turn-Milling of Ruled Surfaces, in: Adv. Mater. Res., Trans Tech Publ, 2012: pp. 436–440.

[22] U. Karaguzel, M. Bakkal, E. Budak, Process modeling of turn-milling using analytical approach, Procedia CIRP. 4 (2012) 131–139.

[23] Z. Jiang, X. Liu, X. Deng, Modeling and simulation on surface texture of workpiece machined by tangential turn-milling based on matlab, in: 2011 2nd Int. Conf. Artif. Intell. Manag. Sci. Electron. Commer., IEEE, 2011: pp. 4072–4075.

[24] K. Rahimzadeh Berenji, U. Karagüzel, E. Özlü, E. Budak, Effects of turn-milling conditions on chip formation and surface finish, CIRP Ann. 68 (2019) 113–116. https://doi.org/10.1016/j.cirp.2019.04.067.

[25] J.M. Crichigno Filho, Prediction of cutting forces in mill turning through process simulation using a five-axis machining center, Int. J. Adv. Manuf. Technol. 58 (2012) 71–80.

[26] L. Zhu, H. Li, C. Liu, Analytical modeling on 3D chip formation of rotary surface in orthogonal turn-milling, Arch. Civ. Mech. Eng. 16 (2016) 590–604.

[27] W. Qiu, Q. Liu, S. Yuan, Modeling of cutting forces in orthogonal turn-milling with round insert cutters, Int. J. Adv. Manuf. Technol. 78 (2015) 1211–1222.

[28] C. Yonglin, M. Yemeng, H. Chao, Y. Xiangkai, Swept area modeling and cutter wear study in turn-milling, Int. J. Adv. Manuf. Technol. 80 (2015) 775–789.

[29] A. Comak, Y. Altintas, Mechanics of turn-milling operations, Int. J. Mach. Tools Manuf. 121 (2017) 2–9.

[30] H. Otalora-Ortega, P.A. Osoro, P.J.A. Arriola, Analytical modeling of the uncut chip geometry to predict cutting forces in orthogonal centric turn-milling operations, Int. J. Mach. Tools Manuf. 144 (2019) 103428.

[31] T. Sun, L. Qin, Y. Fu, C. Liu, R. Shi, Mathematical modeling of cutting layer geometry and cutting force in orthogonal turn-milling, J. Mater. Process. Technol. 290 (2021) 116992.

[32] S.A. Tobias, W. Fishwick, Theory of regenerative machine tool chatter, Eng. 205

(1958) 199–203.

[33] J. Tlusty, M. Polacek, The Stability of the Machine Tool Against Self-Excited Vibration in Machining, ASME Int. Res. Prod. 1 (1963) 465–474. https://doi.org/citeulike-article-id:4000165.

[34] H.E. Merrit, Theory of self-excited machine-tool chatter, Trans. ASME, J. Eng. Ind. 87 (1965) 447.

[35] J. Tlusty, F. Ismail, Basic non-linearity in machining chatter, CIRP Ann. 30 (1981) 299–304.

[36] H.M. Shi, S.A. Tobias, Theory of finite amplitude machine tool instability, Int. J. Mach. Tool Des. Res. 24 (1984) 45–69.

[37] I. Minis, R. Yanushevsky, A new theoretical approach for the prediction of machine tool chatter in Milling, J. Manuf. Sci. Eng. Trans. ASME. 115 (1993) 1–8. https://doi.org/10.1115/1.2901633.

[38] Y. Altintaş, E. Budak, Analytical prediction of stability lobes in milling, CIRP Ann. 44 (1995) 357–362.

[39] T. Insperger, G. Stépán, Updated semi-discretization method for periodic delay-differential equations with discrete delay, Int. J. Numer. Methods Eng. 61 (2004) 117–141. https://doi.org/10.1002/nme.1061.

[40] T. Insperger, G. Stépán, Semi-discretization method for delayed systems, Int. J. Numer. Methods Eng. 55 (2002) 503–518. https://doi.org/10.1002/nme.505.

[41] L. Zhu, H. Zhao, X. Wang, 1424. Research on 3D chatter stability of blade by high-speed turn-milling, J. Vibroengineering. 16 (2014).

[42] R. Yan, X. Tang, F.Y. Peng, Y. Wang, F. Qiu, The effect of variable cutting depth and thickness on milling stability for orthogonal turn-milling, Int. J. Adv. Manuf. Technol. 82 (2016) 765–777.

[43] A. Comak, Y. Altintas, Dynamics and stability of turn-milling operations with varying time delay in discrete time domain, J. Manuf. Sci. Eng. 140 (2018) 101013.

[44] T. Insperger, G. Stepan, Stability analysis of turning with periodic spindle speed modulation via semidiscretization, J. Vib. Control. 10 (2004) 1835–1855.

[45] R.P.H. Faassen, N. Van de Wouw, J.A.J. Oosterling, H. Nijmeijer, Prediction of regenerative chatter by modelling and analysis of high-speed milling, Int. J. Mach. Tools Manuf. 43 (2003) 1437–1446. https://doi.org/10.1016/S0890-6955(03)00171-8.

[46] X.-H. Long, B. Balachandran, B.P. Mann, Dynamics of milling processes with variable time delays, Nonlinear Dyn. 47 (2007) 49–63.

[47] M.X. Zhao, B. Balachandran, Dynamics and stability of milling process, Int. J. Solids Struct. 38 (2001) 2233–2248.

[48] B. Balachandran, Nonlinear dynamics of milling processes, Philos. Trans. R. Soc. London. Ser. A Math. Phys. Eng. Sci. 359 (2001) 793–819.

[49] E. Budak, E. Ozturk, Dynamics and stability of parallel turning operations, CIRP Ann. 60 (2011) 383–386.

[50] M. Azvar, E. Budak, Multi-dimensional chatter stability for enhanced productivity in different parallel turning strategies, Int. J. Mach. Tools Manuf. 123 (2017) 116–128.

[51] E. Budak, A. Comak, E. Ozturk, Stability and high performance machining conditions in simultaneous milling, CIRP Ann. 62 (2013) 403–406.

[52] J. Slavicek, The effect of irregular tooth pitch on stability of milling, in: Proc. 6th MTDR Conf., 1965: pp. 15–22.

[53] J. Tlusty, F. Ismail, W. Zaton, Milling cutters with irregular pitch, Technical Report, McMaster Engineering, 1982.

[54] J. Tlusty, F. Ismail, W. Zaton, Use of special milling cutters against chatter, Technical Report, University of Wisconsin , 1983.

[55] K. Shirase, M. Sano, M. Hirao, T. Yasui, Analysis and suppression of chatter vibration in end milling operation (1st report) - Analysis of chatter vibration for irregular tooth pitch end mill using time domain cutting simulation, Seimitsu Kogaku Kaishi/Journal Japan Soc. Precis. Eng. 65 (1999) 465–469.

[56] Y. Altintaş, S. Engin, E. Budak, Analytical stability prediction and design of variable pitch cutters, J. Manuf. Sci. Eng. Trans. ASME. 121 (1999) 173–178. https://doi.org/10.1115/1.2831201.

[57] E. Budak, An Analytical Design Method for Milling Cutters With Nonconstant Pitch to Increase Stability, Part I: Theory, J. Manuf. Sci. Eng. 125 (2003) 29–34. https://doi.org/10.1115/1.1536655.

[58] E. Budak, An Analytical Design Method for Milling Cutters With Nonconstant Pitch to Increase Stability, Part 2: Application, J. Manuf. Sci. Eng. 125 (2003) 35–38. https://doi.org/10.1115/1.1536656.

[59] A. Iglesias, Z. Dombovari, G. Gonzalez, J. Munoa, G. Stepan, Optimum selection of variable pitch for chatter suppression in face milling operations, Materials (Basel). 12 (2019) 112.

[60] N. Suzuki, R. Ishiguro, T. Kojima, Design of irregular pitch end mills to attain robust suppression of regenerative chatter, CIRP Ann. 65 (2016) 129–132.

[61] A. Comak, E. Budak, Modeling dynamics and stability of variable pitch and helix milling tools for development of a design method to maximize chatter stability, Precis. Eng. 47 (2017) 459–468. https://doi.org/http://dx.doi.org/10.1016/j.precisioneng.2016.09.021.

[62] J. Munoa, X. Beudaert, Z. Dombovari, Y. Altintas, E. Budak, C. Brecher, G. Stepan, Chatter suppression techniques in metal cutting, CIRP Ann. 65 (2016) 785–808. https://doi.org/https://doi.org/10.1016/j.cirp.2016.06.004.

[63] B. Stone, Chatter and machine tools, Springer, 2014.

[64] S.D. Merdol, Y. Altintas, Mechanics and Dynamics of Serrated Cylindrical and Tapered End Mills, J. Manuf. Sci. Eng. 126 (2004) 317–326. https://doi.org/10.1115/1.1644552.

[65] Z. Dombovari, Y. Altintas, G. Stepan, The effect of serration on mechanics and stability of milling cutters, Int. J. Mach. Tools Manuf. 50 (2010) 511–520. https://doi.org/http://dx.doi.org/10.1016/j.ijmachtools.2010.03.006.

[66] N.D. Farahani, Y. Altintas, Chatter Stability of Serrated Milling Tools in Frequency Domain, J. Manuf. Sci. Eng. 144 (2021) 31013.

[67] F. Tehranizadeh, E. Budak, Design of serrated end mills for improved productivity, Procedia CIRP. 58 (2017) 493–498. https://doi.org/10.1016/j.procir.2017.03.256.

[68] F. Tehranizadeh, R. Koca, E. Budak, Investigating effects of serration geometry on milling forces and chatter stability for their optimal selection, Int. J. Mach. Tools Manuf. (2019) 103425.

[69] P. Bari, M. Law, P. Wahi, Improved chip thickness model for serrated end milling, CIRP J. Manuf. Sci. Technol. 25 (2019) 36–49.

[70] Z. Dombovari, G. Stepan, The Effect of Helix Angle Variation on Milling Stability, J. Manuf. Sci. Eng. 134 (2012) 51015–51016. https://doi.org/10.1115/1.4007466.

[71] T. Hayasaka, A. Ito, E. Shamoto, Generalized design method of highly-varied-helix end mills for suppression of regenerative chatter in peripheral milling, Precis. Eng. 48 (2017) 45–59. https://doi.org/10.1016/j.precisioneng.2016.11.004.

[72] S. Turner, D. Merdol, Y. Altintas, K. Ridgway, Modelling of the stability of variable helix end mills, Int. J. Mach. Tools Manuf. 47 (2007) 1410–1416. https://doi.org/10.1016/j.ijmachtools.2006.08.028.

[73] N.D. Sims, Fast chatter stability prediction for variable helix milling tools, Proc. Inst. Mech. Eng. Part C J. Mech. Eng. Sci. 230 (2016) 133–144.

[74] Z. Dombovari, G. Stepan, The effect of harmonic helix angle variation on milling stability, in: Int. Des. Eng. Tech. Conf. Comput. Inf. Eng. Conf., 2011: pp. 467–473.

[75] M. Sanz, A. Iglesias, J. Munoa, Z. Dombovari, The effect of geometry on harmonically varied helix milling tools, J. Manuf. Sci. Eng. Trans. ASME. 142 (2020). https://doi.org/10.1115/1.4046901.

[76] T. No, M. Gomez, R. Copenhaver, J.U. Perez, C. Tyler, T.L. Schmitz, Force and stability modeling for non-standard edge geometry endmills, J. Manuf. Sci. Eng. Trans. ASME. 141 (2019). https://doi.org/10.1115/1.4045057.

[77] F. Tehranizadeh, K.R. Berenji, E. Budak, Dynamics and chatter stability of crest-cut end mills, Int. J. Mach. Tools Manuf. 171 (2021) 103813.

[78] E. Budak, L.T. Tunç, S. Alan, H.N. Özgüven, Prediction of workpiece dynamics and its effects on chatter stability in milling, CIRP Ann. 61 (2012) 339–342.

[79] U. Bravo, O. Altuzarra, L.N.L. De Lacalle, J.A. Sánchez, F.J. Campa, Stability limits of milling considering the flexibility of the workpiece and the machine, Int. J. Mach. Tools Manuf. 45 (2005) 1669–1680.

[80] V. Thévenot, L. Arnaud, G. Dessein, G. Cazenave–Larroche, Influence of material removal on the dynamic behavior of thin-walled structures in peripheral milling, Mach. Sci. Technol. 10 (2006) 275–287.

[81] D. Biermann, P. Kersting, T. Surmann, A general approach to simulating workpiece vibrations during five-axis milling of turbine blades, CIRP Ann. 59 (2010) 125–128.

[82] S. Alan, E. Budak, H.N. Özgüven, Analytical prediction of part dynamics for

machining stability analysis, Int. J. Autom. Technol. 4 (2010) 259–267.

[83] O. Tuysuz, Y. Altintas, Frequency domain updating of thin-walled workpiece dynamics using reduced order substructuring method in machining, J. Manuf. Sci. Eng. 139 (2017).

[84] Altintas Y , Author, Ber AA , Reviewer, Manufacturing Automation: Metal Cutting Mechanics, Machine Tool Vibrations, and CNC Design, Appl. Mech. Rev. 54 (2001) B84–B84. https://doi.org/10.1115/1.1399383.

[85] T.A. Harris, Rolling bearing analysis, John Wiley and sons, 2001.

[86] Y. Cao, Y. Altintas, Modeling of spindle-bearing and machine tool systems for virtual simulation of milling operations, Int. J. Mach. Tools Manuf. 47 (2007) 1342–1350. https://doi.org/10.1016/j.ijmachtools.2006.08.006.

[87] H. Li, Y.C. Shin, Analysis of bearing configuration effects on high speed spindles using an integrated dynamic thermo-mechanical spindle model, Int. J. Mach. Tools Manuf. 44 (2004) 347–364.

[88] O. Özşahin, E. Budak, H.N. Özgüven, Identification of bearing dynamics under operational conditions for chatter stability prediction in high speed machining operations, Precis. Eng. 42 (2015) 53–65.

[89] M. Postel, O. Özsahin, Y. Altintas, High speed tooltip FRF predictions of arbitrary tool-holder combinations based on operational spindle identification, Int. J. Mach. Tools Manuf. 129 (2018) 48–60.

[90] O. Özşahin, E. Budak, H.N. Özgüven, In-process tool point FRF identification under operational conditions using inverse stability solution, Int. J. Mach. Tools Manuf. 89 (2015) 64–73.

[91] G.L. Xiong, J.M. Yi, C. Zeng, H.K. Guo, L.X. Li, Study of the gyroscopic effect of the spindle on the stability characteristics of the milling system, J. Mater. Process. Technol. 138 (2003) 379–384. https://doi.org/10.1016/S0924-0136(03)00102-X.

[92] M.R. Movahhedy, P. Mosaddegh, Prediction of chatter in high speed milling including gyroscopic effects, Int. J. Mach. Tools Manuf. 46 (2006) 996–1001. https://doi.org/10.1016/j.ijmachtools.2005.07.043.

[93] T.L. Schmitz, R.R. Donalson, Predicting high-speed machining dynamics by substructure analysis, Cirp Ann. 49 (2000) 303–308.

[94] T.L. Schmitz, M.A. Davies, M.D. Kennedy, Tool point frequency response prediction for high-speed machining by RCSA, J. Manuf. Sci. Eng. 123 (2001) 700–707.

[95] A. Ertürk, H.N. Özgüven, E. Budak, Analytical modeling of spindle-tool dynamics on machine tools using Timoshenko beam model and receptance coupling for the prediction of tool point FRF, Int. J. Mach. Tools Manuf. 46 (2006) 1901–1912. https://doi.org/10.1016/j.ijmachtools.2006.01.032.

[96] A. Ertürk, E. Budak, H.N. Özgüven, Selection of design and operational parameters in spindle–holder–tool assemblies for maximum chatter stability by using a new analytical model, Int. J. Mach. Tools Manuf. 47 (2007) 1401–1409.

[97] Y. Cao, Y. Altintas, A general method for the modeling of spindle-bearing systems, J Mech. Des. 126 (2004) 1089–1104.

[98] H. Cao, B. Li, Y. Li, T. Kang, X. Chen, Model-based error motion prediction and fit clearance optimization for machine tool spindles, Mech. Syst. Signal Process. 133 (2019) 106252.

[99] C. Wang, X. Zhang, R. Yan, X. Chen, H. Cao, Multi harmonic spindle speed variation for milling chatter suppression and parameters optimization, Precis. Eng. 55 (2019) 268–274.

[100] E. Abele, Y. Altintas, C. Brecher, Machine tool spindle units, CIRP Ann. 59 (2010) 781–802.

[101] G.D. Hagiu, M.D. Gafitanu, Dynamic characteristics of high speed angular contact ball bearings, Wear. 211 (1997) 22–29.

[102] S.-T. Choi, S.-Y. Mau, Dynamic analysis of geared rotor-bearing systems by the transfer matrix method, J. Mech. Des. 123 (2001) 562–568.

[103] G.-H. Bae, C.-H. Lee, J.-H. Hwang, S.-W. Hong, Estimation of axial displacement in high-speed spindle due to rotational speed, J. Korean Soc. Precis. Eng. 29 (2012) 671–679.

[104] H. Senda, R. Sato, T. Moriwaki, Estimation of thermal displacement under varying rotational condition of spindle, Trans. JSME. 70 (2005) 2813–2818.

[105] J. JĘDRZEJEWSKI, W. Modrzycki, Compensation of thermal displacements of high-speed precision machine tools, J. Mach. Eng. 7 (2007) 108–114.

[106] J.S. Chen, Y.W. Hwang, Centrifugal force induced dynamics of a motorized high-speed spindle, Int. J. Adv. Manuf. Technol. 30 (2006) 10–19. https://doi.org/10.1007/s00170-005-0032-y.

[107] J. Jedrzejewski, W. Kwasny, Modelling of angular contact ball bearings and axial displacements for high-speed spindles, CIRP Ann. 59 (2010) 377–382.

[108] I. Zverv, Y.-S. Pyoun, K.-B. Lee, J.-D. Kim, I. Jo, A. Combs, An elastic deformation model of high speed spindles built into ball bearings, J. Mater. Process. Technol. 170 (2005) 570–578.

[109] G.H. Bae, C.H. Lee, J.H. Hwang, S.W. Hong, Evaluation of axial displacement in high-speed spindle supported by angular contact ball bearings, in: Proc. KSPE Autumn Conf., 2011: pp. 299–300.

[110] E. Budak, Y. Altintaş, E.J.A. Armarego, Prediction of milling force coefficients from orthogonal cutting data, J. Manuf. Sci. Eng. Trans. ASME. 118 (1996) 216–224. https://doi.org/10.1115/1.2831014.

[111] Y. Altintas, Manufacturing automation: metal cutting mechanics, machine tool vibrations, and CNC design, Cambridge university press, 2012.

[112] G. V Stabler, The chip flow law and its consequences, Adv. Mach. Tool Des. Res. 5 (1964) 243–251.

[113] R.H. Brown, E.J.A. Armarego, Oblique machining with a single cutting edge, Int. J. Mach. Tool Des. Res. 4 (1964) 9–25. https://doi.org/10.1016/0020-7357(64)90006-X.

[114] E. Budak, Analytical models for high performance milling. Part I: Cutting forces, structural deformations and tolerance integrity, Int. J. Mach. Tools Manuf. 46

(2006) 1478–1488.

[115] G. Urbikain, L.N.L. De Lacalle, F.J. Campa, A. Fernández, A. Elías, Stability prediction in straight turning of a flexible workpiece by collocation method, Int. J. Mach. Tools Manuf. 54 (2012) 73–81.

[116] H. Manikandan, T.C. Bera, A turning simulation environment for geometric error estimation of thin-walled parts, Int. J. Adv. Manuf. Technol. 119 (2022) 789–809.

[117] E. Budak, Y. Altintas, Analytical prediction of chatter stability in milling—part I: general formulation, J. Dyn. Syst. Meas. Control. 120 (1998) 22–30.

[118] T. Insperger, G. Stepan, Semi-Discretization for Time-Delay Systems Stability and Engineering Applications, 1st ed., Springer-Verlag New York, 2011.

[119] C. Eksioglu, Z.M. Kilic, Y. Altintas, Discrete-time prediction of chatter stability, cutting forces, and surface location errors in flexible milling systems, J. Manuf. Sci. Eng. 134 (2012).

[120] S.D. Merdol, Y. Altintas, Mechanics and Dynamics of Serrated End Mills, ASME Int. Mech. Eng. Congr. Expo. . (2002) 337–342. https://doi.org/10.1115/IMECE2002-39114.

[121] E. Budak, An analytical design method for milling cutters with nonconstant pitch to increase stability, part I: theory, J. Manuf. Sci. Eng. 125 (2003) 29–34.

[122] E. Budak, Y. Altintas, Analytical prediction of chatter stability in milling—part II: application of the general formulation to common milling systems, J. Dyn. Syst. Meas. Control. 120 (1998) 31–36.

[123] P. Bari, Z.M. Kilic, M. Law, P. Wahi, Rapid stability analysis of serrated end mills using graphical-frequency domain methods, Int. J. Mach. Tools Manuf. 171 (2021) 103805. https://doi.org/10.1016/j.ijmachtools.2021.103805.

[124] E. Ozturk, E. Budak, Modeling of 5-axis milling processes, Mach. Sci. Technol. 11 (2007) 287–311. https://doi.org/10.1080/10910340701554808.

[125] E. Budak, E. Ozturk, L.T. Tunc, Modeling and simulation of 5-axis milling processes, CIRP Ann. - Manuf. Technol. 58 (2009) 347–350. https://doi.org/10.1016/j.cirp.2009.03.044.

[126] MAL Inc, CUTPRO V15.0, Advanced Machining Simulation Software ©MAL Inc, (n.d.). https://www.malinc.com/.

[127] E. Budak, An analytical design method for milling cutters with nonconstant pitch to increase stability, part 2: application, J. Manuf. Sci. Eng. 125 (2003) 35–38.

[128] F. Tehranizadeh, K.R. Berenji, S. Yıldız, E. Budak, Chatter stability of thin-walled part machining using special end mills, CIRP Ann. (2022).

[129] S.D. Merdol, Y. Altintas, Multi frequency solution of chatter stability for low immersion milling, J. Manuf. Sci. Eng. 126 (2004) 459–466.

[130] T. Insperger, G. Stépán, P. V Bayly, B.P. Mann, Multiple chatter frequencies in milling processes, J. Sound Vib. 262 (2003) 333–345.

[131] M.A. Davies, J.R. Pratt, B. Dutterer, T.J. Burns, Stability prediction for low radial immersion milling, J. Manuf. Sci. Eng. 124 (2002) 217–225.

[132] E. Budak, L.T. Tunç, Identification and modeling of process damping in turning and milling using a new approach, CIRP Ann. 59 (2010) 403–408.

[133] E. Budak, L. Kops, Improving productivity and part quality in milling of titanium based impellers by chatter suppression and force control, CIRP Ann. 49 (2000) 31–36.

[134] O. Özşahin, A. Ertürk, H.N. Özgüven, E. Budak, A closed-form approach for identification of dynamical contact parameters in spindle–holder–tool assemblies, Int. J. Mach. Tools Manuf. 49 (2009) 25–35.

[135] J.M. de Mul, J.M. Vree, D.A. Maas, Equilibrium and Associated Load Distribution in Ball and Roller Bearings Loaded in Five Degrees of Freedom While Neglecting Friction—Part II: Application to Roller Bearings and Experimental Verification, J. Tribol. 111 (1989) 149–155. https://doi.org/10.1115/1.3261865.

[136] T. Harris, M. Kotzalas, N. Michael, Roller Bearing Analysis: Advanced Concepts of Bearing Technology, (2007).

[137] S.-W. Hong, C.-S. Choi, C.-H. Lee, Effects of Bearing Arrangement on the Dynamic Characteristics of High-speed Spindle, J. Korean Soc. Precis. Eng. 30 (2013) 854–863.

[138] B. Fang, K. Yan, J. Hong, J. Zhang, A comprehensive study on the off-diagonal coupling elements in the stiffness matrix of the angular contact ball bearing and their influence on the dynamic characteristics of the rotor system, Mech. Mach. Theory. 158 (2021) 104251.

[139] B. Bossmanns, J.F. Tu, A thermal model for high speed motorized spindles, Int. J. Mach. Tools Manuf. 39 (1999) 1345–1366.

[140] B. Bossmanns, J.F. Tu, A power flow model for high speed motorized spindles—heat generation characterization, J. Manuf. Sci. Eng. 123 (2001) 494–505.

[141] T.L. Schmitz, G.S. Duncan, Three-component receptance coupling substructure analysis for tool point dynamics prediction, (2005).

[142] H.N. Özgüven, Structural modifications using frequency response functions, Mech. Syst. Signal Process. 4 (1990) 53–63.

[143] A. Ertürk, H.N. Özgüven, E. %J I.J. of M.T. Budak, Manufacture, Analytical modeling of spindle–tool dynamics on machine tools using Timoshenko beam model and receptance coupling for the prediction of tool point FRF, 46 (2006) 1901–1912.